UNIVERSITY OF LEICESTER

DOCTORAL THESIS

Stellar Feedback in Giant Molecular Clouds and Dwarf Galaxies

---

Lilian Garratt-Smithson

A thesis submitted in fulfillment of the requirements for the degree of Doctor of Philosophy

in the

Theoretical Astrophysics Group
Department of Physics and Astronomy

2018

Abstract

Lilian GARRATT-SMITHSON

Stellar Feedback in Giant Molecular Clouds and Dwarf Galaxies

The primary aim of this thesis is to investigate the interplay between time resolved 'gradual' feedback processes, such as line-driven stellar winds and HMXBs (High Mass X-ray Binaries), with 'instantaneous' SNe (supernovae). I do this through high resolution SPH (smoothed particle hydrodynamical) simulations of isolated GMCs (Giant Molecular Clouds) and dSphs (Dwarf Spheroidal Galaxies). These systems are of particular interest since their shallow potential wells mean they are susceptible to stellar feedback processes. By modelling HMXBs and SNe in GMCs across a range of parameters, I find that SNe feedback can carve low density chimneys in the gas, offering a path of least resistance for the energy to escape. Once this occurs the more stable, but less energetic, gradual feedback is able to keep the chimneys open. By funneling the hot destructive gas away from the centre of the cloud, chimneys can have a positive effect on both the efficiency and duration of star formation.

Furthermore, I included both stellar winds and HMXB feedback on top of SNe in high redshift dwarf galaxies, finding the mass of gas unbound by stellar feedback across a 1 Gyr starburst is uniformly lowered if gradual feedback mechanisms are included, independent of metallicity, galaxy mass, halo concentration and the duration of the starburst. Furthermore, I find including gradual feedback in the smallest galaxies (of halo mass $\sim 10^7$ $M_\odot$) delays the unbinding of the gas and facilitates the production of chimneys in the dense shell surrounding feedback-generated hot, pressurised 'superbubbles'. These chimneys vent hot gas from the galaxy interior, lowering the temperature of the central 10 kpc of the gaseous halo. Intriguingly, the underlying dark matter halo of the smallest galaxy is less effected by the gaseous outflows generated by the stellar feedback than the larger halo.

Papers associated with this thesis (submitted to Monthly Notices of the Royal Astronomy Society):

1) "Does slow and steady win the race? Investigating feedback processes in giant molecular clouds" Garratt-Smithson et al. (2018) MNRAS, 480, pp. 2985-3016
2) "Galactic chimney sweeping: Investigating gradual stellar feedback in dwarf galaxies" Garratt-Smithson et al. (2019) To be submitted to MNRAS

Acknowledgements

I would like to thank my supervisor Graham Wynn for his support and encouragement throughout my PhD, along with Chris Nixon for all his help and advice. Furthermore, I am very grateful to Chris Power, Martin Bourne and Claire Cashmore for their invaluable advice on GADGET and their helpful discussions during my PhD. As well as this I thank the theory group, both staff and fellow members of the bat cave, for their many discussions and for maintaining a friendly, supportive environment. I also thank Lisa Brandt for her help in organising my various trips, along with Gary Gilchrist for providing excellent computational support.

I am very grateful to the University of Leicester for giving me the chance to study Physics and for a fantastic 9 years. I'd also like to say thank you to STFC for giving me the studentship to fund this project. Additionally, this work would not have been possible without the DiRAC Complexity system, operated by the University of Leicester IT Services. Furthermore, I would like to acknowledge SPLASH (Price, 2007), which I used to generate many of the plots in this thesis.

Finally, I would like to thank my parents Simon and Beverley for their constant support over the entirety of my education and for showing me the importance of working hard but also enjoying yourself while you do it. They have given me the confidence to follow my passion and pursue this career. I am also very thankful to Josh for all of his encouragement and for letting me drag him across the world so that I can continue to work in this fascinating area of science.

Contents

List of Figures vii

List of Tables xii

List of Abbreviations xiii

1 An introduction to stellar feedback 1

1.1 The importance of stellar feedback in galaxy evolution 1

1.2 SNe, HMXBs and Stellar Winds 4

1.2.1 SNe 4

1.2.1.1 The Evolution of Supernova Remnants (SNRs) . . 5

1.2.1.2 Computational modelling of SNe and the 'over-cooling' problem 6

1.2.2 High Mass X-ray Binaries (HMXBs) 8

1.2.2.1 A note on the importance of binary systems 11

1.2.2.2 Computational modelling of HMXBs 12

1.2.3 Line-driven stellar winds 12

1.2.3.1 Computational modelling of stellar winds 13

1.3 Introducing Giant Molecular Clouds and Dwarf Spheroidal Galaxies 14

1.3.1 Giant Molecular Clouds (GMCs) 14

1.3.1.1 Computational Modelling of Stellar Feedback Inside GMCs 14

1.3.2 Dwarf Spheroidal Galaxies (dSphs) 15

1.4 This thesis 17

2 Numerical Modelling 19

2.1 The non-baryonic components 19

2.1.1 The tree algorithm 20

2.2 SPH - Smoothed Particle Hydrodynamics 21

2.2.1 Neighbour number 21
2.2.2 Choice of smoothing kernel 22
2.2.3 The equations of motion of SPH particles 23
2.2.4 Artificial viscosity and SPHS 24
2.3 The time integration scheme 26
2.4 Cooling 28
2.4.1 Below 10^4 K 28
2.4.2 10^4 K - 10^6 K 29
2.4.3 Above 10^6 K 29
2.4.4 Cooling in GADGET-3 31

3 Investigating stellar feedback in GMCs: Part I ($Z_\odot$) 32
3.1 Introduction 32
3.2 The numerical model 33
3.2.1 Basics of the model 33
3.2.2 Binary Population Synthesis 35
3.2.3 Feedback Mechanisms 38
3.3 Sedov-Taylor Comparison 40
3.4 Initial Conditions 42
3.5 Results, [Fe/H] = 0 45
3.5.1 Runs with no feedback: D, G, J, M 45
3.5.2 The injection of HMXB: Runs A (HMXB and SNe), C (Just SNe) 46
3.5.3 Changing the virial parameter, $\alpha_{vir} = 1.2$: Runs E,F 66
3.5.4 Changing the size of the molecular cloud: Runs R, S, V, W . 73
3.5.5 Thermal vs Kinetic HMXB feedback: Runs A and B 80
3.6 Discussion: $Z_\odot$ Runs 83
3.6.1 The set-up in context 85
3.7 Next chapter, low Z runs 87

4 Investigating stellar feedback in GMCs: Part II (low Z) 88
4.1 Introduction 88
4.1.1 The numerical model 89
4.2 Results, [Fe/H] = -1.2 91
4.2.1 The injection of HMXB: Runs H, I 91
4.2.2 $\alpha_{\rm vir} = 1.2$ Runs: K (HMXB and SNe), L (SNe), M (no feedback) 103

4.2.3 Changing the gas cloud size: 5×10^5 $M_\odot$ – T, U, 5×10^6 $M_\odot$ – X, Y . . . 104
4.3 Resolution Tests . . . 106
4.3.1 Nyquist Frequency . . . 106
4.3.2 Convergence Testing . . . 108
4.4 Discussion . . . 115
4.4.1 The results: chimneys . . . 115

5 Investigating stellar feedback in dSphs 118
5.1 Introduction . . . 118
5.2 Numerical Model . . . 120
5.3 Initial Conditions . . . 121
5.3.1 Massive Star Population . . . 123
5.4 Feedback Prescriptions . . . 124
5.5 Results . . . 125
5.5.1 The massive star population of each galaxy . . . 125
5.5.2 Simulations with no stellar feedback included . . . 128
5.5.3 Gradual versus instantaneous feedback (Runs 1 and 2) . . . 131
5.5.4 Changing the dark matter softening length . . . 149
5.5.5 Decreasing σ_{star} (Runs 9 and 10) . . . 151
5.5.6 Changing metallicity (Runs 7 and 8) . . . 161
5.5.7 Increasing the concentration parameter (Runs 3 and 4) . . . 165
5.5.8 A smaller galaxy (Runs 5 and 6) . . . 171
5.5.9 Evaluating the relative impact of HMXBs and stellar winds (Runs NoHMXB and NoWinds) . . . 184
5.6 Discussion . . . 188
5.6.1 The results in context . . . 189

6 Conclusions 192
6.1 Investigating stellar feedback in GMCs . . . 192
6.2 Investigating stellar feedback in dSphs . . . 193
6.3 Future work . . . 193

Bibliography 195

List of Figures

2.1 GADGET-3 Cooling curves 30

3.1 GMCs: Sedov Taylor Test; density slices 41
3.2 GMCs: Sedov Taylor Test; multiple plots 43
3.3 GMCs: Time evolution of the total energy in runs without feedback 47
3.4 GMCs: Energy plots for Run D 48
3.5 GMCs: Time evolution of the sink mass fraction in runs without feedback 49
3.6 GMCs: Density slices taken at 35 Myr, $Z_\odot$ 50
3.7 GMCs: Temperature slices taken at 35 Myr, $Z_\odot$ 51
3.8 GMCs: Density slices at 35 Myr in the xz plane, Run A 52
3.9 GMCs: θ bins, $Z_\odot$ 54
3.10 GMCs: Net radial momentum etc., $Z_\odot$ 55
3.11 GMCs: Density slices taken 12 Myr into Run A 57
3.12 GMCs: Density slices taken 12 Myr into Run C 58
3.13 GMCs: Temperature slices taken 12 Myr into Run A 58
3.14 GMCs: Temperature slices taken 12 Myr into Run C 59
3.15 GMCs: Time evolution of the total energy, $Z_\odot$ runs 60
3.16 GMCs: Number of HMXBs and SNe active, $Z_\odot$ runs 61
3.17 GMCs: Time evolution of the cumulative injected energy, Runs A,B,C 62
3.18 GMCs: Plots to show fraction of initial gas mass that has been unbound or formed sinks, $Z_\odot$ runs 63
3.19 GMCs: Number of sink particles produced between snapshots, $Z_\odot$ runs 64
3.20 GMCs: Temperature versus density at 14 Myr, Runs A and C 65
3.21 GMCs: Temperature versus density, at 19 Myr and 22 Myr for Runs E and F 67
3.22 GMCs: Temperature slices, at 19 Myr and 22 Myr for Runs E and F 68

3.23 GMCs: Plots to show the time evolution of the temperature, density and velocities of 4600 gas particles heated in Run F 70
3.24 GMCs: Sink mass histogram, Runs A and E 72
3.25 GMCs: Temperature versus density plot taken at 35 Myr, Runs V and W 76
3.26 GMCs: Cumulative feedback energy plot, Runs V and W 78
3.27 GMCs: The mean cooling times and densities in θ bins taken at 14 Myr, Run V and W 79
3.28 GMCs: Mean radial velocity and momentum versus radius at t = 35 Myr, Runs A and B 81

4.1 GMCs: Density slices taken at 35 Myr, low Z runs 92
4.2 GMCs: Temperature slices taken at 35 Myr, low Z runs 93
4.3 GMCs: θ bins, low Z runs 94
4.4 GMCs: Cumulative injected energy, low Z runs 95
4.5 GMCs: Number of HMXBs and SNe active across simulations, low Z runs 96
4.6 GMCs: Time evolution of the ratio between the energy injected by HMXBs and SNe in Runs A, E, H and X 97
4.7 GMCs: Time evolution of the total energy, low Z runs 98
4.8 GMCs: Plots to show the fraction of initial gas mass that has been unbound or formed sinks, low Z runs 100
4.9 GMCs: Plots to show the number of sinks produced between snapshots, low Z runs 101
4.10 GMCs: Histogram of cooling times and densities for Runs H and I, low Z runs 102
4.11 GMCs: Density slices taken at 11.7 Myr, Nyquist resolution test . . 107
4.12 GMCs: Temperature slices taken at 11.7 Myr, Nyquist resolution test 108
4.13 GMCs: Number of HMXBs active between snapshot times, Nyquist resolution test 109
4.14 GMCs: Energy injected between snapshot times, Nyquist resolution test 110
4.15 GMCs: Density slices taken at 35 Myr, convergence tests 111
4.16 GMCs: Temperature slices taken at 35 Myr, convergence tests . . . 112

4.17 GMCs: Fraction of gas that has been unbound/ expelled from the simulations, convergence tests . . . 113
4.18 GMCs: Temperature versus density plot at 11 Myr, convergence tests 114

5.1 dSphs: Primary and companion masses assigned . . . 126
5.2 dSphs: Histogram to show the distribution of primary and companion lifetimes along with star particle wake-up times . . . 127
5.3 dSphs: The energetics of the runs which do not include feedback . 128
5.4 dSphs: Gas density profiles at varying times, runs without feedback 129
5.5 dSphs: Dark matter density profiles at varying times, runs without feedback . . . 130
5.6 dSphs: Gas density profiles taken at various times, Runs 1 and 2 . . 133
5.7 dSphs: The time evolution of the mass inflow and outflow rate at various radii, Runs 1 and 2 . . . 134
5.8 dSphs: The time evolution of the gas mass contained inside various radii, Runs 1 and 2 . . . 135
5.9 dSphs: The time evolution of the unbound mass fraction for all dSphs runs . . . 136
5.10 dSphs: The time evolution of the global energetics, Runs 1 and 2 . . 137
5.11 dSphs: The gas mass in 20 temperature bins, Runs 1 and 2 . . . 138
5.12 dSphs: The time evolution of the gas temperature, Runs 1 and 2 . . 139
5.13 dSphs: The time evolution of the mean radius of gas particles, Runs 1 and 2 . . . 141
5.14 dSphs: Density and temperature slices at 1 Gyr, Runs 1 and 2 . . . 142
5.15 dSphs: Temperature versus density of the gas at 1 Gyr, Runs 1 and 2 143
5.16 dSphs: Density slices at varying times, Runs 1 and 2 . . . 144
5.17 dSphs: Dark matter density profiles taken at various times, Runs 1 and 2 . . . 146
5.18 dSphs: The total energy of 4 dark matter particles taken from various radii, Runs 1 and 2 . . . 148
5.19 dSphs: Unbound gas mass fraction, Run 1 and runs with varying dark matter softening length . . . 149
5.20 dSphs: The time evolution of the gas energetics, Run 1 and runs with varying dark matter softening length . . . 150

5.21 dSphs: Dark matter density profiles taken at 1 Gyr, Run 1 and runs with varying dark matter softening length 151
5.22 dSphs: The energy injected via SNe, HMXBs and winds across Runs 1, 9 and 7 153
5.23 dSphs: Comparison of the global energetics of Runs 1, 2, 9 and 10 . 154
5.24 dSphs: Density and temperature slices taken at 1 Gyr, Runs 9 and 10 155
5.25 dSphs: Gas density profiles taken at various times, Runs 9 and 10 . 156
5.26 dSphs: Dark matter density profiles taken at various times, Runs 9 and 10 159
5.27 dSphs: The time evolution of the total energy of 4 dark matter particles taken from various radii, Runs 9 and 10 160
5.28 dSphs: The time evolution of the net radial momentum, mean temperature and mean radius of the gas in Runs 7 and 8 162
5.29 dSphs: Gas density profiles taken at various times, Runs 7 and 8 . . 163
5.30 dSphs: Dark matter density profiles taken at various times, Runs 7 and 8 164
5.31 dSphs: Density and temperature slices taken at 1 Gyr, Runs 3 and 4 166
5.32 dSphs: Gas density profiles taken at various times, Runs 3 and 4 . . 167
5.33 dSphs: The time evolution of the global energetics of the gas, Runs 3 and 4 168
5.34 dSphs: Dark matter density profiles taken at various times, Runs 3 and 4 169
5.35 dSphs: The time evolution of the total energy of 4 dark matter particles taken from various radii, Runs 3 and 4 170
5.36 dSphs: Density and temperature slices taken at 1 Gyr, Runs 5 and 6 172
5.37 dSphs: Temperature versus density for the gas at 489 Myr, Runs 5 and 6 173
5.38 dSphs: Density versus radius for a sample of particles, Runs 5 . . . 174
5.39 dSphs: Radial velocity versus radius for a sample of particles, Runs 5 175
5.40 dSphs: Density versus radius for all particles, Runs 5 176
5.41 dSphs: Density and temperature slices at 489 Myr, Runs 5 and 6 . . 177
5.42 dSphs: Density and temperature slices taken between 587 Gyr and 665 Gyr, Run 5 178
5.43 dSphs: Time evolution of gas temperature, Runs 5 and 6 179

5.44 dSphs: Time evolution of the global energetics of the gas, Runs 5 and 6 180
5.45 dSphs: Gas density profiles taken at various times, Runs 5 and 6 . . 181
5.46 dSphs: Dark matter density profiles taken at various times, Runs 5 and 6 182
5.47 dSphs: The time evolution of the total energy of 4 dark matter particles taken from various radii, Runs 5 and 6 183
5.48 dSphs: The time evolution of the unbound gas fraction, Runs 1, 2, NoWinds and NoHMXB 185
5.49 dSphs: The time evolution of the global energetics of the gas, Runs 1, 2, NoWinds and NoHMXB 186
5.50 dSphs: The dark matter profiles taken at various times, Runs 1, 2, NoWinds and NoHMXB 187

List of Tables

3.1 GMCs: The initial conditions of the $Z_\odot$ runs 44
3.2 GMCs: Table showing sink properties in the $Z_\odot$ runs 71

4.1 GMCs: Table showing initial conditions for low Z runs 90
4.2 GMCs: Table showing sink properties in the low Z runs 91

5.1 dSphs: Table to summarise the initial conditions of the dSph runs . 122

List of Abbreviations

AGN	**A**ctive **G**alactic **N**uclei
BCD	**B**lue **C**ompact **D**warf Galaxies
BH	**B**lack **H**ole
BH-HMXB	**H**igh **M**ass **X**-ray **B**inary containing a **B**lack **H**ole
CMD	**C**olour **M**agnitude **D**iagram
CRs	**C**osmic **R**ays
dSphs	**D**warf **Sph**eroidal Galaxies
GMC	**G**iant **M**olecular **C**loud
GRB	**G**amma **R**ay **B**urst
HMXB	**H**igh **M**ass **X**-ray **B**inary
IGM	**I**nter**G**alactic **M**edium
ISM	**I**nter**S**tellar **M**edium
LMXB	**L**ow **M**ass **X**-ray **B**inary
LMC	**L**arge **M**agellanic **C**loud
MC	**M**olecular **C**loud
$\mathbf{M}_{200}$	Virial Mass
NS	**N**eutron **S**tar
$\mathbf{r}_{200}$	Virial Radius
SFH	**S**tar **F**ormation **H**istory
SFR	**S**tar **F**ormation **R**ate
SNe	**S**upernovae
SNR	**S**uper**N**ova **R**emnant
SPH	**S**moothed **P**article **H**ydrodynamics
ULX	**U**ltra **L**uminous **X**-ray source
XRB	**X**-**R**ay **B**inary
QSO	**Q**uasars
z	Redshift
Z	Metallicity

This is dedicated to my parents,
Beverley and Simon

Chapter 1

An introduction to stellar feedback

1.1 The importance of stellar feedback in galaxy evolution

The focus of this thesis is on how various different types of stellar feedback can affect their environments. Stellar feedback is the injection of energy into the surrounding ISM (Interstellar Medium) via a variety of stellar processes. One of the most compelling pieces of evidence for stellar feedback is the low ($1-3\%$) efficiency of the conversion of gas mass to stellar mass observed in both galaxies and MCs (molecular clouds) that are star-forming (Myers et al., 1986; Evans et al., 2009; Murray, Quataert, and Thompson, 2010; Dale and Bonnell, 2011; Walch et al., 2012; Krumholz, 2014; Skinner and Ostriker, 2015; Rahner et al., 2017). This is known as 'negative' feedback since it suppresses further star formation by heating the surrounding gas and preventing the collapse of cold ($\sim$ 10K) molecular gas into stars. There have also been near-ubiquitous observations of gaseous outflows associated with star forming galaxies, both at low and high redshift and with outflow velocities ranging from 100-1000kms^{-1} (e.g. Frye, Broadhurst, and Benítez, 2002; Kornei et al., 2012; Tang et al., 2014; Arribas et al., 2014). Moreover, these outflows, along with the subsequent removal of metals, are considered integral to the evolution of galaxy metallicity (Z), as evidenced by the correlation between Z and stellar mass (this is known as the MZ relation - Lequeux et al., 1979), which is itself dependent on both SFR (star formation rate - Andrews and Martini, 2013) and stellar age (e.g. Lian et al., 2015).

Furthermore, stellar feedback is likely to have played a fundamental role in the re-ionisation of the universe between redshifts z $\sim 20-6$. The Epoch of Reionisation (EoR) is the transition of the neutral IGM (Intergalactic Medium) to ionised and its signature can be observed using absorption lines in the spectra of high redshift QSOs (Quasars - McGreer, Mesinger, and D'Odorico, 2015), GRBs (Gamma Ray Bursts - Chornock et al., 2013) and galaxies (e.g. Tilvi et al., 2014). The absorption lines indicate the presence of neutral gas, since they arise due to the electron Ly-α transition in neutral Hydrogen. The 'Ly-α forest' can be observed as a series of absorption lines in the spectra of sources between $z = 6 - 0$, however beyond this redshift there is such an excess of neutral Hydrogen the spectrum flattens into the 'Gunn - Peterson trough' (Gunn and Peterson, 1965). This indicates the IGM underwent a rapid phase transition at $z \sim 6$. The relative impact of the contribution of stellar feedback processes on cosmic re-ionisation is a matter of debate (for a review see McQuinn, 2016), however there is a consensus that star forming galaxies drove the ionisation of the IGM (e.g. Faucher-Giguère et al., 2008; Becker and Bolton, 2013). This is due to both observational and theoretical evidence that star forming galaxies were a significant source of ionisation between $z = 12 - 6$ (e.g. Robertson et al., 2013; Finkelstein et al., 2015; Robertson et al., 2015).

Stars can impact their environment through a number of processes; photoionisation (e.g. Dale et al., 2014; Geen et al., 2015; Walch et al., 2015), radiation pressure (e.g. Murray, Quataert, and Thompson, 2010; Krumholz and Thompson, 2012; Kim, Kim, and Ostriker, 2016), stellar winds (e.g. Rogers and Pittard, 2013; Mackey et al., 2015; Fierlinger et al., 2015) and SNe (Supernovae) explosions (e.g. Martizzi, Faucher-Giguère, and Quataert, 2015; Walch and Naab, 2015a; Haid et al., 2016). For a review on the numerical implementation of stellar feedback processes see (Dale, 2015). This thesis focuses on feedback from massive stars, motivated by the fact it is these stars that dominate the energy input from a stellar population (e.g. Agertz et al., 2013). The efficiency of each feedback process at coupling to the ISM and ultimately suppressing star formation (on galactic and local scales) is highly dependent on environment, in particular the ISM density/ inhomogeneity (e.g. Dwarkadas and Gruszko, 2012; Martizzi, Faucher-Giguère, and Quataert, 2015; Li et al., 2015; Kim and Ostriker, 2015; Iffrig and Hennebelle, 2015; Gatto et al., 2015), which is altered by the action of prior feedback events (e.g. Rogers and Pittard, 2013; Walch et al., 2015).

There have been numerous numerical simulations modelling stellar feedback and its effects on galaxy evolution. The numerical implementation of stellar feedback is resolution dependent (e.g. see section 1.2.1.2 for a description of the overcooling problem). Difficulties arise due to the large dynamic range involved; for example, locally, stellar feedback drives supersonic turbulence in the ISM, which inhibits the gravitational collapse of the cold molecular gas in MCs (for a review of the processes driving interstellar turbulence see Klessen and Glover, 2016). On the other hand, stellar feedback also drives the kpc-scale galactic outflows mentioned above. Additionally, to investigate the effect of stellar feedback on galaxy evolution the timescales involved need to be Gyr, however the lifetime of a main sequence star with mass greater than 8 $M_{\odot}$ is of the order of 10 Myr (for example Table 45 of Schaller et al., 1992, lists lifetimes ranging between 3 Myr and 29 Myr, corresponding to 120 $M_{\odot}$ and 9 $M_{\odot}$ respectively and a metallicity of $Z = 0.02$), making stellar feedback impossible to resolve temporally (as well as spatially) in cosmological-scale simulations. In this case simulators employ sub-grid models for the net momentum/energy input of entire stellar populations, often tuned to match present day galaxy properties such as SFRs, metallicities and baryon-dark matter mass ratios (e.g. Vogelsberger et al., 2014; Schaye et al., 2015; Davé, Thompson, and Hopkins, 2016).

One of the main benefits of cosmological hydrodynamical simulations is that they can evolve tens of thousands of galaxies in a wide range of environments, producing statistical catalogs of galaxies in order to investigate global trends such as galaxy luminosity functions, cosmic star formation densities and global star formation efficiencies. Furthermore, a popular option to increase the dynamic range of cosmological simulations is to undertake zoom-in simulations of individual haloes/ galaxies (e.g. Stinson et al., 2013; Naab et al., 2014; Hopkins et al., 2014; Wetzel et al., 2016). These simulations identify and isolate individual galaxies in cosmological simulations and re-simulate them at a higher resolution. This allows these simulations to better resolve the multi-phase ISM and the impact of feedback processes on a smaller scale. However, the typical gas particle/ star particle mass in these simulations is between 100-10^5 $M_{\odot}$, hence feedback events from individual massive stars can still not be spatially/ temporarily resolved. In order to investigate stellar feedback mechanisms in detail, particularly how individual feedback events interplay, it becomes necessary to simulate either individual galaxies, molecular clouds, or even galactic regions such as spiral arms and isolated regions of gas (e.g Rogers and Pittard, 2013; Martizzi, Faucher-Giguère, and Quataert, 2015; Walch and Naab, 2015a; Girichidis et al., 2016; Martizzi et al., 2016; Cashmore et al., 2017). For a recent review on the current status of simulations investigating stellar feedback see Dale (2015).

This work is primarily interested the interplay between 'gradual' types of stellar feedback and 'instantaneous' feedback. The term 'gradual' is used throughout this thesis to refer to individual stellar feedback events which are continuous over a set period; for example the energy input from stellar winds. Whereas 'instantaneous' feedback refers to an instant explosive event, in other words a SNe. In this thesis I investigate the gradual heating of the ISM via the jets associated with High Mass X-ray Binaries (HMXBs) along with the shock-heating of the ISM by line-driven stellar winds from massive OB-type stars. How these 'gradual' types of feedback interplay with 'instantaneous' feedback is explored in later chapters. The next section gives a brief introduction into each of these three feedback processes.

1.2 SNe, HMXBs and Stellar Winds

1.2.1 SNe

In August 1885, at Dorpat observatory, E. Hartwig detected a SNe located in the Andromeda Nebula. This represented the first detection of a SNe outside our own galaxy. However, it was only recognized as such beyond 1933, when a SNe was posited as an end point of stellar evolution (Baade and Zwicky, 1934a; Baade and Zwicky, 1934b). Since then researchers have observed over 9000 SNe (Barbon et al., 1999), increasing our understanding of the mechanisms that drive these massive explosions and also of the contribution they make to galactic evolution.

There are now considered to be two main drivers of SNe explosions. Firstly, if the main sequence mass of a star is greater than 8 $M_{\odot}$, it will undergo a supernova explosion at the end of its life. This is known as a core-collapse SNe and the mechanism is still poorly understood (for recent reviews see Vink, 2012; Janka, 2012). Secondly, the thermonuclear explosion of degenerate nuclear material inside a stellar core (Hoyle and Fowler, 1960). The progenitors of thermonuclear SNe are generally considered to be white dwarfs in a binary system that are approaching the Chandrasekhar limit due to accreting matter from a companion star (for a review see Maoz, Mannucci, and Nelemans, 2014).

In 1941, SNe were further categorised into two broad spectral types; Type II and Type I (Minkowski, 1941). These categories are defined by the elemental absorption lines seen in their spectra. A supernova is classified as either Type II or Type I based on whether Hydrogen absorption is (or is not) present in its spectra. Both Type I and Type II can be further categorised based on their spectra. In particular, if Hydrogen is not present, however a large amount of Si+ absorption is, the supernova is classed as Type Ia (Elias et al., 1985). Type Ia supernovae are associated with thermonuclear explosions, while Type II SNe are invariably core-collapse SNe.

SNe inject $\sim 10^{51}$ erg of kinetic energy into the ISM, contained in $\sim 10\ \mathrm{M}_\odot$ of ejecta, moving at velocities of $10^{3-4}\mathrm{kms}^{-1}$. When this ejecta collides with the surrounding ISM, it shock heats the gas. This creates a shock wave consisting of ejecta and swept-up ISM. There exists an analytic solution for the expansion of the resulting SNR (Supernova Remnant) into a homogeneous ISM. This will be presented in the next section.

1.2.1.1 The Evolution of Supernova Remnants (SNRs)

SNRs undergo four phases; free expansion, the Sedov-Taylor phase (Taylor, 1950; Sedov, 1959), the 'snowplough' phase (Ostriker and McKee, 1988; Cioffi, McKee, and Bertschinger, 1988) and the final mixing phase (Woltjer, 1972). In order to undergo free expansion, the mass ejected during the SNe should be much less than the mass swept up in the expansion. As soon as the two values become comparable the SNR enters the Sedov-Taylor phase. For this thesis, it is of particular interest to focus on the Sedov-Taylor phase, since the simulations presented do not have the resolution to capture the free expansion phase, however they can capture the Sedov-Taylor phase.

At the beginning of the Sedov-Taylor phase the reverse shock has reached the centre of the expanding remnant and the pressure inside the remnant is greater than that of the surrounding medium. If it can be approximated that the source of the remnant is a point and that it is expanding into a homogeneous ISM with density ρ_0, the remnant's expansion can be tracked using the Sedov-Taylor solution;

$$R_s = 1.15 \left(\frac{E_{SN}}{\rho_0} \right)^{\frac{1}{5}} t_{SN}^{\frac{2}{5}}, \tag{1.1}$$

where R_s is the shock radius, t_{SN} is the age of the SNR and E_{SN} is the energy input from the SNe, typically 10^{51} erg. The pressure inside the bubble, P_b, during the phase can be found using the equation for the pressure of a bubble of ideal gas;

$$P_b = (\gamma - 1)\frac{E_{SN}}{V}, \tag{1.2}$$

which in the case of the expanding supernova remnant can be re-written;

$$P_b = \frac{E_{SN}}{2\pi {R_s}^3}, \tag{1.3}$$

assuming the volume, V, of the hot bubble is $\frac{4}{3}\pi R_s^3$ and $\gamma = \frac{5}{3}$ (in other words the gas is monatomic). The final snowplough stage of the remnant occurs when radiative cooling becomes significant and the expansion is no longer adiabatic. The expansion of the bubble then starts to decelerate. The swept up mass is much greater than the ejected mass during this phase. Eventually, the remnant will break up and mix with the ISM.

In reality, SNe are likely to be expanding into a multi-phase ISM with a complicated density profile due to pre-processing by other types of stellar feedback, for example; stellar winds, photo-ionising radiation, stellar radiation pressure (e.g. Hopkins, Quataert, and Murray, 2012; Rogers and Pittard, 2013; Martizzi, Faucher-Giguère, and Quataert, 2015; Walch et al., 2015; Geen et al., 2015). This can lead to the formation of 'chimneys', which are hot, low density, collimated regions in the gas (e.g. Rogers and Pittard, 2013). The idea of chimneys will be returned to regularly in this thesis. Prior massive stellar feedback processes can also act to enhance the work done on the ISM by SNe feedback by lowering the density of the surrounding ISM, leading to inefficient cooling, enhancing any SNe-generated winds (e.g. Agertz et al., 2013).

1.2.1.2 Computational modelling of SNe and the 'over-cooling' problem

Hydrodynamical simulations of SNe are limited by gas particle resolution. Often the $\sim 10\,M_\odot$ of ejecta generated in the explosion is far below the gas particle mass of the simulation. It was therefore initially preferred to model SNe as a thermal energy injection into the surrounding gas (e.g. Katz, Weinberg, and Hernquist, 1996), representing the hot, pressurised bubble of the Sedov-Taylor phase.

Moreover, this prescription is only valid so long as the simulation has the mass resolution to resolve the SNR prior to the onset of the cooling enhancement. However, if the particle mass is too high, the thermal energy will be radiated efficiently and the SNe feedback will artificially stall. As a consequence, the momentum injection of the Sedov-Taylor phase is severely underestimated since the SNe energy is radiated prior to performing a significant amount of work on the ISM. This result is called 'numerical over-cooling' and is particularly prevalent in cosmological simulations (e.g. Dalla Vecchia and Schaye, 2012).

One proposed solution to this problem is to artificially switch-off radiative cooling in order to follow the adiabatic Sedov-Taylor expansion, turning it on once the analytical lifetime of the Sedov-Taylor phase is exhausted (e.g. Stinson et al., 2006; Governato et al., 2010; Agertz et al., 2013; Teyssier et al., 2013). This method has the clear limitation that it makes the same assumption as the Sedov-Taylor solution; that the ISM is homogeneous on local scales. This can lead to an overestimation of the SNR lifetime; for example Martizzi, Faucher-Giguère, and Quataert (2015) investigate the effects of an inhomogeneous ISM and find the timescale during which cooling is shut off in Stinson et al. (2006) is between 2-30 times longer than the lifetime of a typical SNR in their simulations. Moreover, by delaying the cooling of certain regions of gas, some gas particles inevitably end up with unphysical temperature/densities; for example, hot, high density regions that would otherwise have cooled.

Another solution is to inject momentum, mimicking the SNR resolution beyond the Sedov-Taylor phase. This method is reliant on the momentum-boosting factor used, which can be calculated either analytically (e.g. Hopkins et al., 2014; Kim and Ostriker, 2015; Smith, Sijacki, and Shen, 2017) or based on the output from higher resolution simulations (e.g. Martizzi et al., 2016). In their recent paper, Smith, Sijacki, and Shen, 2017 compare both the delayed cooling and momentum injection schemes, finding delayed cooling overestimates the work done on the ISM, while momentum feedback is able to reproduce the Kennicutt-Schmidt (Kennicutt, 1998) relation in isolated disc galaxies. Despite this, since the momentum injection method resolves the SNR at a later time in its evolution, its predictive power is limited compared with models that directly resolve the hot, pressurised bubble associated with the Sedov-Taylor phase.

Simulations investigating galaxy evolution have determined the importance of SNe feedback. SNe have been linked to turbulence in the ISM, along with galactic-scale outflows and galactic winds (e.g. Oppenheimer et al., 2010; Creasey, Theuns, and Bower, 2013; Hopkins et al., 2014; Peters et al., 2015). Multiple spatially/temporally coherent SNe events can lead to 'superbubbles' (Sharma et al., 2014), such as those observed in dwarf galaxies (e.g. Ott, Walter, and Brinks, 2005). Moreover, SNe feedback is also thought to drive the cusp-core transformation (Flores and Primack, 1994; Moore, 1994) of the underlying dark matter halo in small-scale galaxies (e.g. Trujillo-Gomez et al., 2015; Pontzen and Governato, 2014). For a recent review of the cusp-core problem see Bullock and Boylan-Kolchin (2017). Furthermore, SNe play a significant role in the metallicity evolution of both the ISM and IGM (see Borgani et al., 2008, for a review). They are also the primary source of CRs (Cosmic Rays - see Bykov et al., 2018, along with associated references), which are created via the acceleration of ions to relativistic velocities (Krymskii, 1977; Bell, 1978; Blandford and Ostriker, 1978). CRs provide a separate energy source coupled to the galactic magnetic field, leading to pressure gradients which can drive galactic outflows (e.g. Dorfi and Breitschwerdt, 2012; Hanasz et al., 2013; Girichidis et al., 2016).

1.2.2 High Mass X-ray Binaries (HMXBs)

HMXBs consist of an OB-type stellar companion orbiting a neutron star or black hole. Observations of HMXBs are rarer than their low mass counterparts (Low Mass X-ray Binaries, or LMXBs) and they are typically associated with areas of star formation (e.g. see Fabbiano, 2006; Mineo, Gilfanov, and Sunyaev, 2012, and references therein) due to their relatively short formation time of approximately $1 - 10$ Myr (set by the main sequence lifetime of the massive primary star, which is usually short). This association of HMXBs with star formation is also evidenced by the positive correlation seen between the observed star formation rates (SFRs) of galaxies and the X-ray luminosities of HMXBs (e.g. Lehmer et al., 2010; Mineo, Gilfanov, and Sunyaev, 2012). The compact object (or primary star) in HMXBs is fed either by winds or Roche lobe overflow from the companion star. The winds associated with OB stars are such that, despite a very small capture fraction ($\sim 10^{-2} - 10^{-1}$ %), they still transfer mass at a high enough rate to produce high luminosity from accretion on to the compact object. Ultra-Luminous X-ray Sources (ULXs) are thought to be HMXBs in a high mass transfer rate phase. For example, the HMXB SS433 is thought to be a ULX on its side (Begelman, King, and Pringle, 2006) and would look brighter if viewed along the outflow axis. Its high luminosity is thought to be the result of the companion star filling its Roche lobe and transferring mass to the primary on a thermal timescale (King, Taam, and Begelman, 2000).

HMXBs are thought to play a particularly important role at high redshift since there is an observed increase in HMXB mass with a corresponding decrease in metallicity (e.g. Dray, 2006; Mirabel et al., 2011). Furthermore, using a large XRB (X-ray Binary) population synthesis model, Fragos et al. (2013b) found the X-ray emission of the XRB population is dominated by HMXBs (over LMXBs) beyond $z \gtrsim 2.5$. As well as this, beyond $z \gtrsim 6-8$ HMXB X-ray emission is expected to dominate over that of Active Galactic Nuclei (AGN - Fragos et al., 2013a). In particular, both Power et al. (2009) and Mirabel et al. (2011) investigated the contribution of HMXBs to cosmic re-ionisation, concluding HMXBs are a comparable source of photo-ionisation to their progenitor massive stars. However, Knevitt et al. (2014) found the high spectral energy distributions of the X-rays emitted by HMXBs, along with their long mean free path lengths, limited their impact on the ionisation of the IGM. Despite this, HMXBs can also affect their environment via the kinetic energy input from relativistic jets and these are the focus of this thesis.

Jets are common in HMXBs and recent work suggests there exists a universal relation between the radio luminosity and the kinetic power of jets, spanning supermassive black holes down to stellar mass black holes (Fender and Muñoz-Darias, 2015). The properties of jets in HMXBs are broadly split into two categories. Firstly, persistent jets in the low-luminosity state; where the X-ray spectrum is predominantly hard and the jet is prolonged with Lorentz factors ~ 1.4 (Fender, Belloni, and Gallo, 2004). Secondly, powerful ballistic jets in the high-luminosity high-variability state, which describes the transition from the X-ray spectrum being dominated by hard to soft X-rays and is associated with Lorentz factors of ~ 2 (Fender, Belloni, and Gallo, 2004). An example of an HMXB that shows transitions from a hard state to a soft state is Cygnus X-1. This is a highly luminous system consisting of a $14.8 \pm 1.0 M_{\odot}$ black hole accreting material via stellar winds from a super-giant O-type companion of mass $19.2 \pm 1.9 M_{\odot}$ (Orosz et al., 2011). It has been extensively investigated in multiple wavelengths; for example Gallo et al. (2005, radio), Sell et al. (2015, X-ray) and Russell, Fender, and Jonker (2007, optical). Associated with Cygnus X-1 is an inflated radio lobe, which is surrounded by a ring-like shock approximately 5 pc in scale (Gallo et al., 2005). This lobe is thought to have been inflated by a steady jet and Gallo et al. (2005) used the lobe to conclude the kinetic power of Cygnus X-1 could be as high as the total X-ray luminosity of the system. Additionally, recently Fender et al. (2006) reported a transient, extended radio jet from Cygnus X-1.

Recent work on the relation between the mechanical power of relativistic compact objects compared with their bolometric X-ray luminosities has concluded the former could be equal to, if not greater than, the X-ray luminosity. For example, observations of SS433 indicate relativistic jets ($\sim 0.26\,c$) with a mechanical energy of $> 10^{39}$ erg/s (e.g. Blundell, 2001; Mirabel et al., 2011; Goodall, Alouani-Bibi, and Blundell, 2011). These jets are thought to have interacted with the preceding supernova remnant, inflating the surrounding W50 nebula (Lockman, Blundell, and Goss, 2007; Goodall, Alouani-Bibi, and Blundell, 2011). Moreover, Pakull, Soria, and Motch, 2010 reported a jet-inflated bubble, with a diameter of 300 pc, surrounding the microquasar S26 in the galaxy NGC 7793. The authors also reported S26 has a greater mechanical power output than SS433, while the jets were found to be 10^4 times more energetic than its associated X-ray emission. Given these rates of kinetic energy injection into the ISM, depending on the lifetime of the HMXB and the mode of accretion, it is possible their jets release ten times the amount of energy associated with a single SNe event across their lifetime (assuming the canonical value of 10^{51} erg). This makes them energetically significant, particularly in the context of GMCs (Giant Molecular Clouds) and dwarf galaxies with shallow potential wells.

There has also been a great deal of interest in jets associated with ULXs; for example Justham and Schawinski, 2012 investigated the potential impact of a ULX population in models/simulations of galaxy formation. They argued the stochasticity of ULX events, coupled with their significant energetic contribution to the ISM, could result in a variety of different star formation histories, particularly in dwarf galaxies. Moreover, the authors also discussed the intriguing possibilities that may result from the interplay between SNe and XRB feedback. One such possibility is that the XRB feedback dominates initially, resulting in a warm, heated but not unbound ISM, which stops star formation and decreases the efficiency of SNe feedback at unbinding the gas in the galaxy.

Additionally, Artale, Tissera, and Pellizza, 2015 also focussed on the interplay between SNe and BH-HMXB (HMXBs containing a black hole) feedback and their impact on the early evolution of a dwarf galaxy. They investigated this using SPH (Smoothed Particle Hydrodynamics) simulations and concluded that although BH-HMXBs acted to reduce the star formation rate earlier on in their simulations, the overall star formation efficiencies in their simulated galaxies were increased (particularly in low mass galaxies).

1.2.2.1 A note on the importance of binary systems

Sana et al. (2013) used observations of the Tarantula Nebula in the LMC (Large Magellanic Cloud) to conclude over over 50% of O stars in this region will undergo mass transfer with a companion star. Furthermore, galaxy-wide surveys of O-stars indicate a multiplicity fraction of at least 50% (e.g. Sana, James, and Gosset, 2011; Sana et al., 2013). Existing as part of a binary system can alter the evolutionary track of a massive star, particularly when the system is undergoing mass transfer. Recent work has concluded interactions in close binary systems (such as Roche lobe overflow) can significantly affect the evolution of both the primary star and its companion (e.g. Eldridge, Izzard, and Tout, 2008; Yoon, Woosley, and Langer, 2010; Song et al., 2016). Moreover, the merging of black hole binary pairs (or BH-BH mergers), along with pairs of neutron stars (NS-NS mergers), have been of particular interest recently due to the detection of a gravitational wave transient resulting from the merging of two black holes in a binary system (Abbott et al., 2016). As a result, existing binary population synthesis codes (e.g. Hurley, Tout, and Pols, 2002; Izzard, Ramirez-Ruiz, and Tout, 2004; Eldridge and Stanway, 2009; Mennekens and Vanbeveren, 2016; Eldridge et al., 2017) have particularly focused on predicting merger rates of binary BHs.

However, it is also important to take binary evolutionary pathways into account when inferring characteristics of an underlying stellar population (for example stellar ages and metallicities) from its ionising spectra (e.g. Xiao, Stanway, and Eldridge, 2018). Moreover, recent papers (Ma et al., 2016; Stanway, Eldridge, and Becker, 2016) have argued including the altered evolutionary pathways due to mass transfer within binary systems can increase the escape fraction of ionising photons during Re-ionisation. As well as this, there is considerable interest in using XRBs to infer underlying galaxy properties, such as SFR, stellar mass, stellar ages and metallicity, since both observations and models indicate the luminosity of HMXBs and LMXBs is highly dependent on these properties (Lehmer et al., 2010; Lehmer et al., 2014; Brorby et al., 2016; Aird, Coil, and Georgakakis, 2017).

1.2.2.2 Computational modelling of HMXBs

This thesis is particularly focussed on the mechanical energy input from the jets associated with HMXBs. This is not generally included in computational models of star-forming molecular clouds or galaxies. However, previous work has focussed on proto-stellar jets in MCs/star clusters (e.g. Federrath et al., 2014), which are considered ubiquitous in proto-stellar systems (for a recent review see Bally, 2016). In Federrath et al. (2014), the authors model the jet as two spherical cones of specified opening angle. Furthermore, the resolution in their simulations is such that they can expel a fraction of the accreted mass into these cones, with velocities related to the mass of the star forming region (represented by a sink particle).

This inclusion of jet feedback in simulations as a bipolar outflow of specified energy is also used to model large-scale jets associated with AGN. Here simulations commonly inject a combination of momentum (or kinetic energy) along with thermal energy into two lobes or cones (see Bourne and Sijacki, 2017, and references therein).

However, in their recent paper, Artale, Tissera, and Pellizza (2015) included a prescription for the kinetic feedback from HMXBs in simulations of galaxies with halo masses between 10^9 $M_\odot$ and 10^{13} $M_\odot$. Here the authors model stellar populations as star particles and input the energy injected via BH-HMXB jets as a fixed thermal energy injection into the cold gas phase surrounding a star particle (it is assumed the kinetic energy has been efficiently thermalised).

1.2.3 Line-driven stellar winds

The primary mass loss mechanism during the main sequence lifetime of massive stars is via line-driven stellar winds (see Puls, Vink, and Najarro, 2008; Smith, 2014, for reviews on this topic). Winds are the result of the transfer of momentum via the absorption and re-emittance of photons by UV-metal ions in the stellar photosphere (a process known as 'line-driving'). Lucy and Solomon (1970) and Castor, McCray, and Weaver (1975) hypothesised that the metal ions which have been radially accelerated via outward propagating radiation, could also transfer radial momentum to both Hydrogen and Helium (which are in greater abundance), leading to a non-negligible mass loss rate of 10^{-6} $M_\odot$ yr^{-1} in OB stars.

This mass loss also has an effect on the evolution of the star (as we saw in section 1.2.2.1). For an in-depth discussion of this mass loss mechanism see Puls, Vink, and Najarro (2008). The production of line-driven winds is dependent on the metal content of the star, along with its temperature (in other words its level of ionisation) and fundamentally its luminosity (Puls, Vink, and Najarro, 2008).

1.2.3.1 Computational modelling of stellar winds

As with HMXBs and SNe, how stellar winds are implemented is highly dependent on resolution. When modelling individual stars, the mass loss rates and wind velocities (i.e. the two key parameters when evaluating stellar wind feedback) are commonly taken from Vink, de Koter, and Lamers (2001). However, these relations are only known to hold down to $Z = 0.2\ Z_{\odot}$, making their application to primordial metallicities uncertain.

Focusing on modelling the interplay between the stellar winds and the surrounding ISM, which is the primary concern of this thesis; Castor, McCray, and Weaver (1975) and Weaver et al. (1977) explored the interplay of a strong stellar wind with the surrounding ISM. Here the stellar winds collided with the surrounding gas and shocked, efficiently converting the kinetic energy to thermal and producing hot (10^6 K) bubbles of gas surrounded by a shell of swept-up mass. Furthermore, Harper-Clark and Murray (2009) also modified this model to allow for a non-uniform ISM, finding leakage of hot gas through channels in the swept-up shell. This also produced a better fit to the X-ray luminosity of the Carina Nebula.

Moreover, recent papers modelled the interaction of multiple stellar wind bubbles, which formed large-scale winds (e.g. Stevens and Hartwell, 2003), along with low density cavities. This also resulted in leakage of the wind energy (e.g. Rogers and Pittard, 2013; Rosen et al., 2014). This leakage is thought to be occurring in 30 Doradus, also known as the Tarantula Nebula (Lopez et al., 2011). In their simulations Rogers and Pittard (2013) have the mass resolution to model the mass ejected via stellar winds directly. However, in larger-scale simulations stellar winds are necessarily modelled as an injection of momentum into the surrounding ISM (e.g. Dale, 2017; Rey-Raposo et al., 2017).

1.3 Introducing Giant Molecular Clouds and Dwarf Spheroidal Galaxies

In this section I will give a brief overview of the two star-forming systems this thesis is concerned with; namely GMCs and dSphs (Dwarf Spheroidal Galaxies).

1.3.1 Giant Molecular Clouds (GMCs)

GMCs are cold, molecular gas reservoirs and are the main sites for star formation in galaxies such as the Milky Way (for a review on the subject see Heyer and Dame, 2015). GMCs are dynamic environments with gas exhibiting supersonic motions which is commonly attributed to turbulence (Larson, 1981). The majority of the molecular gas in the Milky Way is found in clouds with a mass greater than $10^5\,\mathrm{M}_\odot$, while there also exists an upper mass limit of $\sim 6 \times 10^6\,\mathrm{M}_\odot$ (Williams and McKee, 1997; Rosolowsky, 2005). The lifetime of GMCs is a heavily debated topic; predicted lifetimes range from very short ($< 3\,\mathrm{Myr}$) to 10^8 yrs (for a discussion on this see Heyer and Dame, 2015). Arguments for smaller lifetimes include the lack of old ($> 3\,\mathrm{Myr}$) stars associated with molecular gas in the Large Magellanic Cloud (Elmegreen, 2000) as well as in clouds in the Milky Way (Heyer and Dame, 2015). However, there also exists observational evidence for longer/intermediate cloud lifetimes ($\sim$ tens of Myr; e.g. Kawamura et al., 2009; Murray, 2011).

1.3.1.1 Computational Modelling of Stellar Feedback Inside GMCs

Due to the large range of scales involved, there are several approaches to numerical models in this context. For example, modelling the formation of GMCs in galaxies (e.g. Dobbs, Burkert, and Pringle, 2011) where the mass of each resolution element is much more than a single star but small enough to resolve the GMC, to modelling the assembly of individual stars on smaller scales (e.g. Bate, 2009), where the properties of individual stars are robust but only a few hundred solar masses of gas can be simulated. Dale, 2015 provides a coherent review of the current methods for numerical modelling of stellar feedback processes inside molecular clouds. Galactic-scale simulations of (spiral) disc galaxies are advantageous as they allow the environmental effects of the host galaxy to be included self-consistently. However, given the lower mass resolution of these simulations, it is harder to model the effects of stellar feedback on the ISM. For example, low resolution can result in the over-cooling problem (see section 1.2.1.2).

Computational work that includes the large-scale environment of molecular clouds ranges from modelling a shearing box, in order to mimic conditions in a spiral arm (e.g. Kim, Ostriker, and Kim, 2013), to simulating whole galaxies (e.g. Springel and Hernquist, 2003; Agertz, Teyssier, and Moore, 2011; Dobbs, Burkert, and Pringle, 2011; Dobbs and Pringle, 2013; Renaud et al., 2013). These simulations are able to investigate global trends, such as the offset between molecular gas clouds and star formation, along with the effect of feedback on the overall stellar population. There have also been numerous simulations of star formation and feedback on GMC scales or lower. Often this involves applying a fractal-like initial density field onto either a gas cloud or periodic box of gas, using either a turbulent velocity spectrum (e.g. Dale, Ercolano, and Bonnell, 2012) or by design (e.g. Walch et al., 2013). Furthermore, scales range from resolving individual stars (e.g. Bate, 2009; Clark et al., 2011) to modelling stellar populations, often as sink particles (e.g. Dale, Ercolano, and Bonnell, 2012).

GMCs are highly inefficient at forming stars ($\sim$ 2 per cent of their mass is converted into stars; Murray, 2011) and this is commonly attributed to stellar feedback effects. Recent papers have focused on the energy and momentum injection by stellar winds from massive O-stars (e.g. Ntormousi et al., 2011; Ngoumou et al., 2015), the radiation from low to high mass stars (e.g. Matzner, 2002; Gritschneder et al., 2010), SNe explosions (e.g. Walch and Naab, 2015b; Iffrig and Hennebelle, 2015) and protostellar jets (e.g. Matzner, 2007; Federrath et al., 2014). Other works investigate how these processes interplay (e.g Freyer, Hensler, and Yorke, 2003; Krumholz and Thompson, 2012; Pelupessy and Portegies Zwart, 2012; Rogers and Pittard, 2013; Fierlinger et al., 2015; Dale, 2017).

1.3.2 Dwarf Spheroidal Galaxies (dSphs)

Dwarf galaxies are traditionally recognized by their low halo masses (of $\lesssim 10^9$ $M_\odot$), their large mass-to-light ratios (Mateo, 1998) and their low absolute magnitude (e.g. Sandage and Binggeli, 1984). They are the most common type of galaxy in the universe (Mateo, 1998) and offer an interesting area of study due to their wide range of morphologies and other properties. For example, the dwarf galaxies of the Milky Way have an array of metallicities, luminosities, stellar populations and hence star formation histories (e.g. McConnachie, 2012). For an overview of the properties (metallicities, stellar kinematics, star formation histories) of the dwarf galaxies of the local group see Tolstoy, Hill, and Tosi (2009) and references therein.

Dwarf galaxies are typically split into sub-categories, based on metal and baryon content, surface brightness and effective radii. The focus of this thesis is on a subset of dwarf galaxies known as dSphs. These are high ellipticity (e.g. Hodge, 1971), low luminosity (e.g. Koposov et al., 2008), metal-poor (e.g. Geisler et al., 2007), dark matter dominated/ devoid of gas (e.g. Mateo, 1994; Olszewski, 1998; Gilmore et al., 2007) systems with old (>1 Gyr) stellar populations (e.g. Grebel and Gallagher, 2004; Weisz et al., 2014) and velocity dispersions of 6-25 km/s (e.g. Aaronson, 1983; Mateo, 1998; Wilkinson et al., 2004; Tolstoy, Hill, and Tosi, 2009). There are a large number of these systems surrounding the Milky Way and M31.

There are a number of questions on the formation of dSphs, some of which are still unanswered. For a review of these see Bullock and Boylan-Kolchin (2017). For example, a key question is how dSphs are metal-poor yet have undergone multiple bursts of star formation across the last $\sim$ 12 Gyr (Weisz et al., 2014). A possible explanation is the expulsion of metal-rich gas via galactic winds (e.g Madau, Ferrara, and Rees, 2001; Carigi, Hernandez, and Gilmore, 2002). These winds are considered to be the result of SNe driving hot, metal-enriched gas from dwarf galaxies. This process is evidenced by a high abundance of metals in the IGM (Schaye et al., 2003), along with observations of 'superbubbles' of hot, diffuse gas in star forming dwarf galaxies (e.g. Ott, Walter, and Brinks, 2005). As such, another key question in the formation of current day dSphs is how they retained/accreted enough gas to undergo multiple starbursts, despite evidence of these large feedback-generated outflows (e.g. Cashmore et al., 2017). Moreover, the shallow potential wells of dwarf galaxies means they can also be significantly influenced by a number of external factors, for example; ram pressure stripping, cosmic re-ionisation and tidal effects (e.g Gatto et al., 2013; Emerick et al., 2016; Sawala et al., 2016; Zhu et al., 2016; Simpson et al., 2017).

Another key problem in the formation of the dSphs is that cosmological simulations over-predict the number of smaller haloes by at least 2 orders of magnitude (e.g. Garrison-Kimmel et al., 2014; Griffen et al., 2016). Dubbed the 'Missing

Satellite problem' (Klypin et al., 1999; Moore et al., 1999), recent explanations for this discrepancy include baryonic processes; for example dark matter haloes below a mass threshold cannot support efficient atomic cooling in the early universe (e.g. Glover, 2005; Moore et al., 2006), while the gas in the smallest galaxies could have been lost via re-ionisation (e.g. Wheeler et al., 2015) and stellar feedback processes (e.g. Sawala et al., 2010; Nickerson et al., 2011). Another issue is the low velocity dispersions observed at the centre of dwarf satellite halos, indicating a lower density in the centre of the galactic halo (e.g. Kuzio de Naray, McGaugh, and de Blok, 2008; Walker and Peñarrubia, 2011); in other words a 'cored' rather than a 'cuspy' dark matter density profile. Once again, stellar feedback is considered to play a critical role here, driving this cusp-core transformation (e.g. Governato et al., 2010; Trujillo-Gomez et al., 2015; Pontzen and Governato, 2014). Furthermore, SNe feedback is considered the primary cause of the observed flattening of the M_{halo} - $M_{\star}$ relation seen with galaxies of mass $< 10^9$ $M_{\odot}$ (Sawala et al., 2015). Additionally, recent work has focussed on the stochasticity of SNe events and how this can drive the range of star formation histories seen in the dwarf spheroidal satellite galaxies of the Milky Way today (e.g. Ricotti and Gnedin, 2005; Weisz et al., 2014).

There have been a large number of hydrodynamical simulations modelling stellar feedback in dwarf galaxies, however due to resolution constraints these are often isolated galaxies (e.g. Sawala et al., 2010; Nickerson et al., 2011; Shen et al., 2014; Wheeler et al., 2015; Cashmore et al., 2017), with parameters based on observations and cosmological simulations. The key idea is the results from these smaller scale simulations can then feed into the less-resolved cosmological simulations.

1.4 This thesis

The aim of this thesis is to investigate the impact of stellar feedback on the multiphase ISM of individual GMCs and dwarf spheroidal galaxies. This will be done using hydrodynamical simulations at a novel mass resolution, which is aimed at bridging the gap between small-scale simulations that resolve the formation of individual stars and cosmological-scale simulations. The following chapter (Chapter 2) gives the details of the simulations to be run. The results of the simulations are then given in Chapters 3, 4 and 5. The focus of Chapters 3 and 4 is to investigate the interplay between HMXB and SNe feedback in GMCs, at solar metallicity (Chapter 3) and at a lower metallicity (Chapter 4). Additionally, Chapter 5 investigates the interplay between stellar winds, HMXB and SNe feedback during a 1 Gyr starburst in isolated dwarf galaxies. Finally, the conclusions of the thesis are presented in Chapter 6.

Chapter 2

Numerical Modelling

In order to achieve the science goals of this thesis, numerical simulations needed to be run which could capture the small scale physics of the ISM, along with the gravitational interactions between the gas, stars and dark matter. The inevitable by-product of stellar feedback is gaseous shocks (i.e. the SNRs seen in section 1.2.1.1), along with gaseous outflows which transfer gas from high to low density regions. Any numerical models are therefore required to include thermal conduction and (artificial) viscosity to capture shock thermodynamics, while balancing computational cost between high and low density regions. Moreover, on GMC scales the simulations also needed to capture something of star formation physics (although nowhere do I resolve the formation of individual stars). In order to achieve this I undertook simulations using the code GADGET-3. This is a hybrid N-body/SPH code that is a modified version of the publicly available code GADGET-2 (Springel, 2005).

2.1 The non-baryonic components

GADGET-3 models dark matter and stars as self-gravitating collisionless fluids (Springel, 2005) with a gravitational potential given by Poisson's equation

$$\nabla^2\phi(\mathbf{r},t) = 4\pi G \int f(\mathbf{r},\mathbf{v},t)d\mathbf{v}, \tag{2.1}$$

given $f(\mathbf{r},\mathbf{v},t)$ is the phase space mass density while $\mathbf{v}$ and $\mathbf{r}$ are particle velocity and position. When taking the integral of f over a section of phase space, one is effectively calculating the probability that a particle at a time t can be found in that section. The evolution of f with time can be tracked using the CBE (Collisionless

Boltzmann Equation)

$$\frac{\delta f}{\delta t} + \mathbf{v} \cdot \frac{\delta f}{\delta x} - \frac{\delta \Phi}{\delta x} \cdot \frac{\delta f}{\delta v} = 0, \tag{2.2}$$

where Φ is the gravitational potential. The CBE represents the fact f does not vary with time, or the probabilistic fluid representing the system in phase space is incompressible (Binney and Tremaine, 2008).

2.1.1 The tree algorithm

Gravitational forces between particles (both SPH and N-body) in GADGET are computed via a tree algorithm. Since the time to compute the gravitational forces between particles is proportional to N^2 (where N is the number of particles in the simulation), directly summing the forces between particle pairs becomes inviable for large N. Instead, when GADGET calculates the total gravitational force on a single particle, it partitions all other particles according to their distance from the particle and computes their lowest order multipole moment (Springel, Yoshida, and White, 2001).

The division of space is commonly done using the method in Barnes and Hut (1986), where the computational domain is split into a hierarchical structure of cubes, beginning with a single cube which is then split into 8 daughter cubes of half its side length (Springel, Yoshida, and White, 2001). This process is continued until cubes contain single particles, known as 'leaf nodes' (Springel, 2005). At each level of the hierarchy, the gravitational force from the particles contained in a cube can be approximated under the assumption all of the mass contained in the cube is located at its centre. The forces on a single particle can then be determined by 'walking' this hierarchical tree. In this way, the accuracy of the tree-walk can be set by a parameter θ, where the 'walk' of the tree is discontinued if $r > l/\theta$, where r is the distance of the point of reference to the centre of the cube being assessed and l is the side length of the cube (Springel, Yoshida, and White, 2001). This is known as an opening criterion (e.g. Springel, Yoshida, and White, 2001; Springel, 2005) and by decreasing θ the method becomes more accurate.

2.2 SPH - Smoothed Particle Hydrodynamics

On the other hand, the ISM gas was modelled using SPH. SPH was originally conceived by Lucy and Solomon (1970) and Gingold and Monaghan (1977) as a way of modelling 2 and 3 dimensional astrophysical fluids. Fundamentally, SPH models fluids as a set of N particles of mass m_N. The higher N is, the more accurate the method. SPH is a Lagrangian, rather than Eulerian, method. This means the coordinates are not fixed in space but move with the fluid.

The fluid dynamical properties of each particle are calculated as a weighted sum over the properties of its neighbours. The weight given to specific neighbours is determined using a symmetric smoothing kernel $W(r, h)$. This is a function of both the distance between the particle and its neighbours (r) and a smoothing length (h). In other words, the smoothing length h determines the spatial extent over which fluid dynamical properties are averaged. Gingold and Monaghan (1977) set h to a value that would adapt in time with respect to the region with the densest packing of SPH particles. However, GADGET-3 uses a h which adapts to the local SPH particle density, ensuring the same resolution in areas of low and high density.

In this way, any field of the gas (A($\mathbf{r}$); for example, the velocity field) can be approximated by

$$A(\mathbf{r}) = \sum_{i=1}^{N} m_i \frac{A_i}{\rho_i} W(\mathbf{r} \text{ - } \mathbf{r}_i, h) \tag{2.3}$$

where N represents the neighbour number, which I set as a free parameter in these simulations (although in actuality this is a mean value, dependent on the strength of the density gradient - Price, 2012), while $r - r_i$ is the separation between neighbours. It is clear the effectiveness of SPH at capturing fluid properties is governed by the choice of kernel and neighbour number. I will discuss these in further detail in the next two sections, beginning with my choice of neighbour number.

2.2.1 Neighbour number

It would seem to increase resolution one would want to decrease the number of neighbours. However, there is a balance between numerical convergence and resolution. This is due to the fact the SPH particles are not evenly distributed but instead mostly in a glass-like configuration (Dehnen and Aly, 2012), therefore at small scales the evaluation of fluid properties becomes noisy if the neighbour number is too low.

On the other hand, the number of neighbours cannot be increased arbitrarily for a particular kernel, otherwise this could lead to the pairing instability (see Price, 2012, and references therein). This is an instability which causes particles which are radially located at points where the kernel gradient is at a maximum (or minimum) to experience zero repulsive force and form a pair which gradually get closer together. In order to avoid this error the ratio of the smoothing length to the mean particle spacing (η) needs to be > 1 (Price, 2012).

2.2.2 Choice of smoothing kernel

In this thesis I use a smoothing kernel given by

$$W(r,h) = \frac{21}{2\pi}(1-u)^4(1+4u), \tag{2.4}$$

(Wendland, 1995; Dehnen and Aly, 2012) where u is equal to $\frac{r}{h}$. This is known as the Wendland-2 kernel (Wendland, 1995). The basic properties a smoothing kernel needs to have in order to be a viable option for SPH are, following Price (2012) and Dehnen and Aly (2012);

1. it needs to be a function that decreases (symmetrically) with radius and be twice differentiable, with smooth first and second derivatives.

2. The kernel also needs to flatten towards the centre, so that small changes in radii by closest neighbours will not drastically alter the evaluated properties.

The Wendland-2 kernel satisfies both these criteria. Moreover, it is advocated by Dehnen and Aly (2012), over alternative B-spline (Schoenberg, 1946) functions (which are generated as 1D Fourier transforms Monaghan, 1985) due to the fact it is stable to the pairing instability to higher neighbour number (I use 100 neighbours), achieving good convergence. It is also computationally inexpensive. At this neighbour number it is also stable to the E_0 error (Dehnen and Aly, 2012).

2.2.3 The equations of motion of SPH particles

The gas in these simulations is modelled using an ideal equation of state, defined by $P = (\gamma - 1)\rho u$, where P is the gas pressure, γ is the adiabatic constant, set to $5/3$ in my simulations, u is gas internal energy and ρ is gas density. The first law of thermodynamics can therefore be used to describe the evolution of the internal energy with time, although an additional term needs to be added to describe the heating/cooling of the gas;

$$\frac{du}{dt} = -\frac{P}{\rho}\nabla \cdot \mathbf{v} - \frac{\Lambda(u,\rho)}{\rho}, \tag{2.5}$$

(e.g. Springel, Yoshida, and White, 2001). Here $\Lambda(u,\rho)$ represents the cooling rate per unit volume minus the heating rate per unit volume (see section 2.4 for more details). Furthermore, in SPH this is discretised to

$$\frac{du_i}{dt} = \frac{1}{2}\sum_{j=1}^{N} m_j \left(\frac{P_i}{\rho_i^2} + \frac{P_j}{\rho_j^2}\right) \mathbf{v}_{ij} \cdot \nabla_i W_{ij} - \frac{\Lambda}{\rho}, \tag{2.6}$$

(e.g. Mo, Bosch, and White, 2010). Additionally, the continuity equation applies since the mass of the system conserved, and is written

$$\frac{\delta\rho}{\delta t} + \rho\nabla \cdot (\mathbf{v}) = 0, \tag{2.7}$$

which, again, can be discretised to

$$\frac{\delta\rho_i}{\delta t} = \sum_{j}^{N} m_j \mathbf{v}_{ij} \nabla_i W_{ij}. \tag{2.8}$$

Finally, the Euler equation can be derived from Newton's second law and reads

$$\rho\frac{d\mathbf{v}}{dt} = -\nabla P - \rho\nabla\Phi, \tag{2.9}$$

where Φ is the potential. In the absence of sinks or sources this then reads

$$\rho\frac{d\mathbf{v}}{dt} = -\nabla P. \tag{2.10}$$

Inherent to this derivation is the assumption the fluid is dissipationless. However, in order to correctly model the shocks which are produced by stellar feedback, the gas needs to dissipate energy. In order to reconcile this, GADGET-3 uses an 'artificial viscosity' switch (Cullen and Dehnen, 2010), along with the SPHS scheme described in Read and Hayfield (2012). This will be discussed in more detail in section 2.2.4. Furthermore, when equation 2.10 is discretised, it becomes

$$\frac{d\mathbf{v}_i}{dt} = -\sum_j^N m_j\left(\frac{P_i}{\rho_i^2} + \frac{P_j}{\rho_j^2}\right)\nabla_i W_{ij}, \tag{2.11}$$

while the SPHS higher order dissipation switch further modifies 2.11 to

$$\frac{d\mathbf{v}_i}{dt} = -\sum_j^N \frac{m_j}{\rho_i\rho_j}(P_i + P_j)\nabla_i \overline{W}_{ij}, \tag{2.12}$$

(Read and Hayfield, 2012), where $\overline{W}_{ij} = (1/2)[W_{ij}(h_i) + W_{ij}(h_j)]$.

2.2.4 Artificial viscosity and SPHS

As stated in section 2.2.3, an inevitable by-product of stellar feedback is the convergence of hot, high velocity gas with cold, low velocity gas. In real gas this would result in the loss of kinetic energy to thermal energy in shocks, resulting in an increase in entropy of the gas. However, given the underlying SPH equations of motion assume a constant entropy, in SPH this would instead result in multiple values for the fluid properties (such as momentum and pressure) at the point particles converge.

To avoid this, GADGET-3 has an artificial viscosity, which ensures converging particles have a single-valued momentum. Additionally, GADGET-3 has SPHS implemented (as described in Read and Hayfield, 2012), which ensures the other fluid dynamical properties, such as internal energy and pressure, are not multi-valued.

The artificial viscosity generates an additional acceleration term

$$\frac{d\mathbf{v}_{diss,i}}{dt} = -\sum_j^N m_j \Pi_{ij} \nabla_i \overline{W}_{ij}, \tag{2.13}$$

where

$$\Pi_{ij} = \begin{cases} \frac{-\bar{\alpha}_{ij}}{2} \frac{v_{sig,ij} w_{ij}}{\bar{\rho}_{ij}} & if\ \mathbf{v}_{ij} \cdot \boldsymbol{r}_{ij} < 0 \\ 0 & otherwise \end{cases} \tag{2.14}$$

(e.g. Springel, 2005; Read and Hayfield, 2012). Here $\bar{\rho}_{ij} = \frac{\rho_i + \rho_j}{2}$ and w_{ij} is the relative velocity of particles i and j projected onto their separation. The condition $\mathbf{v}_{ij} \cdot \boldsymbol{r}_{ij} < 0$ ensures the artificial viscosity is only switched on when the flow is converging. Furthermore, $\bar{\alpha}_{ij}$ is defined as the sum of the dissipation parameters of particles i and j, α_i and α_j, divided by 2, while $v_{sig,ij}$ is defined as

$$v_{sig,ij} = c_i + c_j - 3w_{ij}, \tag{2.15}$$

where c_i and c_j are the mean sound speeds of the gas in particle i and its neighbour j. In order to conserve energy, this deceleration by particles in a converging flow results in an increase in entropy ($A_{diss,i}$) given by

$$\dot{A}_{diss,i} = -\frac{1}{2}\frac{\gamma - 1}{\rho_i^{\gamma-1}} \sum_j^N m_j \bar{\alpha}_{ij} \Pi_{ij} \boldsymbol{v}_{ij} \cdot \nabla_i \overline{W}_{ij}, \tag{2.16}$$

(e.g. Springel, 2005; Read and Hayfield, 2012). Moreover, as in Read and Hayfield (2012) and Cullen and Dehnen (2010), I use the Balsara (1989) shear viscosity limiter, which helps ensure non-converging shear flows do not trigger artificial viscosity, since this work is just interested in the bulk viscosity generated in shocks. This limiter is directly applied to the dissipation parameter α_i as a factor $f_{Balsara}$ given by

$$f_{Balsara,i} = \frac{|\nabla \cdot \boldsymbol{v}|_i}{|\nabla \cdot \boldsymbol{v}|_i + |\nabla \wedge \boldsymbol{v}|_i + 0.0001\frac{c_i}{h_i}} \tag{2.17}$$

(Balsara, 1989; Read and Hayfield, 2012; Cullen and Dehnen, 2010).

The dissipation parameter itself (α_i), which ranges from 0 to $\alpha_{max} = 1$, is modified in GADGET-3 according to Read and Hayfield (2012), in a method similar to Cullen and Dehnen (2010). In this scheme, α_i is modified using the spatial derivative $\nabla \cdot v$ in order to not only detect converging flows (which can be found from $\nabla \cdot v$), but also whether the particle is in a pre-shock region, or in other words whether or not the flow will converge in the future (Read and Hayfield, 2012).

This is done using

$$\alpha_{loc,i} = \begin{cases} \frac{h_i^2|\nabla(\nabla\cdot\boldsymbol{v}_i)|}{h_i^2|\nabla(\nabla\cdot\boldsymbol{v}_i)|+h_i|\nabla\cdot\boldsymbol{v}_i|+n_s c_i}\alpha_{max} & \nabla\cdot\boldsymbol{v}_i < 0, \\ 0 & otherwise, \end{cases} \tag{2.18}$$

where n_s is a noise parameter set to 0.05, which defines the magnitude of the velocity perturbations required to trigger the viscosity switch (Read and Hayfield, 2012). If $\alpha_{loc,i}$ is greater than α_i, α_i is immediately set to $\alpha_{loc,i}$. If, however, the reverse is true, α_i decays to 0 according to

$$\dot{\alpha_{loc,i}} = \begin{cases} \left(\frac{\alpha_{loc,i}-\alpha_i}{\tau_i}\right) & \alpha_{min} < \alpha_{loc,i} < \alpha_i, \\ \left(\frac{\alpha_{min}-\alpha_i}{\tau_i}\right) & \alpha_{loc,i} < \alpha_{min}, \end{cases} \tag{2.19}$$

where α_{min} is 0.2 and τ_i represents the decay timescale; given by $\frac{h_i}{v_{max,sig,i}}$ (where $v_{max,sig,i}$ is the maximum signal velocity).

Through SPHS, the dissipation of entropy is included as

$$\dot{A}_{diss,ij} = \sum_j^N \frac{m_j}{\bar{\rho}_{ij}}\bar{\alpha}_{ij}v^P_{sig,ij}L_{ij}\left[A_i - A_j\left(\frac{\rho_j}{\rho_i}\right)^{\gamma-1}\right]K_{ij}, \tag{2.20}$$

(Read and Hayfield, 2012) which ensures energy is conserved. Here $K_{ij} = \hat{r}\cdot\nabla_i W_{ij}$ and $v^P_{sig,ij}$ is the signal velocity if is is positive, however 0 if v_{sig} is negative. Additionally, the factor L_{ij} is a pressure limiter of the form

$$L_{ij} = \frac{|P_i - P_j|}{P_i + P_j}, \tag{2.21}$$

which is included to avoid driving pressure waves caused by particles with large differences in entropy inside a smoothing kernel.

2.3 The time integration scheme

Using the equations of motion described in sections 2.1 and 2.2.3, one can follow the motion of both SPH and N-body particles over time. However, how accurate this is depends on the time integration scheme. GADGET-3 uses a leapfrog time integrator with a prediction step (Springel, 2005).

Fundamentally the process of time-stepping in GADGET-3 can be split into two operators; a 'drift' operator $D(\Delta t)$ and a 'kick' operator $K(\Delta t)$, which advance the positions and velocities of SPH particles respectively. Written in full, these are

$$D(\Delta t)\begin{cases} \boldsymbol{p}_i & \longmapsto \boldsymbol{p}_i \\ \boldsymbol{x}_i & \longmapsto \boldsymbol{x}_i + \frac{\boldsymbol{p}_i}{m_i}\int_t^{t+\Delta t}\frac{dt}{a^2} \end{cases} \tag{2.22}$$

$$K(\Delta t)\begin{cases} \boldsymbol{x}_i & \longmapsto \boldsymbol{x}_i \\ \boldsymbol{p}_i & \longmapsto \boldsymbol{p}_i - \sum_j m_i m_j \frac{\partial \phi(\boldsymbol{x}_{ij})}{\partial \boldsymbol{x}_i}\int_t^{t+\Delta t}\frac{dt}{a} \end{cases} \tag{2.23}$$

(Quinn et al., 1997; Springel, 2005), where $\phi(x_{ij})$ is the potential between particles i and j. GADGET-3 uses a combination of these operators to dictate the time evolution of both the velocity and position. Known as the 'Kick'-'Drift'-'Kick' or K-D-K configuration, the overall time evolution operator; $U(\Delta t)$, is defined as

$$U(\Delta t) = K\left(\frac{\Delta t}{2}\right) D(\Delta t) K\left(\frac{\Delta t}{2}\right) \tag{2.24}$$

(Springel, 2005). Here the particles are 'kicked' by half of a set time interval and the positions are updated. These updated positions are then fed into the 'Drift' operator which advances the particle momentum by the full time interval. Finally, the updated momentum is then fed into the 'Kick' operator and the positions are advanced another half-interval.

The timesteps of particles are assigned using the following criterion;

$$\Delta t = min\left[\Delta t_{max}, \frac{2\eta\,\epsilon}{|a|}\right] \tag{2.25}$$

(Springel, 2005), where a is the acceleration of the particle, ϵ is the gravitational softening, η is an accuracy factor and t_{max} is a maximum timestep set as a free parameter of the simulation. This timestep criterion is used for both SPH and N-body particles in the simulation. However, SPH particles have a further timestep criterion;

$$\Delta t_i = \frac{C_{courant} h_i}{max_j(v_{sig,ij})} \tag{2.26}$$

(Springel, 2005), where $C_{courant}$ is the Courant factor (Courant, Friedrichs, and Lewy, 1928), while w_{ij} is defined in section 2.2.4. The timestep of an SPH particle is taken to be either equation 2.25 or 2.26 depending on which is the smallest.

Additionally, particles are assigned timesteps which are factors of 2 lower than a global timestep. If the motion of a particle is changing rapidly (for example, if its undergoing gravitational collapse), this means a smaller timestep can be assigned. If, however, the reverse is true, this means the particle can be assigned a longer timestep. Moreover, if a particle timestep needs to increase it can only do so every other timestep. This method means all times-steps are synchronized while allowing an efficient distribution of computational resources (Springel, 2005).

2.4 Cooling

In order to bridge the gap between star forming gas and hot ionised gaseous outflows, the simulations in this thesis are required to follow gas across a large range of temperatures, from 20 K up to 10^8 K. In order to do so, one must take into account the variety of cooling processes in different temperature regimes. Here I will discuss the dominant cooling processes in different temperature bands, along with how these depend on the metallicity of the gas. I will then detail how cooling is implemented in GADGET-3.

2.4.1 Below 10^4 K

Below 10^4 K, Hydrogen is considered to be neutral and cooling predominantly occurs via the collisional excitation of electrons into the low-lying fine structure energy levels of ions such as O I and N II (Spitzer, 1978). The subsequent de-excitation and loss of energy as radiation has the net result of cooling the gas. Since this cooling process requires the collision between two particles, it is known as a two-body process. All the cooling processes presented in this thesis are considered to be two-body, rather than three-body, due to the relatively low density of astrophysical fluids (e.g. Mo, Bosch, and White, 2010). Furthermore, cooling can also occur via the collisional excitation of molecules such as H_2, where the rotational and/or vibrational states are excited. This means gas containing no metals (known as primordial gas) requires the presence of significant amounts of H_2 in order to cool (Saslaw and Zipoy, 1967). The formation of H_2 is enhanced by the presence of dust grains in the gas. Therefore, through the presence of metal ions and the enhanced rate of H_2 formation, higher metallicity gas is able to cool more efficiently below 10^4 K. How primordial gas cools below ~ 100 K (the limit of cooling via H_2 molecules e.g. Bromm and Larson, 2004) and form the first (Population III) stars, is still a matter of debate (see Bromm, Coppi, and Larson, 2002, for a recent review on the topic).

2.4.2 10^4 K - 10^6 K

In this temperature band three main radiative cooling processes are at play; collisional excitation, collisional ionisation and recombination. During collisional ionisation, a bound electron is ionised during a collision with a free electron, causing the free electron to lose the ionisation threshold energy and the gas to cool. On the other hand, during recombination an electron is captured by an ion, radiating the energy difference between its free and bound state. As we can see from Figure 2.1, which plots the cooling curves used in the simulations presented in this thesis (where different colours/line-styles indicate different metallicities), there a multiple peaks in the cooling rate corresponding to specific excited states associated with different ions. For example, in both enriched and primordial gas there is a peak at $\sim 10^{4.2}$ K, due to the collisional excitation of Hydrogen, as well as a peak at $\sim 10^5$ K, which is due to excited energy levels associated with the He^+ ion. Moreover, this second peak is stronger in higher metallicity gas due to excited levels in Oxygen, Carbon and Nitrogen. There is also a peak at $\sim 10^6$ K present in metal-enriched gas that is not present in primordial gas, which is due to elements such as Neon and Iron. For an overview of radiative cooling processes see Spitzer (1978), along with Mo, Bosch, and White (2010).

2.4.3 Above 10^6 K

Above 10^6 K (or 10^7 K in metal-enriched gas) the dominant cooling process is considered to be Bremsstrahlung (or free-free) cooling. Bremsstrahlung cooling describes the acceleration and subsequent emission of electromagnetic radiation by an election when it interacts with the electromagnetic field associated with positive ions. This is the main cooling process in this temperature regime due to the fact the majority of the gas is considered to be ionised.

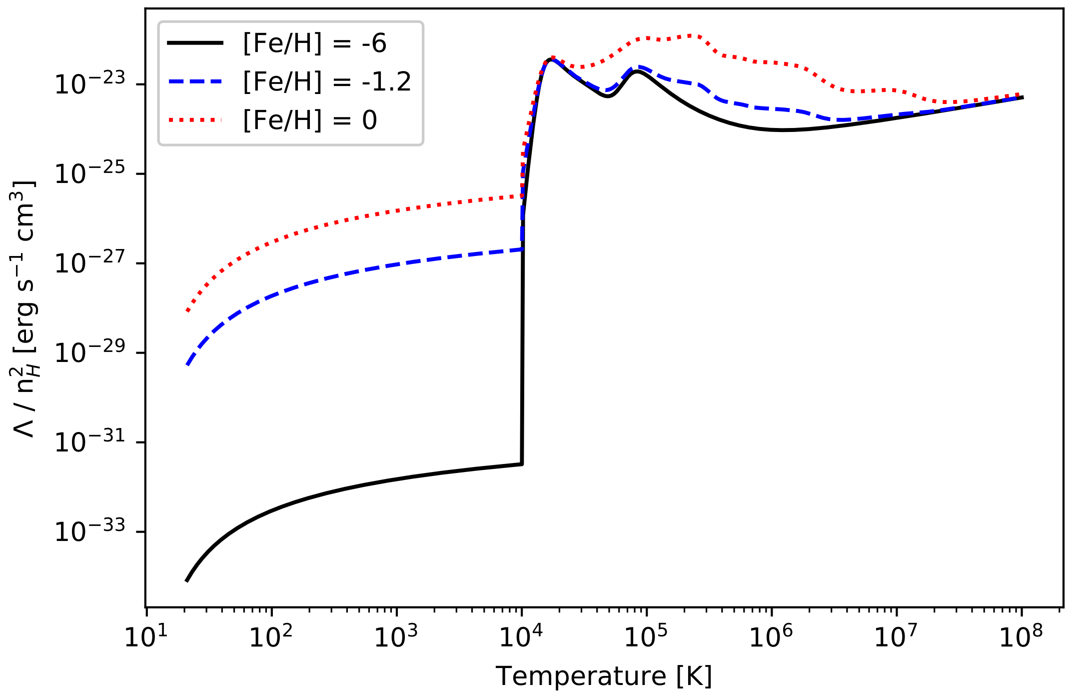

FIGURE 2.1: Plot to show the normalised cooling rate (Λ/n_H^2) across a temperature range 20 K - 10^8 K, where n_H is the number density of Hydrogen atoms in cm^{-3}. The solid black line is the cooling curve for primordial metallicity gas, while the blue (dashed) and red (dotted) lines show the cooling curves for gas with metallicities [Fe/H] = -1.2 and [Fe/H] = 0 (solar metallicity) respectively. Here [Fe/H] is the $\log_{10}$ of the ratio between the metal content of the gas compared with that of our sun. These metallicity values were plotted since they are those used for the simulations presented in this thesis.

2.4.4 Cooling in GADGET-3

The simulations in this thesis use look-up tables representing the cooling curves shown in Figure 2.1, along with the density and temperature of each gas particle, in order to calculate the cooling rate of the gas. The cooling curves shown in Figure 2.1 are a combination of two methods; below 10^4 K I use the method described in Mashchenko, Wadsley, and Couchman (2008). Here the metal-dependent cooling rate is calculated using the expression;

$$log(\Lambda/n_H^2) = -24.81 + 2.928x - 0.6982x^2 + log(Z/Z_\odot) \tag{2.27}$$

where $x \equiv log(log(log(T)))$, T is temperature, $Z/Z_\odot$ is the gas metallicity in solar units and n_H is the number density of Hydrogen atoms in cm^{-3} (Mashchenko, Wadsley, and Couchman, 2008). This is an approximation of the cooling function between 20 K and 10^4 K which takes into account the fine structure transitions of C, N, 0, Fe, S and Si.

Above 10^4 K the cooling function is approximated using look-up tables generated using the MAPPINGS III code (an updated version of the MAPPINGS II code presented in Sutherland and Dopita, 1993). MAPPINGS III follows the electronic transitions of 16 atomic species across the temperature range from 10^2 K to 10^8 K, including all associated ionisation states.

Chapter 3

Investigating stellar feedback in GMCs: Part I ($Z_\odot$)

3.1 Introduction

The next two chapters of the thesis focus on the interplay between different feedback processes in GMCs. As we saw in Chapter 1, stellar feedback is integral to galaxy evolution; it affects both the formation of individual stars, as well as the global gas reservoir in a galaxy. This large dynamic range makes disentangling the complex mix of positive and negative stellar feedback effects a difficult task. Cosmological simulations often invoke subgrid prescriptions to encompass the global effects of an entire stellar population, focusing on the larger scale impacts of stellar feedback. Here stellar feedback is studied on resolved scales, instead looking at the effects of individual massive stars on the star formation rate and the state of the gas in isolated GMCs. In this way complex feedback effects that would be missed on larger scales can be studied. However, through these smaller scale interactions between different stellar feedback processes there can be larger global impacts on the galaxy.

In this thesis high mass GMCs of mass $\sim 10^6$ $M_\odot$ are investigated. The clouds have a large enough stellar mass to support multiple high mass stars (although this is dependent on the star formation efficiency of the cloud gas) and hence they offer an interesting laboratory for investigating the effects of stellar feedback. Moreover, the free-fall timescales of these clouds are over 10 Myr, which is enough time for the most massive stars to leave the main sequence (which occurs beyond 3 Myr). Furthermore, a typical OB-type star will have left the main sequence by 29 Myr (Schaller et al., 1992), which represents the timescale of the simulations run in this chapter.

Molecular clouds can in principle be disrupted due to other stellar feedback processes prior to the onset of SNe feedback. One of the processes that can lead to molecular cloud disruption is the expansion of HII regions, ionised by stellar radiation. However, Dale, Ercolano, and Bonnell (2012) find that clouds of mass $\sim 10^6$ M$_\odot$ are not significantly disrupted by photo-ionising winds prior to the onset of SNe feedback. Rogers and Pittard (2013) find that molecular clouds are able to survive the stellar winds from O-stars by forming low-density pillar-like chimneys in the cloud, through which hot gas can escape, allowing the dense star forming material to survive until SNe feedback begins. Also, taking the galactic environment into account, Dobbs and Pringle (2013), find typical GMC lifetimes ranging between $4 - 25$ Myr for clouds with masses greater than $\sim 10^5$ M$_\odot$. This puts them in the regime where SNe feedback can become important.

As stated in Chapter 1, the primary interest of this thesis is in the interplay between gradual feedback mechanisms and instantaneous energy injections. This follows on from work by Rogers and Pittard (2013); in this case the 'gradual feedback' I refer to would be stellar winds, which represents a constant (comparatively low power) heat source for the ISM, while SNe feedback is an instantaneous injection of the canonical 10^{51} ergs of energy. However, rather than focusing on stellar winds as a gradual heating source, the next two chapters investigate the mechanical energy input from a population of HMXBs (High Mass X-ray Binaries, see Chapter 1 for a review).

3.2 The numerical model

3.2.1 Basics of the model

The simulations in the next two chapters both used GADGET-3; a hybrid N-body/SPH code that is an updated version of the publicly available code GADGET-2 (Springel, 2005). The SPH method, along with GADGET-3 was introduced earlier. I also used the SPHS extension described in Read and Hayfield (2012) and detailed in Chapter 2, which is designed to model mixing of multiphase gas. Moreover, the Wendland-2 kernel was used (Wendland, 1995; Dehnen and Aly, 2012) with 100 neighbours. In all simulations presented in this thesis I use an ideal equation of state, $P = (\gamma - 1)\rho u$, where P is the gas pressure, γ is the adiabatic constant, set to 5/3, u is gas internal energy and ρ is particle density. For temperatures above 10^4 K, gas cooling is implemented using the look-up tables generated by the MAPPINGS III code (Sutherland and Dopita, 1993). Below 10^4 K I use the metal line cooling scheme described in Mashchenko, Wadsley, and Couchman (2008). For more details on radiative cooling and how it is implemented into GADGET-3 see Section 2.4. A maximum temperature of $\sim 10^8$ K is set for the gas, in order to avoid prohibitively small timesteps. I note that typically only ~ 10 particles in my simulations are at this temperature limit, so the results are unaffected by this. Whilst I vary parameters between different simulations, the canonical values are a total mass of 2×10^6 M$_\odot$ modeled using 5 million SPH particles, meaning the mass of each individual particle is ~ 0.4 M$_\odot$. I employ both adaptive smoothing lengths and softening lengths for the SPH particles with a minimum value of 0.1 pc. For convenience, any unbound gas particles beyond an outer radius of 5 kpc are removed from the simulation.

In these simulations the minimum resolvable mass is given by $2N_{\mathrm{neigh}}m_{\mathrm{p}}$, where N_{neigh} is the number of neighbours within a smoothing kernel and m_{p} is the mass of an SPH particle (Bate and Burkert, 1997). Therefore gas particles are replaced with sink particles if they reach a density corresponding to the Jeans density for this minimum resolvable mass, i.e.

$$\rho_{\mathrm{J}} = \left(\frac{\pi k_{\mathrm{B}} T}{G \mu m_{\mathrm{H}}}\right)^3 \frac{1}{(2N_{\mathrm{neigh}} m_{\mathrm{p}})^2} \tag{3.1}$$

where k_{B} is the Boltzmann constant, μ is the mean molecular weight and m_{H} is the mass of Hydrogen. I also require that the gas must be converging (i.e. $\nabla \cdot \mathbf{v} < 0$) and that the temperature of the gas particle must be < 500 K. In calculating ρ_{J} I use approximate values of μ (1.291 for $Z_\odot$) for simplicity (Sutherland and Dopita, 1993). However, for calculating the cooling rates, μ is calculated self-consistently using the electron fraction. Once the sink particles are formed, they accrete any gas particles that enter within a radius of 0.5 pc with a kinetic energy less than the gravitational potential energy with respect to the sink particle. This avoids gas particles being assigned prohibitively small timesteps within the simulation and also allows sink particles, which represent unresolved star forming regions, to grow in mass.

Once a sink particle accretes enough gas to reach a mass of 180 M$_\odot$, it is considered to contain 1 massive (> 8 M$_\odot$) star, which in a fraction of cases is situated in a binary system with a second high mass star - see below for details. The value of 180 $M_\odot$ lies in the range between 95 $M_\odot$ and 210 $M_\odot$, which correspond to the masses inferred from a Kroupa IMF (initial mass function) (Kroupa, 2001) without/ with the contribution from unresolved binaries, evaluated in the mass range 0.01 $M_\odot$ – 100 $M_\odot$. These values are arrived upon using the mean masses, along with the number fractions, given in supplementary table 2 in Kroupa (2002). The number fraction I use, 0.2%, is conservative compared with that found in Power et al. (2009) (hereafter P09); which was 1.1%.

Furthermore, it is assumed all stars with a mass >8 $M_\odot$ are in binaries, which is consistent with the high multiplicity fractions (>50 %) observed for massive stars (e.g. Sana, James, and Gosset, 2011; Chini et al., 2012). The properties of the binary system within the sink particle are determined using a Monte-Carlo approach described below. Furthermore, a physical selection process is used to determine which systems go on to become HMXBs. These processes are described in detail in the next section (Section 3.2.2).

There is only one HMXB system (1-2 linked SNe events) per sink particle, as the likelihood of a second within the time window of the 33 Myr simulations is small. This method results in a random distribution of SNe/HMXB events in likely locations of dense star formation. Moreover, using this method the number of SNe/HMXB events obtained is roughly consistent with star forming mass.

It is important to note that throughout these simulations, the binary properties of the stellar population are considered separately to the properties of the sink particle within the simulation. In other words, each sink particle has a mass from which its gravity in the simulation is calculated, and an associated 'primary star mass' of the binary which is a virtual property solely used to set the HMXB feedback properties of the sink particle.

3.2.2 Binary Population Synthesis

The relevant parameters when considering a population of binaries are: the initial mass of the primary star, the mass ratio, q, of the primary to secondary star and the lifetime of both stars. Since a HMXB consists of a neutron star or black hole accreting material from an O or B companion star, the primary star needs to exceed $\sim$ 8 $M_\odot$ to form a neutron star or 20 $M_\odot$ to form a black hole. Therefore, as soon as a sink particle exceeds the minimum mass of 180 $M_\odot$, a Kroupa IMF is sampled between 8 $M_\odot$ and 100 $M_\odot$ to determine the primary star mass. Next, the binary mass ratio is sampled uniformly between 0 to 1 since the distribution of q values is still considered to be largely flat (e.g. Sana et al., 2013). If this sampling results in a secondary mass of less than 8 $M_\odot$, then the system is discounted as a HMXB progenitor since the secondary is required to be a massive OB type companion.

A lifetime of the primary star is then determined and, in the case when the secondary mass meets the criteria, a companion stellar lifetime. The primary lifetime will determine the time of the first Type II supernova and the secondary lifetime sets a limit on the lifetime of the HMXB feedback phase, along with the time of the companion supernova. In order to obtain the lifetime of the primary star and its companion I use the same method as in Power et al. (2009). This method uses a lookup table which lists mass versus lifetime in order to interpolate the stellar lifetimes. I use results from Table 1 of Meynet and Maeder (2000) and Table 45 of Schaller et al. (1992) and calculate lifetime of massive stars by making the approximation $t_{\rm life} \sim t_{\rm H} + t_{\rm He}$ (where $t_{\rm H}$ is the lifetime of the Hydrogen burning phase of the star and $t_{\rm He}$ is the same for Helium). The mean delay time between a sink particle being created and accreting enough gas to reach 180 $M_\odot$, is $\sim$ 0.8 Myr (dependent on the simulation). Furthermore, sink particles begin to be created at $\sim$ 5-6 Myr in all runs (see Fig. 3.19). This delay time depends on the initial velocities of the gas particles (e.g. comparing Runs A and E in Fig. 3.19), along with the size of the cloud (for example the sink particles are formed earlier in Run V - a larger cloud - than Run A; see Fig. 3.19). I take into account the age of the sink particle when determining the delay time before the first SNe. If this delay time is longer than the lifetime of the primary star, the sink particle immediately undergoes SNe feedback. Therefore, given the minimum lifetime of a massive star in the simulations is $\sim$ 3 Myr (corresponding to 100 $M_\odot$), this results in the first SNe and HMXB events occurring at $\sim$ 9-10 Myr (see Fig. 3.16).

It is worth noting a limitation to this method is that I do not include the effect of binarity on the evolution of the massive stars. Recent work has concluded interactions in close binary systems (such as Roche-lobe overflow) can significantly affect the evolution of both the primary star and its companion (e.g. Eldridge, Izzard, and Tout, 2008; Yoon, Woosley, and Langer, 2010; Song et al., 2016). Focusing on stellar lifetimes, mass accretion onto the primary star in a binary system could prolong its lifetime by providing addition nuclear fuel, however the additional stellar mass also acts to speed up the nuclear burning process. Moreover, the loss of mass from the secondary star can also prevent it undergoing core-collapse at the end of its life. The interplay between these two conflicting processes was explored in Zapartas et al. (2017), where the delay times of core-collapse SNe (or SNe rate versus time) was compared between a single-star stellar population and a population containing binary stars. The paper found the largest differences between the distribution of delay times occurred beyond 20 Myr. Prior to this the two distributions were very similar - indicating there are no significant divergences in SNe rate between single star/ binary star populations in the time-frame I am interested in.

A fraction of the possible HMXB progenitors will not survive the supernova of the primary, becoming unbound when mass is lost. In order to estimate this fraction, as in P09, the assumption is made that the binary system becomes unbound if over half its mass is lost in the supernova. A significant factor in determining the surviving remnant mass is the amount of 'fallback' that occurs during the SNe explosion, a quantity that is metal-dependent. For example, Zhang, Woosley, and Heger (2008) found the supernova of massive stars at lower metallicity are more likely to result in a black hole, compared with those at solar metallicity. In order to calculate the mass of the system post-supernova, I use look-up tables with remnant masses taken from a combination of Tables 4-5 from Sukhbold et al. (2016), Table 4 of Maeder (1992) and Table 4 from Zhang, Woosley, and Heger (2008). Zhang, Woosley, and Heger (2008) also explore the difference between explosion mechanisms; altering piston locations and explosion energies. For this work, I average over the results for each initial mass at $Z = Z_\odot$. From Zubovas, Wynn, and Gualandris (2013) I expect > 93 per cent of all (including low mass) binary systems to be disrupted. The remaining systems then switch on their HMXB phase immediately and this lasts for the lifetime of the secondary star. At the end of the secondary lifetime the sink particle switches off HMXB feedback and undergoes SNe feedback for a second time. After this the sink particle ceases to produce feedback. The lifetime of the HMXB feedback is typically of the order of 10 Myr, while the timestep of the simulation is $\sim 10^4$ yrs. This ensures the gradual heating of the HMXB feedback is resolved.

I implemented this binary population synthesis method into GADGET in such a way as to tie the random seed to the particle identity and the number of the current time step, neither of which should vary between runs with identical initial conditions prior to the onset of feedback. In this way, for runs with identical initial conditions, prior to the first HMXB event, the gas will have the same phase/morphology and the massive stars will occur at the same locations. For example, Runs A and C will be identical prior to the first HMXB event, when they will diverge. At this point the underlying stochasticity of massive star feedback will play a role. The same is true of Runs E and F, V and W and so on. This facilitates easy comparison between different feedback effects.

3.2.3 Feedback Mechanisms

Throughout the simulations supernova feedback is implemented by injecting the canonical value of 10^{51} erg of thermal energy into the surrounding $N_{\rm neigh} \sim 100$ neighbouring gas particles. The amount of energy each gas particle receives is kernel weighted, hence those particles closest to the star particle receive the most energy. As I saw in Chapter 1, thermal supernova feedback commonly results in the 'over-cooling' problem. This is a consequence of low resolution simulations, where energy is initially injected into a large gas mass, causing the gas to cool artificially quickly and stall feedback (Springel and Hernquist, 2003; Stinson et al., 2006; Creasey et al., 2011). However, the mass resolution of this set of simulations is such that they can capture the Sedov-Taylor phase of the shock expansion and hence are not significantly affected by over-cooling, as I will see in section 3.3.

In this chapter I explore HMXB feedback with two different implementations; the first is using thermal energy injection and the second is using kinetic energy injection. For the thermal case the internal energy of the particles is increased, while for the kinetic case the energy is delivered as a radial velocity kick. Similarly to the SNe feedback, the HMXB schemes weight the amount of energy given to their neighbouring particles using the SPH kernel. Here I have assumed the shock-heating of the jets has isotropically raised the temperature of the surrounding gas. This assumption is dependent on factors such as the angle of jet precession and cone angle (Goodall, Alouani-Bibi, and Blundell, 2011), along with jet power and the density of the surrounding ISM (Abolmasov, 2011). These factors are beyond the scope of this work, however would be interesting to investigate in future work. Moreover, there are multiple observations of superbubbles around ULXs , which have been collisionally energized by jets (e.g. Russell et al., 2011), which support the inclusion of HMXB as a isotropic heating of the surrounding gas.

Both the thermal and kinetic HMXB feedback schemes inject the same amount of energy across the total HMXB lifetime. This value is set to 10^{52} erg and the amount of energy a sink particle injects is proportional to its time-step. This results in a mean energy injection rate of 3×10^{37} erg/s for a lifetime of 10 Myr. I find lifetimes between $5 - 35$ Myr in the simulations reported below. I have chosen this rate of energy injection as it is consistent with rates observed for HMXBs. For example, the wind-fed jet in Cygnus X-1 is estimated to input $\sim 10^{35-37}$ erg/s into the ISM (Gallo et al., 2005), and SS433 inputs $\sim 10^{39}$ erg/s into the ISM (Brinkmann, Kotani, and Kawai, 2005). Thus the value of injected energy falls in the observed range. Similar numbers were used by Artale, Tissera, and Pellizza (2015). HMXBs exhibit time variability in their luminosity and energy injection rate, associated with a spectral transition from hard to soft X-ray (as is seen in Cygnus X-1), however this is on a much smaller timescale than the time resolution of these simulations, where a single time-step roughly corresponds to 10^4 yrs.

I note that massive star winds inject $\sim 10^{36}$ erg/s of energy into the ISM. This value is based on a mass loss rate of 10^{-5} $M_\odot$/yr (Repolust, Puls, and Herrero, 2004) and wind velocities of 1,000 km/s (Leitherer, Robert, and Drissen, 1992). Thus the energy input from a single massive star wind is expected to be smaller than the energy input I assume for an HMXB, owing to the fact jets are produced further into the potential well of the stellar object than line-driven winds, along with the fact observations indicate much of the accretion energy in XRBs is channeled into the mechanical power of the jets (Gallo et al., 2005; Sell et al., 2010; Soria et al., 2010). However, there are many massive stars for every HMXB. Very crudely, if I assume all massive stars are in binaries, and I expect only 1-10% of these systems to form HMXBs, then I would expect 10-100 massive stars per HMXB. Thus the energy injected by massive stars would be comparable to that injected by HMXBs. I therefore anticipate that the results will be qualitatively similar to considering feedback from massive star winds. Although including HMXBs as an anisotropic source of heating would most likely affect this comparison. Moreover, stellar winds would be present prior to the first SNe event, which could affect the efficiency of the SNe feedback by lowering the density of the surrounding ISM (e.g. as in Rogers and Pittard, 2013). This will be considered in more detail in Chapter 5.

3.3 Sedov-Taylor Comparison

In order to ascertain whether the SNe implementation in GADGET-3 can capture the Sedov-Taylor phase of the shock expansion, I performed a simulation of a single supernova explosion in a homogeneous gaseous sphere and compared the results with the Sedov-Taylor solution. The particle resolution was set to 1 $M_\odot$ (lower than the result runs), while the SNe injected 2×10^{51} erg of thermal energy into the surrounding ~ 100 SPH neighbours according to the kernel weighted scheme I described in the previous section (3.2). The radius of the cloud was set to 60 pc and the initial temperature of the gas was set to the virial temperature, which was 534 K. The simulations are unable to resolve the initial free expansion phase of the shock, since this breaks down when the swept-up mass equals the mass ejected during the supernova explosion; a condition which is instantly met when I inject the SNe energy into the surrounding 100 SPH particle neighbours.

Firstly, Figure 3.1 plots density slices taken in the x-y plane at varying times into the evolution of the supernova remnant (SNR). The dashed circle on each plot indicates the expected radius at that time (calculated using the Sedov-Taylor solution). From Figure 3.1 we can see the simulation can recover the expected location of the shock front during the Sedov-Taylor phase. Additionally, Figure 3.2 plots the shock radius, velocity, post-shock temperature and total internal energy inside the SNR, against the analytic Sedov-Taylor solution. The shock radius, velocity and temperature were defined as the mean values of particles in a 2 pc radial bin, centered on the position of maximum density. The total internal energy is just the sum of the internal energies of the gas particles located inside the spherical shock front. The SNe energy was injected at ~ 0.01 Myr. From 3.2, it can be seen the shock radius, velocity and temperature align well with the analytic solution until ~ 0.6 Myr, when the temperature of the particles in the 2 pc radial bin drops steeply. There is also a corresponding drop in shock velocity and total internal energy inside the remnant. The drop in temperature indicates the post-shock medium immediately behind the shock-front has been able to cool efficiently, forming a cool shell. This shell is being pushed forwards by the hot, lower density gas in the centre of the remnant and indicates the SNe remnant (SNR) has left the Sedov-Taylor phase. As a result, the expansion of the SNR is

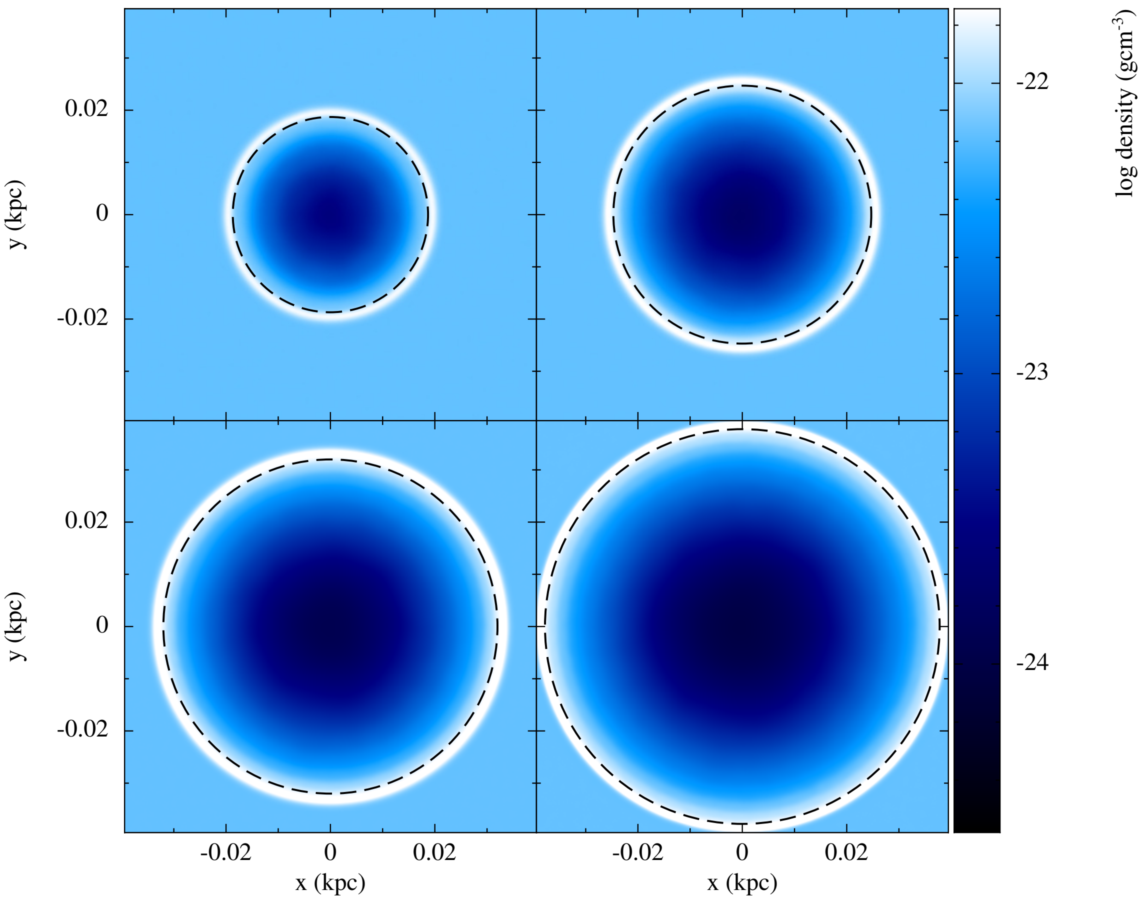

FIGURE 3.1: Density slices for the Sedov-Taylor test, taken in the x-y plane at z = 0 at t = 0.1 Myr (top left), 0.2 Myr (top right), 0.4 Myr (bottom left) and 0.6 Myr (bottom right). The dashed circles on each plot indicate the expected shock radius at that time (calculated using the Sedov-Taylor solution).

no longer adiabatic, which can be seen in the total internal energy plot in Fig. 3.2; at $\sim$ 0.6 Myr, the total internal energy of the gas inside the shock front begins to drop. Once the gas inside the centre of the remnant has cooled, it will have entered the 'snowplough', or momentum-conserving phase.

The roughly constant radial power-law is likely due to the fact the simulation volume is finite and the shock has reached the outer-parts of the gaseous sphere. The lack of gas outside the shock causes a break-down in the analytic progression of the shock, however it would be expected once the SNR enters the snowplough phase, the radius would increase as $t^{1/4}$ instead of the $t^{2/5}$ power law seen in Fig. 3.2.

The fact the Sedov-Taylor phase of the SNR expansion can be resolved indicates the resolution and SNe feedback implementation are both sufficient to capture the effect of SNe explosions on the ISM down to tens of parsec scale.

3.4 Initial Conditions

In the next two chapters the GMCs modelled range from being globally bound to marginally unbound. I measure the boundedness of each cloud using the virial parameter $\alpha_{\mathrm{vir}} = |E_{\mathrm{kin}} + E_{\mathrm{therm}}|/|E_{\mathrm{pot}}|$, which is varied between 0.7 and 1.2 (the cloud is considered virialised at $\alpha_{\mathrm{vir}} = 0.5$). The cloud mass is taken to be $2 \times 10^6\,\mathrm{M}_\odot$, with some additional simulations run with $2 \times 10^5\,\mathrm{M}_\odot$ for comparison. The clouds are initially seeded with a non-driven turbulent velocity spectrum based on Dubinski, Narayan, and Phillips (1995). I use a Kolmogorov power spectrum with $P(k) \sim k^{-11/3}$ to generate a velocity field with homogeneous, incompressible (divergence-free) turbulence. This is achieved by defining the velocity field as the curl of a vector potential $\mathbf{A}$. The Fourier transform of this vector potential is then taken and each k mode is assigned an amplitude drawn from a Rayleigh distribution of variance $\sim k^{-(11/3+2)/2}$; and an associated phase is drawn uniformly from 0 to 2π. I then take the inverse Fourier transform of the curl of $\mathbf{A}$ in order to obtain the real velocity components. As I take the inverse Fourier transform, I sum over k values between k_{max} and k_{min}. These limiting values are set by the minimum length scale and maximum length scale of the simulation respectively, for the simulations in the next two chapters $k_{min} = 2\pi/R_{\mathrm{out}}$,

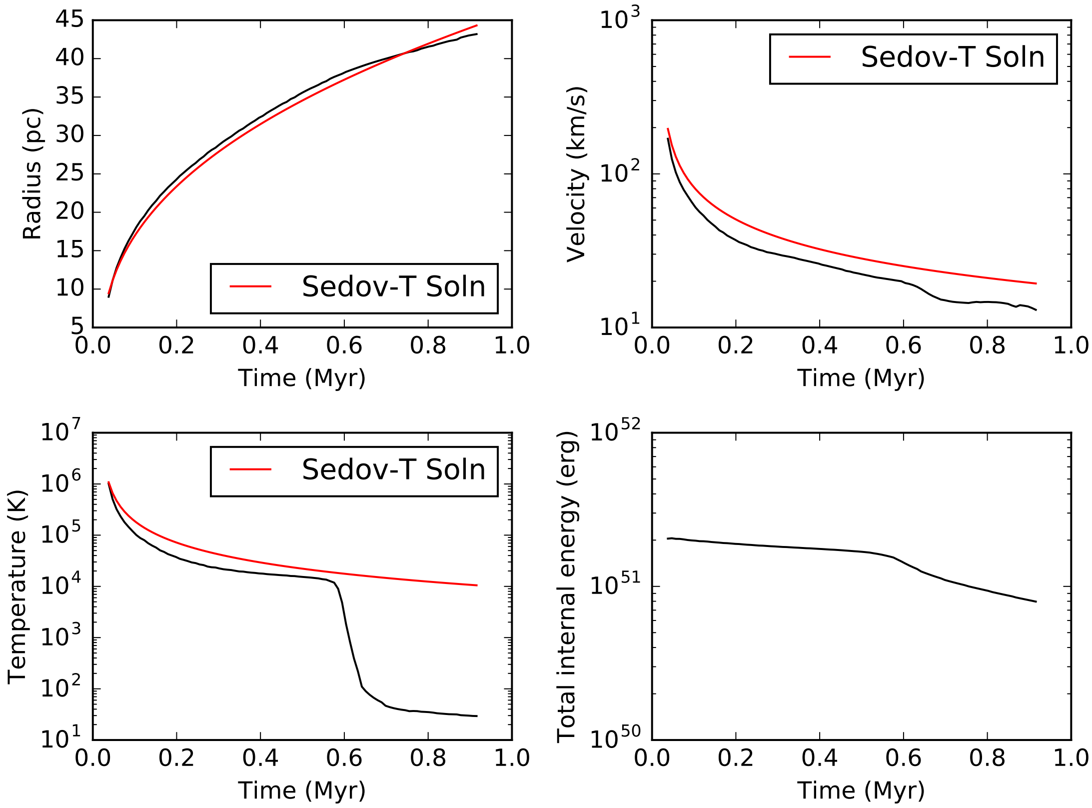

FIGURE 3.2: Plots to show the time evolution of the shock radius (in pc, upper left), velocity (in km/s, upper right), the post-shock temperature (in K, lower left) and the total internal energy of the gas inside the shock front (in erg, lower right). The Sedov-Taylor analytic solution for the radius, velocity and temperature of the shock is plotted in red. At $t \approx 0.6$ Myr the shell is able to cool, meaning the expansion is no longer adiabatic and the solution deviates from the Sedov-Taylor result.

TABLE 3.1: The different simulations run through the course of this chapter. All runs are at [Fe/H] = 0, aside from J and M which are at [Fe/H] = 1.2 and contain no feedback (where [Fe/H] is the $\log_{10}$ of the ratio between the metal content of the cloud compared with that of our sun). Here M_0 is the initial gas mass (in $M_\odot$) of each simulation, R_0 is the initial cloud radius in pc, T_i is the initial temperature in K, α_{vir} is the initial virial parameter ($|E_{kin} + E_{therm}|/|E_{pot}|$), t_{ff} is the free-fall time of the cloud, m_{pcl} is the gas particle mass in each simulation, and HMXB is the type of HMXB feedback present (either kinetic or thermal).

Run	M_0 ($\times 10^6$ $M_\odot$)	R_0 (pc)	T_i (K)	α_{vir}	Mach No.	t_{ff} (Myr)	m_{pcl} ($M_\odot$)	HMXB	SNe (Y/N)
A	2	100	50	0.7	14.9	11.7	0.4	Therm	Y
B	2	100	50	0.7	14.9	11.7	0.4	Kin	Y
C	2	100	50	0.7	14.9	11.7	0.4	None	Y
D	2	100	50	0.7	14.9	11.7	0.4	None	N
E	2	100	50	1.2	19.5	11.7	0.4	Therm	Y
F	2	100	50	1.2	19.5	11.7	0.4	None	Y
G	2	100	50	1.2	19.5	11.7	0.4	None	N
R	0.5	65	50	0.7	9.1	12.3	0.1	Therm	Y
S	0.5	65	50	0.7	9.1	12.3	0.1	None	Y
V	5	150	50	0.7	19.3	13.6	1	Therm	Y
W	5	150	50	0.7	19.3	13.6	1	None	Y
J	2	100	150	0.7	8.3	11.7	0.4	None	N
M	2	100	150	1.2	11.0	11.7	0.4	None	N

where R_{out} is the outer radius of the gaseous sphere and $k_{max} = N^{1/3}/2R_{out}$, corresponding to the Nyquist frequency (which is set by the number of particles, N, in the initial conditions).

Table 3.1 summarises the different parameters used in the simulations. I vary the mass and size of the clouds, along with the virial parameter. In Chapter 4 the simulations are repeated at a lower metallicity. The initial conditions were chosen in accordance with the parameter space used by Dale, Ercolano, and Bonnell (2012), which in turn was derived from a catalogue of 158 galactic molecular clouds collated by Heyer et al. (2009). I perform simulations with the two (kinetic and thermal) HMXB feedback schemes. I also performed control simulations containing no HMXB feedback, however with SNe feedback still included and others with no feedback at all. The results of these simulations are presented in the next section. Finally I explore the effects of numerical resolution on the results in Chapter 4.

3.5 Results, [Fe/H] = 0

In the next two chapters I present the main results of this work. I split these into two main categories; simulations run with $[Fe/H] = 0$ (this chapter) and those run at $[Fe/H] = -1.2$ (Chapter 4). However, firstly I discuss the results of the simulations with no feedback at both metallicities, for comparison in later sections.

On a general note, during the results and discussion I refer to 'star-forming gas' and the 'star formation efficiency'. In the context of this work, I am actually referring to the mass contained in sink particles and the efficiency of the gas particle to sink particle conversion. Once the gas has been accreted onto a sink particle I have no further information on its fate and it is assumed that a fraction of the mass contained in sink particles will actually be involved in star formation. However, this is beyond the scope of the simulations in this thesis. Furthermore, once a sink particle has reached $180\,M_\odot$ the properties of the massive star(s) that are considered to be located there are calculated and further accretion is ignored. However, the mean mass accreted by a sink particle with a mass of $180\,M_\odot$ or higher is 41 $M_\odot$ across all runs which included stellar feedback, hence I consider this to have negligible impact on the massive star population in the simulations and therefore on the results.

3.5.1 Runs with no feedback: D, G, J, M

Fig. 3.3 plots the total energy of the gas in clouds (or Runs) D, G, J and M. None of these runs include feedback, instead the cloud is allowed to evolve under the action of the initial turbulent velocity field and collapse under its own gravity. Furthermore, Fig. 3.4 gives an example of the time evolution of $\alpha_{\rm vir}$ along with the thermal, kinetic and potential energies of the gas for a run with no feedback (in this case Run D). From Fig. 3.3 and Fig. 3.4, we can see the initial kinetic energy given to the gas particles at the beginning of the simulation is quickly converted into thermal energy and radiated away prior to the first snapshot time. The cloud then collapses and gravitational potential energy is converted to kinetic energy until 10-13 Myr (which is roughly the free-fall time for each cloud - see Table 3.1). At this point the majority (> 90 %) of the gas is converted into sink particles. The high sink particle mass and resulting low gas mass in the simulation beyond this point leads to a high gravitational potential (see Fig. 3.4), which explains the rapid jump in total energy seen in Fig. 3.3. This can also be seen in Fig. 3.5, which plots the time evolution of the fraction of the initial gas mass contained in sink particles. Beyond the free-fall time, the remaining gas in each cloud continues to collapse, increasing the kinetic energy of the gas as the gravitational potential energy decreases.

From Fig. 3.5 it is noticeable the mass fraction contained in sink particles is less in the runs at a metallicity [Fe/H]$= -1.2$; G and M. This is expected as cooling is less efficient at lower metallicity below 10^4 K, due to a lower amount of ions such as OII, OIII and CII (Mo, Bosch, and White, 2010). This relatively inefficient cooling means the temperature of the gas in the low metallicity runs is higher, resulting in a higher Jeans density and a reduction in the number of particles reaching this required density to form stars. However, the sink mass fraction still reaches 90% by 35 Myr in the low metallicity runs, indicating the majority of the gas is able to become star-forming within the time frame of the simulation.

Overall, despite the initial velocity field imposed on each cloud, the majority of the gas is able to cool and collapse to form sink particles in the free-fall time. Furthermore, the free-fall time of the clouds corresponds to the lower end of the lifetimes of massive stars (which can be as short as 3 Myr). However, in this suite of simulations, the average formation time. As a result, the number and locations of feedback events between $9 - 13$ Myr is expected to be crucial in determining the star formation efficiency of each cloud.

3.5.2 The injection of HMXB: Runs A (HMXB and SNe), C (Just SNe)

Density slices for the $Z = Z_\odot$ runs, taken at $t = 35$ Myr into each simulation, are shown in Fig. 3.6. Focusing on Runs A (HMXB and SNe feedback) and C (just SNe feedback), the addition of HMXB feedback on top of SNe feedback has resulted in a larger amount of high density (10^{-24} gcm^{-3}) gas inside the inner 2 kpc. Moreover, a lobe of lower density gas can be seen to extend from the inner $\sim$ 100 pc out to 5 kpc of cloud A. This low density lobe represents a possible 'chimney' – a region of lower density gas through which hot, feedback-heated gas can expand and escape the core of the molecular cloud. Looking instead at the temperature slice for Run A (Fig. 3.7), we see the lower right chimney does indeed contain hot gas, extending to the outer regions of the simulation ($\sim$ 5 kpc).

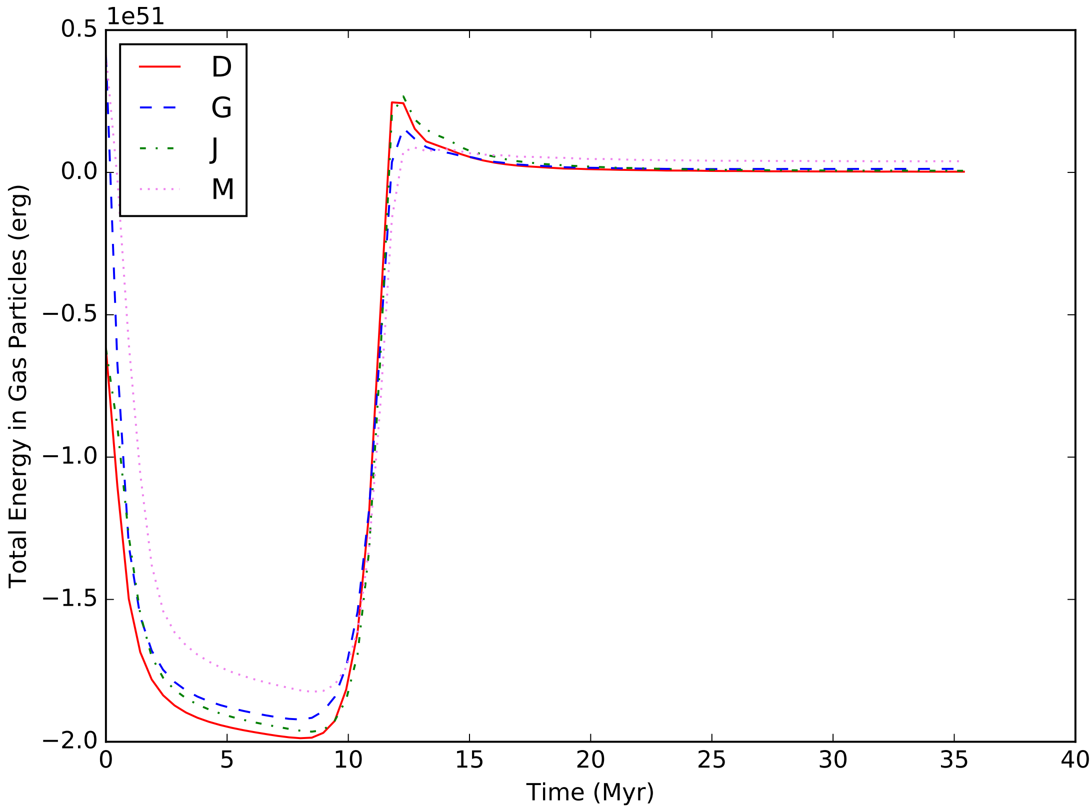

FIGURE 3.3: The time evolution of the total energy (calculated as the sum of the total potential, kinetic and thermal energies of the gas particles (i.e. minus sink particle mass) in the simulation) of the clouds with no feedback included; D, G, J and M.

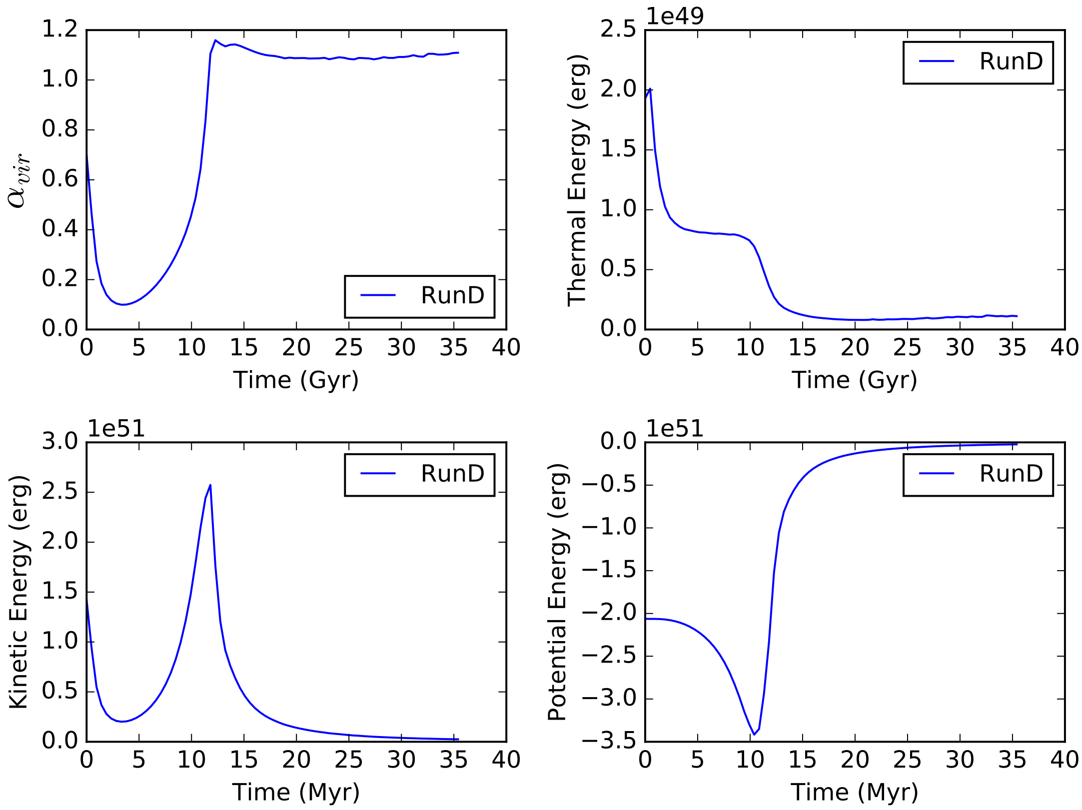

FIGURE 3.4: An example of the time evolution of the virial parameter (upper left plot), thermal energy (upper right), kinetic energy (lower left) and potential energy (lower right) of the gas particles in a run without feedback (Run D).

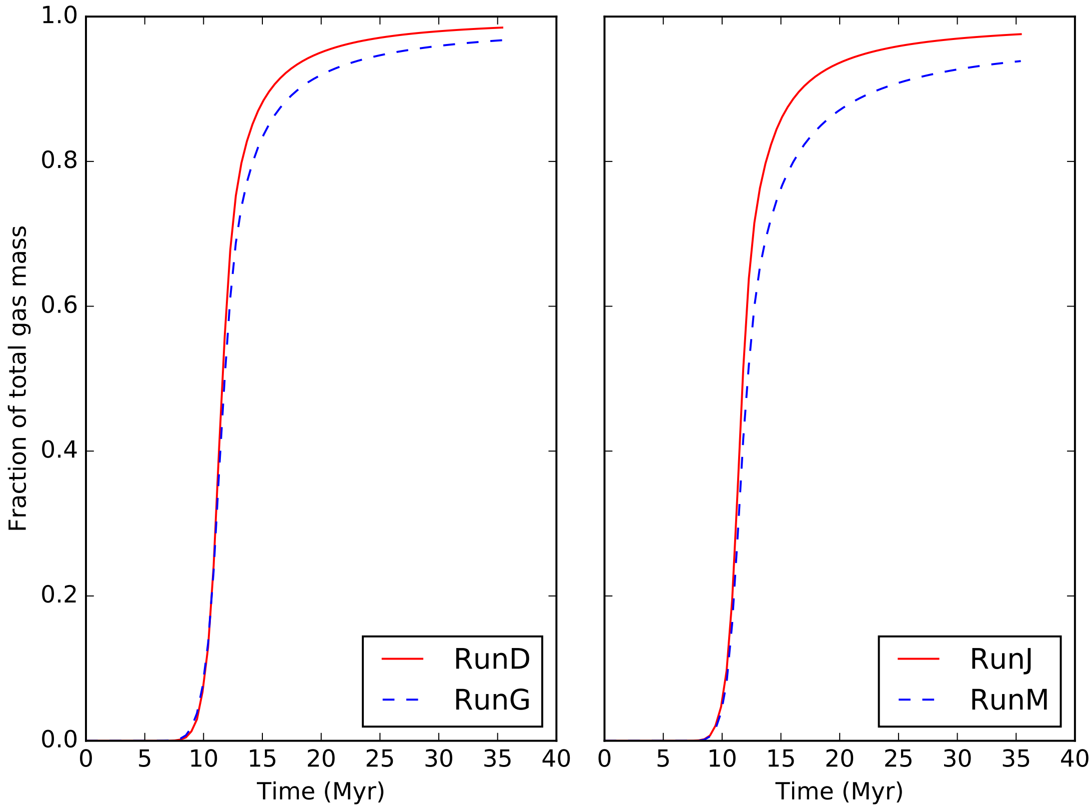

FIGURE 3.5: The time evolution of the fraction of the initial gas mass contained in sink (f_{sink}) particles for the runs with no feedback: D, G, J and M.

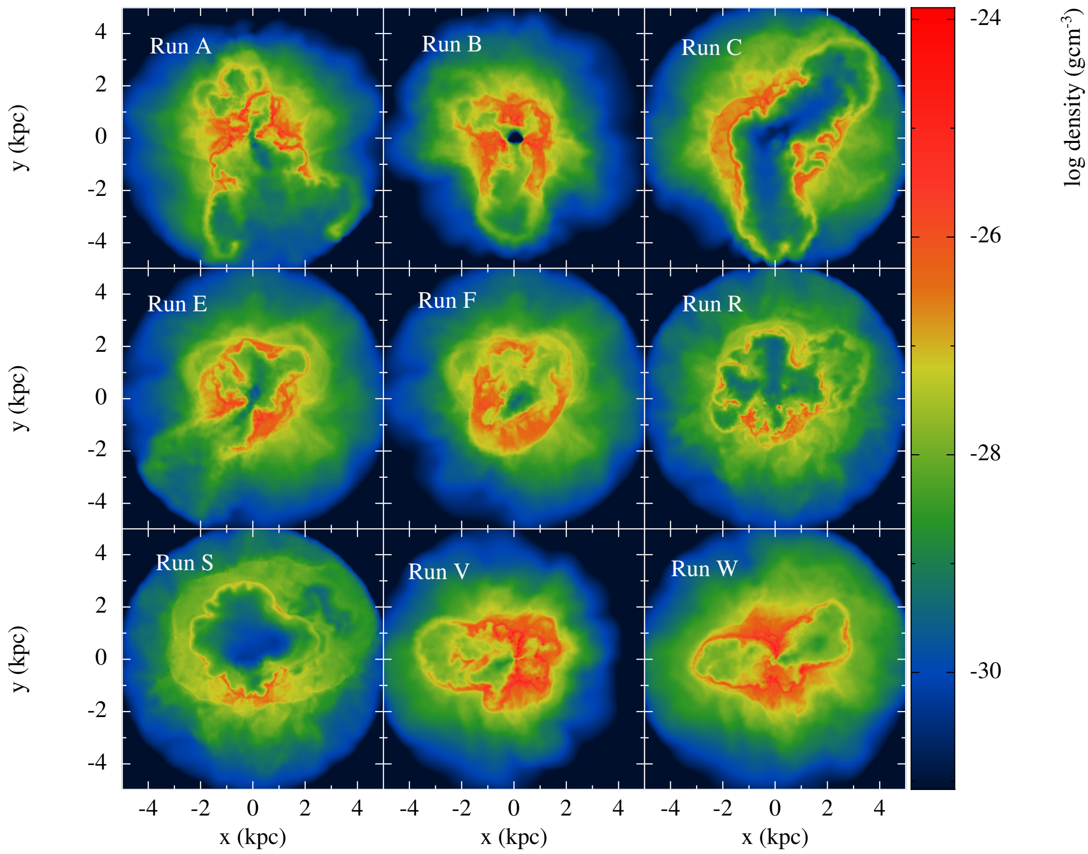

FIGURE 3.6: Density slices in the x-y plane at z=0, for the simulations run at solar metallicity, taken $t = 35\,\mathrm{Myr}$ into each simulation.

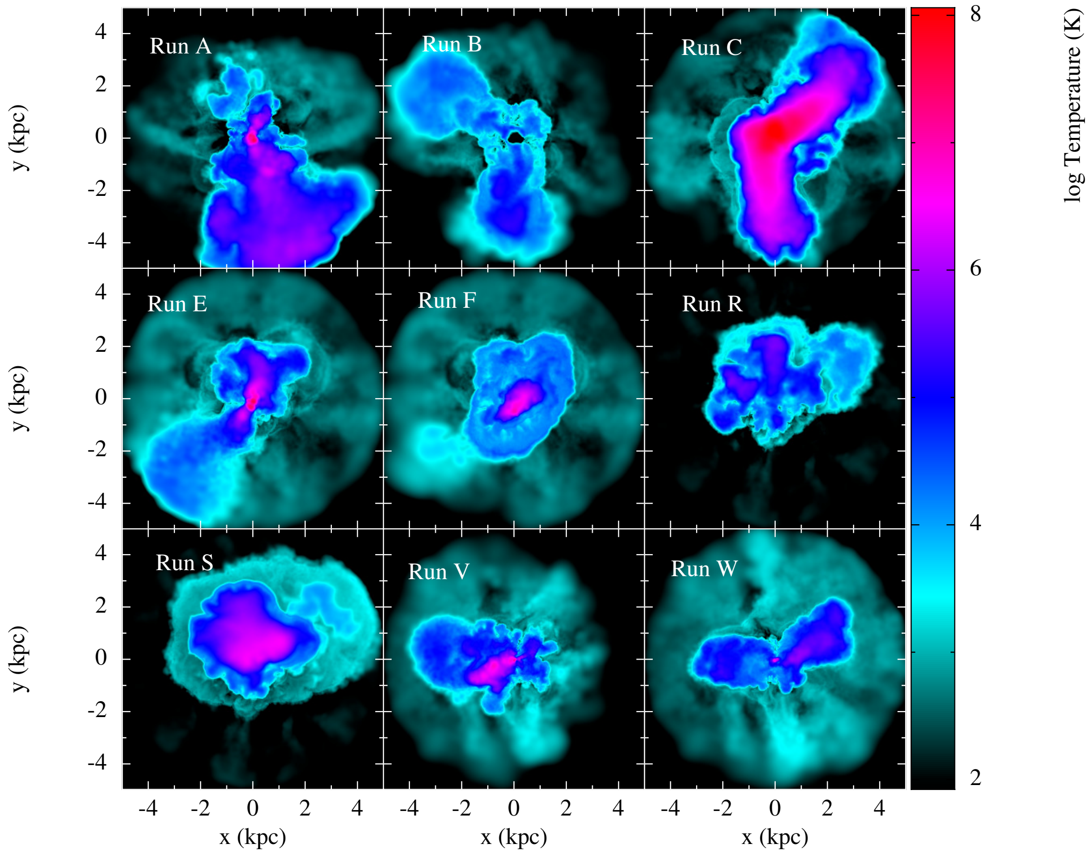

FIGURE 3.7: Temperature slices in the x-y plane at z=0, for the simulations run at solar metallicity, taken $t = 35\,\mathrm{Myr}$ into each simulation.

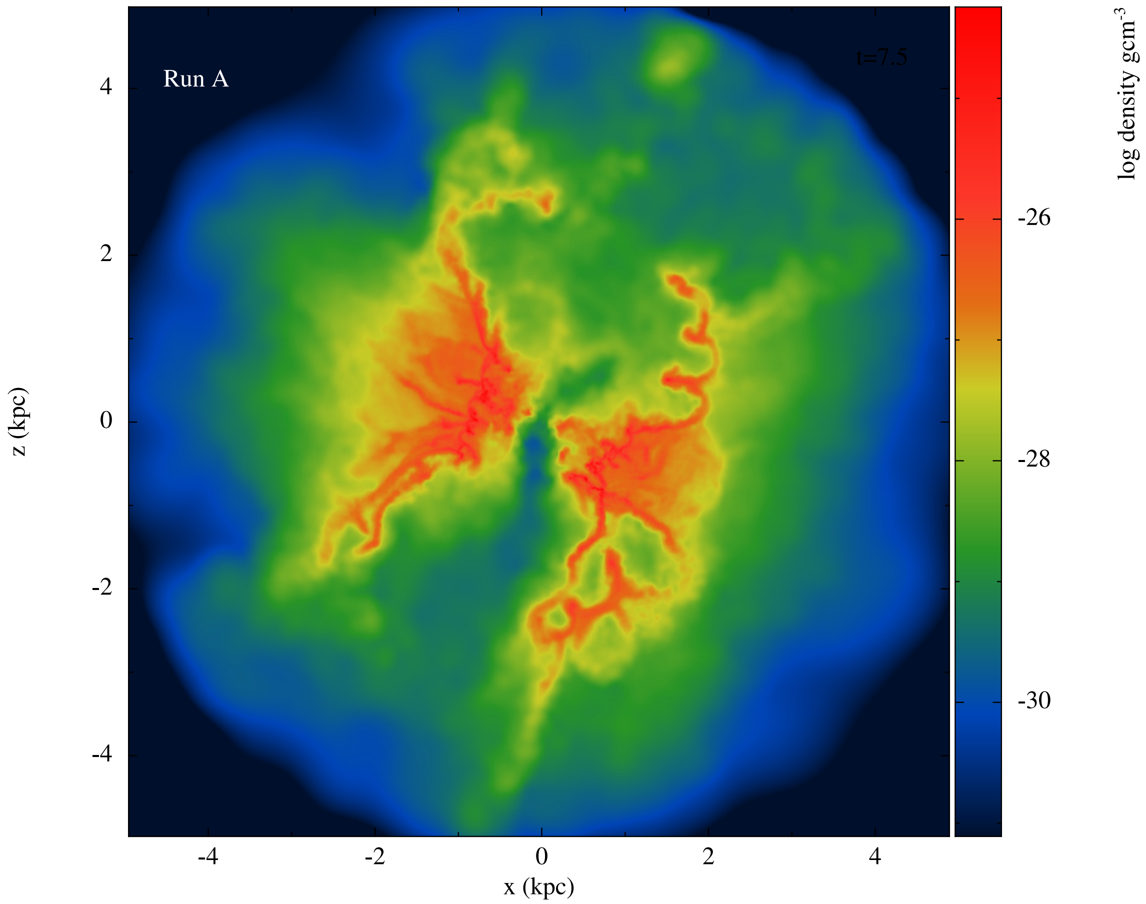

FIGURE 3.8: Density slice in the x-z plane at y=0, for Run A at $t = 35\,\mathrm{Myr}$.

These chimneys are also present in the corresponding x-z density slice (see Fig. 3.8). For Run C in Fig. 3.6, the dominant feature is the multi-lobed superbubble. It is also evident the central kpc of the molecular cloud has been efficiently cleared of gas (this can also be verified in the corresponding x-z and y-z plane density slices). Moreover, this isotropic heating of the central kpc can also be seen in the corresponding temperature slice for Run C (Fig. 3.7), where the inner kpc is filled with gas heated to $\sim 10^8$ K. There is no obvious correlation between the superbubble lobes visible in Run C and the chimneys in Run A at the end of each simulation. However, both the chimney and the superbubbles are surrounded by arcs of cold gas (seen in Fig. 3.7).

To ascertain the difference between the global properties of the gas in Runs A and C, I plot the net radial momentum of the gas, along with the mean temperature, mean radius and maximum radius in Fig. 3.10. From this plot we can see both the net (outwards) radial momentum and mean radius of the gas in Run C is consistently higher than in Run A. Moreover, the mean temperature of Runs A and C converge beyond $\sim 10\,$Myr, at a value of $\sim 10^{4.4}$ K. This indicates the mean temperature of both runs is dominated by the 10^4 K gas, where cooling via collisional excitation is highly inefficient.

To investigate the formation of the low density chimneys of Run A further, I binned the density and temperature data in spherical polar azimuthal angle θ (ranging from -π to π), using a maximal radius set by the largest radius of each θ bin, and plotted the mean temperature and density in each bin (Fig. 3.9) at 3 different snapshot times; 12 ($\sim$ a free-fall time) Myr, 24 Myr and 35 Myr ($\sim$ 2 and 3 times the free-fall time of the cloud respectively). It should be noted the temperature seen in Fig. 3.9 is expected to be lower than that seen in Fig. 3.7 since it represents an average value, encompassing all radii within each θ bin. On Fig. 3.9, a chimney manifests as a peak in the temperature at a specific θ, corresponding with a trough in density at the same θ value. The steepness of the temperature and density gradient indicates the prominence and efficiency of the chimney. Using Fig. 3.9 we can therefore investigate when and where chimneys develop. I chose the x-y plane since this corresponds with the density and temperature slices in figures 3.6 and 3.7.

At 12 Myr, the θ-density profiles of A and C have already diverged, despite the initial conditions prior to the first HMXB feedback event (inside Run A) being identical. The density is consistently lower in Run C than Run A, across all θ bins.

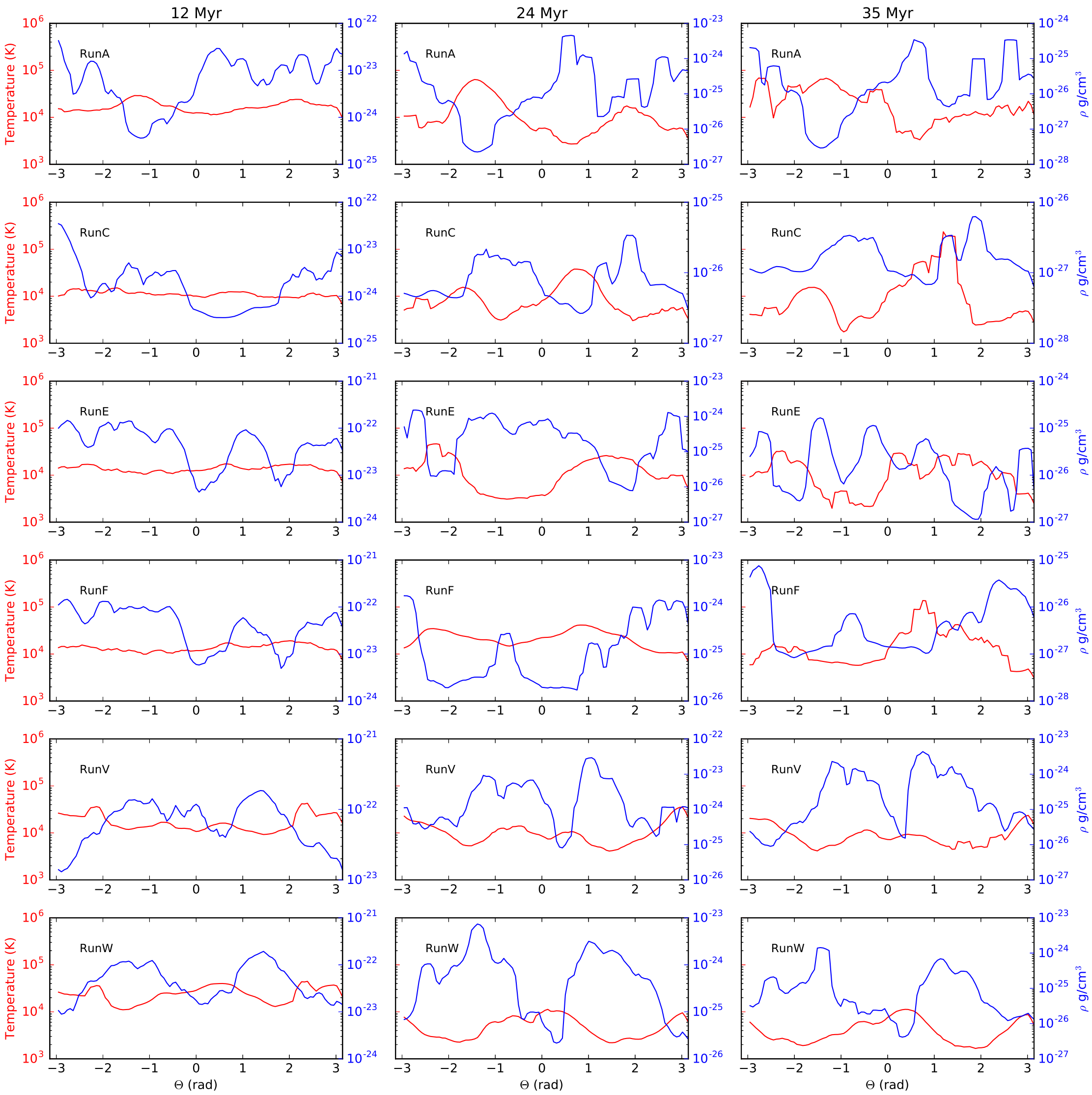

FIGURE 3.9: Plots to show the mean temperature (red) and density (blue) in θ bins ranging from -π to π radians. The maximal radius of each θ bin is set to the maximum radius of the gas in the individual bin. The left column is for snapshots taken at 12 Myr, the middle column is for 20 Myr and the right column shows snapshots at 32 Myr. The name of the corresponding run is in the upper left hand corner of each plot.

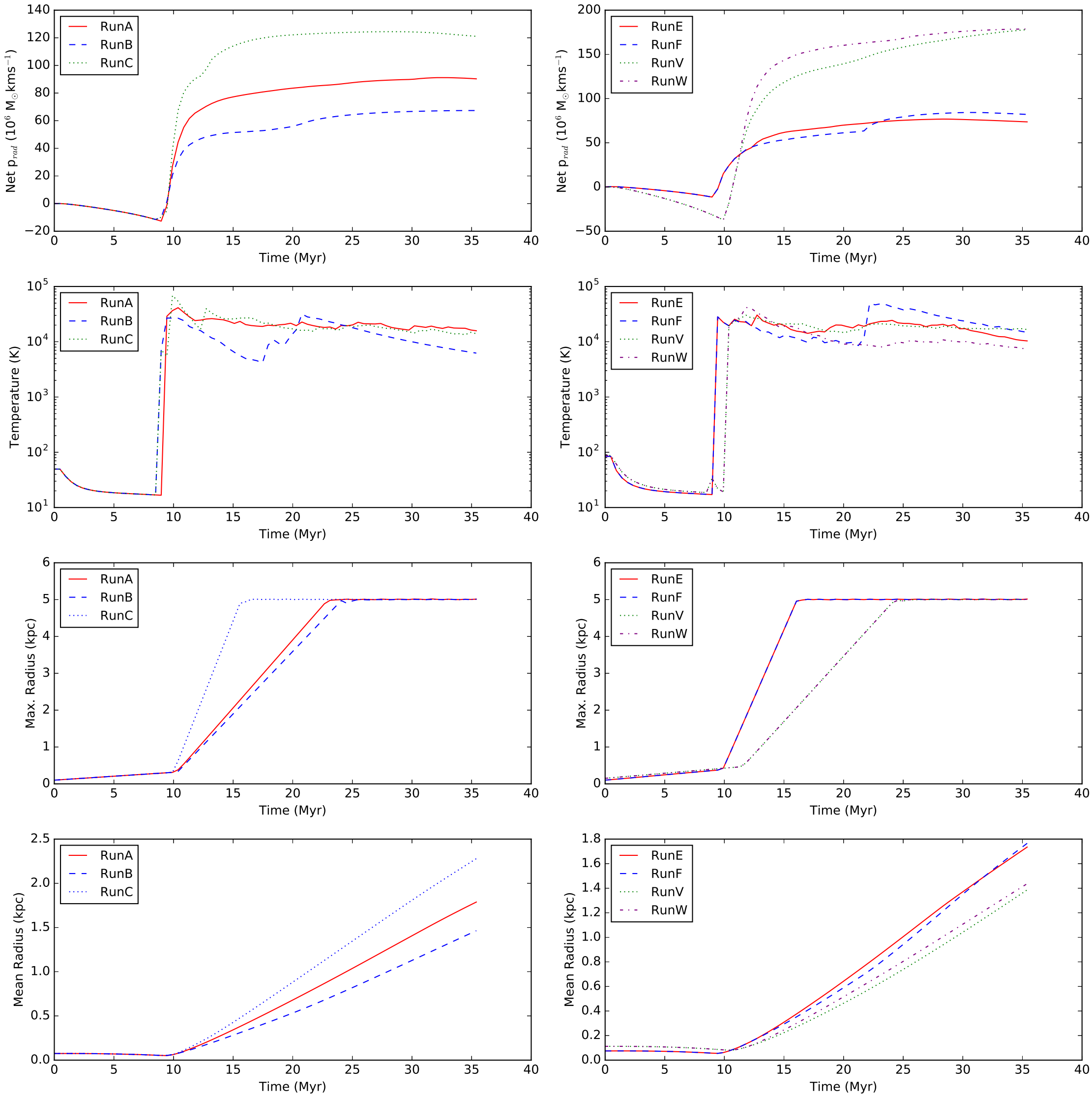

FIGURE 3.10: Upper row - the net radial momentum of the gas across Runs A,B,C,E,F,V and W (evaluated at each snapshot time). Second row - the time evolution of the mean temperature of the gas across each simulation. Third row - the time evolution of the maximum radius of the gas. Bottom row - the time evolution of the mean radius of the gas particles.

This indicates gas has been heated isotropically (as was seen in the inner kpc of Run C in Fig. 3.7) and that the maximal radii of the gas in each θ bin is larger in Run C than Run A (as verified in Fig. 3.10). There is also a two orders of magnitude density drop at $\theta \sim -2.5$ rad and no corresponding positive density gradient until beyond 2 rad. On the other hand, Run A contains both a two orders of magnitude density drop and rise within -2 to 0 rad. This indicates a clearly defined low density chimney. Moreover, comparing the location of the chimney in Run A with the corresponding location in Run C, we can see there is a density peak in Run C spanning a single order of magnitude. Again, given that Run A and Run C are identical (with respect to both the gas density inhomogeneities and the locations of massive stars) prior to the onset of stellar feedback, this suggests the gas in Run C was able to cool efficiently, preventing a chimney forming. On the other hand, the addition of HMXB feedback in Run A kept the gas in the chimney hot and retained the low density channel, through which hot gas can be funneled.

The chimney in Run A (seen in Fig. 3.9) develops in prominence from 24-35 Myr, finally spanning approximately 3 orders of magnitude in density and one order of magnitude in temperature. Looking at Fig. 3.10, we can see by 35 Myr the maximum radius is the same in Runs A and C, hence the higher density peaks in Run A indicate mass clustering in particular directions. Chimney-like features can also be seen to develop in Run C, however the density gradient across these features only spans 1 order of magnitude, while the temperature of the gas associated with them is consistently lower than in the chimney in Run A. It is also worth noting the x-z and y-z planes were also investigated, which showed the same behavior as the x-y plane; i.e. the density in each θ bin was lower in Run C than Run A, while there were hot, low density chimneys present in Run A which were not present in Run C.

In order to visualise the developing chimneys in 3D I plotted the density and temperature slices across z slices spanning z = -0.2 kpc to 0.2 kpc for both Runs A (figures 3.11 and 3.13) and C (3.12 and 3.14) at 12 Myr ($\sim$ 1 free-fall time). Comparing figures 3.11 and 3.12, we can see there are chimneys present in both Runs, however those in Run A are filled with lower density gas ($< 10^{-26}$ gcm^{-3}). They also appear to be more spatially extended, particularly in the z=-50 pc slice.

Looking at figures 3.13 and 3.14, we can see the gas inside the chimneys in Run A is also an order of magnitude hotter than in Run C. The hot gas in Run

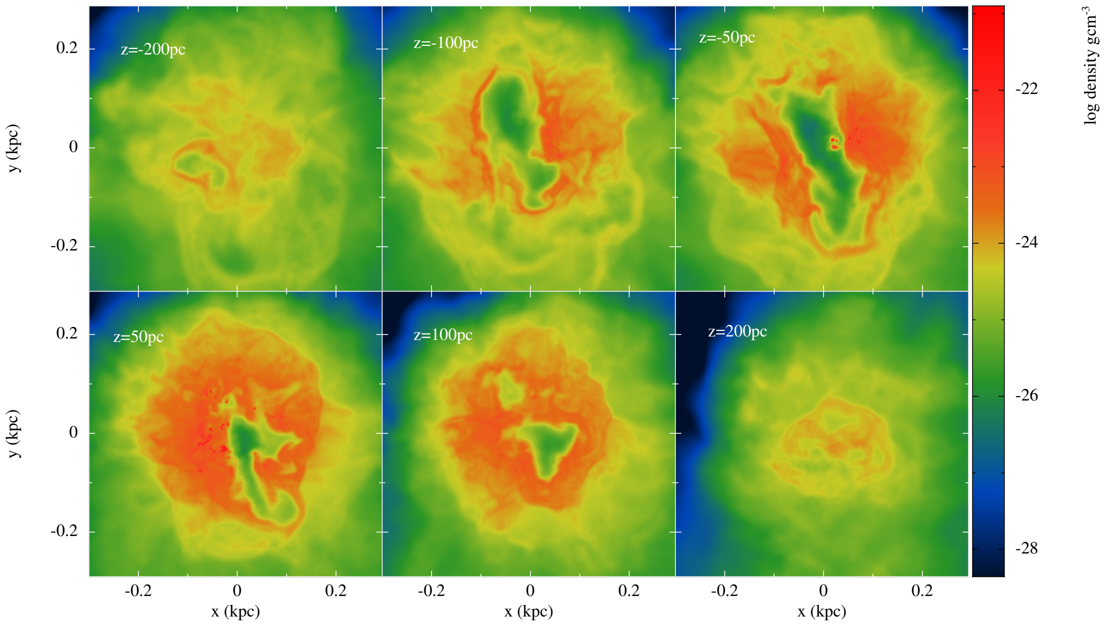

FIGURE 3.11: Density slices in the x-y plane of Run A at z=-0.2, -0.1, -0.05, 0.05, 0.1 and 0.2 kpc at 12 Myr into the simulation ($\sim$ 1 free-fall time.)

C reaches a peak in temperature of $\sim 10^6$ K, which corresponds to an enhanced region of the cooling function for solar metallicity gas; primarily due to the collisional excitation of elements such as neon and iron. However, the hot gas in the chimneys in Run A peaks around 10^7 K, corresponding to Bremsstrahlung dominated cooling, which is relatively inefficient, particularly due to the low densities in the chimneys. In this way, the HMXB feedback has acted to increase the temperature of the gas in the chimneys and in so doing has reduced its ability to cool efficiently. The chimneys can then continue to provide a 'path of least resistance' through which hot gas can escape, allowing star formation to continue in other regions of the cloud.

In Fig. 3.15 I plot the time evolution of the total energy; $E_{\rm tot}$ (where $E_{\rm tot}$ is the sum of the total thermal, kinetic and potential energy of the gas in the system) of selected solar metallicity runs. Again, focusing on the results for Runs A and C, we see the addition of HMXB feedback on top of SNe feedback (Run A) has resulted in a lower total energy of the system. Moreover, Fig. 3.16 plots the number of SNe and HMXBs active between snapshot times, where we see Runs A and C have similar numbers of SNe throughout the simulation, however Run A has an additional energy source from the $\sim$ 10 extra HMXB feedback events

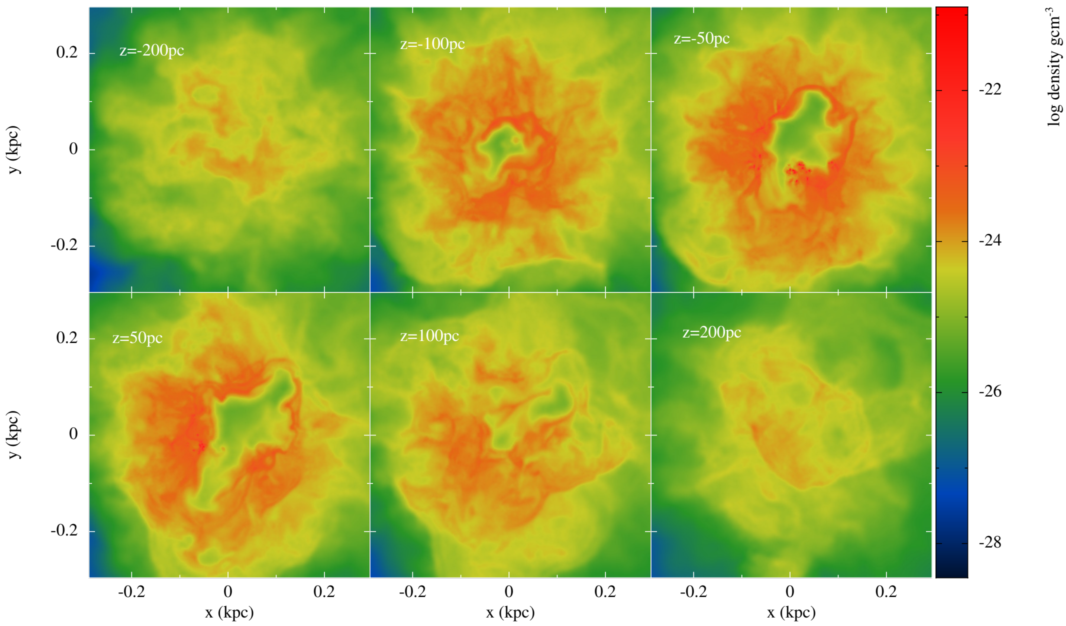

FIGURE 3.12: Density slices in the x-y plane of Run C at z=-0.2, -0.1, -0.05, 0.05, 0.1 and 0.2 kpc at 12 Myr into the simulation ($\sim$ 1 free-fall time.)

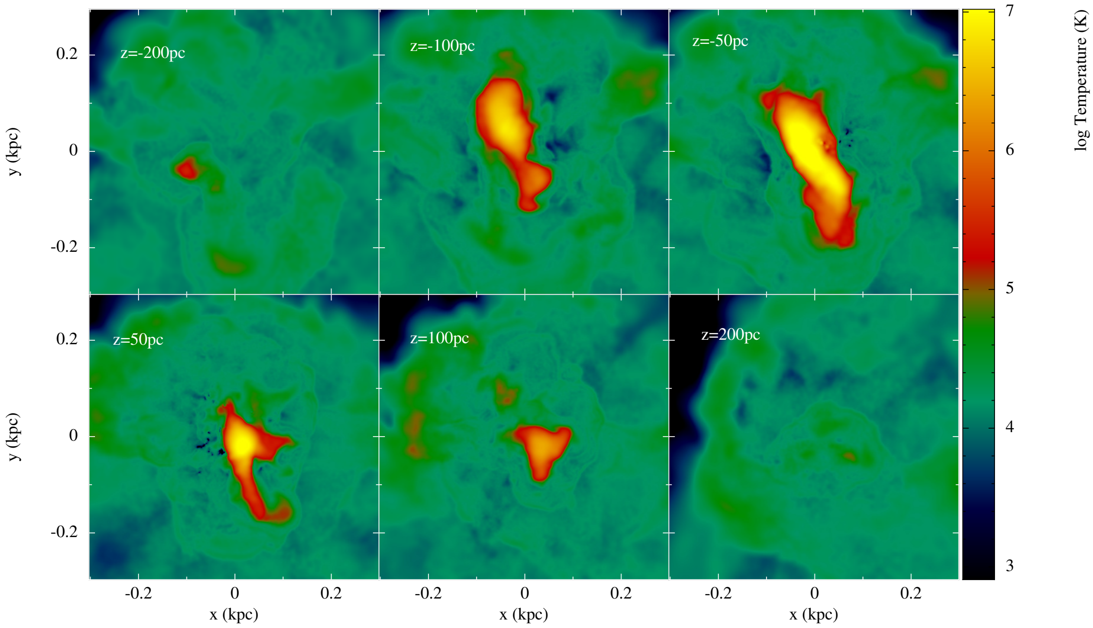

FIGURE 3.13: Temperature slices in the x-y plane of Run A at z=-0.2, -0.1, -0.05, 0.05, 0.1 and 0.2 kpc at 12 Myr into the simulation ($\sim$ 1 free-fall time.)

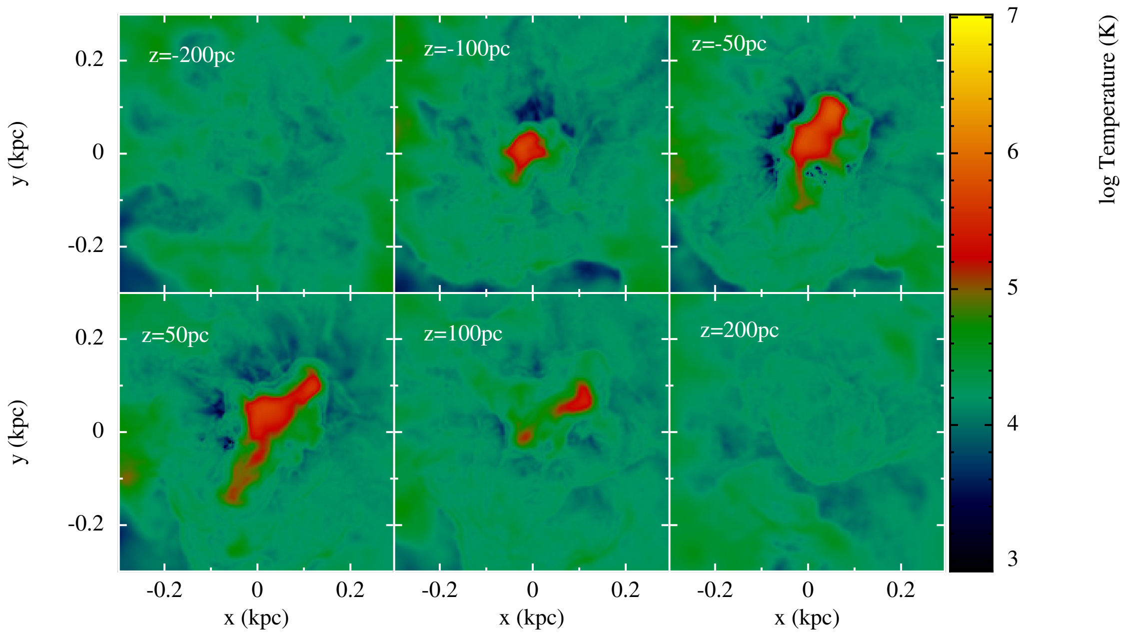

FIGURE 3.14: Temperature slices in the x-y plane of Run C at z=-0.2, -0.1, -0.05, 0.05, 0.1 and 0.2 kpc at 12 Myr into the simulation ($\sim$ 1 free-fall time.)

occurring at any one time. Furthermore, Fig. 3.17 plots the cumulative injected energy from both HMXB feedback in Run A and just SNe feedback in Run C and it is clear the injected energy for Run A is greater than Run C.

In Fig. 3.18 I plot the fraction of the original gas mass in each run that has; (a) become unbound (first column) or (b) ended up in sink particles (second column). Fig. 3.18 shows 5% less gas has been unbound in Run A compared with Run C. This gas has instead become star forming, adding to the total sink particle mass in the simulation. Furthermore, as expected from Fig. 3.15, fractionally more gas has been ejected from the simulation domain in Run C than in Run A. From the sink mass fraction, we can also see the majority of the star formation has occurred in the free-fall time of the cloud, making the first 11.7 Myr crucial in determining the star formation efficiency of the cloud.

Fig. 3.19 plots the number of sink particles created between snapshots versus time into the simulation. The chimney seen in Run A, e.g. Fig. 3.6, has acted to keep a fraction of the gas cool and dense enough to become star forming beyond 11.7 Myr. This has resulted in additional sink particles being formed at 16 Myr and 23-24 Myr ($\sim$ 2 free-fall time-scales). In contrast, the gas in Run C ceases to produce sink particles beyond 14 Myr (just over 1 free-fall time of the molecular

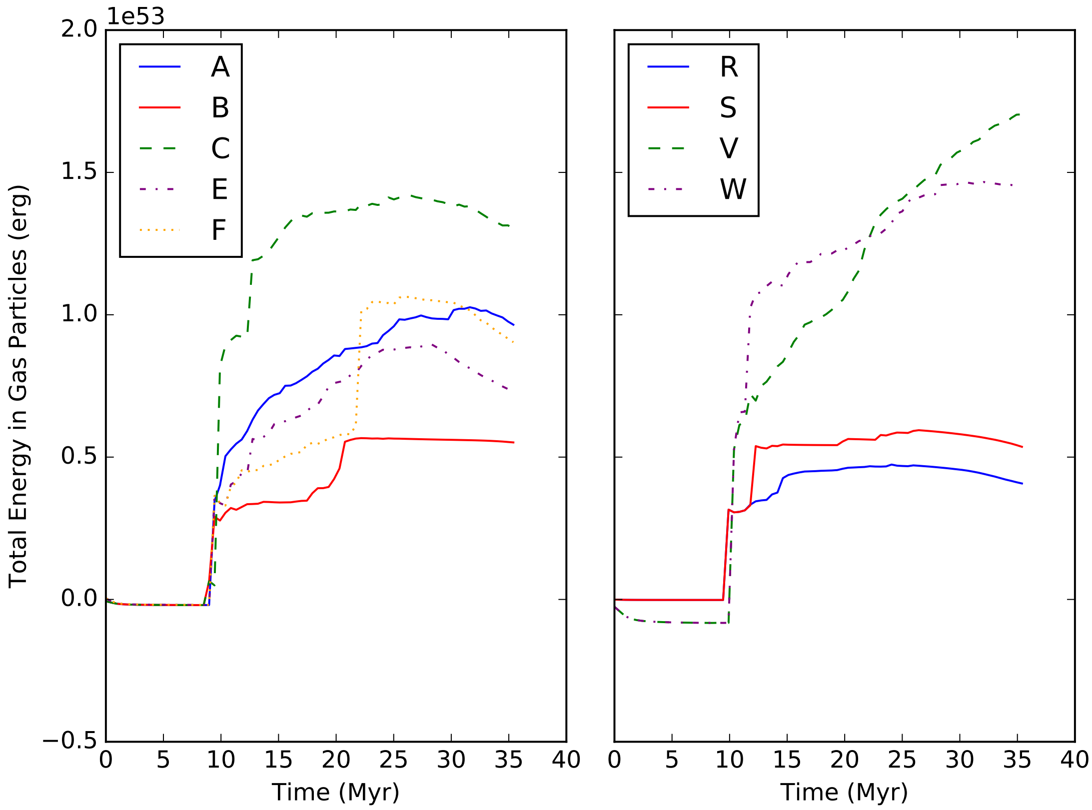

FIGURE 3.15: Plots to show the time evolution of the total energy of Runs A, B,C,E,F,R,S,V and W. The total energy was found by summing the total thermal, kinetic and potential energies across all gas particles in each simulation.

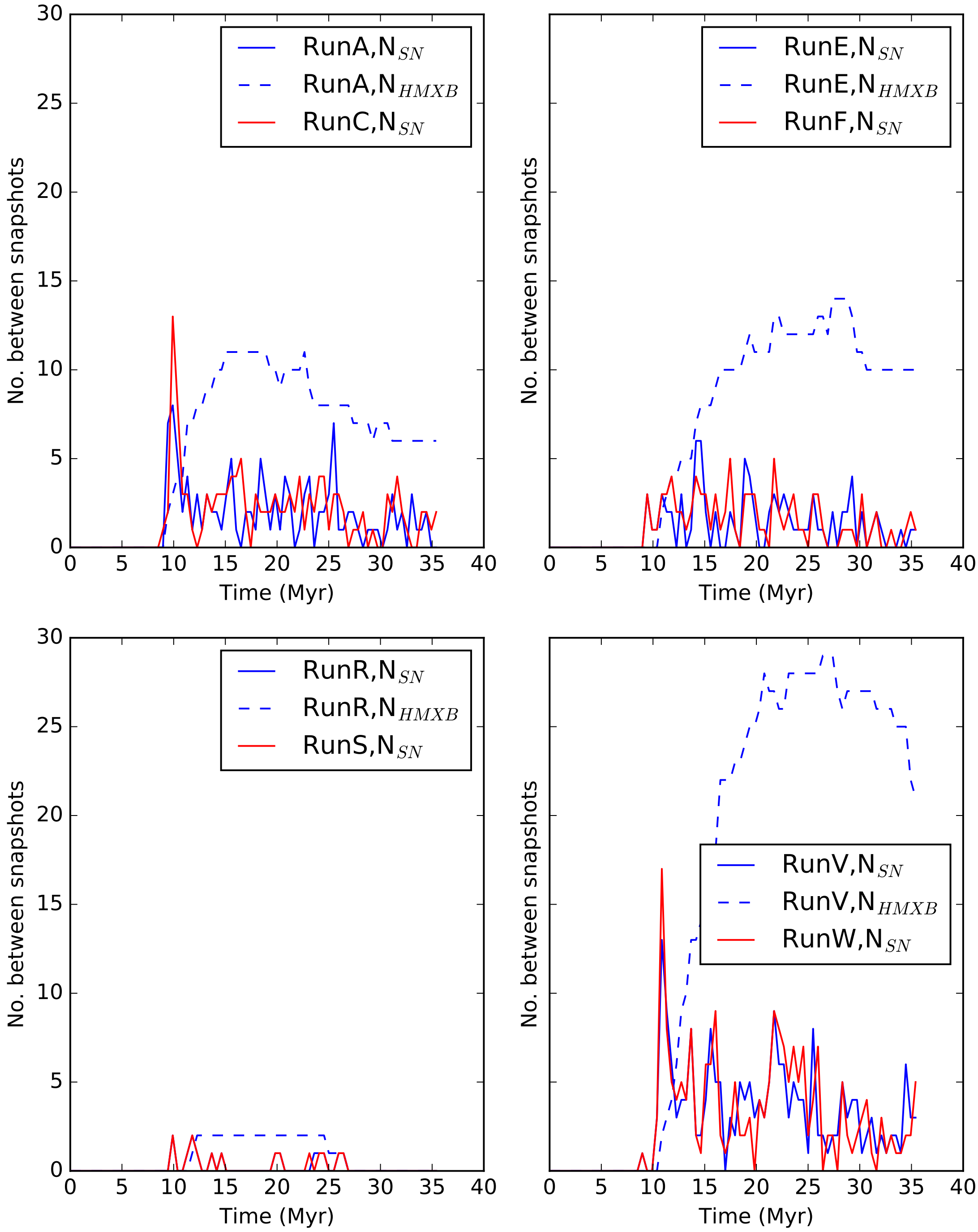

FIGURE 3.16: Plots to show the number of SNe (solid lines) and HMXB (dashed lines) active between snapshots for Runs A,C,E,F,R,S,V and W.

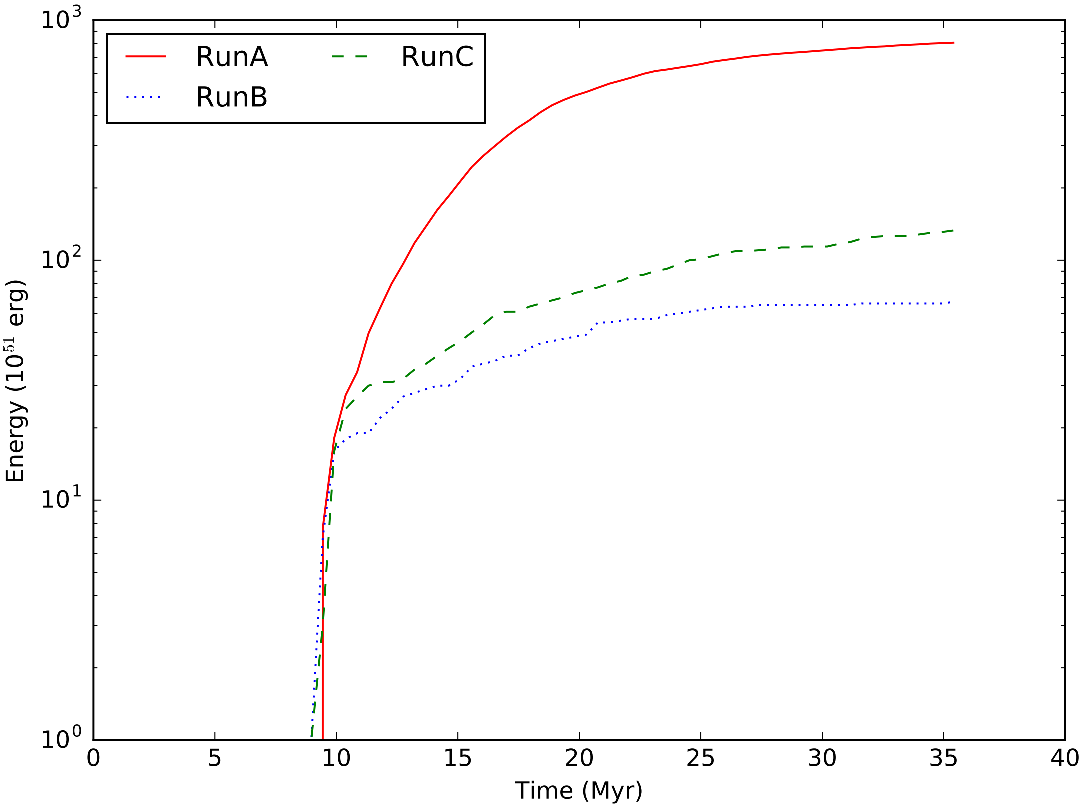

FIGURE 3.17: Figure to show the time evolution of the cumulative injected energy for Runs A,B and C.

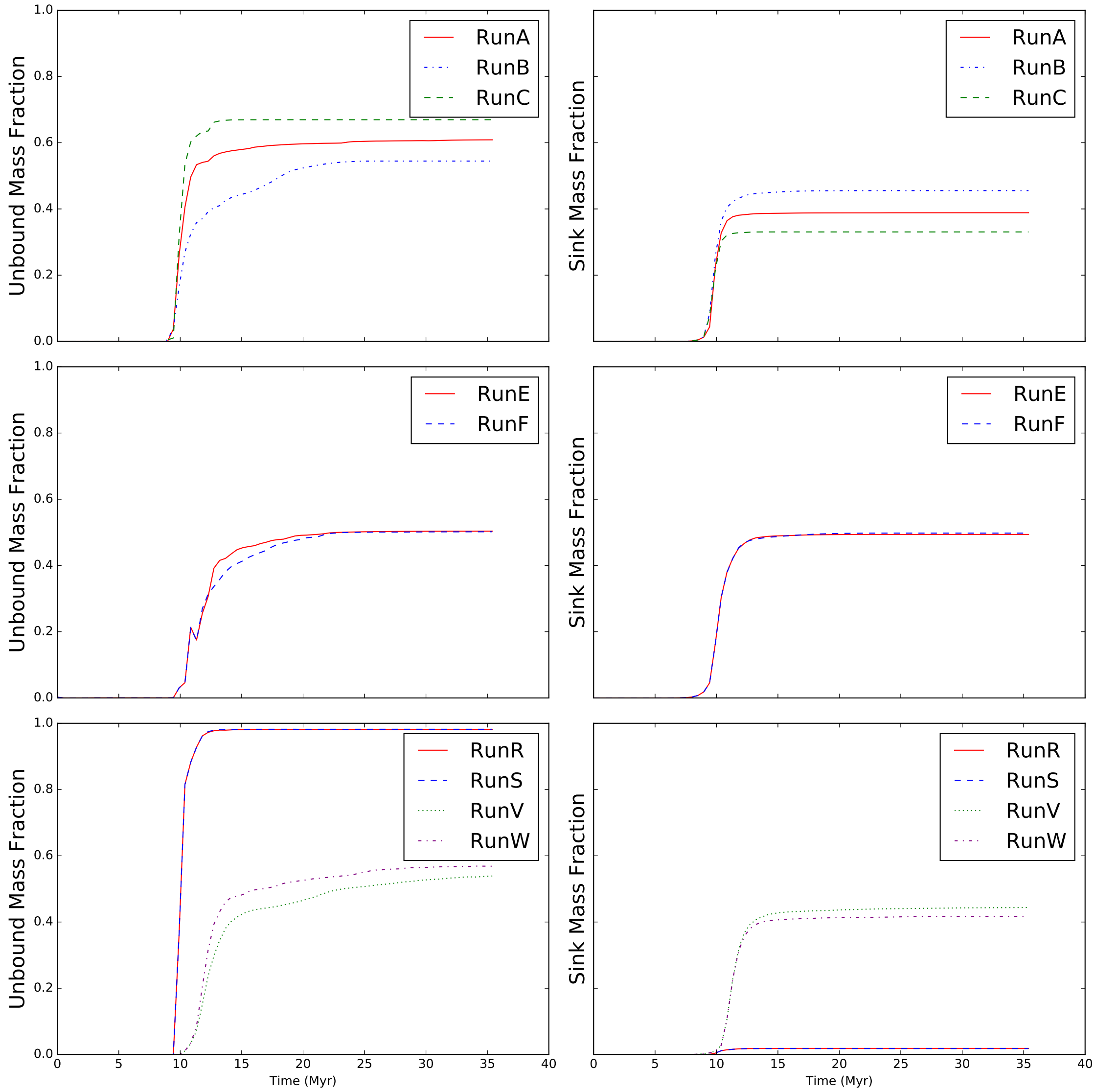

FIGURE 3.18: Plots to show the fraction of the initial mass that has (a) been unbound (first column) or (b) either been accreted by, or become sink particles (second column). The runs plotted are: A,B,C,E,F,R,S,V and W (which are all at solar metallicity).

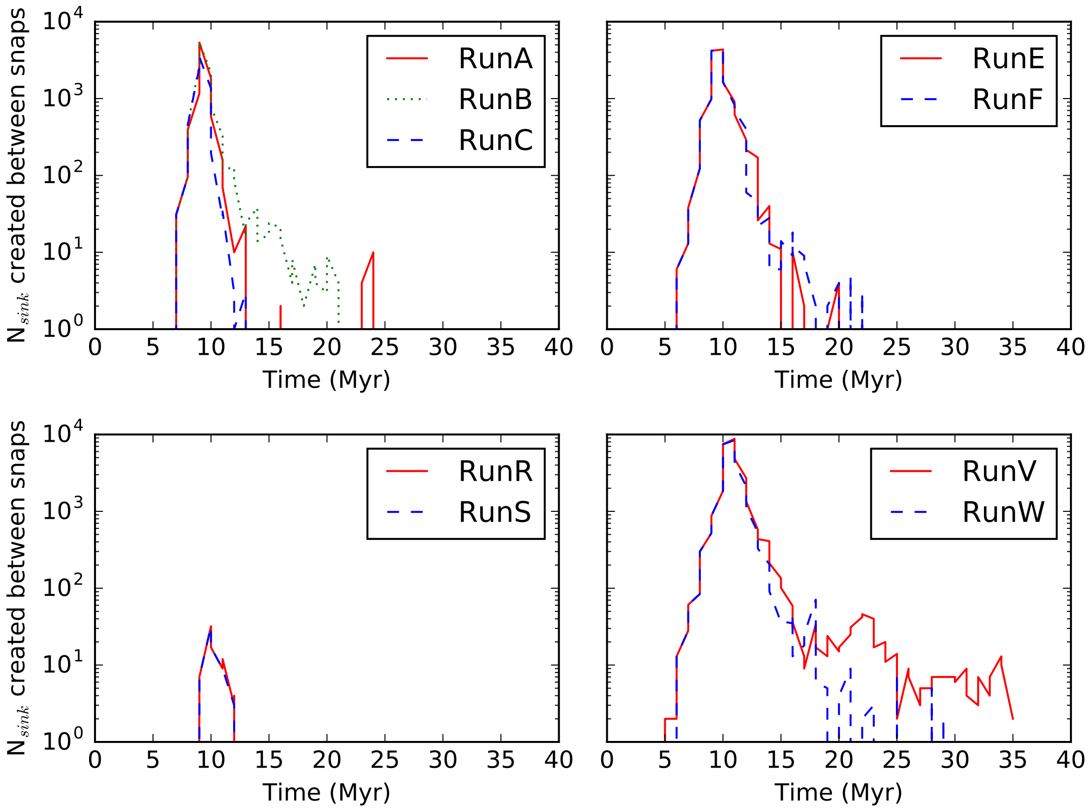

FIGURE 3.19: Plots to show the number of sink particles produced between timesteps for Runs A,B,C,E,F,R,S,V and W (solar metallicity).

cloud).

Comparing Fig. 3.19 to Fig. 3.5, we can see the addition of feedback in Runs A and C has had little impact on when the majority of sink particles are formed inside the cloud. Most of the sink particles in each simulation are produced in a single burst of star formation between 6-13 Myr.

In Fig. 3.20 I investigate the state of the gas in Runs A and C at t = 14 Myr, in order to ascertain why Run A continues to form sink particles beyond this point and Run C does not. I plot the temperature versus density of the gas in the simulation, rendered according to the number of particles. From Fig. 3.20, we can see both Runs A and C have a 'tail' of low temperature gas, formed primarily by fine structure cooling of the heavier elements (e.g. C II, O I), however this 'tail' contains more gas particles in Run A, resulting in the extended sink particle formation seen in Fig. 3.19.

Overall, by comparing Runs A and C we can see that adding HMXB feedback

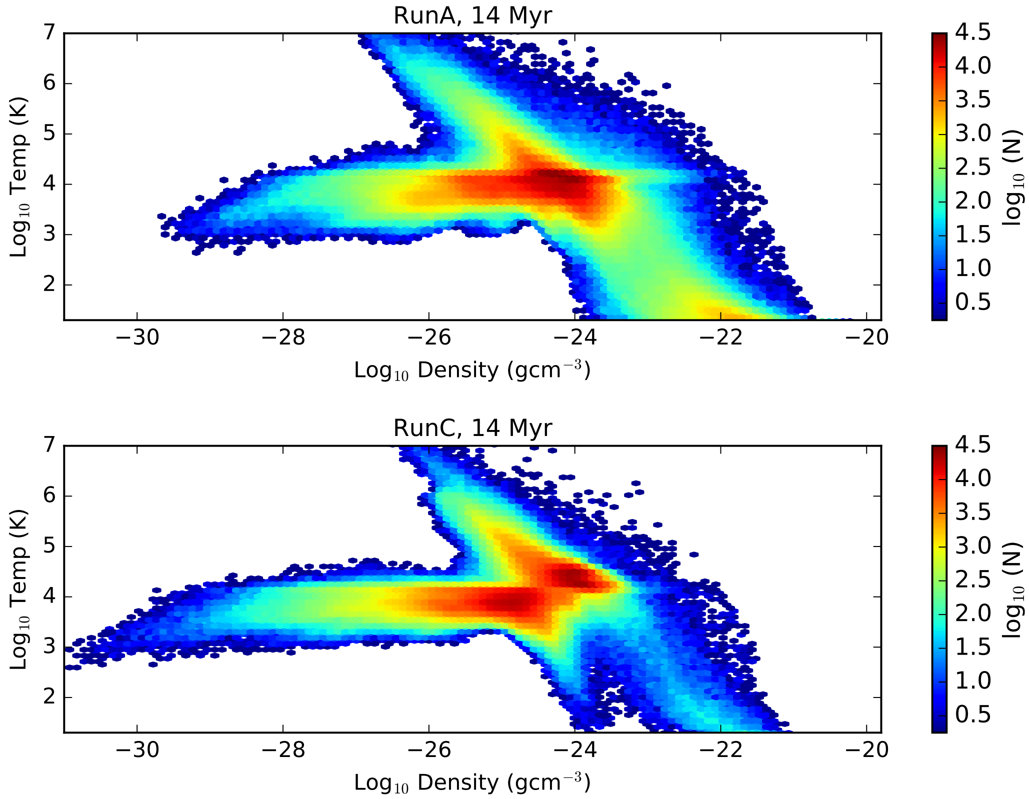

FIGURE 3.20: Plots to show the temperature versus density of the gas in Runs A (top) and C (bottom), 14 Myr into each simulation. The plot is rendered according to the number of gas particles.

on top of SNe feedback can result in an increase in star formation efficiency and period, despite more energy being injected into the ISM. This result arises primarily through the action of low density 'chimneys', funneling hot gas from the inner regions, maintaining enough cool, dense gas to fuel further star formation. These chimneys are also present when just SNe feedback is present (see Fig. 3.14), however the gradual heating from HMXBs acts to increase the temperature of the hot gas in these chimneys and reduces its ability to cool efficiently – enhancing their effectiveness at funneling hot, destructive gas away from the inner regions of the cloud. Despite this, the majority of star formation in clouds A and C still occurs within the free-fall time of the cloud, as in Run D, making the first ~ 11.7 Myr pivotal in determining the star formation efficiency and rate of these molecular clouds.

3.5.3 Changing the virial parameter, $\alpha_{vir} = 1.2$: Runs E,F

Looking at the density slices for Runs E (including HMXB feedback) and Run F (just SNe feedback) in Fig. 3.6, the differences are less apparent than between Runs A and C. Immediately, we can see making the molecular cloud marginally unbound has particularly affected the run containing just SNe feedback (F). Cloud F has retained a larger amount of higher density ($> 10^{-24}$ gcm^{-3}) gas inside the inner region than Run C. This is likely the work of chimneys; a few cavities of low density ($\sim 10^{-(26-27)}$ gcm^{-3}) gas can be seen in the inner 1 kpc of Run F.

On the other hand, comparing Runs E and F, we still see a larger fraction of higher density gas towards the centre of Run E, as well as two clearly defined chimneys. Indeed, the mean density of the gas inside a radius of 500 pc is 1.5 $\times 10^{-24}$ gcm^{-3} for Run E, compared with 5.6 $\times 10^{-25}$ gcm^{-3} in Run F. Moreover, the total gas mass inside the inner 500 pc of Run E is 3.8 $\times 10^4$ M$_\odot$, compared with 3.3 $\times 10^4$ M$_\odot$ for Run F. The fact that the mean density inside this radius varies more widely than the total gas mass between the two simulations, suggests the gas is more clustered inside the inner 500 pc of Run E than Run F. The chimneys visible in the x-y plane of Run E (Fig. 3.6) are also apparent on the corresponding temperature slice (Fig. 3.7), which shows two lobes of high temperature gas expanding from the centre of the gas cloud through the chimneys. One chimney of low density gas is visible in cloud F in Fig. 3.6 and the hot gas filling it can be seen in Fig. 3.7. The chimney seen in Run F roughly corresponds to the top-right chimney seen in Run E. This suggests the early SNe (i.e. those initialised prior to the first feedback event and hence shared between Run E and Run F) were primarily responsible for determining the location of this chimney in both clouds. Furthermore, the x-z and y-z planes were also considered; with both clouds showing a hot, dense chimney in the upper right corner of the y-z plane, of similar spatial extent and both containing gas heated to $\sim 10^8$ K. Moreover, the x-z plane showed very similar density and temperature trends to the x-y plane, with Run E containing two chimneys (one in the upper right corner and one in the lower left corner) and Run F containing one in the upper right corner. This is indicative of the 3-d structure of the chimneys visible in the x-y plane.

However, looking instead at the time evolution of the total energy in both Runs E and F (Fig. 3.15), the picture is more complicated than in Runs A and C. This is due to the fact the total energy of Run E initially exceeds that of the

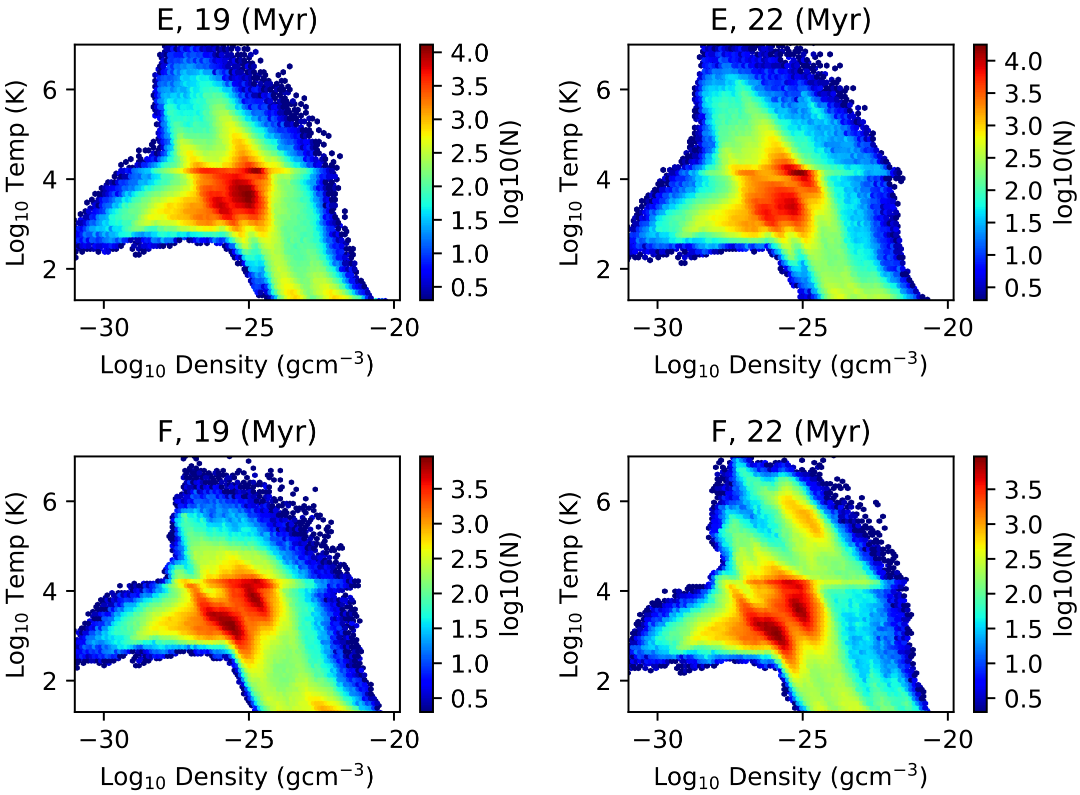

FIGURE 3.21: Temperature versus density plot, rendered according to gas particle number, for Runs E and F, 19 Myr and 22 Myr into each simulation.

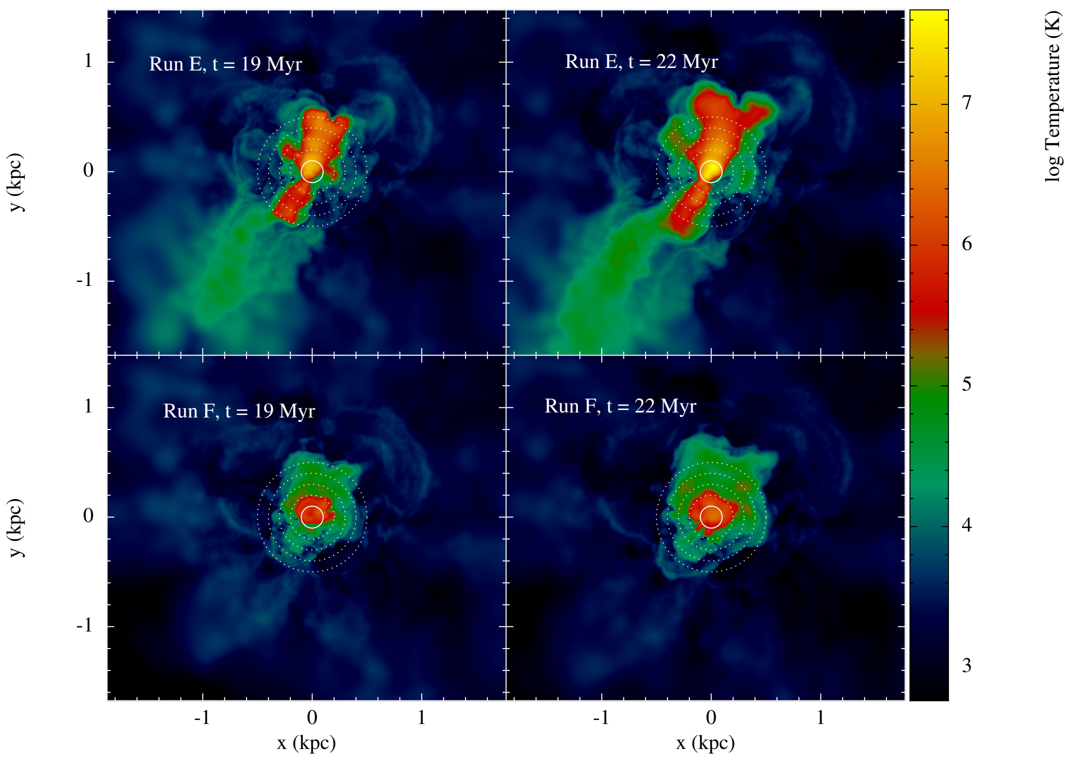

FIGURE 3.22: Temperature slices taken at z = 0 in the x-y plane, for Runs E and F, at 19 Myr and 22 Myr. The solid white circle indicates a radius of 100 pc from the origin, while the successive dotted circles beyond this indicate radii at 100 pc intervals (until 500 pc.)

gas in Run F, until 22 Myr, when this situation is reversed. Additionally, Fig. 3.10 shows the mean temperature and net radial momentum of the gas in Run F is less than that of Run E prior to 22 Myr and then exceeds it afterwards. At the end of Run E and F, Run F has $\sim$ 25 % more energy than Run E. In order to investigate this large energy jump in Run F, I plot temperature versus density at 19 Myr and 22 Myr for Runs E and F in Fig. 3.21. We see the energy jump in Run F is caused by approximately 5000, high density (>10^{-25} gcm^{-3}), gas particles, located inside the inner 200 pc of the cloud, being heated to above 10^6 K (shown in the top right hand corner of plot). Fig. 3.16 shows there are only $\sim$ 5 SNe during this simulation snapshot, however Fig. 3.15 shows the rise in total energy is equivalent to $\sim$ 50 SNe.

In order to ascertain the underlying mechanism driving this leap in energy, I ran Run F again between 19 Myr to 23 Myr at higher time resolution between snapshots ($\sim$ 0.02 Myr). I then plotted the evolution of the temperature, density, radius and velocity of $\sim$ 4600 of the high density particles that were heated to 10^6 K at 22 Myr. We can see the particles were heated to above 10^6 K at 21.75 Myr and prior to this they occupied radii between $\sim$ 100 – 350 pc and had correspondingly high densities of between 10^{-25} gcm^{-3} to $10^{-22.5}$ gcm^{-3}. However, at 21.75 Myr we can see the peak density of the gas particles has increased and the radii have converged to a value of $\sim$ 120 pc. Furthermore, the absolute velocities of the particles have increased by an order of magnitude. The increase in density of the particles, coupled with the velocity increase, indicates this region has undergone gravitational collapse, which has resulted in the shock-heating of the gas particles. Furthermore, there were no SNe active between 21.72 Myr and 21.75 Myr, indicating this heating was not due to direct heating via SNe feedback. Beyond 21.75 Myr the gas particles have begun to cool, however the mean radius of the particles has increased. This, coupled with the fact the velocities are still larger than they were prior to the gravitational collapse, indicates the gravitational shock-heating has generated an outflow.

Looking instead at the z = 0 temperature slice in the x-y plane, for Runs E and F at 19 Myr and then at 22 Myr (shown in Fig. 3.22), we see Run E in the process of funneling large amounts of hot gas away from the central 100 pc of the molecular cloud, inflating the two high temperature lobes between 19 Myr and 22 Myr. However, Run F only shows a small increase in the amount of hot gas outside 200 pc, indicating the gas heated by SNe/gravitational collapse inside the

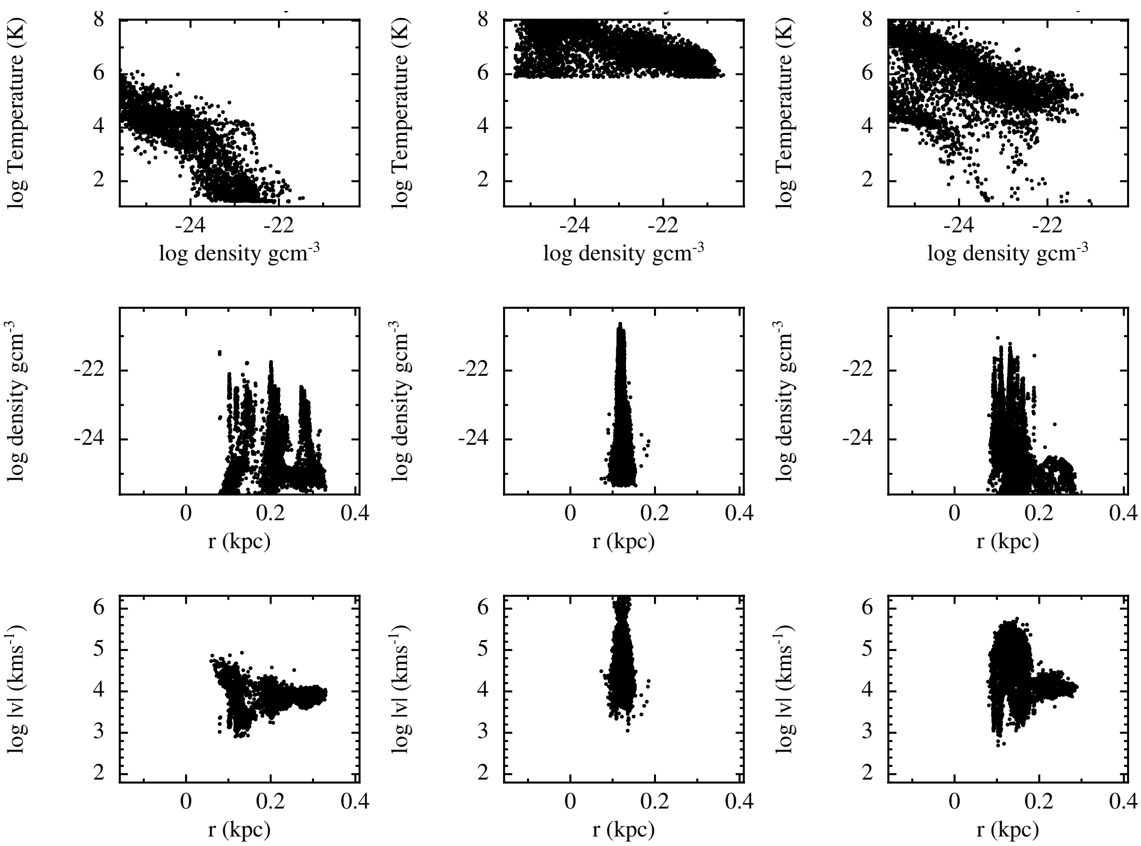

FIGURE 3.23: Plots to show the time evolution of 4604 high density ($> 10^{-25}$ gcm^{-3}) particles that were heated to above 10^6 K 21.75 Myr into Run F. The first column shows the properties of the gas particles at 21.72 Myr, the second column shows the same at 21.75 Myr and the third column corresponds to t = 21.77 Myr. Top row - plot to show the temperature and density of the particles at 3 different times. Middle row - plots to show the densities and radii of the particles at the 3 different times. Bottom row - plots showing the magnitude of the particle velocities and how this varies with radius.

TABLE 3.2: A table listing the total sink mass as a fraction of the initial gas mass at the end of each [Fe/H] = 0 simulation ($mf_{\rm sink}$), the number of sink particles present at the end of each run ($N_{\rm sink}$), the total number of SNe ($N_{\rm SNe}$) and HMXBs ($N_{\rm HMXB}$) across the whole simulation, the mean sink particle mass ($mp_{\rm sink}$), the fraction of the total number of sinks with a mass > 180 M$_{\odot}$ and finally the mean mass accreted by sinks with masses above 180 M$_{\odot}$ (denoted $M_{mean,180}$).

Run	$mf_{\rm sink}$	Total $N_{\rm sink}$	$N_{\rm SNe}$	$N_{\rm HMXB}$	Mean $mp_{\rm sink}$ (M$_{\odot}$)	Number fraction of sinks $>$ 180 M$_{\odot}$ (%)	$M_{mean,180}$ (M$_{\odot}$)
A	0.39	9898	119	17	78.5	1.4	23
B	0.46	12615	67	7	72.2	0.72	25
C	0.33	8372	133	21	79.0	1.9	26
E	0.49	14376	86	15	68.7	0.9	24
F	0.50	14246	92	14	69.9	0.9	24
R	0.02	88	15	2	104.4	19.3	61
S	0.02	82	15	2	109.4	20.7	62
V	0.44	31501	209	32	70.4	0.9	27
W	0.42	28652	208	30	72.7	1.0	28

inner region of the cloud has not escaped this central 200 pc. Instead, it has shock heated a large amount of gas in this region and resulted in the high temperature, high density region of gas visible in Fig. 3.21, along with the total energy jump seen in Fig. 3.15. These results point to the effectiveness of HMXBs at using the SNe-generated low density chimneys to funnel hot gas away from the central $\sim$ 200 pc of the cloud.

As a result of the energy jump in Run F seen in Fig. 3.15, the unbound mass fraction for Run F converges on ~ 0.5, indicating the majority of the remaining gas in the cloud (that has not been accreted onto/ become sink particles) has been unbound (Fig. 3.18). Comparing with Runs A and C, it is clear the increase in the initial virial parameter of the cloud has resulted in a greater fraction of the initial gas mass in sink particles, along with a decrease in the mass fraction of gas being unbound. As well as this, the period of sink particle formation has increased in both Runs E and F, when compared with the bound cloud in Fig. 3.19. This appears to be largely due to a lower number of HMXBs and SNe events (see Fig. 3.16 and Table 3.2) acting across the simulation. Looking at Table 3.2, the mean sink particle mass in Runs E and F is lower than Run A, while the fraction of sinks with a mass above 180 M$_{\odot}$ is also smaller in these runs. However, the mean mass accreted by sinks with masses above 180 M$_{\odot}$ is comparable with Run A.

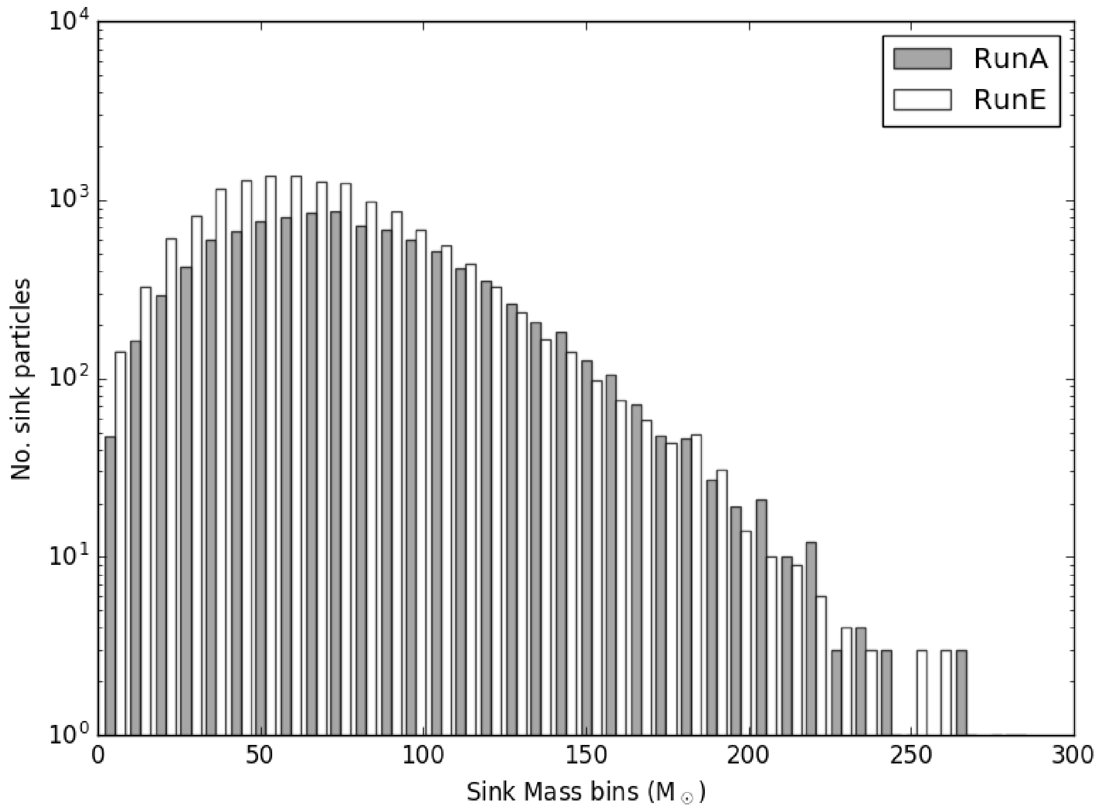

FIGURE 3.24: The number of sink particles occupying different mass bins in Runs A and E.

I compare the distribution of sink masses between Run A and E in Fig. 3.24. Here we see Run E has a stronger peak at 70 $M_\odot$, along with a sharper negative gradient beyond its mean sink particle mass than Run A. As such, Run E has consistently more sink particles than Run A in mass bins below 125 $M_\odot$, however this situation is more or less reversed beyond this sink mass. Therefore, by increasing the turbulent velocity of the gas initially, the net effect has been to reduce the number of massive stars (> 180 $M_\odot$) and increase the number of stars with masses less than 125 $M_\odot$, reducing the mean sink mass in these clouds. Moreover, the higher virial parameter has also resulted in a marginal difference between the run containing HMXB feedback (E) and the run containing just SNe feedback (F).

I next investigate the ineffectiveness of the chimneys in Run E at prolonging, as well as increasing, star formation with respect to Run F, as was seen in Run A (and C). To do this I focus on Fig. 3.9; at 12 Myr ($\sim$ the free-fall time of the clouds) we see the density and temperature versus θ profiles are remarkably similar between Runs E and F. The peaks and troughs in both density and temperature are at the same locations in both clouds. However, the two runs diverge significantly at t = 24 Myr, where a large fraction of the gas has been blown out in Run F, corresponding to the large regions of lower density (which indicate a larger maximal radius). In contrast, two clear chimneys are present in Run E. These are still present at t = 35 Myr, meanwhile, although there two wide-angle chimney-like structures in Run F, from the density scale we can see the density has dropped by at least an order of magnitude when compared with Run E.

These results point to the fact the chimneys, though present and working efficiently beyond 11.7 Myr in Run E, did not form early enough to have an impact on the star formation and gas expulsion in that crucial free-fall timescale. The most likely cause for this delay is the reduced number of SNe and HMXB active prior to the free-fall timescale, as seen in Fig. 3.16. Comparing Run E to Run A in the table, we see Run A has approximately 1/3 more SNe, although a similar number of HMXB events. However, in Fig. 3.16 we see the HMXB feedback is initiated sooner ($\sim$ 9 Myr) in Run A than Run E ($\sim$ 11 Myr). These results suggest SNe and a higher number of HMXB events are crucial in the process of chimney formation in the cloud. This is likely due to the fact SNe help to carve the chimneys, while HMXBs act to increase the temperature above 10^7 K (as in Run A, figure 3.13), preventing the collapse of the chimneys via efficient cooling. Furthermore, the gravitational collapse-generated outflow seen in Run F indicates the cooling and subsequent gravitational collapse of material inside the central region of the cloud can be more effective at heating the highest density gas than SNe. It is likely subsequent SNe are then more efficient at maintaining hot gaseous outflows since their environment has a lower density, which decreases the internal energy losses of the gas particles by limiting radiative cooling.

3.5.4 Changing the size of the molecular cloud: Runs R, S, V, W

This sections looks at the results of increasing (Runs V and W) and decreasing (Runs R and S) the size of the molecular cloud in the simulation. Firstly, using the z=0 density slices in Fig. 3.6 we can immediately see the gas inside the inner 2 kpc of both cloud R and S has been efficiently blown out. However, the run with HMXB feedback included (R) has more high density gas inside a radius of

~ 2 kpc, compared with Run S (just SNe feedback). Similarly to previous results at solar metallicity, this is likely due to multiple low density chimneys, extending from the inner kpc to the outskirts of the cloud. However, these chimneys are only just visible in the temperature slice for Run R (Fig. 3.7) and the temperature of the gas being funneled is between $10^{6-6.5}$ K, as opposed to the 10^{7-8} K gas seen in earlier runs. Although the gas is hotter in Run S, extending to $\sim 10^7$ K, the temperature distribution is more isotropic and concentrated at the centre of the cloud. This suggests the SNe heated gas in the inner regions of Run S has been unable to escape to the outskirts of the simulation and has instead collided with, and shock heated, the surrounding high density gas. This has raised the temperature in the central 2 kpc more or less uniformly.

Instead comparing the density slices of Run V (HMXB and SNe feedback) and W (just SNe feedback), we can see, contrary to previous results, Run W contains two low density chimneys, while Run V contains only one. Similarly to Runs E and F in section 3.5.3, the left-hand chimney of Run W corresponds with the chimney seen in Run V. This also points to the fact it is the initial SNe feedback events in both clouds V and W (prior to the onset of HMXB feedback) that determines the chimney locations.

Focusing instead on the temperature slices of Runs V and W (Fig. 3.7), we see the left hand chimney visible in Fig. 3.6 in both clouds V and W, has hotter gas in Run V ($\sim 10^7$ K). However, the right-hand chimney, which is only present in Run W, is efficiently funneling hot gas from the inner regions.

From Fig. 3.15, the total energy of Run R at the end of the simulation is less than Run S. However, for the larger cloud the situation is different; at ~ 20 Myr the total energy of Run V converges with Run W and beyond this, the total energy of Run V is larger than in Run W. Additionally, Fig. 3.10 shows the net radial momentum of the gas in Run W is consistently higher than Run V beyond 12 Myr. However, beyond 15 Myr the mean temperature of the gas is lower in Run W than Run V. This helps to explain the lower total energy seen in Fig. 3.15 for Run W beyond 20 Myr. Finally, the maximum and mean radius of the gas in Runs V and W follow the same values across each simulation, indicating the bulk of the gas mass is distributed similarly across cloud radius in each run.

It is also interesting to note the number of SNe/HMXB feedback events active between snapshots for Runs V and W – shown in Fig. 3.16. Like in Run E, the HMXB feedback kicks in at a time of 11 Myr, 2 Myr later than in Run A. The effect of the delayed HMXB feedback on the effectiveness of the chimneys is perhaps negated due to the longer free-fall time (13.6 Myr), which is due to a higher initial density. There are also a higher number of SNe and HMXBs active throughout Runs V and W, compared with the other runs at solar metallicity. Looking at Table 3.2, we can see Run V contains almost twice as many SNe and HMXB feedback events throughout its lifetime as Run A. On the other hand, Run R also shows the delayed HMXB phase and only contains 2 HMXB events, along with 15 SNe across the simulation.

Despite only a few HMXBs acting at 12 Myr, Run V shows a clear chimney towards the edges of the θ versus temperature/density plot in Fig. 3.9. This was likely carved by the ~ 20 SNe events seen in Fig. 3.16. This chimney is also visible in the corresponding plot for Run W. At later times (24 and 35 Myr) a second prominent chimney can also be seen at ~ 0.5 radians in Run W. This chimney can also be seen in Run V in the density profile - there is a corresponding density drop across 3 orders of magnitude. However, there is no clear corresponding peak in temperature, as is seen in cloud W. It is also narrower in θ than the chimney present in Run W. These results point to the fact HMXBs are not necessary for chimneys to form. They also support the assertion that the efficiency of a chimney is determined by the feedback power; HMXBs are not necessary to keep the gas hot inside the chimneys if the power required to do so is supplied by SNe. The gradual heating of HMXBs simply offers a ready power source to keep the gas in the chimneys hot and working efficiently.

Focusing on Fig. 3.19, the creation of sink particles in both Runs R and S occurs at around 10 Myr and beyond this there is no further star formation in either simulation. However, Run V continues to produce 10-100 sink particles between snapshots from 15 Myr up until the end of the simulation. In contrast, sink particle formation continues sporadically up until 29 Myr in Run W, with fewer sink particles being produced beyond 13.6 Myr (the free-fall time) than in Run V.

Fig. 3.18 looks at the unbound mass fractions for Runs R,S,V and W. A large fraction of the initial gas mass (> 90 %) is unbound in Runs R and S as soon as feedback is turned on at around 10 Myr into each simulation. This is due to the lower binding energy of the gas in clouds R and S and is despite only 15 SNe being present throughout the simulation. As a result, the 2 HMXBs, which were switched on after the majority of the star formation (and unbinding) had

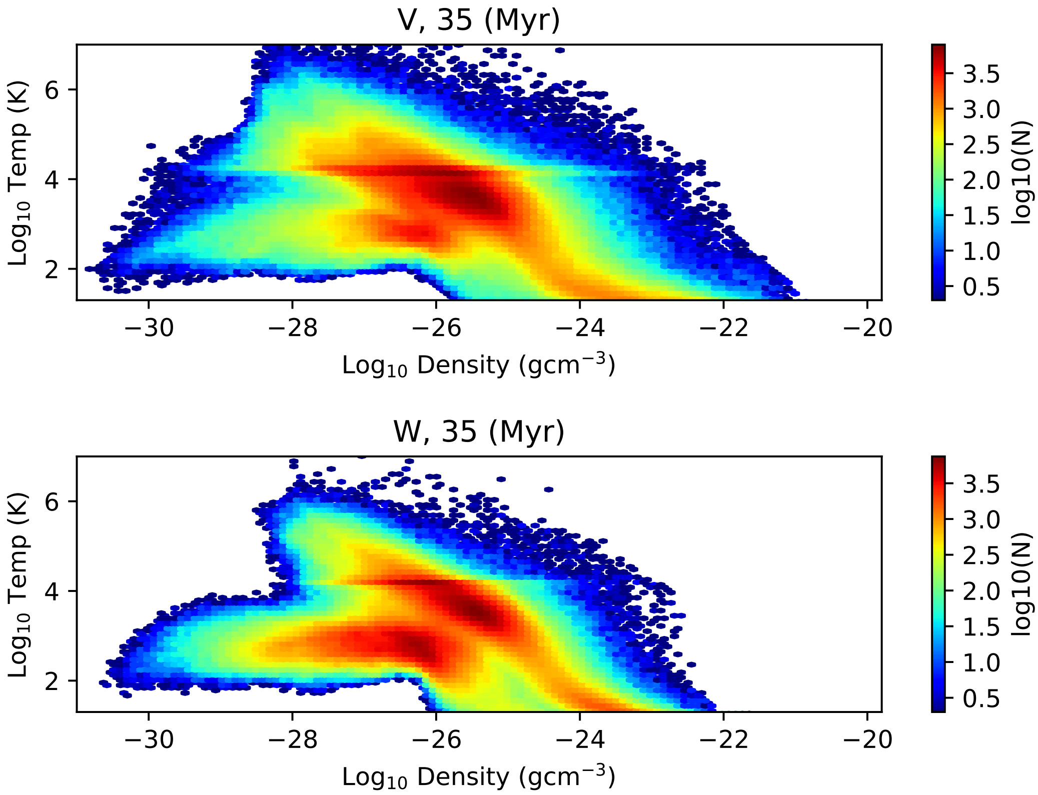

FIGURE 3.25: Temperature versus density plot, rendered according to gas particle number, for Runs V and W, at 35 Myr.

occurred, have had a negligible impact on the fraction of gas that is star forming or expelled. Despite the total energy of Run V being greater than Run W beyond 20 Myr, a larger fraction of the gas is unbound in Run W, while a smaller fraction becomes star forming (i.e. goes into sink particles).

In Fig. 3.25 I plot the temperature of the gas in Runs V and W, versus density at t = 35 Myr. From this plot, we can see although there is a larger amount of high temperature ($> 10^5$ K), low density ($< 10^{-28}$ gcm^{-3}) gas in Run V than in Run W, there is also a larger amount of gas with temperatures $<$ 100K and densities $> 10^{-24}$ gcm^{-3}. Moreover, in Fig. 3.26 I plot the cumulative feedback injection energy in both runs against time. We see despite the fact less gas is unbound in Run V, the energy injected across the simulation is an order of magnitude higher than Run W through the addition of HMXB feedback.

In order to help ascertain the cause of the higher sink mass fraction in Run V compared with Run W, despite an order of magnitude more energy being injected into the simulation, I use Fig. 3.27 to plot the mean cooling time in 200 different θ bins 14 Myr into Runs V and W. I only use particles within a 200 pc radius of the centre of the cloud. I chose 14 Myr since this represents the free-fall time of both clouds and where the star formation histories of both clouds diverge; from Fig. 3.19 it is at this point Run V continues to form between 10-100 sink particles between snapshots and Run W drops noteto between 1-10. Looking at Fig. 3.27 we can see the order of magnitude drop in density towards both -π and π radians, which corresponds with the low density, hot chimney also seen in Fig. 3.9. Looking at the cooling times, we can see the cooling time is generally higher inside the chimney for Run V: reaching as high as 10 Myr at $\sim$ 2.5 rad, as well as 1 Myr at -π rad (compared with $\sim 10^{-2}$ Myr in Run W). This provides evidence for the hypothesis that the HMXB feedback in Run V has acted to increase the cooling times of the gas in the chimneys, keeping it hot and flowing outwards. This has allowed star formation to continue in the inner parts of the cloud. It is, however, worth noting there is a second chimney visible in Run W, that is not present in Run V. This was also visible in figures 3.7 and 3.6. The gas in this chimney peaks at a cooling time of around 1 Myr, which indicates SNe feedback is also acting to efficiently keep hot gas flowing outwards from the centre of the cloud. The presence of the second chimney in Run W is perhaps a product of a higher number of SNe within 14 Myr – 171 exploded within cloud W prior to this time, as opposed to 153 in cloud V.

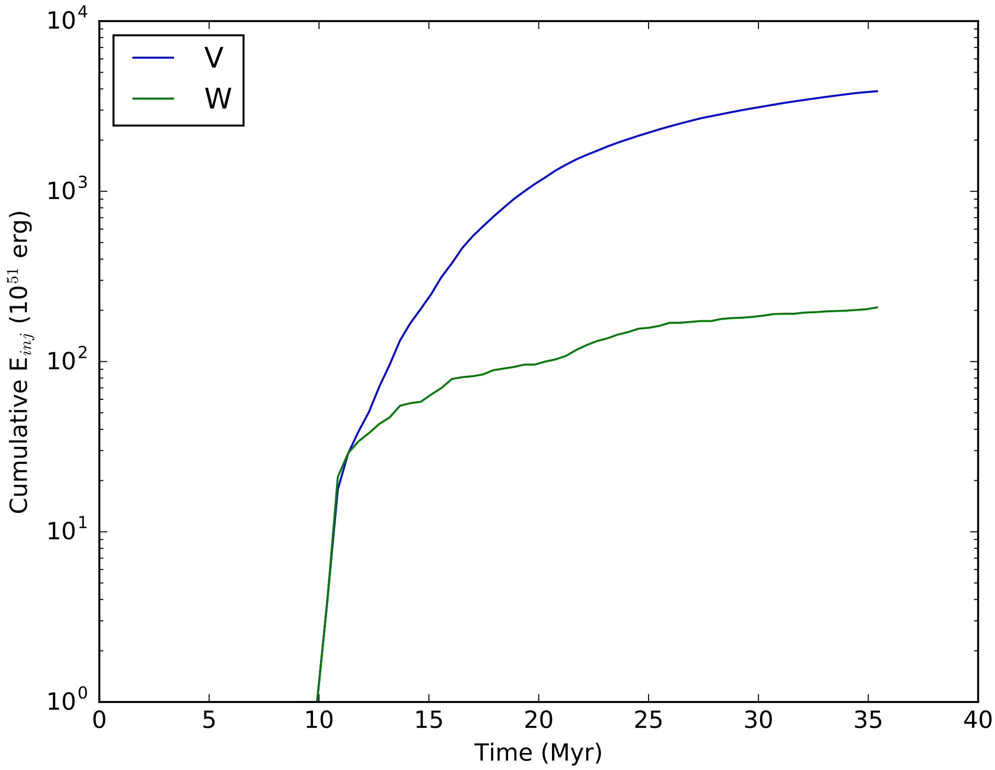

FIGURE 3.26: The cumulative energy injected via SNe and HMXB feedback mechanisms in Runs V and W, against time.

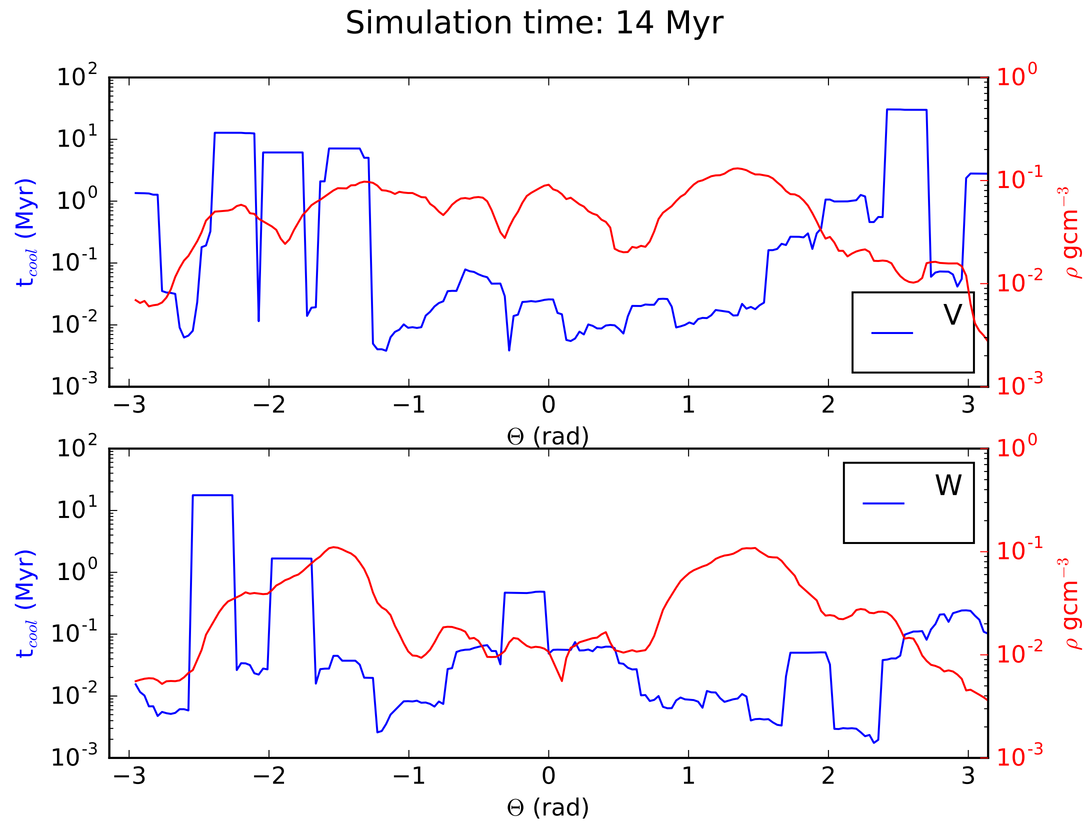

FIGURE 3.27: Blue lines - the mean cooling times in 200 θ bins at t = 14 Myr, for both Run V (top plot) and W (bottom plot), out to a radius of 200 pc. Red lines - the mean density in each θ bin. A chimney corresponds to an order of magnitude drop in density. One can be seen at the far ends of both plots.

In summary, the effect of adding a prescription for HMXB feedback on top of SNe feedback is largely washed out in smaller molecular clouds, where the number of massive stars is smaller and the binding energy is lower. However, in larger molecular clouds the combination of HMXB and SNe feedback can lead to an increase in star formation efficiency and period, compared with the clouds which just include SNe feedback. Just as for Runs E and F, the results from the larger molecular cloud also suggest it is the SNe feedback that determines the underlying density profile of the cloud, while in order for the chimneys to be effective, they must form within the crucial free-fall timescale of the cloud. Moreover, from Fig. 3.27 there is evidence to suggest HMXBs act to increase the efficiency of chimneys at funneling hot gas away from star-forming material by increasing its cooling time to between 1-10 Myr. As well as this, from the additional chimney present in Run W, there is also evidence to suggest a higher number of SNe leads to a higher number of chimneys.

3.5.5 Thermal vs Kinetic HMXB feedback: Runs A and B

Firstly, looking at the density slices for both Runs A (thermal HMXB feedback) and B (kinetic HMXB feedback) in Fig. 3.6, Run A appears to have a more anisotropic gas distribution than Run B out to 2 kpc, with long extended filaments of high density gas and multiple bubble-like cavities filled with lower density gas. However, there is a cavity spanning ~ 200 pc present in Run B, indicating the feedback has effectively blown out this inner region of gas. The cavity has been maintained by the additional thermal energy injection of SNe and the continuous energy injection from HMXBs (see Fig. 3.17), similar to the bubbles described in Weaver et al. (1977). This cavity is also present in the x-z and y-z planes, excluding the possibility the cavity seen in the x-y plane is a chimney viewed outside its principal axis. No gas above 10^6 K can be seen inside Run B, indicating any thermalisation of the kinetic feedback, along with the internal energy inputted into the ISM via SNe, has been rapidly lost via radiative cooling. Additionally, in Fig. 3.28 we plot the mean radial velocity and the net radial momentum in radial bins up to 1 kpc for both Runs A and B. Looking at Run B, we see the kinetic feedback has resulted in a momentum driven outflow, which can be seen at 400 pc. This also corresponds to a small dip in the mean radial velocity, indicating the outflow has been slowed by the swept up mass.

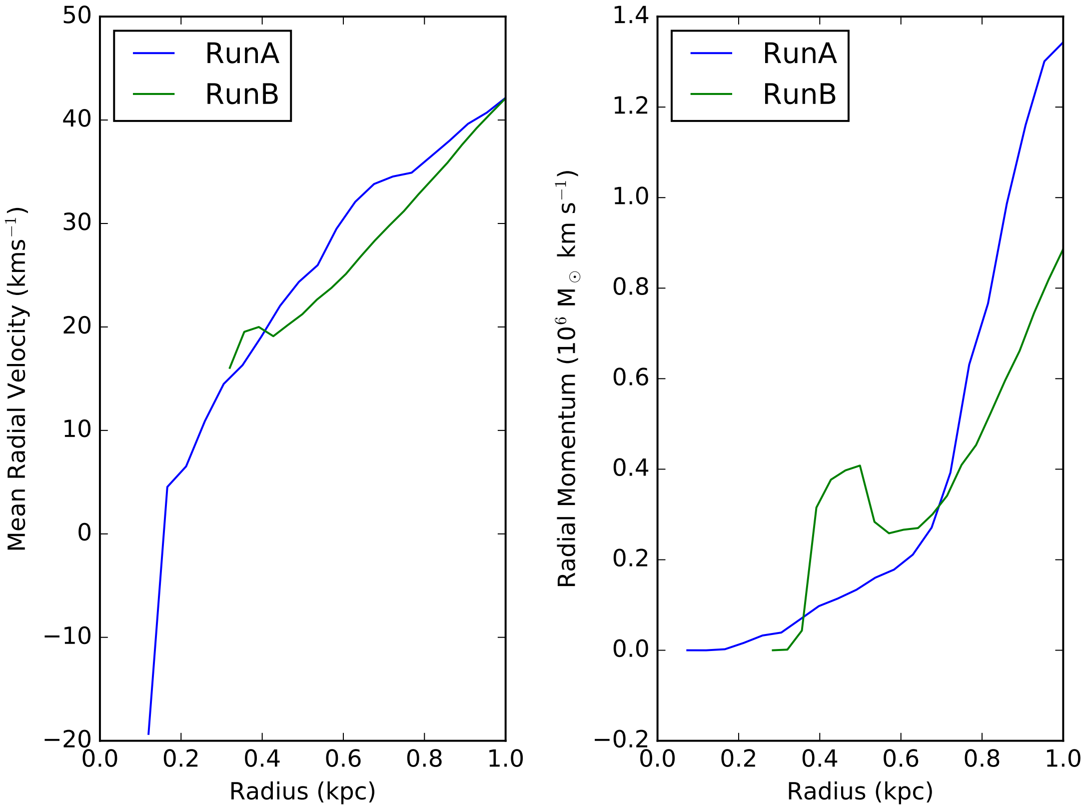

FIGURE 3.28: The mean radial velocity and momentum versus radius taken at t = 35 Myr into Runs A (blue lines) and B (green lines).

Next, comparing the temperature slices of Runs A and B in Fig. 3.7 the temperature of the gas cloud is lower in Run B, while Fig. 3.10 shows the mean temperature of Run B is lower than Run A across the the majority of the simulation. This indicates efficient cooling by any shock-heated gas in the central 100 pc, along with possible 'leaking' of high velocity gas through low density cavities such as the one visible in Fig. 3.6. Two such cavities are seen to be working in the temperature slice for Run B. They are chimney-like, however the gas inside these regions is cooler than is seen in the chimneys for the other runs, indicating a momentum-driven flow as opposed to a pressure-driven outflow. Additionally, Fig. 3.10 shows the net radial momentum is consistently lower in Run B than Run A, while the mean radius of the gas is smaller across the simulation. This points to the fact the stellar feedback in Run B has been less effective at driving large-scale outflows.

Looking instead at Fig. 3.15, the total energy of Run B is consistently lower than Run A, with two jumps in energy, initially when feedback kicks in at $\sim$ 10 Myr, and again after 20 Myr. The lower total energy of Run B is reflected in Fig. 3.18, where Run A contains a higher unbound mass fraction than Run B, along with a smaller sink particle mass fraction.

Fig. 3.19 shows the number of sink particles formed is not only higher in Run B, but occurs over a single longer period of star formation (between 6 - 23 Myr). This is in contrast to the 'bursty' sink particle formation seen in Run A. However, despite 27% more sinks forming in Run B (see Table 3.2), the number fraction of these that have masses above 180 $M_\odot$ is half that of Run A, resulting in $\sim$ 45% fewer SNe and $\sim$ 60% fewer HMXBs than Run A. Hence, by including momentum-driven HMXB feedback the mean mass of the sink particles has been reduced, resulting in fewer massive stars and hence feedback events. A contributing factor to the lower sink masses in Run B is likely to be the lower mean temperature seen in Fig. 3.10. This will lower the Jeans mass (M_J), which scales as $T^{3/2}$, resulting in smaller sink particles masses forming from the Jeans criterion.

Another contributing factor to the lower total energy seen for Run B in Fig. 3.15 is the 'leaky' nature of the kinetic feedback; high velocity gas particles will escape through the path of least resistance, while others are expected to hit the surrounding high density gas and thermalise, as well as subsequently cool, efficiently. The dissipation of the feedback energy via cooling can be artificially fast due to the high density of the surrounding material. This is a common problem encountered when modelling SNe feedback using radial kicks of the surrounding particles. In their 2003 paper (Springel and Hernquist, 2003), Springel and Hernquist provided a solution to this problem by kinetically decoupling the wind particles until their density has dropped to a threshold value or a set amount of time has elapsed. The cold, low density central region of cloud B (see Fig. 3.6) indicates the rapid dissipation of SNe energy has manifested inside Run B. This may have artificially limited the effectiveness of the feedback in quenching star formation beyond this radius.

To conclude, implementing HMXB feedback as kinetic energy has resulted in a momentum-driven outflow which has been slowed at a radius of $\sim$ 400 pc due to the large swept up mass. Furthermore, it is likely this 'stalling' has resulted in the thermal SNe events occurring in dense environments, which has caused the rapid dissipation of thermal energy via radiative cooling, perhaps artificially limiting its effectiveness at reducing star formation at radii beyond $\sim$ 200 pc. As well as this, the efficient cooling seen in Run B, compared with Run A, has resulted in lower sink particle masses, due to a reduction in M_J, which in turn has led to fewer HMXB/SNe events (as a consequence of the numerical method).

3.6 Discussion: $Z_\odot$ Runs

This chapter has investigated the effects of including a prescription for HXMB feedback (a gradual heating source) on top of SNe feedback in star-forming giant molecular clouds at solar metallicity. The simulations follow the molecular cloud over 3 free-fall times. Simulations were run which varied metallicity, cloud size, and the way the HMXB feedback was implemented. Below I summarise the main results of the chapter.

- In the clouds studied here, the addition of feedback does not change the fact the majority of star formation occurs within the free-fall time of the clouds.
- However, the combination of SNe and HMXB feedback can lead to efficient use of low density 'chimneys' in the gas cloud, funneling hot gas from the central regions of the cloud in order to maintain cold, high density gas to fuel further star formation at later times.
- At solar metallicity, primarily through the action of chimneys, the combination of HMXB and SNe can extend the period of star formation as well

as increase the star-formation efficiency compared with clouds that just include SNe.

- Due to the similarity between density profiles of runs with just SNe feedback and runs with HMXB feedback included on top, it appears that the initial SNe events (prior to the onset of HMXB feedback) set the preferential direction of the hot gaseous outflows from the centre of the cloud. In other words, SNe set the locations of the chimneys and the addition of HMXB feedback increases their effectiveness at funneling hot gas outwards. This is despite the addition of HMXBs increasing the energy injected into the cloud.

- There is evidence to suggest HMXBs increase the efficiency of chimneys at removing energy from the cloud by increasing the temperature of the gas inside to beyond 10^7 K, where the cooling is predominantly Bremsstrahlung dominated and relatively inefficient.

- The number of HMXBs and SNe in each simulation seems to be the defining factor of the fate of the gas in the cloud. This can vary between clouds due to the inherent stochasticity in HMXB formation. For example, simulations A and C were re-run with different seeds for the turbulence generator (which introduced stochasticity into the massive star properties that were assigned to sink particles). I found the defining factor in these runs was the inherent stochasticity in the number of massive stars and hence feedback events. In this way, clouds with the same initial conditions can have different fates based purely on the random sampling of the underlying IMF.

- However, the main factor in determining the number of stellar feedback events in these simulations was the average sink particle mass. For example, efficient cooling (as was seen in the kinetic HMXB feedback run; Run B) led to a higher number of sink particles with lower mean masses and hence ultimately fewer HMXBs/ SNe (see Table 3.2).

- At solar metallicity, the positive feedback effects of combining SNe and HMXBs are more apparent in larger molecular clouds ($>10^6$ $M_\odot$). This is because the gravitational binding energy of the smaller clouds is small enough that ~ 10 SNe can unbind the majority of the gas in the cloud. Also, the rarity of HMXB events means there are typically just ~ 2 HMXBs acting in the lower mass clouds.

- Kinetic HMXB feedback resulted in a momentum-driven outflow, which was slowed at ~ 400 pc due to the large swept up mass. The continuous injection of energy within the central 200 pc of the cloud resulted in a low density, cold cavity. Furthermore, the effects of feedback beyond ~ 400 pc were limited by the efficient cooling of injected SNe energy and thermalised HMXB kinetic energy input.

- The results are comparable to the case when the stellar wind feedback from massive stars is included on top of SNe feedback. The key element in chimney efficiency is the presence of a constant heating source of sufficient power.

3.6.1 The set-up in context

The initial conditions, while typical of those in other works investigating feedback effects in molecular clouds (e.g. Dale, Ercolano, and Bonnell, 2012; Federrath et al., 2014), represent an idealised set up. In reality, molecular clouds are dynamic objects which are often unbound (Dobbs, Burkert, and Pringle, 2011). Also the galactic environment likely plays an important role in cloud evolution (Rey-Raposo et al., 2017). However, to isolate the effects of different processes and parameters a relatively simple set of initial conditions is required. Furthermore, in this paper I employ a basic method to produce a population of massive stars with a set of lifetimes and masses that are physically motivated. An alternative method would have been to use the outputs from the existing binary population code BPASS (Eldridge and Stanway, 2009; Eldridge et al., 2017). This would allow us to follow the properties (e.g. temperature, luminosity) of individual stars, taking into account those in binaries. This would be particularly useful in future work where I want to take into account the radiative luminosity of the stars alongside their mechanical luminosity.

The simulations have followed the evolution of the clouds for 35 Myr. This is longer than the lowest estimates for molecular cloud lifetimes which range from ~ 1 Myr to 10^2 Myr. Thus the simulated cloud lifetimes represent an intermediate value (Heyer and Dame, 2015; Cohen et al., 1980). From observations of the solar neighborhood, shorter lifetimes are favoured due to a missing population of older (over 3 Myr) stars inside molecular clouds (e.g. Ballesteros-Paredes and Hartmann, 2007). This suggests molecular clouds are destroyed before this, whether by photo-ionising radiation, stellar winds, SNe or a combination of these effects (e.g. Rahner et al., 2017; Skinner and Ostriker, 2015; Dale and Bonnell, 2011; Krumholz, 2014). Furthermore, work by Elmegreen (2000) and Hartmann, Ballesteros-Paredes, and Bergin (2001) suggests molecular clouds should be destroyed within 1 free-fall time. However, the clouds studied here are of masses comparable with GMCs and their free-fall time is ~ 12 Myr, which is comparable to the lifetimes of massive stars. This means they exist towards the upper limit of molecular cloud masses and in a regime where the feedback from massive stars becomes important. Moreover, Dale, Ercolano, and Bonnell (2012) found that such clouds are unlikely to be significantly disrupted by photo-ionising radiation within 3 Myr, while Matzner (2002) predict cloud lifetimes between 10-30 Myr on the grounds this represents the time it would take HII regions generated by the photo-ionising flux, predominantly from massive stars, to evaporate the cloud. Furthermore, work by Murray (2011) which cross-correlates 32 star-forming complexes identified by WMAP in the Milky Way with a GMC catalogue and found the mean free-fall time of the massive GMCs in the Milky Way to be 27 ± 12 Myr.

All of the clouds in these simulations exist below the upper mass limit 6×10^6 $M_\odot$, which represents the largest of the molecular clouds in the Milky Way (Williams and McKee, 1997). As the upper limit of the expected lifetimes is comparable to the length of the simulations, it would be interesting, in future work, to investigate the effect of including photo-ionising radiation from massive stars on top of HMXBs and explore how this influences the formation of chimneys and ultimately the star formation efficiency of the clouds. The impact of prior feedback mechanisms on the way SNe interact with their environment has been investigated in a number of works; for example Walch et al. (2015) (photo-ionisation), Fierlinger et al. (2015) (winds) and Kim, Kim, and Ostriker (2016) (radiation pressure).

I have described the simulated clouds as either 'bound' or 'unbound' with virial parameters ranging from 0.7 to 1.2. However, this relates to the initial conditions. In reality both clouds are free-falling by the time feedback kicks in (see section 3.5.1). This is due to the fact the initial turbulent velocity field is quickly thermalised and lost due to subsequent cooling, as was also seen in work by Dale, Ercolano, and Bonnell (2012). Therefore, in reality the higher virial parameter in the initial conditions manifested as an alteration to the distribution of sink masses (see Fig. 3.24), with a lower mean sink particle mass (see Table 3.2) and hence fewer HMXB and SNe events. However, how HMXB and SN feedback would interplay in an unbound cloud remains an interesting and important question, hence a method of modeling an unbound cloud would be of interest the future.

Despite focusing on HMXB feedback in this paper, the results are also comparable to including massive stellar winds in the GMC. Table 3.2 shows the number of HMXBs in each simulation is between 10% and 20% of the number of massive stars leaving the main sequence. Given the 35 Myr timescale of the simulations, this means the energy injected via stellar winds would be comparable to the power input from HMXBs. Crucially, it would also mimic the gradual heating from HMXBs and hence would likely lead to the formation of the kpc-scale chimneys (as was seen in previous work by Rogers and Pittard, 2013). In Chapter 5 I therefore include both stellar winds and HMXBs. In future work I would also like to scale the energy injected by HMXBs according to the mode of accretion and mass of the companion star.

Beyond the alternative modes of accretion in HMXBs (as well as the several orders of magnitude increase in luminosity this can produce), another key difference between HXMB feedback and stellar wind feedback is that, on the spatial scale of the jets, the energy input is delivered to the medium an-isotropically in the HMXB case and isotropically by stellar winds. I have shown chimneys can be produced without any directionality to the feedback, however in future work it will be interesting to investigate the interaction of directional HMXB jet feedback with an inhomogeneous ISM, along with how this affects chimney formation.

3.7 Next chapter, low Z runs

In the next chapter I will present the result of running the simulations in this chapter, at low metallicity instead. I will also the discuss the results of numerical convergence tests. Finally the chimneys seen here are discussed in the context of wider literature.

Chapter 4

Investigating stellar feedback in GMCs: Part II (low Z)

4.1 Introduction

This chapter will investigate the interplay between HMXB feedback and SNe feedback in low metallicity GMCs. These results are directly comparable to those in Chapter 3, since they have the same initial conditions.

I chose to run two sets of simulations at metallicities of $Z = Z_{\odot}$ (or [Fe/H] $= 0$) and $Z \sim 0.001$ (or [Fe/H] $= -1.2$) in order to compare the effects of the altered cooling regimes and HMXB populations on the gas cloud. In particular, the $Z \sim 0.001$ value was chosen since this is beyond the 'critical metallicity' for Population II stars, hence the gas in the simulations has been metal enriched via the SNe of Population III stars. This allows cooling below 200 K via metal-line cooling, which is inhibited at zero metallicity since here cooling is limited to the rotational/vibrational excitations associated with H_2 molecules (Larson, 2005). For further details on low temperature cooling and its implementation in GADGET-3 see Section 2.4. The mass resolution is such that the gas in the [Fe/H]$= -1.2$ runs can cool enough to meet the Jeans density criterion and undergo star formation, something that was not possible at zero metallicity.

It is of particular interest to model HMXBs in low Z environments since there is evidence HMXBs play an enhanced role at high redshift (e.g. Basu-Zych et al., 2013b; Basu-Zych et al., 2013a; Fragos et al., 2013a), both due to these systems being more numerous (e.g. Dray, 2006; Douna et al., 2015), as well as more luminous due to a higher fraction following the ULX/Roche-Lobe overflow evolutionary pathway (e.g. Linden et al., 2010). Blue Compact Dwarf galaxies (BCDs) are often used to investigate this hypothesis, since they are low metallicity and are thought to be analogous to high redshift environments. Recent work into these systems has found a significant increase in the HMXB population of BCDs, compared with solar metallicity environments (e.g. Kaaret, Schmitt, and Gorski, 2011; Brorby, Kaaret, and Prestwich, 2014).

Projects such as BPASS (Eldridge et al., 2017) have also highlighted the importance of considering binaries when exploring stellar feedback at high redshift. BPASS is a stellar population synthesis code which includes the effects of binary evolution and in this case it was used to explore the role of binary interactions during re-ionisation (e.g. Stanway, Eldridge, and Becker, 2016). It was found that including binaries in a stellar population increases the population of massive stars beyond 3 Myr into star formation, which provides a supply of ionising photons that can escape through channels/ chimneys carved in the surrounding ISM by previous stellar feedback events, thereby increasing the escape fraction of ionising photons into the IGM (Ma et al., 2016).

Altering the metallicity of the simulations presented in Chapter 3 will shorten the lifetimes assigned to massive stars (e.g. Schaller et al., 1992) and therefore increase the input power of the HMXB events. As well as this, lowering the metallicity of the ISM will reduce the cooling efficiency of the gas (as we saw in Chapter 3, section 3.5.1), which could effect the distribution of sink masses, as discussed in Chapter 3, section 3.6.

In this chapter I will briefly discuss my numerical method before presenting the results of the low metallicity runs, along with a number of numerical convergence tests, before discussing the results of both this chapter and Chapter 3 in the context of wider literature.

4.1.1 The numerical model

As in Chapter 3 this work uses GADGET-3 (Springel, 2005), along with the SPHS extension described in Read and Hayfield (2012). Furthermore, the Wendland-2 kernel (Wendland, 1995; Dehnen and Aly, 2012) is used with 100 neighbours. Once again, the gas is modeled using an ideal equation of state, with separate cooling schemes for gas above and below 10^4 K (Sutherland and Dopita, 1993; Mashchenko, Wadsley, and Couchman, 2008) and a temperature cap of 10^8 K. These simulations use the same sink particle accretion and formation criterion as

TABLE 4.1: The different simulations run through the course of this chapter. All runs are at [Fe/H] = -1.2. Here M_0 is the initial gas mass (in $M_\odot$) of each simulation, R_0 is the initial cloud radius in pc, T_i is the initial temperature in K, α_{vir} is the initial virial parameter ($|E_{kin} + E_{therm}|/|E_{pot}|$), t_{ff} is the free-fall time of the cloud, m_{pcl} is the gas particle mass in each simulation, and HMXB is the type of HMXB feedback present (either kinetic or thermal).

Run	M_0 ($\times 10^6$ $M_\odot$)	R_0 (pc)	T_i (K)	α_{vir}	Mach No.	t_{ff} (Myr)	m_{pcl} ($M_\odot$)	HMXB	SNe (Y/N)
H	2	100	150	0.7	8.3	11.7	0.4	Therm	Y
I	2	100	150	0.7	8.3	11.7	0.4	None	Y
K	2	100	150	1.2	11.0	11.7	0.4	Therm	Y
L	2	100	150	1.2	11.0	11.7	0.4	None	Y
T	0.5	65	150	0.7	5.0	12.3	0.1	Therm	Y
U	0.5	65	150	0.7	5.0	12.3	0.1	None	Y
X	5	150	150	0.7	10.8	13.6	1	Therm	Y
Y	5	150	150	0.7	10.8	13.6	1	None	Y

described in section 3.2, however the mean molecular weight used in equation 3.1 is 1.242 for $Z \sim 0.001$.

Regarding the binary population synthesis, the method is principally the same as that described in section 3.2.2, however with two differences. Firstly, the lookup tables used to interpolate the massive star lifetimes were generated using Table 46 from Schaller et al. (1992) (again making the approximation $t_{life} \sim t_H + t_{He}$). Secondly, revised remnant masses were obtained from Table 4 of Maeder (1992).

Again, the random seed associated with the binary population synthesis scheme in GADGET-3 is tied to the particle identity and the number of the current time step, neither of which should vary between runs with identical initial conditions prior to the onset of feedback. Moreover, the turbulent velocity spectrum in each GMC was seeded in the same way as section 3.4.

The initial parameters of the runs in this chapter are summarised in Table 4.1. The main difference is that the initial temperature for the gas in these runs is set to 150 K instead of 50 K, reflecting the relative inefficiency of cooling seen at low metallicity. This is due to the fact the primary cooling mechanism below 10^4 K is via electronic excitation of the fine structure levels associated of metal ions (e.g. Mo, Bosch, and White, 2010).

TABLE 4.2: A table listing the total sink mass as a fraction of the initial gas mass at the end of each [Fe/H] = -1.2 simulation ($mf_{\rm sink}$), the number of sink particles present at the end of each run ($N_{\rm sink}$), the total number of SNe ($N_{\rm SNe}$) and HMXBs ($N_{\rm HMXB}$) across the whole simulation, the mean sink particle mass ($mp_{\rm sink}$), the fraction of the total number of sinks with a mass > 180 M$_\odot$ and finally the mean mass accreted by sinks with masses above 180 M$_\odot$ (denoted $M_{mean,180}$).

Run	$mf_{\rm sink}$	Total $N_{\rm sink}$	$N_{\rm SNe}$	$N_{\rm HMXB}$	Mean $mp_{\rm sink}$ (M$_\odot$)	Number fraction of sinks $>$ 180 M$_\odot$ (%)	$M_{mean,180}$ (M$_\odot$)
H	0.16	2739	334	45	116.3	14.9	36
I	0.17	2835	389	74	118.1	15.5	42
K	0.11	1913	184	25	113.6	12.6	35
L	0.11	1905	190	24	114.3	12.5	38
T	0.02	105	16	2	104.2	19.0	112
U	0.02	84	30	6	141.8	38.1	65
X	0.08	3681	418	65	114.7	11.9	35
Y	0.10	4557	452	71	112.0	11.9	33

4.2 Results, [Fe/H] = -1.2

Overall, the lower metallicity runs contain more SNe and HMXBs than their solar metallicity counterparts due to a higher mean sink particle mass (see Tables 3.2 and 4.2) - resulting from a higher M_J (see section 3.5.5).

4.2.1 The injection of HMXB: Runs H, I

Figures 4.1 and 4.2 show the density and temperature slices for the low metallicity runs ([Fe/H]=-1.2) 35 Myr into each simulation. Looking at the density and temperature slices for Run H, we see the inner region of the cloud has been effectively blown out to a radius of $\sim$ 1.5 kpc, whereupon the remaining hot gas has carved a low density 'hole' on the right of the slice. This hole cannot be considered to be a chimney since it does not extend and narrow towards the central kpc of the cloud. The morphology does, however, resemble a champagne flow (Tenorio-Tagle, 1979) - in this case formed by the hot pressurised gas generated by the SNe and HMXB events escaping into the lower density ISM of the cloud's outer regions. As in the case of champagne flows, the anisotropic morphology of this outflow is most likely due to the fact the HMXB and SNe events are not spatially isotropic and hence will be closer to one edge of the cloud than another.

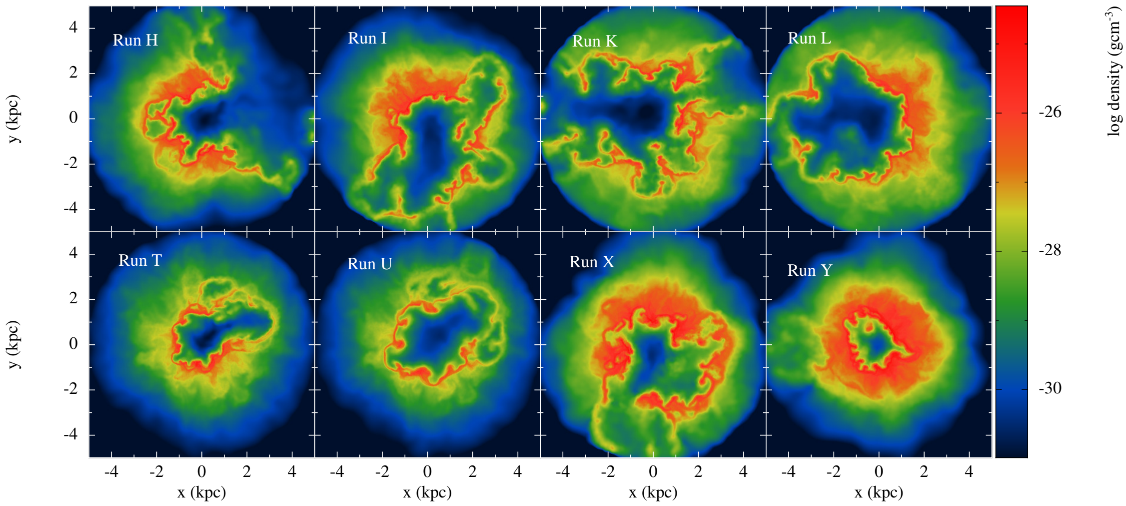

FIGURE 4.1: Density slices taken in the x-y plane at z=0 for runs at a metallicity of [Fe/H] = -1.2, taken 35 Myr into each simulation.

The temperature of the gas within ~ 1.5 kpc of cloud H is uniformly 10^8 K (which is radiatively inefficient), indicating there is no cool dense gas remaining in this region which can collapse to form stars within the timescale of the simulation. Similarly in cloud I, the gas has been blown out to 1 kpc and the remainder of the feedback-heated gas has carved a hole towards the bottom of the density slice. Once again the inner 1.5 kpc of cloud I has been uniformly heated, ceasing all star formation in this region. However, the temperature of the hot gas is slightly cooler than in cloud H - between 10^{7-8} K.

Looking instead at Fig. 4.3, which plots the mean density and temperature across various θ bins for the [Fe/H] = -1.2 runs, there is a chimney-like structure in the θ-density profile of Run H, which develops from 12 Myr to 35 Myr. However, looking at the density scale at 12 Myr, it is clear this trough in the density profile represents less than an order of magnitude drop in density. This is in stark contrast to the two orders of magnitude density drop seen in the corresponding plot for Run A (Fig. 3.9). Even 35 Myr into the simulation, the 'chimney' seen in Run H only represents < 1 order of magnitude density drop. The corresponding peak in the mean gas temperature, however, is 3 orders of magnitude larger in Run H (10^8 K) than Run A (10^5 K). Moreover, the rise in temperature in Run H

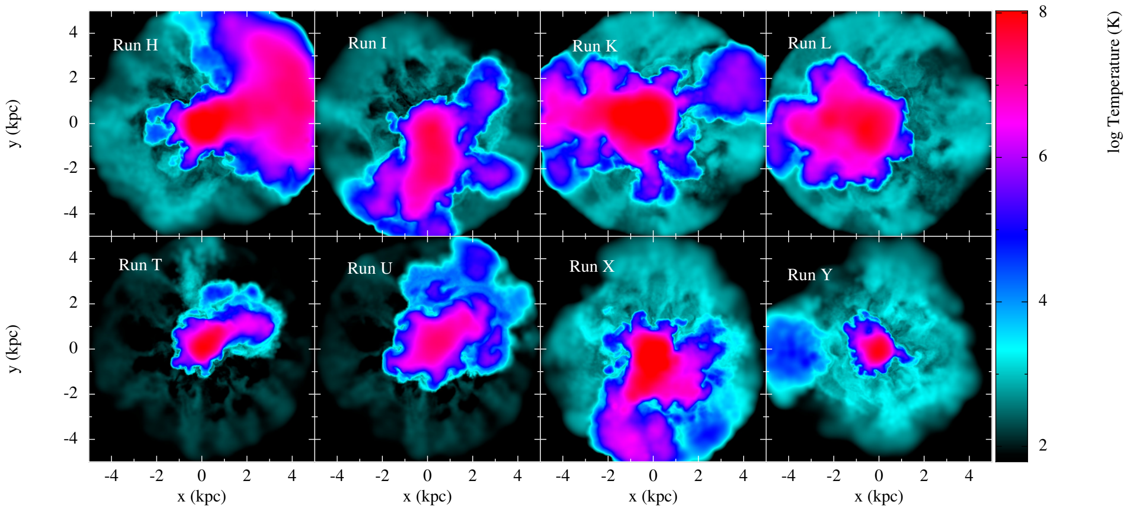

FIGURE 4.2: Temperature slices taken in the x-y plane at z=0 for runs at a metallicity of [Fe/H] = -1.2, taken 35 Myr into each simulation.

spans 3-4 orders of magnitude, while the chimney in Run A spans ~ 2. Run I follows a similar trend in density across different θ bins as Run H; the 'chimneys' only span ~ 1 order of magnitude in density. However, the gas in Run I has a lower peak temperature than Run H at 35 Myr.

Fig. 4.4 plots the cumulative injected energy for each [Fe/H]=-1.2 run, while Fig. 4.5 plots the number of SNe and HMXBs between snapshots. The injected energy for Run H is greater than Run I, due to a similar number of SNe events in each run and an additional $\sim$ 10-50 HMXBs active between snapshots. Moreover, if we compare the number of HMXB events and SNe events in Runs A and H (Tables 3.2 and 4.2), we see Run H has nearly 3 times as many SNe and over 2.5 times as many HMXBs as Run A. Also, the number of SNe is higher in Run I than Run A. In Fig. 4.6 I plot the time evolution of the ratio between the energy injection from HMXBs to the energy injected by SNe events for a selection of runs. From Fig. 4.6, we can see the ratio between the energy injected by HMXBs and the energy injected via SNe is typically above 1 in all runs plotted. However, the ratios are particularly high in Run X, while Run H also has peaks above 5, where Runs A and E do not. This helps explain the high peaks in gas temperature seen for Run H in Fig. 4.3.

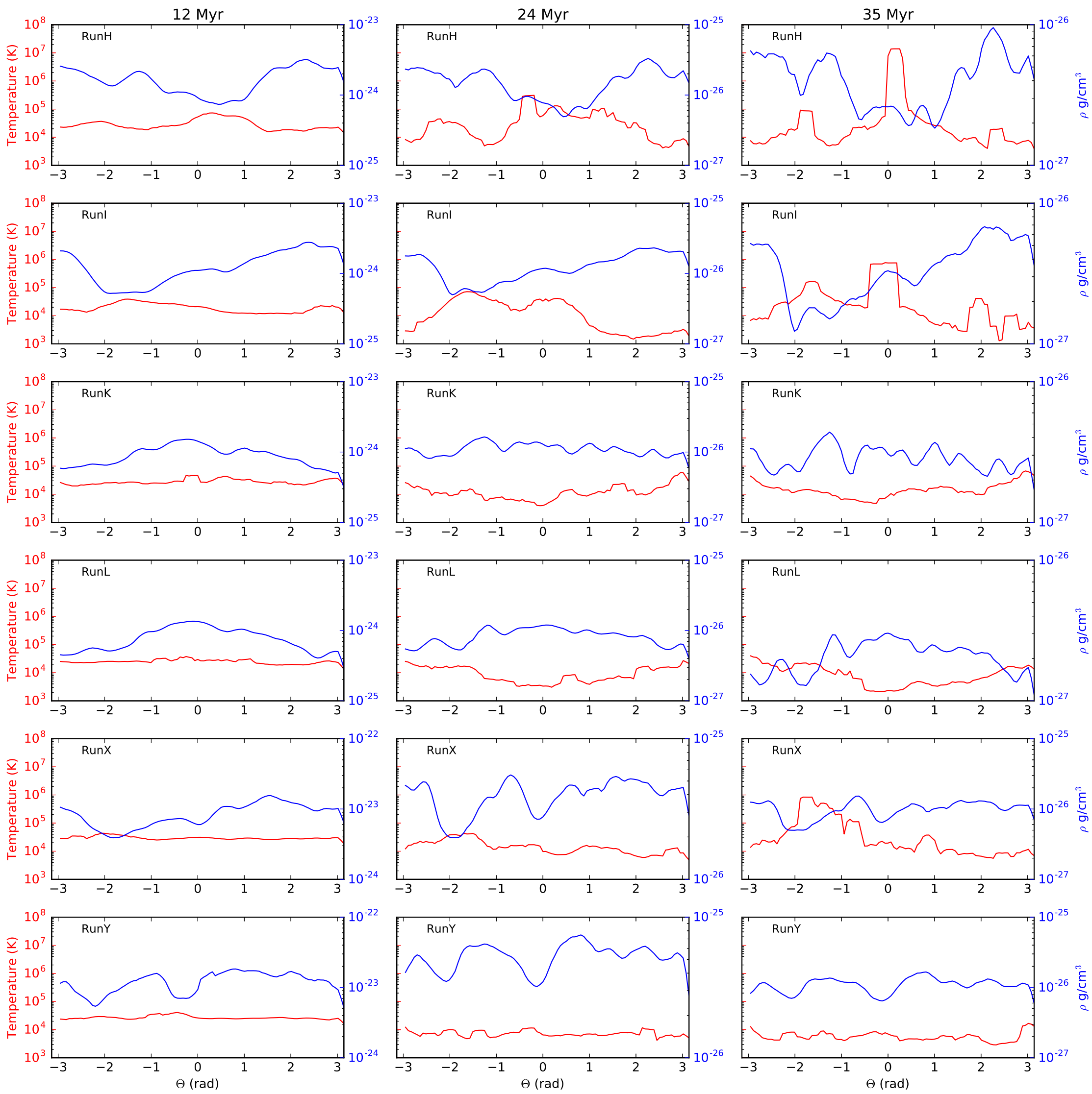

FIGURE 4.3: Plots to show the mean temperature (red) and density (blue) in θ bins ranging from -π to π radians for runs at [Fe/H] = -1.2. The maximal radius of each θ bin is set to the maximum radius of the gas in the individual bin. The left column is for snapshots taken at 12 Myr, the middle column is for 24 Myr and the right column shows snapshots at 35 Myr. The name of the corresponding run is in the upper left hand corner of each plot.

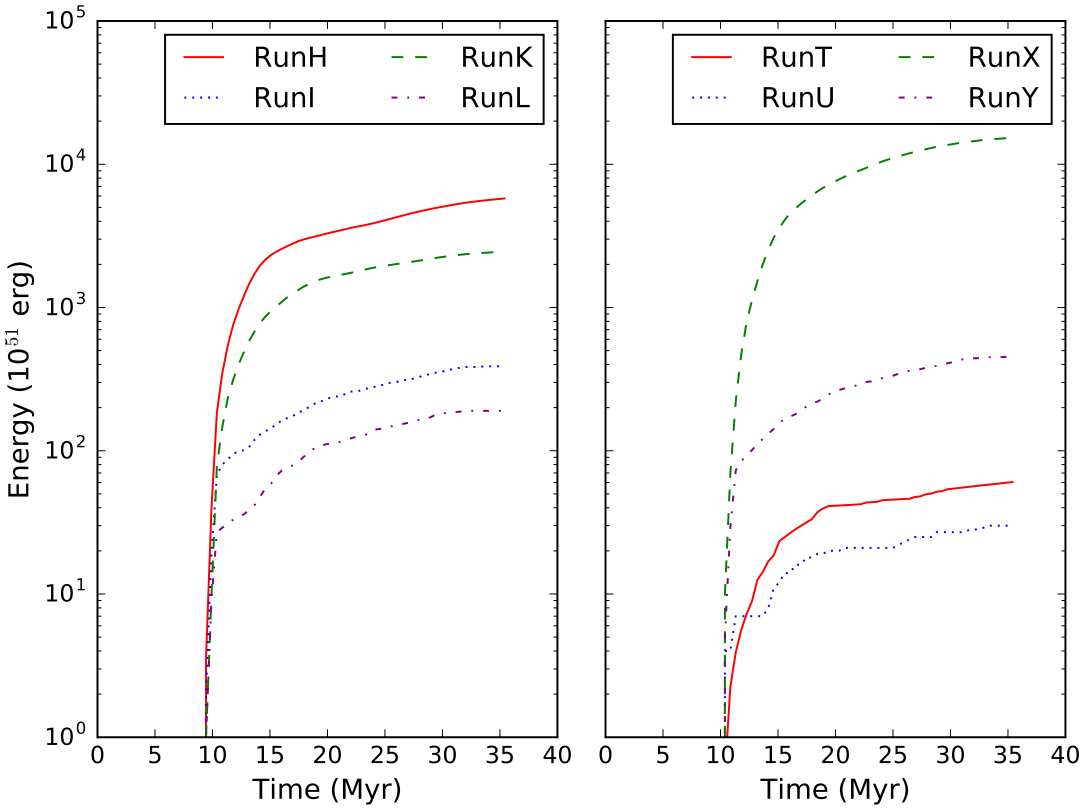

FIGURE 4.4: The cumulative energy injected across the simulation for the [Fe/H] = -1.2 runs which include feedback.

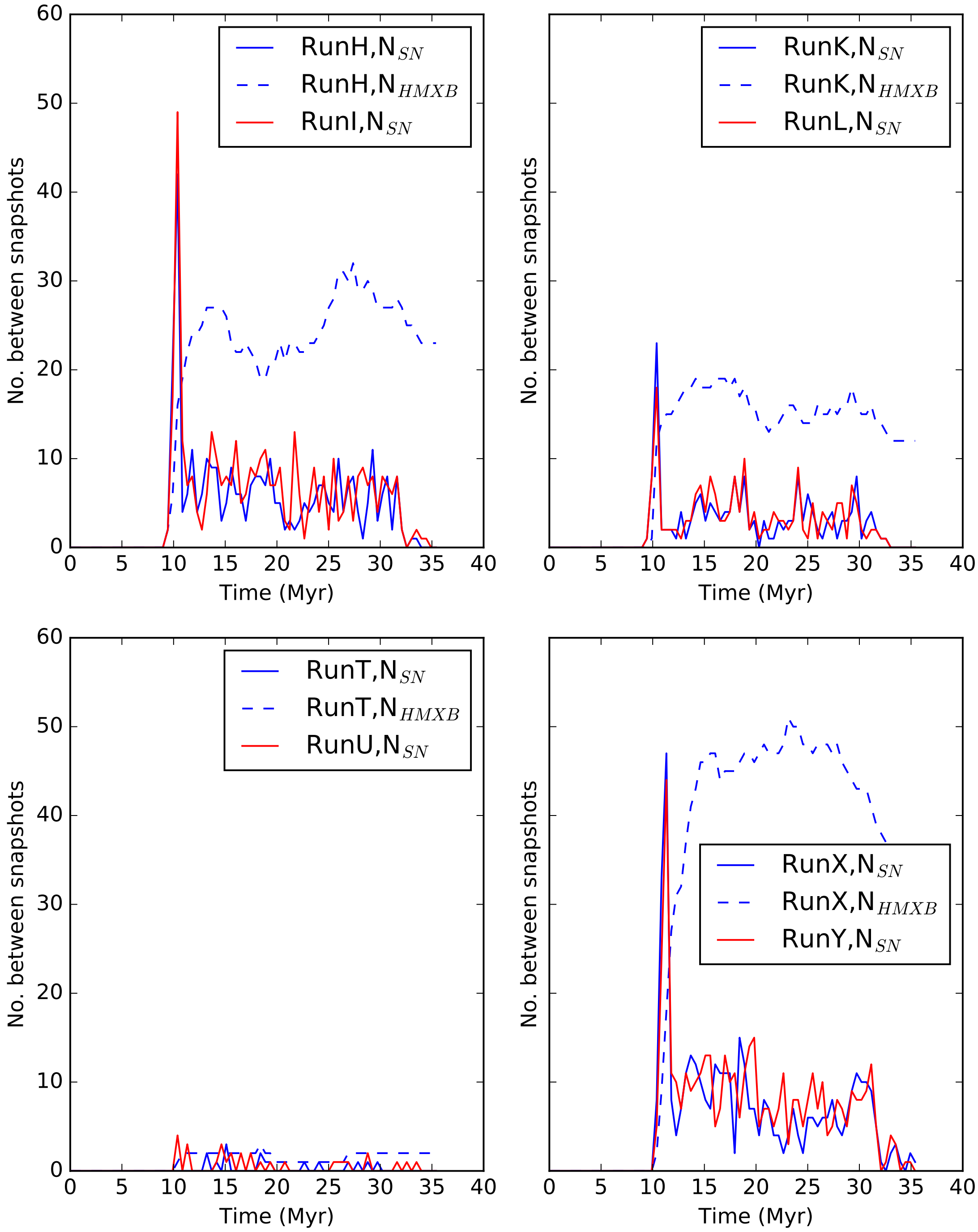

FIGURE 4.5: Plots to show the number of SNe (N_{SN}, solid lines) and HMXBs (N_{HMXB}, dashed lines) between snapshot times across simulations at [Fe/H] = -1.2.

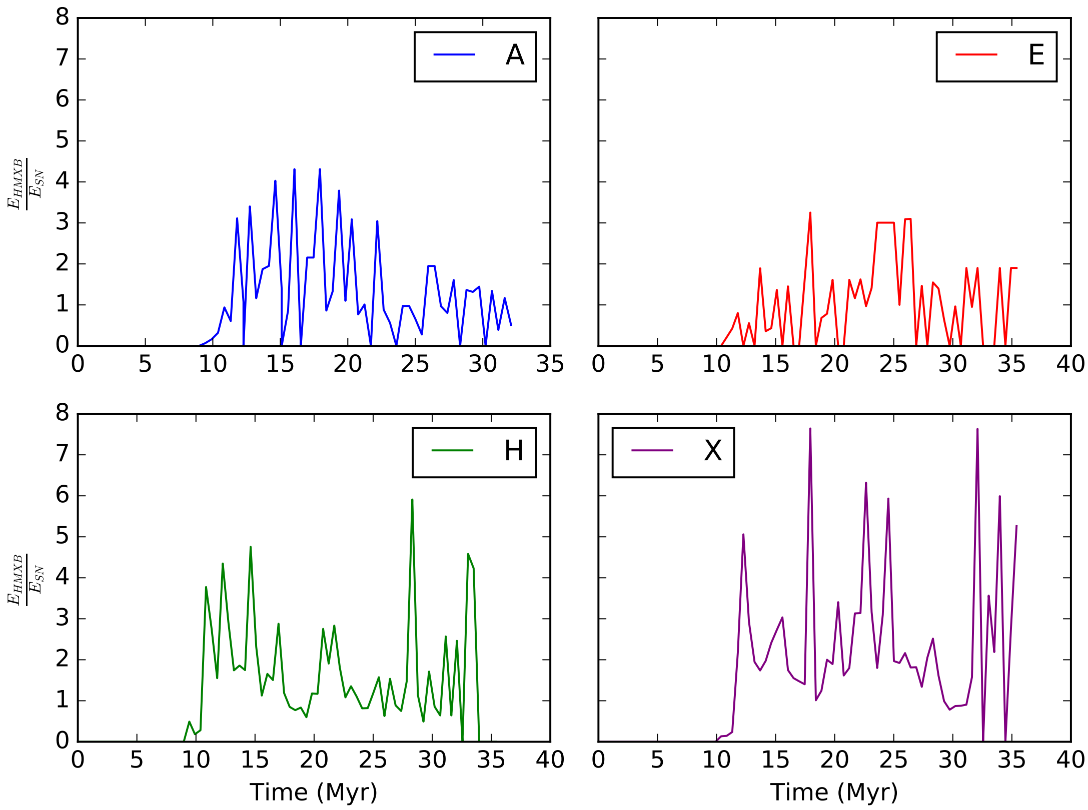

FIGURE 4.6: The time evolution of the ratio between the energy injected by HMXBs and the energy injected by SNe between snapshot times for Runs A (top left), E (top right), H (bottom left) and X (bottom right).

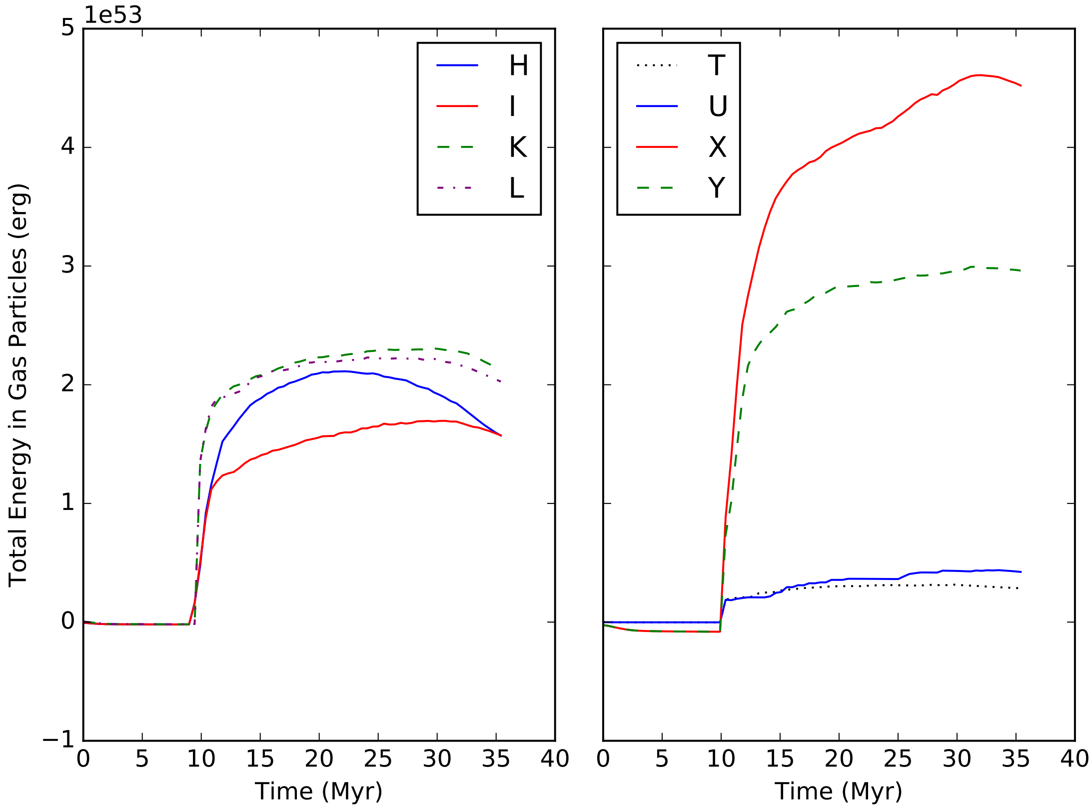

FIGURE 4.7: Plots to show the time evolution of the total energy of each run at a metallicity of [Fe/H] = -1.2

Looking at the total energy of the gas in Runs H and I, plotted in Fig. 4.7, we see between 10-35 Myr the total energy of Run H is greater than Run I, due to the higher amount of energy injected through feedback (see Fig. 4.4). However, at 35 Myr the total energies of the two simulations converge to the same value. This suggests the hot, feedback-heated gas has cooled faster in Run H.

Fig. 4.8 plots the fraction of the initial gas mass that has been unbound (left column) or formed sinks (right column). We can see there is marginal difference between these fractions for Runs H and I, with a slight increase in the sink mass fraction in Run I, with a corresponding decrease in the mass unbound. Since these fractions are so similar, we can rule out significant mass loss in Run H compared with Run I. Overall, the mass fraction in sink particles (which is also displayed in Tables 3.2 and 4.2) in Run H is much lower than for Run A. This is true of all the low metallicity runs and is down to inefficient cooling due to a relative lack of heavier ions (e.g. OII, OIII).

Fig. 4.9 plots the number of sinks produced between snapshots versus time. Similar to the solar metallicity runs, the majority of the sinks are formed around 10 Myr into the simulation (i.e. at the cloud's free-fall time). Comparing figures 4.9 and 3.5, we see the addition of feedback has not altered the sink particle formation time significantly in either Run H and Run I, compared with Run G (the Z=0.001 run without feedback).

Since the fate of these gas clouds appears to be decided 10-12 Myr into each simulation, I use Fig. 4.10 to plot the average cooling time and the average value of the ratio $R=\rho/\rho_{\mathrm{Jeans}}$ in three different temperature bins, all under 10^4 K, at 10 Myr. Only bound gas is included in these plots. From Fig. 4.10, we can see the average cooling time, predominantly through excitation of the fine structure levels of ions such as OI (Mo, Bosch, and White, 2010), is lower for Run I than Run H in each temperature bin. We can also see from Fig. 4.10, the ratio R is higher in Run I, indicating the lower temperature gas in Run I is denser than the corresponding gas in Run H, leading to the marginal increase in star formation efficiency in Run I seen in Fig. 4.9.

Overall, compared with Runs A and C, the overall effect of adding HMXB feedback on top of SNe feedback in Run H (compared with Run I) is far less pronounced. This is likely due to the larger numbers of both HMXBs and SNe seen in Table 4.2, which are in turn a result of the higher Jeans masses present at low metallicity and the resulting top-heavy sink particle mass distribution compared

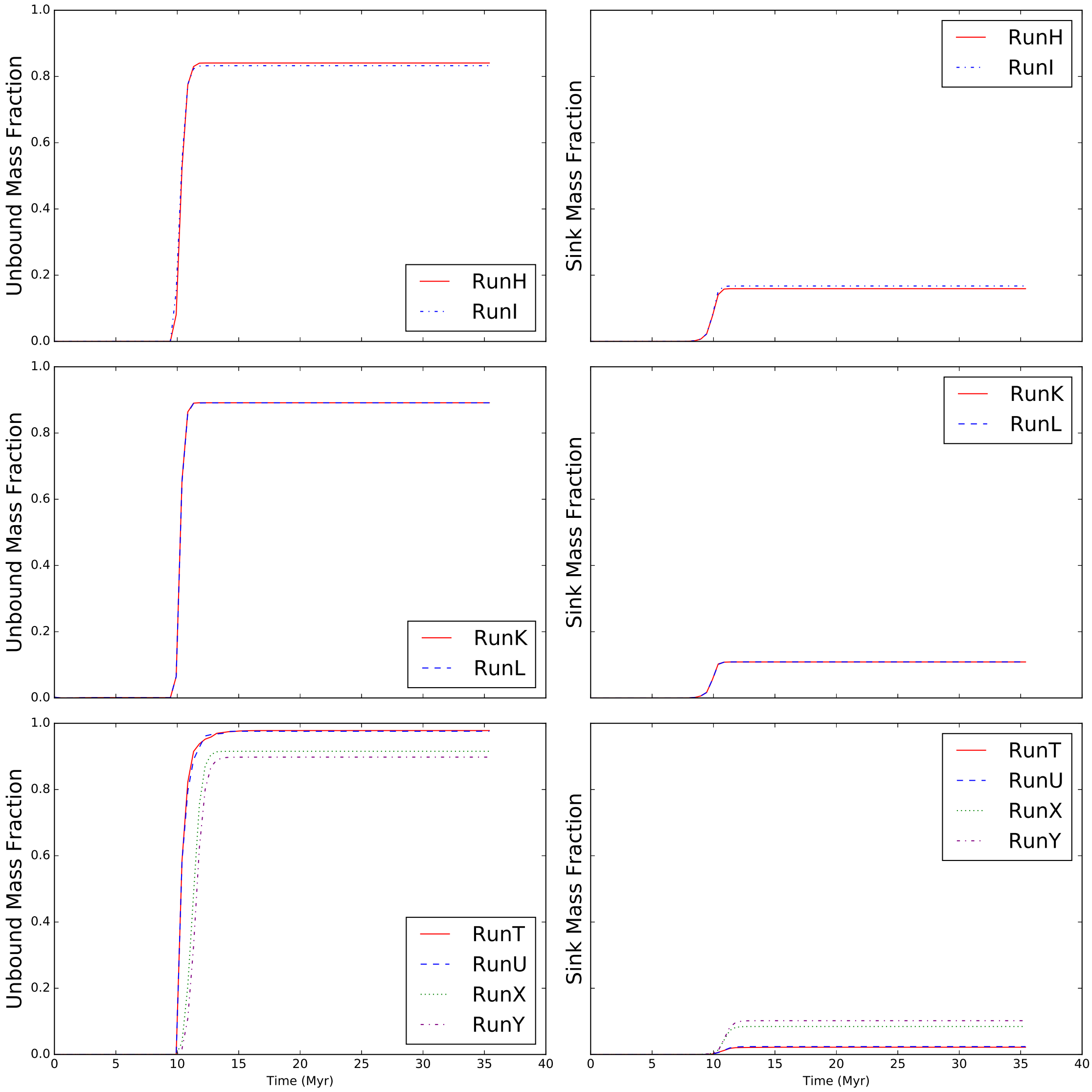

FIGURE 4.8: Plots to show the fraction of the initial gas mass in each [Fe/H] = -1.2 run that has (a) been unbound (left column) and (b) been accreted onto/ become sink particles (right column).

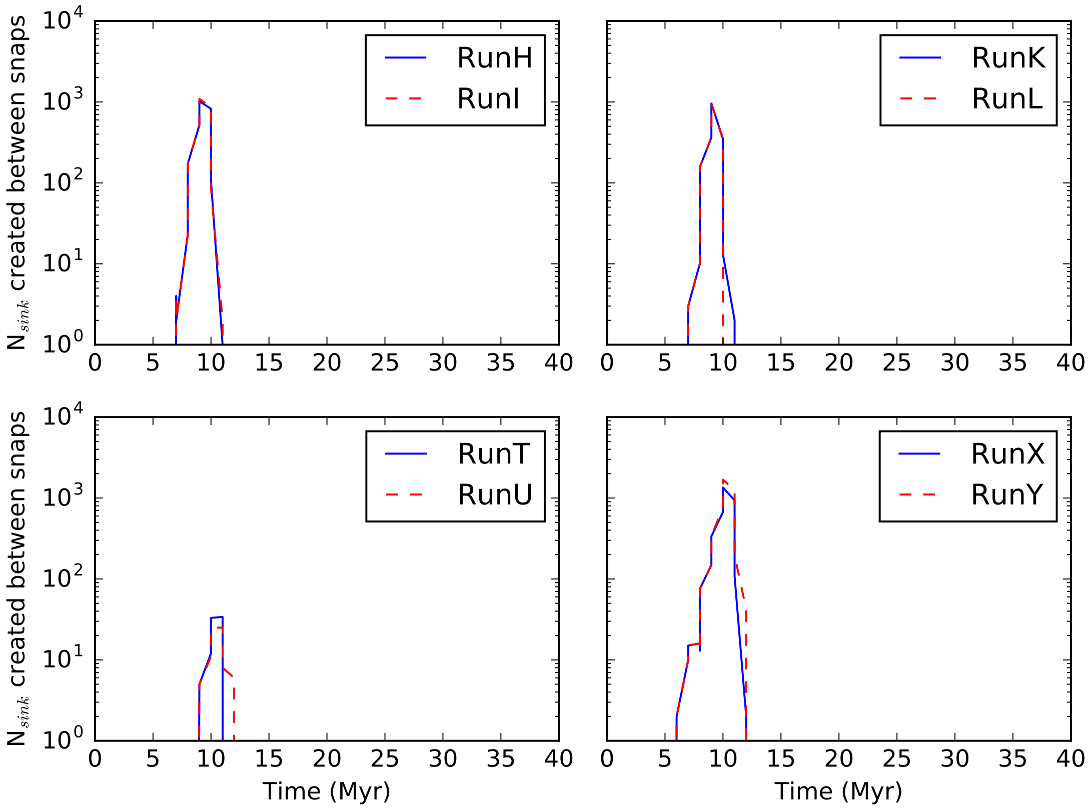

FIGURE 4.9: Plots to show the number of sink particles produced between snapshots for the runs at a metallicity of [Fe/H] = -1.2.

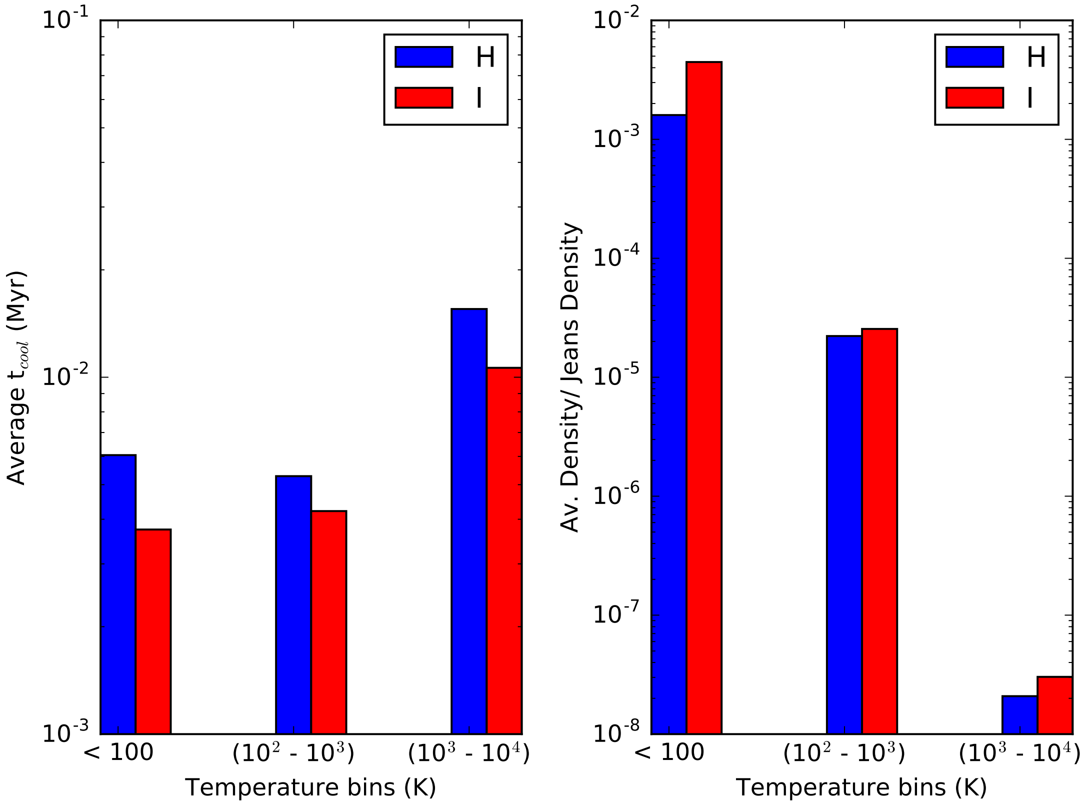

FIGURE 4.10: Left: plot to show the average cooling time in three different temperature bins (< 100 K, 100-10^3 K and 10^3-10^4 K) for runs H and I. Right: plot to show the ratio between the average density in the different temperature bins, divided by the corresponding Jeans density for the average temperature in that bin in runs H and I.

with solar metallicity. These additional HMXB and SNe events prevent the gas in the cloud from cooling and forming any more stars.

4.2.2 $\alpha_{\rm vir} = 1.2$ Runs: K (HMXB and SNe), L (SNe), M (no feedback)

Runs K ($\alpha_{\rm vir}$=1.2, with HMXB and SNe feedback) and L ($\alpha_{\rm vir} = 1.2$, with SNe feedback) show very similar density structures in Fig. 4.1, while there are no obvious chimneys present in Fig. 4.3. As seen in the corresponding temperature slices in Fig. 4.2 and again in Fig. 4.3, the temperature of Run K is marginally higher the Run L at three free-fall times, however very similar at 12 Myr and 24 Myr. This similarity in temperature has resulted in a similar total energy in Runs K and L (see Fig. 4.7). This contrasts with the large energy gap seen when $\alpha_{\rm vir} = 0.7$ (Runs H and I). Looking at Fig. 4.7, we see the total energy of cloud K is consistently higher than cloud L between 10-35 Myr.

Moreover, approximately the same mass of gas has been unbound/formed sinks in Runs K and L - Fig. 4.8. Comparing figures 3.5 and 4.9, we can see the duration of star formation has been shortened by the addition of feedback in Runs K and L (where Run M had the same initial conditions as K and L, with no feedback included). From Fig. 4.9, sink particle formation ceases at 10 Myr in Run L and 2 Myr later in Run K. Hence the addition of both HMXB and SNe feedback in the gas cloud has acted to increase the period of sink particle formation, compared with the purely SNe feedback case, similar to previous results (e.g. Runs A and C, along with V and W).

Fig. 4.4 shows the injected energy (top plot) of Run K is significantly higher than Run L, due to a similar number of SNe (middle plot) and around 10 HMXBs being active at any point in the simulation beyond 11 Myr (bottom plot). Furthermore, looking at Table 4.2, the number of HMXBs and SNe in Run K is just over half of the corresponding numbers in Run H. This difference in the number of feedback events is also evident in Fig. 4.4, which shows the cumulative injected energy of Run H is approximately twice that of Run K. However, Fig. 4.7 shows the total energy (of the gas) in Run H is lower than Run K. This is in part due to the fact Run H contains 5% more mass in sink particles, lowering the total energy of the gas in the system. Also, it indicates the gas in Run H is cooling more efficiently than the gas in Run K.

Overall, contrary to the results at solar metallicity, by increasing the virial parameter at low metallicity the star formation efficiency of the cloud has been decreased. This is likely to be due to inefficient cooling, which, given the higher initial energy of the gas particles, leads to less sink particle formation due to fewer gas particles meeting the required Jeans density criterion. The same result is seen when comparing Runs G and M in Fig. 3.5, where Run G(M) has the same initial conditions as Run E(K), only without feedback. In this figure, the mass fraction in sink particles is marginally less for Run M than Run G by the end of the simulation. Another important factor is the number of HMXBs and SNe - Run K contained fewer of each and, as we have seen previously, this can lead to a reduction in effectiveness of the SNe and HMXB at producing and utilising chimneys in the gas to funnel hot gas outwards, leading to a reduction in star formation.

4.2.3 Changing the gas cloud size: 5×10^5 $M_\odot$ – T, U, 5×10^6 $M_\odot$ – X, Y

Firstly, the density slices (Fig. 4.1) for the smaller molecular cloud (T - with HMXB feedback, U - just SNe feedback) follow a similar structure with or without HMXB feedback. Again, this suggests that it is the SNe feedback that determines the underlying density structure. The main difference is cloud U is slightly more spatially extended than Run T and contains more 10^{-24} gcm^{-3} density gas. Furthermore, from Fig. 4.2, the cloud containing HMXB feedback along with SNe feedback, Run T, has a higher global temperature of around 10^8 K within the central kpc, while the same region in Run U has a temperature of $\sim 10^7$ K.

The temperature slices for the larger molecular cloud (X – with HMXB feedback, Y – just SNe feedback) show a much greater contrast than those for the smaller cloud. Cloud X shows a much larger fraction of hot (10^8 K) gas, with a limb extending to the outer edge of the simulation. On the other hand, Run Y contains a single sphere of uniform 10^8 K gas extending to approximately 1 kpc.

Moreover, focusing on the density slices in Fig. 4.1; Run X is more spatially extended than Run Y and more rarefied in places. Run Y contains a more-or-less isotropic shell of higher ($\sim 10^{-24}$ gcm^{-3}) density gas, with a region of lower density in the centre.

Focusing on Fig. 4.7, we see the total energies for the smaller molecular clouds, T and U, are similar, with the cloud without HMXB feedback included finishing the simulation with a higher total energy. On the other hand, the larger molecular clouds, X and Y, show the opposite – the run which included HMXB feedback (X) has a much higher total energy than the cloud just including SNe feedback (Y).

Fig. 4.4 shows that the injected energy for Run T is initially lower at the beginning of feedback ($\sim$ 11 Myr), however ends the simulation a factor 2 higher than Run U. This difference in injected energy can be explained by Fig. 4.5, where 1-2 HMXBs are active at any one time in Run T, beyond 11 Myr. In contrast, Run X contains 30-50 active HMXBs between snapshots. As well as this, the injected energy in Run X is at least two orders of magnitude higher than Run Y, most likely due to the 65 HMXBs present in Run X (see Table 3.1).

The sheer amount of excess injected energy in Run X compared with Run Y has led to the increased unbound mass fraction seen in Fig. 4.8, coupled with a decrease in the sink particle mass fraction. On the other hand, both fractions are approximately the same in Runs T and U. As was seen for the smaller molecular cloud at solar metallicity, 90% of the gas in Runs T and U is unbound within the free-fall time of the cloud, due to the lower binding energies. As such, the addition of 1-2 extra HMXB events on top of the 16 SNe has made little difference to the star formation efficiency of the cloud.

Looking at Fig. 4.3 we can see tentative evidence for a chimney at 24 and 35 Myr in Run X. However, as has been seen previously, it only spans less then 1 order of magnitude in density and also appears beyond the free-fall time of the cloud, making it unlikely to influence star formation in the cloud.

Finally, comparing the numbers of sink particles formed between snapshots as a function of time in Fig. 4.9, we see the duration of star formation is largely unchanged between Runs Y and X, while Run T has a marginally smaller star formation period than Run U, however a larger peak in sink particle formation.

To conclude, while the a larger molecular cloud increases the efficiency of both SNe and HMXB feedback at increasing star formation duration and efficiency (compared with the purely SNe case) at solar metallicity, this is not the case at lower metallicity. Instead, the larger number of HMXBs present (due to larger sink particle masses) results in an order of magnitude jump in energy between the cloud that includes just SNe feedback (Y) and the cloud that includes both SNe and HMXBs (X). Although this number is highly stochastic, it is still likely the larger energy injection of both SNe and HMXB (due to the higher numbers of massive stars seen in Table 4.2) would wash out any effects of the combination of the two types of feedback, were the runs to be repeated with a different random seed for the binary population synthesis model. On the other hand, the smaller molecular clouds at low metallicity have the same pitfalls as the smaller ones at solar metallicity; the lower binding energies and smaller number of HMXBs make their effect negligible when compared with molecular clouds just containing SNe.

4.3 Resolution Tests

A number of resolution tests were run in order to test for convergence in the results of both Chapters 3 and 4. Initially, I varied the initial conditions of Run A between 3-12$\times 10^6$ particles whilst keeping the total gas mass 2×10^6 $M_\odot$ and found significant differences in the star formation efficiency and unbound gas fractions between resolutions. In order to ascertain the source of this disparity, I first explored whether or not the initial random turbulent velocity field was having a significant impact on the cloud's fate.

4.3.1 Nyquist Frequency

When I set up the initial turbulent velocity field, the minimum length scale corresponds to the maximum k value ($k_{\rm max}$), which is the Nyquist frequency and is set by the particle resolution of the simulation. In order to investigate whether it is the choice of $k_{\rm max}$ that is determining the results of each simulation, I ran 5 simulations, with 3,5,6,7 and 10 million particles respectively, each with a $k_{\rm max}$ value corresponding to the lowest resolution run (3×10^6 particles). The initial conditions were the same as Run A in each case (see Table 3.1). If our choice of Nyquist frequency were the determining factor in the results of Chapters 3 and 4, it would be expected that these simulations converge.

Figure 4.11 shows the density slice in the x-y plane, at z=0 and taken at the free-fall time of the cloud; 11.7 Myr, for each resolution. Low density chimneys can be seen in all runs, however, their spatial extent, location and number do not appear to significantly correlate between resolutions. This points to another factor determining the fate of each cloud. This can also be seen in the corresponding temperature slice (Fig. 4.12). However, the run containing 10^7 particles does show a significant increase in the amount of hot gas in the cloud, as well as an

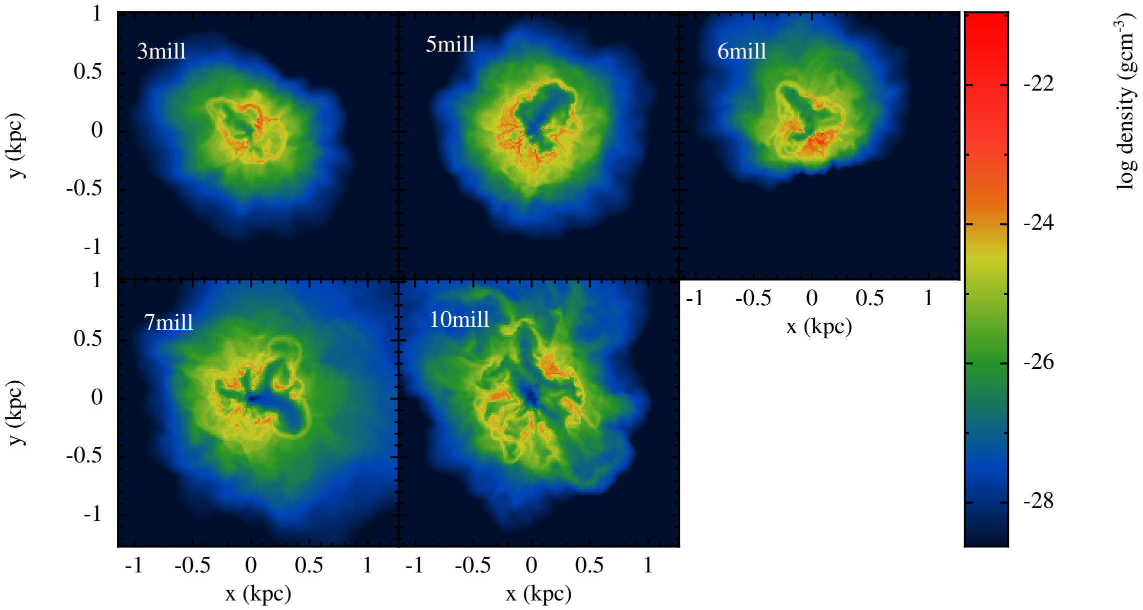

FIGURE 4.11: Plots to show z=0 slices in density, taken at the free-fall time (11.7 Myr) of a cloud with varying resolution (stated on each plot). The Nyquist frequency in each case is set by the value at the lowest resolution (3×10^6 particles).

increase in the spatial extent of the low density, hot gaseous chimneys/bubbles present; in Fig. 4.12 the lower right chimney can be seen to extend to 1 kpc.

In order to find the cause of the differences between each of these simulations, (despite a constant Nyquist frequency), I instead plotted the number of HMXBs active between snapshots in each simulation (Fig. 4.13), along with the amount of energy injected in each snapshot (Fig. 4.14). Fig. 4.13 shows the number of active HMXBs varies between resolutions, however there is no clear trend with increasing resolution. The same is true for the overall injected energy in Fig. 4.14. When the two plots are compared, it is apparent there are discrepancies between the number of HMXBs active and the amount of energy injected between snapshots. This is due to varying SNe numbers, as well as different HMXB lifetimes (and therefore rates of energy injection). Moreover, the origin of the large amount of hot gas seen in Fig. 4.12 can be seen in Fig. 4.14; the energy injected in this run is a factor of ~ 2 greater than the other runs at around the free-fall time, due to a large number of HMXBs being active across the simulation (see Fig. 4.13). The results of these simulations indicate the inherent stochasticity in HMXB feedback is the most significant factor in determining the clouds fate and also an obstacle when attempting to perform convergence tests. This stochasticity was introduced in

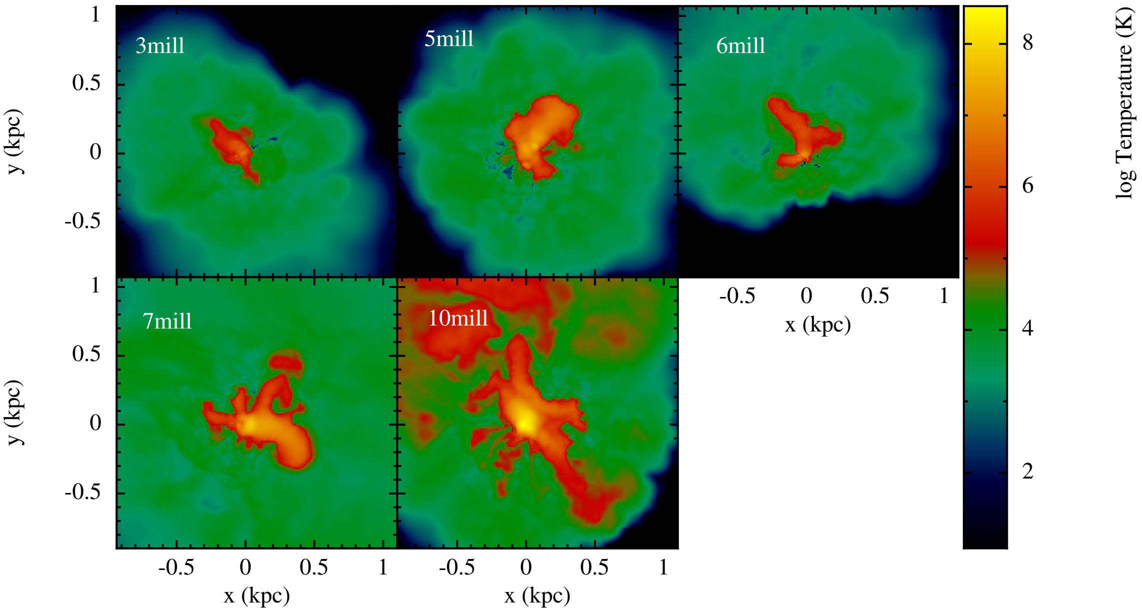

FIGURE 4.12: Plots to show z=0 slices in temperature, taken at the free-fall time (11.7 Myr) of a cloud with varying resolution (stated on each plot). The Nyquist frequency in each case is set by the value at the lowest resolution (3×10^6 particles).

these simulations, since by altering the realization of the turbulent velocity spectrum and hence the random velocities assigned to the gas particles in the initial conditions, the identities and locations of the gas particles that form sink particles were altered, along with their formation time, which in turn changed the random seeds utilised when assigning massive star properties (see section 3.4) between simulations.

In the next section (section 4.3.2) I avoid the stochasticity effects associated with Monte Carlo-type HMXB population synthesis method by inserting a predetermined population of binaries, with set lifetimes, energy injection rates and locations, into each simulation.

4.3.2 Convergence Testing

For simplicity, in order to ascertain numerical convergence, I set up a population of 20 sink particles at set locations inside each cloud (of total gas mass 2×10^6 $M_{\odot}$). The location of each sink particle was set throughout the simulation, along with the lifetime of both the primary and secondary. Each sink particle therefore underwent a SNe feedback event, a HMXB feedback phase, along with a second SNe event. This time I varied the resolution from $3 - 12 \times 10^6$ particles.

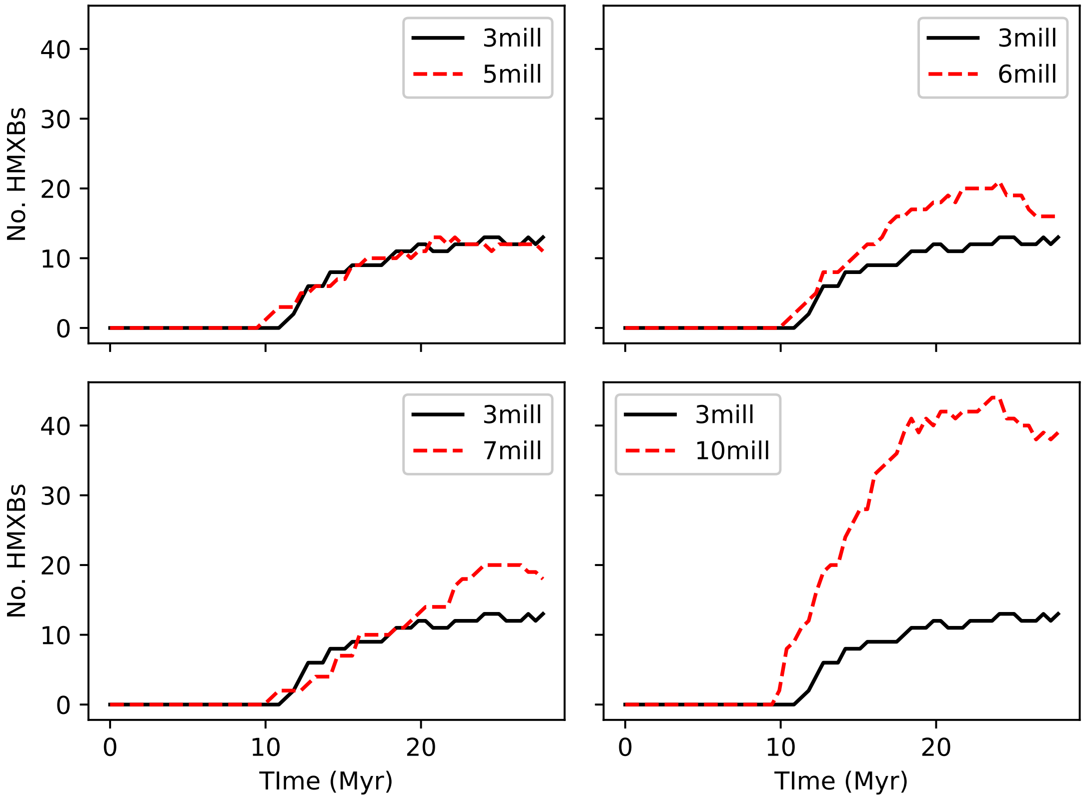

FIGURE 4.13: Plots to show the number of HMXBs active between snapshot times, for particle resolutions varying between 3-10 $\times$ 10^6. The lowest resolution run, 3 $\times$ 10^6 (labelled 3mill), is plotted in the black solid line on each plot for reference.

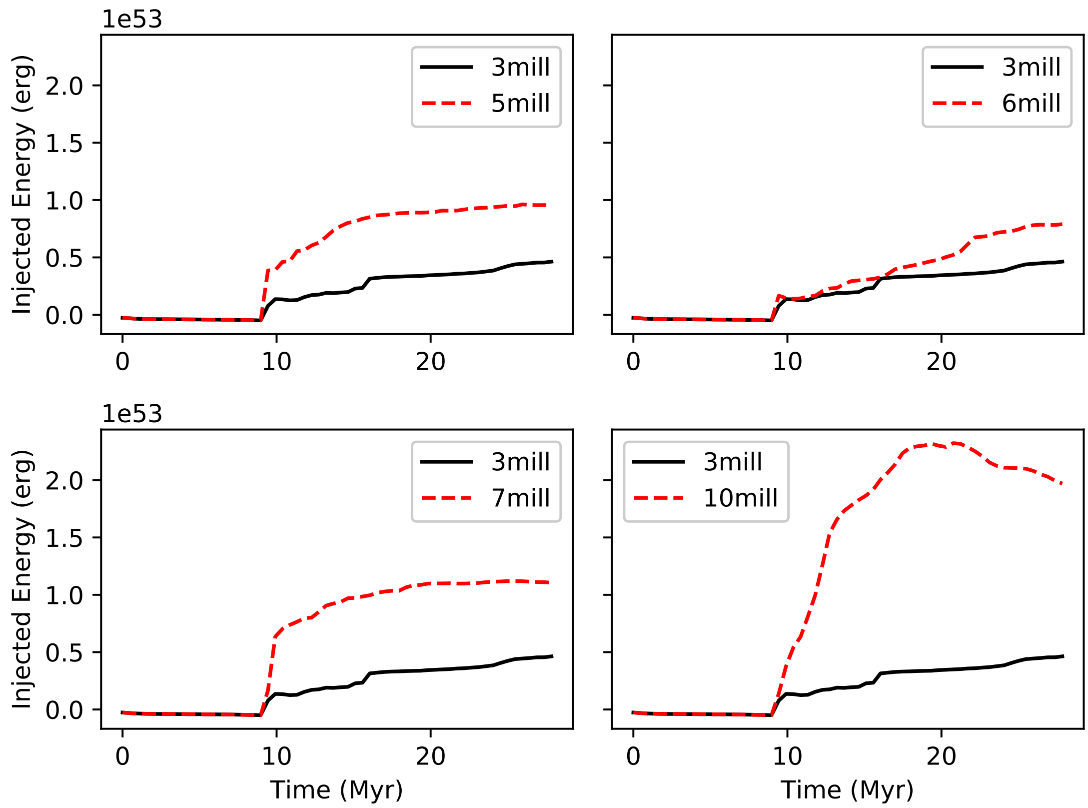

FIGURE 4.14: Plots to show the amount of feedback energy (SNe + HMXB) injected between snapshot times, for particle resolutions varying between 3-10 $\times$ 10^6. The lowest resolution run, 3 $\times$ 10^6 (labelled 3mill), is plotted in the black solid line on each plot for reference.

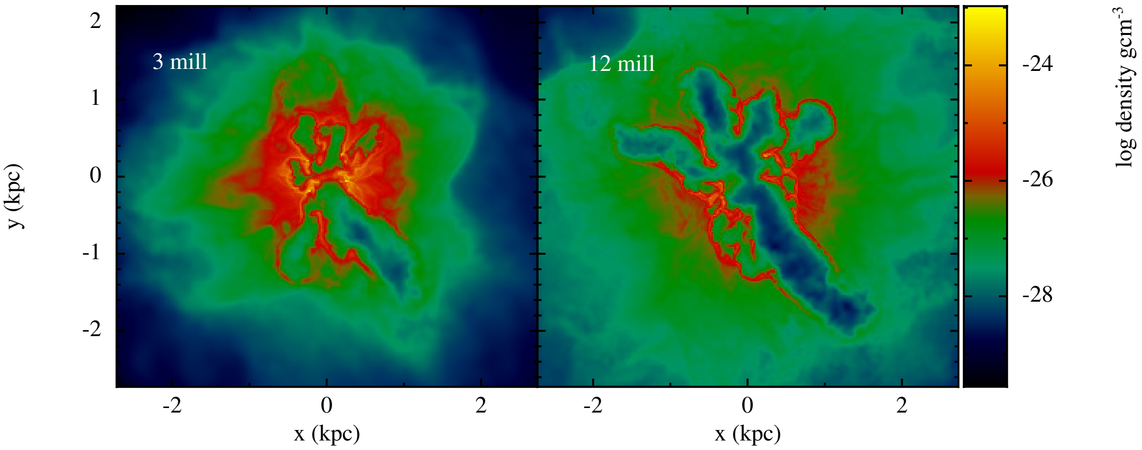

FIGURE 4.15: Density slices taken in the x-y plane at $z = 0$, showing the convergence tests of varying particle resolution (where the total cloud mass is kept the same and 3mill is 3×10^6 particles) at the free-fall time (11.7 Myr) of the cloud.

Figures 4.15 and 4.16 plot the density slices and temperature slices (taken in the $z = 0$ plane) of the lowest and highest resolution runs respectively. Comparing between 3×10^6 particles and 12×10^6 particles, both the temperature and density slices show a high level of agreement, particularly in the location and of the hot, low density chimneys. This agreement is in contrast to figures 4.11 and 4.12. Given the Nyquist frequency was altered according to the particle resolution in each case, this indicates the initial turbulent velocity field is playing a lesser role in the generation of chimneys and the ultimate fate of the gas in the cloud. The spatial extent of the chimneys appears to increase with resolution. This is explored in figures 4.17 and 4.18 below.

The top plots of Fig. 4.17 show the time evolution of the fraction of the initial gas mass that has been unbound in each simulation, minus the corresponding unbound mass fraction of the lowest resolution run (3 million particles). Moreover the bottom plots of Fig. 4.17 show the fraction of the gas that has been unbound and subsequently expelled from each simulation domain. It is clear the main difference between the lowest resolution run and the others is the time delay in the majority of the gas being unbound once feedback kicks in at 7.5 Myr. This is indicated by the peak in the top row plots of Fig. 4.17 at this time. It also appears the unbinding occurs faster in runs with higher resolution. However, beyond this time all runs show good agreement. Furthermore, the amount of gas that has been both unbound and ejected from the simulation (by reaching a radius of 5 kpc) increases with resolution. This is expected since the higher mass particles

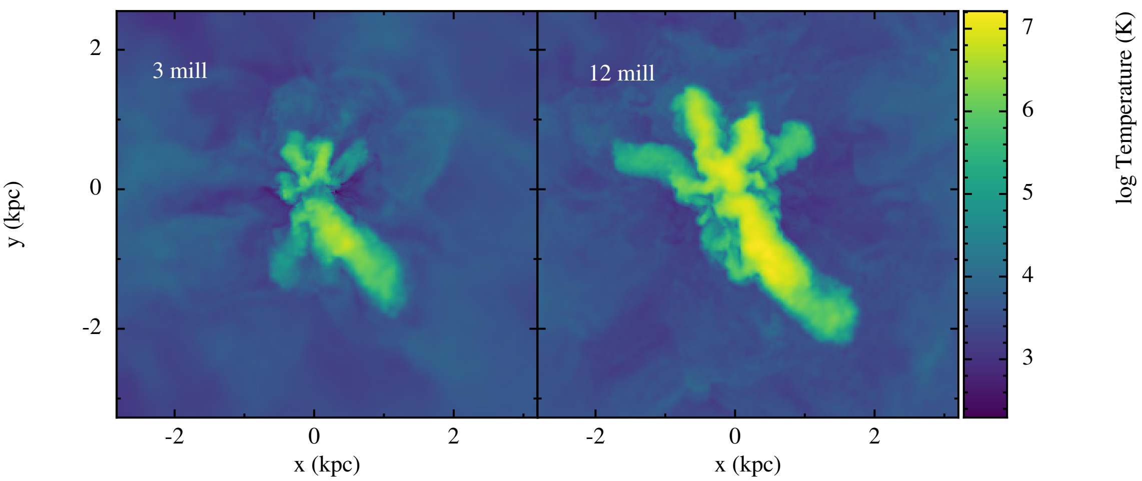

FIGURE 4.16: Temperature slices taken in the x-y plane at $z = 0$, showing the convergence tests of varying particle resolution (where the total cloud mass is kept the same and 3mill is 3×10^6 particles) at the free-fall time (11.7 Myr) of the cloud.

of the lower resolution runs will have lower velocities, arising from the fact the kinetic energy is not varying while the gas mass is. Overall, these plots indicate the agreement between the energetics of the gas (thermal, kinetic, potential) is in good agreement across varying resolution.

I also plot the temperature of the gas versus the density and render this according to particle number in Fig. 4.18. We see the bulk of the gas mass at each resolution is at $\sim 10^4$ K, ranging between $10^{-30} - 10^{-24}$ gcm^{-3}. However, there exists a low temperature (< 100 K), high density (10^{-22} gcm^{-3} tail in the lowest resolution run (3×10^6 particles), that does not exist in the run with the highest particle resolution (12×10^6 particles). This tail represents $> 1\%$ of the gas mass and indicates the higher resolution runs are marginally more effective at quenching star formation. Physically, the difference in the amount of high density, cool gas with resolution can be explained by the higher particle masses in the lower resolution run - which can form higher mass cold clumps that can effectively cool and hence are more resistant to heating than the lower mass clumps in the higher resolution runs.

Overall, the results suggest good agreement between different resolutions, down to the $\sim 1\%$ level (grouping all unbound gas together). I can therefore conclude the results runs are at a resolution that shows a good degree of numerical convergence with runs of higher (and lower) resolution, particularly in terms of the multiphase ISM (as is seen in Fig. 4.18).

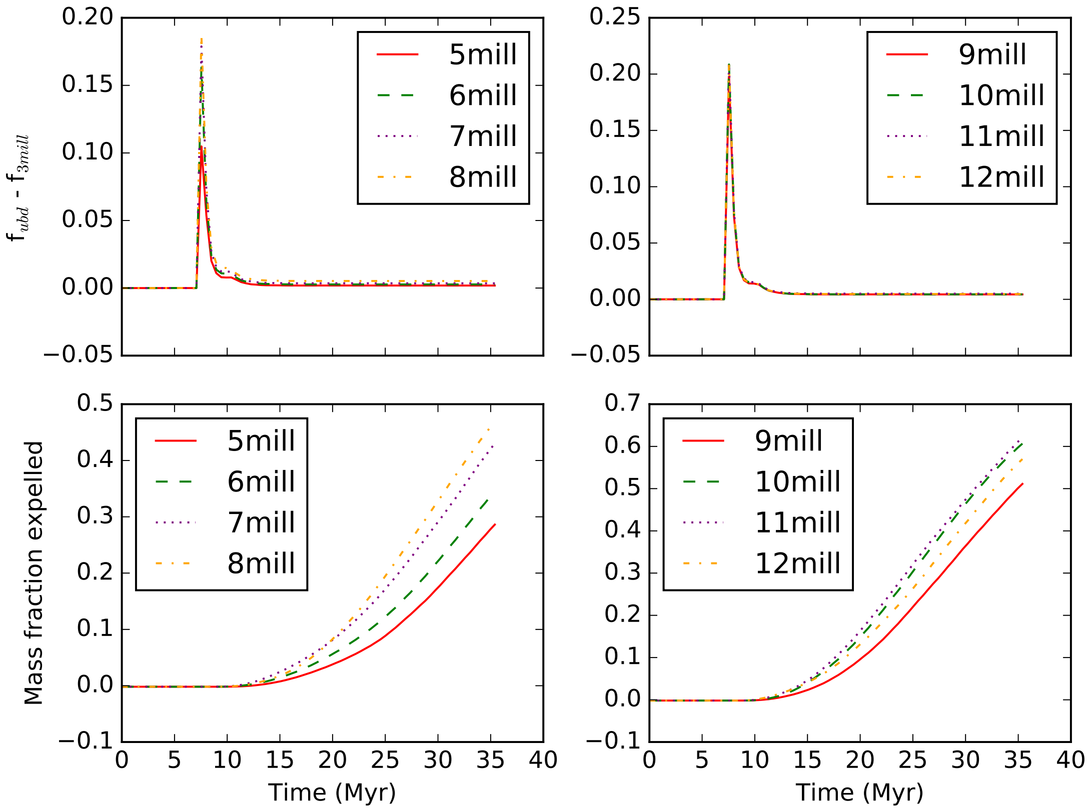

FIGURE 4.17: Top row - the time evolution of the fraction of the initial gas mass that is unbound (f_{Ubd}) in the convergence tests of varying resolution minus the unbound mass fraction of the lowest resolution run (f_{3mill}, 3 million particles). Bottom row - when gas particles are both unbound and reach a radius of 5 kpc, they are expelled from the simulation. This plot shows the fraction of the initial gas mass that has been expelled from each simulation. Here 3mill denotes 3×10^6 particles.

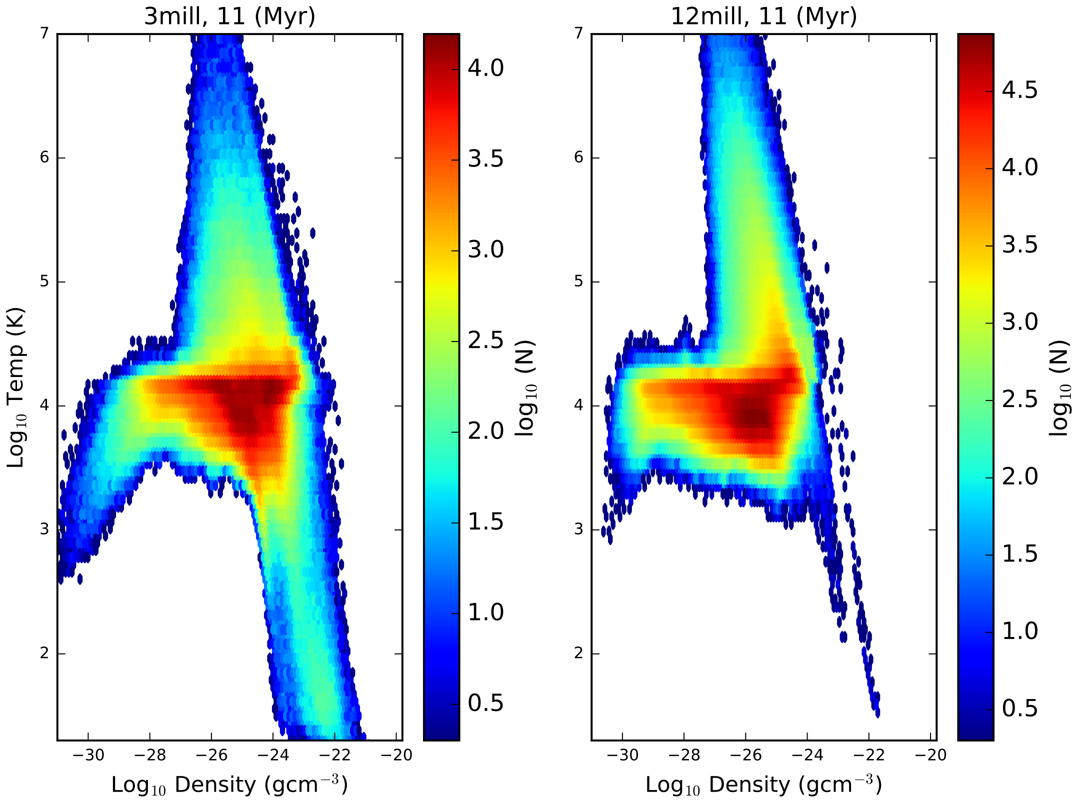

FIGURE 4.18: Plots to show temperature versus density, rendered according to particle number, at the free-fall time ($\sim$ 11 Myr) of clouds of varying resolution. Here 3mill denotes 3×10^6 particles.

4.4 Discussion

Similar to the results of the solar metallicity runs, the main factor in determining the number of stellar feedback events in these simulations was the average sink particle mass. Inefficient cooling led to higher Jeans masses and hence sink particle masses at [Fe/H] = -1.2, which resulted in a higher number of HMXB and SNe events.This meant that the differences between runs that include HMXB feedback and those that just include SNe feedback is far less pronounced in runs at low metallicity.

4.4.1 The results: chimneys

Justham and Schawinski (2012) explore the idea that the combination of SNe and XRB feedback produces 'chimneys' leading to an increase in the star formation efficiency. However, while they suggest XRBs might help create chimneys in the gas, which would help funnel subsequent SNe-heated gas, here it is the SNe feedback that helps evacuate the chimneys and HMXBs instead increase their efficiency. This result comes about because HMXB feedback begins after SNe feedback. This is set by the feedback scheme, which requires one SNe in the binary system before the HMXB feedback can begin. In reality there are a variety of XRB systems ranging from low to high mass and also a variety of lifetimes. Consequently, it is possible XRB feedback may be present before the first SNe and may alter the locations of the chimneys. Justham and Schawinski (2012) also discuss this, referencing the population of lower metallicity stellar mass black holes which have progenitor masses of > 40 $M_{\odot}$ and formed via direct collapse, without forming a SNe shock. Further, Eldridge and Tout (2004) find at a metallicity of 0.001 (the same as I use in the lower metallicity simulations), the transition between partial and direct collapse of black hole progenitors occurs at a lower value of ~ 35 $M_{\odot}$ (see figure 5 in Eldridge and Tout, 2004).

Therefore it is possible that HMXBs can precede the first supernovae, allowing HMXB feedback to significantly alter the gas cloud before SNe feedback kicks in. In order to quantify whether ignoring this population has affected the results, particularly those at low metallicity (where the number of HMXBs was very high) I found the time of the first SNe with a progenitor with an initial mass greater than 35 $M_{\odot}$ contained in an HMXB (hereafter I'll refer to these as SNegt35) in Runs H and X, as well as the times of the first SNe in the simulation, along with the number of SNe events prior to the first SNegt35 event. For run H the first SNe is at 7.6 Myr and the first SNegt35 is at 9.2 Myr, which occurs after 24 further SNe. As such, during Run H, the SNegt35 events would be unable to affect the ISM prior to SNe. However, 25% of the HMXBs in Run H contain a primary with an initial mass greater than 35 Myr. Therefore, these systems represent a significant fraction of the HMXBs operating in Run H and in future work this could be factored in when considering the number of SNe. Moreover, 20% of the HMXBs in Run X contain a $> 35\mathrm{M}_{\odot}$ primary star, however 22 SNe occur before the first SNegt35 event, mirroring the results of Run H.

The idea of SNe feedback carving chimneys (or channels) in the surrounding gas has been studied in the literature over the past twenty years (e.g. De Young and Gallagher III, 1990; Mac Low and Ferrara, 1999). In particular, recent work by Iffrig and Hennebelle (2015) looked at the effect of SNe in turbulent molecular clouds, finding the hot SNe-heated gas was able to escape through low density channels and subsequently form superbubbles. Moreover, work by Martizzi, Faucher-Giguère, and Quataert (2015) and Kim and Ostriker (2015) also look at the interaction of a single SNe in an inhomogeneous medium, focusing on the use of low density channels at smaller scales. Furthermore, Kimm et al. (2015) hypothesise the use of low density channels by SNe heated gas may be crucial in modeling star formation in galaxies. On the other hand, other papers focus on the interaction of stellar winds and SNe feedback and the subsequent formation of chimneys in molecular clouds; Rogers and Pittard (2013) find stellar winds help to remove gas from low density channels, through which hot gas can escape and potentially globally affect the host galaxy. Other works which include chimneys are; Rosen et al. (2014) Fierlinger et al. (2015) and Ibáñez-Mejía et al. (2016).

Additionally, the fact that the mean sink masses in the simulations are higher at low metallicity (see Table 4.2) is consistent with other investigations in the literature. For example, Jappsen et al. (2005) and Bonnell, Clarke, and Bate (2006) both reference the drop in Jeans mass (and therefore greater fragmentation) seen with lowering the temperature of the gas through additional cooling. Since star formation is not resolved in these simulations, I cannot say the top-heavy fragmentation I see in the lower metallicity runs occurs down to small scales, however numerous papers have found massive stars tend to form in isolation at lower metallicity (or higher redshift equivalently); for example Abel, Bryan, and Norman (2002), Bromm, Coppi, and Larson (2002), OShea and Norman (2007) and

Yoshida, Omukai, and Hernquist (2007).

Finally, the hot gaseous chimneys seen in the results could have implications during Re-ionisation; by increasing the UV photon escape fraction from regions of star formation. At $z>6$, the contribution of ionizing photons from stars is thought to outweigh that from quasars (e.g. Madau, Haardt, and Rees, 1999; Fan et al., 2002; Srbinovsky and Wyithe, 2007). There is a possibility the kpc-scale chimneys seen in this thesis could act to enhance the UV photon escape fraction by providing low density 'holes' in the ISM. This would lower the star formation efficiency required to reionize the intergalactic medium at high redshift. The enhancement in escape fraction could be investigated further by including the ionizing photons produced by the stellar population and post-processing the simulations using a radiative transfer model, however this is beyond the scope of this thesis.

Chapter 5

Investigating stellar feedback in dSphs

5.1 Introduction

During this chapter I focus on stellar feedback in dwarf spheroidal galaxies (or dSphs) and in particular its ability to drive gaseous outflows. As we saw in section 1.3.2, the dwarf galaxies of the Milky Way have a wide range of metallicities, luminosities, stellar populations and hence star formation histories (e.g. Tolstoy, Hill, and Tosi, 2009; McConnachie, 2012). The shallow potential wells of dwarf galaxies means they can be significantly influenced by a number of external factors, for example; ram pressure stripping, cosmic re-ionisation and tidal effects (e.g Gatto et al., 2013; Emerick et al., 2016; Sawala et al., 2016; Zhu et al., 2016; Simpson et al., 2017). Moreover, stellar feedback events such as SNe feedback are thought to drive hot, metal-enriched gas from dwarf galaxies, as evidenced by a high abundance of metals in the IGM (Schaye et al., 2003), along with observations of 'superbubbles' of hot, diffuse gas in star forming dwarf galaxies (e.g. Ott, Walter, and Brinks, 2005).

The dwarf galaxies I am investigating here are of relatively low density (the peak density in the canonical simulations is $\sim 10^6$ $M_\odot$ kpc^{-3}), which results in longer cooling timescales and increases the efficiency of heating from shocked stellar winds and SNe. These two processes are expected to dominate over other stellar feedback processes in the creation of galactic-scale gaseous outflows (Hopkins, Quataert, and Murray, 2012).

My choice to simulate individual isolated galaxies over a cosmological box simulation was due to the requirement to resolve individual massive stellar feedback events. Cosmological simulations have the benefit of being able to track galaxy formation from the initial formation of dark matter haloes, while also taking into account merger events and the influence of a galaxy's environment on its evolution. However, the resolution in these large-scale simulations is such that stellar feedback is modelled as the integrated output of whole stellar populations, encompassing multiple SNe events. This means details of the smaller-scale physics are lost. For example, in their recent paper, (Su et al., 2017) argue modelling SNe as discrete events in time and space is pivotal to capturing the multi-phase ISM, galactic winds and reasonable stellar masses in dwarf galaxies.

This work follows on from work in Cashmore et al. (2017), where the authors conducted a similar set of simulations of isolated dwarf galaxies and concluded dwarf galaxies would require an unusual set of properties in order to sustain star formation beyond a 1 Gyr starburst, if SNe feedback was included. I aim to investigate whether the inclusion of 'gradual' feedback mechanisms alters this result. Previous work by Artale, Tissera, and Pellizza (2015) concluded the addition of HMXB feedback on top of SNe feedback led to an decrease in the star formation rate of low mass galaxies ($< 10^{10}$ $M_{\odot}$), however an increase in overall star formation efficiency. This result was also hypothesised by Justham and Schawinski (2012), who concluded X-ray Binaries have the capacity to warm the ISM without unbinding it, leading to further star formation at later times.

As we saw in Chapter 3, the mechanical luminosity of XRB systems have gained interest over the last 10 years due to observations such as Gallo et al. (2005), which found the kinetic power of the jets associated with Cygnus X-1 is comparable to its X-ray luminosity. This was further evidenced by observations of the relativistic jets associated with SS433, which point to a mechanical luminosity of $> 10^{39}$ erg/s (e.g. Blundell, 2001; Mirabel et al., 2011; Goodall, Alouani-Bibi, and Blundell, 2011).

This work is novel in that it will not only include a stellar wind feedback phase and a SNe phase for individual massive stars, but also a HMXB phase and a second SNe (where a HMXB is also considered present). In order to investigate the combined effect of 'gradual' and 'instant' feedback, I have conducted very high resolution simulations of individual dwarf galaxies; this enables me to resolve the effects of single massive stellar feedback events. Previous work has found the action of stellar winds on the surrounding ISM prior to a SNe can reduce the coupling between the SNe energy and the ISM (e.g. Rogers and Pittard, 2013). I aim to investigate the impact of including gradual feedback on the ability of a star-forming dwarf galaxy to retain gas to fuel later episodes of star formation.

5.2 Numerical Model

As in the previous chapters I use GADGET-3, a modified version of the hybrid N-body/ SPH code GADGET-2 (Springel, 2005). I use the SPHS method (Read and Hayfield, 2012) in order to help model mixing of feedback-generated multiphase gas. Furthermore, I use a Wendland-2 kernel with 100 neighbours for the gas (Wendland, 1995; Dehnen and Aly, 2012), coupled with an ideal equation of state. This is governed by the relationship: $P = (\gamma - 1)\rho u$ (where P is the gas pressure, γ is the adiabatic constant, set to 5/3 in the simulations, u is gas internal energy and ρ is particle density). The gas particles have both an adaptive smoothing and softening length, with a minimum softening length of 0.1 pc. I also model cooling down to 10^4K using look-up tables generated using MAPPINGS III (Sutherland and Dopita, 1993), based on the metallicity of each simulation. Below 10^4K I use the method outlined in Mashchenko, Wadsley, and Couchman (2008) in order to model the fine-structure metal line cooling of the metal ions in the gas. For further details on the cooling implementation see Section 2.4. For the runs at primordial metallicity I take an [Fe/H] value of -6 (corresponding to 10^{-6} times solar).

In general I use a gas particle mass resolution of 9 $M_\odot$. In order to model the dark matter halo of the galaxy I used 10^5 N-body particles. For the canonical runs, this means a mass resolution of 1100 $M_\odot$ for the dark matter. These have a set softening length of 10 pc (approximately based on $R_{200}/N^{0.5}$, where R_{200} is the virial radius of the halo and N_{200} is the number of dark matter particles within R_{200} - which I take to be the full 10^5). I verify the choice of softening length is not a defining factor in the results in section 5.5.4. Furthermore, I include stellar populations containing massive stars as star particles within the simulation. These have a fixed softening length of 0.1 pc, corresponding to the minimum softening length of the SPH particles. A sink particle is included at the centre of the galaxy. This repositions on the point of minimum potential within its 100 neighbours and is included to remove gas particles with prohibitively small timesteps by accreting any particles within 0.5 pc, that are also gravitationally bound to the sink particle.

I also include the sink particle formation criterion that was used in the previous chapters, which sets the Jeans mass of the gas particle as the minimum resolvable mass, which in SPH is $2\times N_{neigh} m_p$ (Bate and Burkert, 1997). In order to form a sink particle, gas particles must have a density greater than

$$\rho_\mathrm{J} = \left(\frac{\pi k_\mathrm{B} T}{G\mu m_\mathrm{H}}\right)^3 \frac{1}{(2N_\mathrm{neigh} m_\mathrm{p})^2} \tag{5.1}$$

where k_B is the Boltzmann constant, μ is the mean molecular weight and m_H is the mass of Hydrogen. I also require that the gas must be converging (i.e. $\nabla \cdot \mathbf{v} < 0$) and that the temperature of the gas particle must be $< 500\,\mathrm{K}$ (in order to ensure high temperature and high density gas particles are not considered star forming). I set the mean molecular weight in equation 5.1 to 1.24 in all simulations (note this is not the case when calculating the cooling rates, where μ is calculated self-consistently based on the electron fraction). I do not have the mass resolution to follow star formation in the simulations, however this sink criterion exists to remove high density SPH particle with prohibitively small timesteps.

5.3 Initial Conditions

The initial conditions are summarised in Table 5.1. I chose the initial conditions of this chapter to represent z$\sim$ 6 progenitors of the classical dwarf spheroidal satellite galaxies of the Milky Way. At this point the galaxies are massive enough to support cooling predominately via atomic and molecular Hydrogen (given the virial temperatures of 6000 K and 1600 K for the largest and smallest haloes respectively) (e.g. Glover, 2005; Moore et al., 2006; Power et al., 2014) and the majority of the gas has had time to cool and virialise. Current day halo masses range from 10^{8-9} $\mathrm{M}_\odot$ (e.g. Walker, Mateo, and Olszewski, 2007). Depending on their merger tree, from Power et al. (2014) I expect the 10^8 $\mathrm{M}_\odot$ redshift 0 halos to have a mass of $\sim 1.5\times 10^7$ $\mathrm{M}_\odot$ at z=6 and the 10^9 $\mathrm{M}_\odot$ (z=0) haloes to have a mass of 1.1×10^8 $\mathrm{M}_\odot$ at z=6. I set up each halo according to a Hernquist density profile (Hernquist, 1990), with the virial radius (r_{200}) set according to

$$r_{200} = \left(\frac{M_{200} G}{100 H^2}\right)^{\frac{1}{3}} \tag{5.2}$$

TABLE 5.1: A table summarising the initial conditions of the simulations run in this chapter. The columns listed are: name of run, dark matter halo mass M_{dm}, dark matter halo concentration parameter c, the virial radius of the dark matter halo (r_{200}), gas metallicity, given as [Fe/H] (the $\log_{10}$ of the ratio between the metal content of the galaxy compared with that of our sun), the standard deviation in the 'wake-up' times of the star particles (σ_{star}) and finally the types of feedback included.

Run	M_{dm} (10^7 $M_\odot$)	c	r_{200} (kpc)	[Fe/H]	σ_{star} (Gyr)	Feedback Included
1	11.0	3.54	7.78	-6	0.13	SNe, HMXBs, Winds
2	11.0	3.54	7.78	-6	0.13	SNe
3	11.0	7.08	7.78	-6	0.13	SNe, HMXBs, Winds
4	11.0	7.08	7.78	-6	0.13	SNe
5	1.5	3.68	4.04	-6	0.13	SNe, HMXBs, Winds
6	1.5	3.68	4.04	-6	0.13	SNe
7	11.0	3.54	7.78	-1.2	0.13	SNe, HMXBs, Winds
8	11.0	3.54	7.78	-1.2	0.13	SNe
9	11.0	3.54	7.78	-6	0.06	SNe, HMXBs, Winds
10	11.0	3.54	7.78	-6	0.06	SNe
NoHMXB	11.0	3.54	7.78	-6	0.13	SNe, Winds
NoWinds	11.0	3.54	7.78	-6	0.13	SNe, HMXBs

where M_{200} is the virial halo mass (which I set accordingly) and H is the Hubble constant. I based the concentration parameters on equation 20 of Correa et al. (2015), which is a fitting function for halo mass which is dependent on just redshift and halo mass. The function was fit using WMAP5 cosmology and is valid for $z > 4$, at all halo masses. Using this fitting function, I obtained concentrations of 3.54 and 3.68 for halo masses of 1.1×10^8 $M_\odot$ and 1.5×10^7 $M_\odot$ respectively. I also performed a simulation with double the halo concentration for the halo of mass 1.1×10^8 $M_\odot$, in order to investigate the effect this has on the results.

As discussed in the introduction, the SFH (star formation history), primarily obtained using synthetic colour magnitude diagrams (CMDs) (see review by Tolstoy, Hill, and Tosi, 2009), varies widely between dwarf spheroidal galaxies. This means there is likely to be a variation in the level of metal enrichment in the galaxies, dependent largely on the number of massive stars that have left the main sequence up until this point. I investigate the effect of altering the metallicity, Z, of the gas in the galaxy by varying it between two values: [Fe/H] = -6 and [Fe/H] = -1.2. This alteration in metallicity will manifest as a difference in the cooling rate of the gas, along with a difference in the lifetimes of the massive stars; which in turn will alter the duration of stellar wind feedback and HMXB feedback. I do not follow metal enrichment in the simulations, however this is something I would like to implement in future simulations.

Furthermore, I assume the baryons in the galaxy correspond to the 0.16 baryon fraction of the universe (Planck Collaboration et al., 2014). I further assume the gas follows the same underlying density profile of the dark matter. The temperature of the gas in the centre of the halo is set as virial, with a gradual drop at larger radii in accordance with Komatsu and Seljak (2001). I insert 100 star particles into each simulation, each representing a stellar population containing one massive star in a binary system (this assumption is based on the high multiplicity seen in papers such as Sana et al., 2013). The mass of each star particle is set to 30 $M_{\odot}$ and they are placed at random positions consistent with a stellar bulge that follows a Hernquist density profile with a scale radius of 0.1 times that of the halo. In this way the stellar population of the galaxy contributes to $< 0.02\%$ of the total galaxy mass and is included purely to represent the locations of massive star feedback events within the galaxy.

I allowed the initial conditions to relax for 1 Gyr and I also ran a set of simulations with no feedback included in order to ascertain the changes in the baryons and dark matter we see in this thesis are due to stellar feedback. I show the results of these in section 5.5.2.

5.3.1 Massive Star Population

The properties of the massive stars are set at the beginning of each simulation, using the Monte-Carlo approach summarised in 3.2. I will briefly summarise this method here. Each star particle is assumed to host at least one massive star. The mass of this star is sampled from a Kroupa IMF between 8 $M_{\odot}$ – 100 $M_{\odot}$ (based on the progenitors of Type-II SNe). Beyond this, the star is given a probability of 0.14 of becoming a HMXB. This number is based on Tables 3.2 and 4.2 and is based on a flat mass distribution of binary mass ratios (Sana et al., 2013), along with a survival criterion dependent on whether or not the binary system maintains more than half its mass during the SNe of the primary star. If the primary star is considered to be in a HMXB system, the secondary mass is sampled using the same method as the primary star.

Both primary and secondary stars were assigned lifetimes according to look-up tables based on their mass and metallicity. As in Chapter 4, the [Fe/H] = -1.2 runs used Table 46 from Schaller et al. (1992). For the runs at primordial metallicity, I used Table 2 from Ekström et al. (2008). In both cases I added the lifetimes of the Hydrogen and Helium burning phases in order to estimate the total stellar lifetime.

5.4 Feedback Prescriptions

I assigned 'wakeup' times for each star particle, based on a Gaussian distribution of set standard deviation, or σ_{star}, with a mean set to 0.5 Gyr. The majority of the simulations were run with σ_{star} equal to 0.13 Gyr (see Table 3.1). However a subset were also run with a σ_{star} equal to 0.06 Gyr. The smaller the value of σ_{star}, the shorter and more violent the starburst (given the energy injected across the starburst is the same). Once the simulation has progressed to a star particle's 'wakeup' time, the star particle will initialise stellar wind feedback.

I implement the shock-heating from stellar winds as a thermal energy injection into the 100 SPH neighbours of each star particle, at constant power and across multiple timesteps until the end of the lifetime of the primary star. The energy injected into an individual SPH particle is kernel-weighted, while the total internal energy injected by a star particle is determined by a set power 10^{35} erg/s and is proportional to its timestep. I chose this power input based on a wind velocity of 1000 km/s (Leitherer, Robert, and Drissen, 1992) and a mass outflow rate of 10^{-6} $M_{\odot}$/yr (Repolust, Puls, and Herrero, 2004).

Once the lifetime of the primary star has been reached, the star particle then undergoes SNe feedback and injects 10^{51} erg of thermal energy into its surrounding 100 neighbours in one time-step. Beyond this, if the massive star has been determined to be part of a HMXB, the particle then undergoes HMXB feedback, which lasts the lifetime of the companion star. If not, the star particle ceases all feedback. HMXB feedback is implemented as an internal energy injection of set power; 10^{36} erg/s. I chose this power based on estimations of the power output of the wind-fed jet in Cygnus X-1, which is between 10^{35} to 10^{37} erg/s. This value is conservative when considering the estimated power output of SS433, which is considered to be a ULX on its side and outputs $\sim 10^{39}$ erg/s into the ISM.

At the end of the companion lifetime the star particle will then undergo one more SNe feedback event and feedback will cease for this particle. A limitation to the method is that I do not investigate the anisotropy of the jet feedback associated with HMXBs - which is dependent on the jet precession, power and the density of the surrounding ISM (e.g. Goodall, Alouani-Bibi, and Blundell, 2011). In future it would be of interest to compare and contrast wind feedback and HMXB feedback by including this anisotropy as an additional variable.

In order to avoid spurious effects associated with stars beyond the outer radii of the gaseous halo attempting to heat SPH particles that are well beyond their radius of influence, I choose to ignore stellar feedback for particles beyond the virial radius of the cloud. This only affects 6 star particles across each simulation.

5.5 Results

5.5.1 The massive star population of each galaxy

In Fig. 5.1 I plot the primary and companion stellar masses (top and bottom plot respectively) assigned to the star particles for all simulations. As expected from the IMF, the vast majority of the stars have a primary mass of ~ 10 $M_{\odot}$, while the secondary stellar masses are clustered between 9-10 $M_{\odot}$. These stars were then assigned metallicity-dependent lifetimes, along with wake-up times (which in turn were dependent on the standard deviation used for the underlying Gaussian profile).

In figure 5.2 I plot the lifetimes of both the primary and companion stars in all simulations, along with the wake-up times of the star particles in simulations with either σ_{star} (0.13 Gyr) and $0.5\sigma_{star}$ (0.06 Gyr). By increasing the metallicity of the gas in the galaxy, the assigned primary lifetimes have increased in range from ~ 22 Myr to 30 Myr. Additionally the companion lifetimes have also increased from ~ 21 Myr to ~ 30 Myr. This will mean more energy will be deposited into the ISM of the lower metallicity galaxies across the lifetime of the HMXB phase and the stellar winds phase. Moreover, the delay time until the onset of SNe feedback will be greater.

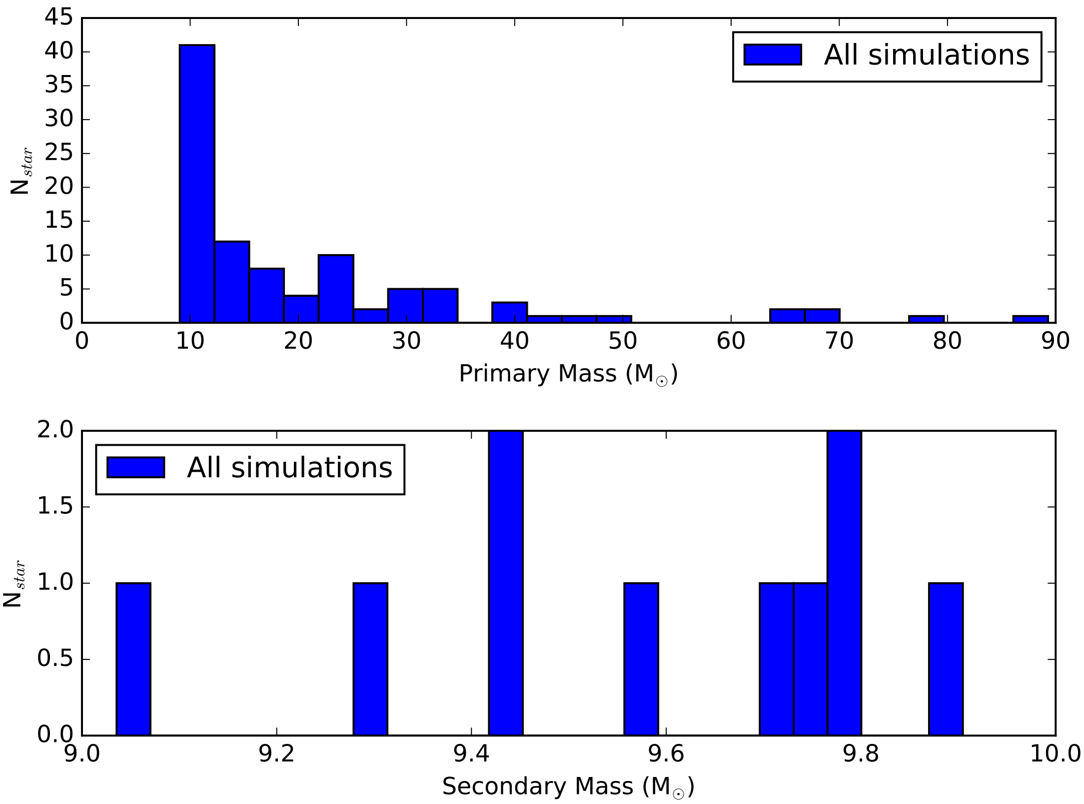

FIGURE 5.1: Top plot - the masses of the primary stars in the 100 binary systems contained in each simulation. Bottom plot - the corresponding masses of the companion stars in HMXB systems.

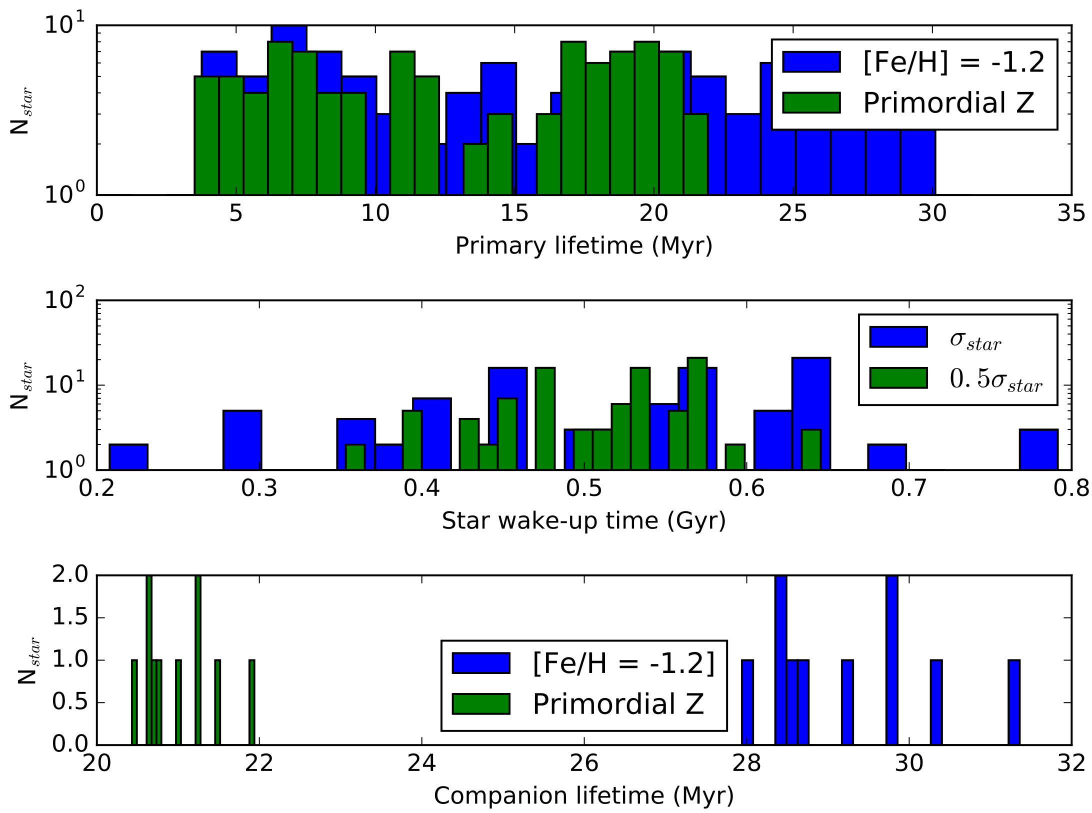

FIGURE 5.2: Upper plot - histograms to show the distribution of assigned primary star lifetimes for the stellar population, either at primordial metallicity (green) or [Fe/H] = -1.2 (blue). Middle plot - the wake-up times assigned to star particles, set using a Gaussian with a standard deviation of either σ_{star} or 0.5 σ_{star}. Bottom plot - a histogram to show the distribution of assigned companion star lifetimes.

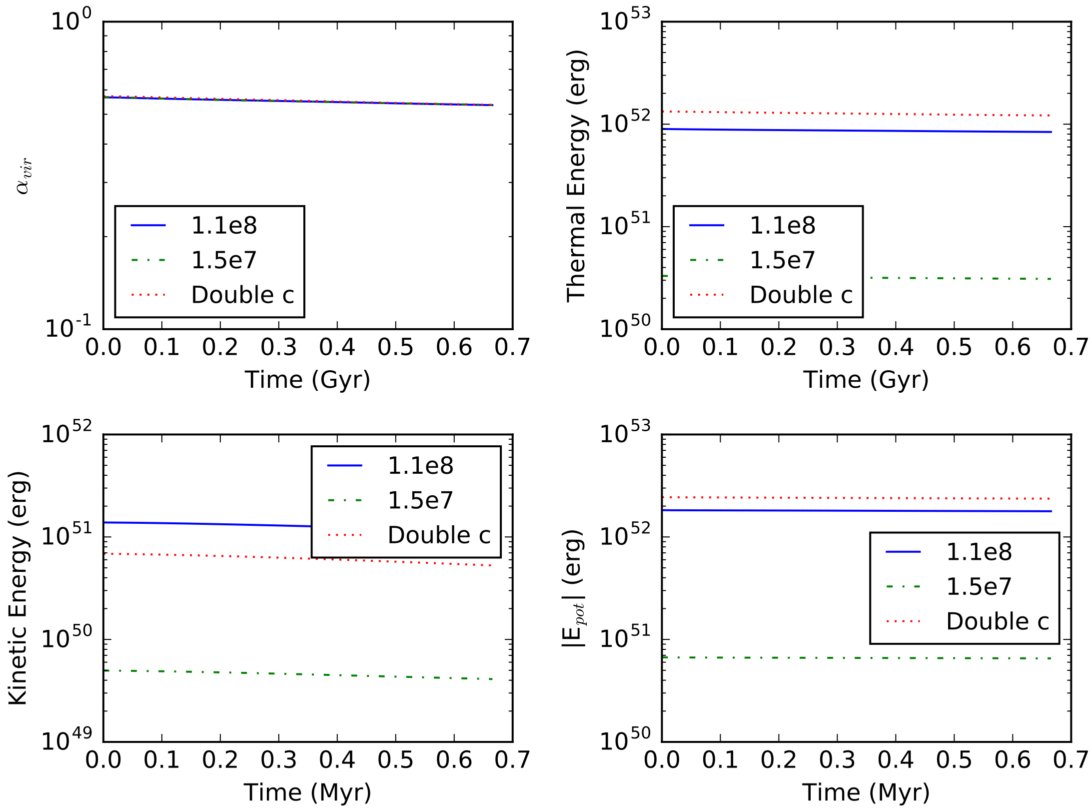

FIGURE 5.3: The time evolution of the virial parameter (evaluated as α_{vir} = E_{kin} + E_{therm} / $|E_{pot}|$), along with the total thermal, kinetic and potential energy of the gas in simulations which do not include feedback.

5.5.2 Simulations with no stellar feedback included

In order to check the changes associated with the gas and the dark matter we see in the results are entirely the result of stellar feedback, I ran three simulations with the initial conditions of Runs 1 (labelled 1.1e8), 3 (labelled Double c) and 5 (labelled 1.5e7), however with no feedback included.

In Fig. 5.3 I plot the time evolution of the energetics of the gas, finding this is unchanging in all three simulations, indicating the gas is in a steady state. Furthermore, the virial parameter is consistently at 0.5, indicating all three systems are virialised.

I also check the density profile of the gas (Fig. 5.4) and dark matter (Fig. 5.5) in all three simulations. I find both are in good agreement across all times, however the gas density profile does show noise at the lowest density end (where there are $\sim 10^2$ particles per kpc^{-3}). This noise is more apparent in the smallest halo

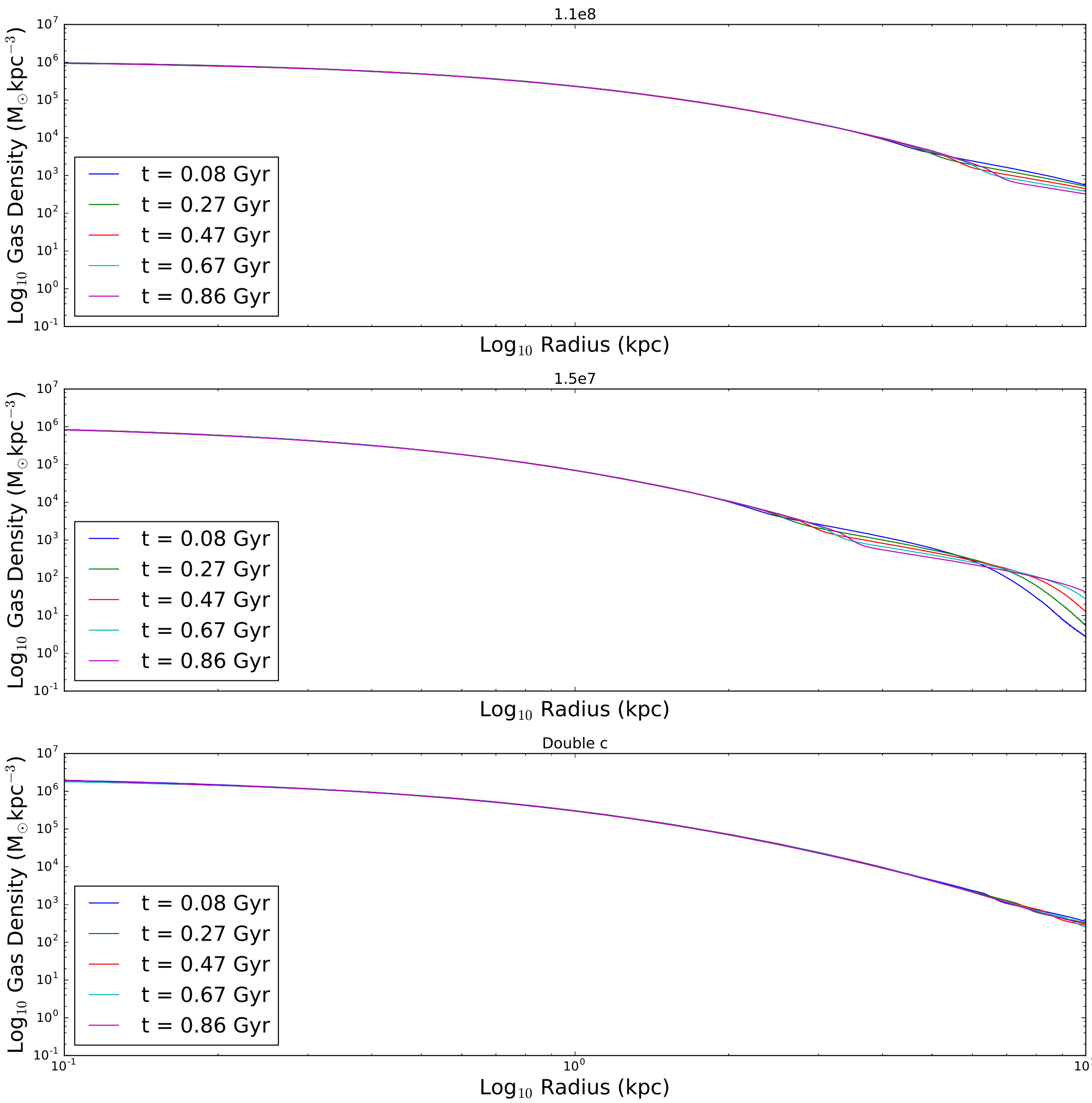

FIGURE 5.4: The gas density profile at varying times in simulations without feedback included.

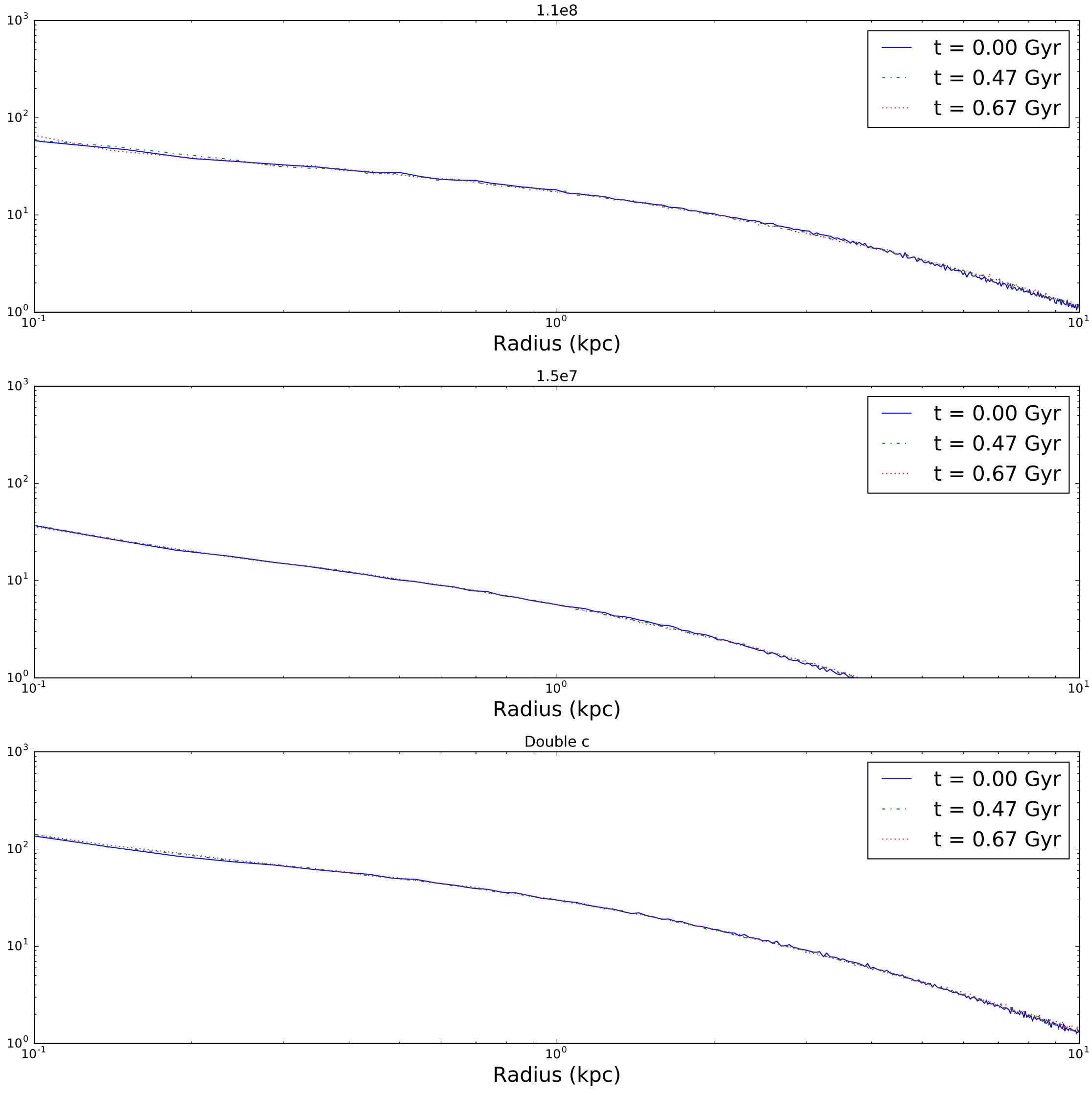

FIGURE 5.5: The dark matter density profile at varying times in simulations without feedback included.

(labelled 1.5e7), however insignificant in the halo with the largest concentration parameter (labelled Double c).

5.5.3 Gradual versus instantaneous feedback (Runs 1 and 2)

In this section I compare the effects of including just instantaneous feedback (SNe, Run 2) or a combination of gradual (HMXB and stellar winds) and instantaneous stellar feedback (Run 1) during a Gyr starburst in a 1.1×10^8 $M_\odot$ primordial metallicity dwarf galaxy. In figure 5.6 I compare the gas density profiles of Runs 1 and 2. It is clear the central kpc of the galaxy in Run 2 has been efficiently cleared of gas by 1 Gyr, however gas has survived down to a radius of a few tens of parsec in Run 1, although with a ~ 2 orders of magnitude drop from the initial central gas density. Furthermore, there is evidence for inflowing gas in both runs, given the density profile for both runs at 1 Gyr extends down to a smaller radius than the corresponding profiles taken at 0.86 Gyr.

I explore this idea in Fig. 5.7 which plots the mass inflow and outflow at various radii, evaluated at snapshot times across Runs 1 and 2. The mass inflow into the central kpc of the galaxy is consistently higher in Run 1, however drops off in both runs beyond 500 Myr, despite mass continuing to outflow beyond this time (see top right plot of Fig. 5.7). Furthermore, the mass inflow and mass outflow at 1 kpc is comparable between $\sim$ 200 - 400 Myr in Run 1, indicating the energy injected into the gas in the centre of the galaxy is being efficiently lost to radiative cooling, resulting in re-accretion of the gas. However, a peak in the mass outflow rate at $\sim$ 250 Myr during Run 2, resulting in the mass outflow rate being ~ 3 times the inflow rate, indicates the cooling is less efficient when gradual feedback is ignored. The mass inflow at 5 kpc and 10 kpc initiates at $\sim$ 450 Myr, indicating a significant mass fraction of the gaseous halo has expanded beyond these radii by this time in both Runs 1 and 2. Furthermore, mass is continuing to inflow into a radius of 5 kpc at the end of both simulations. The mass inflow rate is higher than the mass outflow rate at a radius of 10 kpc between $\sim$ 450 Myr to 700 Myr in both simulations, indicating efficient cooling of the gas at this radii. In general, the mass inflow rate is higher at all radii in Run 1 than Run 2.

On the other hand, at a radius of 1 kpc, the mass outflow rate of Run 1 is generally larger than Run 2 beyond $\sim$ 450 Myr (despite a higher inflow rate). This is most likely due to the lower gas mass towards the centre of the galaxy in

Run 2 (as indicated by the density drop in Fig. 5.6). Indeed, in Fig. 5.8 I plot the total gas mass below each radii (10 kpc, 5 kpc and 1 kpc) for Runs 1 and 2. As expected from the higher mass inflow rate, coupled with the density profile of Fig. 5.6, the gas mass below each radii is higher in Run 1. Moreover, the total gas mass inside the inner 1 kpc of Run 2 drops to 10^3 $M_\odot$ at a time of 650 Myr, compared to 10^4 $M_\odot$ for Run 1. Additionally, the positive trend in the total gas mass inside 1 kpc towards the end of the both Runs 1 and 2 indicates mass inflow that was not captured in Fig. 5.7 and hints at further cooling and collapse of the remaining gas at the centre of the halo, a process which is more efficient in Run 1 than Run 2. Therefore, by including gradual feedback, more cool, dense gas has been retained at the centre of the halo, which could fuel more star formation.

However, the bottom right plot of Fig. 5.8 shows the total gas mass within 5 and 10 kpc is decreasing beyond ~ 550 Myr and 650 Myr respectively, indicating a global outflow of gas. This is further evidenced by the high mass outflow rates (comparative to the inflow rates) seen at these radii in both Runs 1 and 2. This is expected since the energy injection of 100 SNe - 10^{53} erg - is greater than the total binding energy of the dwarf galaxy ($\sim 10^{52}$ erg). The mass outflow rate inside Run 2 is larger than inside Run 1 between ~ 400 - 600 Myr at a radius of 5 kpc and between 600 - 900 Myr at a radius of 10 kpc, indicating a persistent large-scale outflow of gas. However, the mass outflow rates of Runs 1 and 2 have converged at 5 and 10 kpc by the end of each simulation.

As well as this, the top plot of Fig. 5.9 plots the fraction of unbound mass in both Runs 1 and 2. We can see, despite less energy being injected across the simulation, Run 2 has a consistently higher mass fraction of unbound gas throughout the Gyr starburst. By the end of the simulation, including gradual feedback has lowered the unbound mass fraction by 8 %. Moreover, in Fig. 5.10 I plot the virial parameters ($\alpha_{vir} = E_{therm} + E_{kin}/|E_{pot}|$) of both simulations, along with the total kinetic, thermal and potential energies of the gas. We can see Run 2 has a higher total thermal and kinetic energy throughout the starburst compared with Run 1, which results in a higher global virial parameter. These plots indicate the gas in Run 1 is able to cool more efficiently than the gas in Run 2.

In figure 5.11 I plot the mass contained in 20 temperature bins between $10 - 10^{5.5}$ K for Runs 1 and 2. From this plot we can see a general trend of higher gas mass at temperatures $\lesssim 10^{3.5}$ K for Run 1 when compared with Run 2, along with a lower gas mass at 'warm' temperatures above 10^4 K. Moreover, beyond

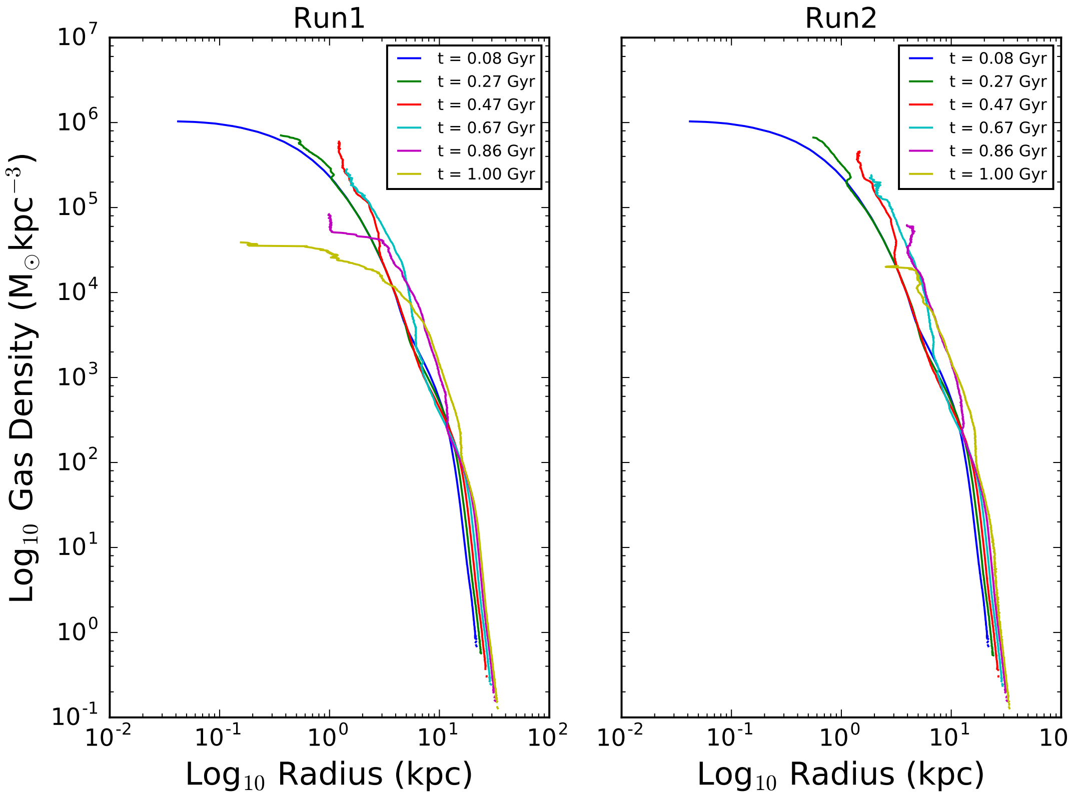

FIGURE 5.6: The density profile for the gas at varying times across the the simulation for Runs 1 (left) and 2 (right). Run 1 includes stellar winds and HMXB feedback on top of SNe feedback, while Run 2 just includes SNe feedback.

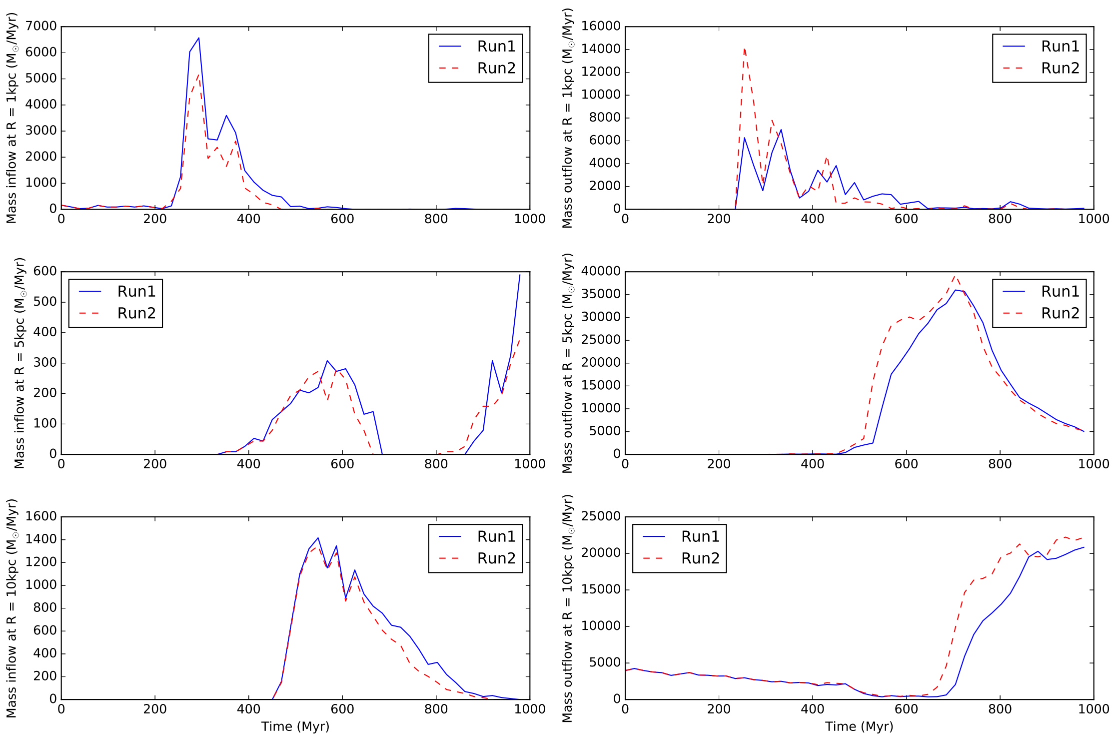

FIGURE 5.7: Left column - the mass inflow rate of bound gas at radii of 1, 5 and 10 kpc, evaluated at snapshot times across Run 1 (blue, solid lines) and Run 2 (red, dashed lines). Right column - the mass outflow rate of unbound gas, evaluated at 1, 5 and 10 kpc at snapshot times for Runs 1 (again, blue solid lines) and 2 (red,dashed lines).

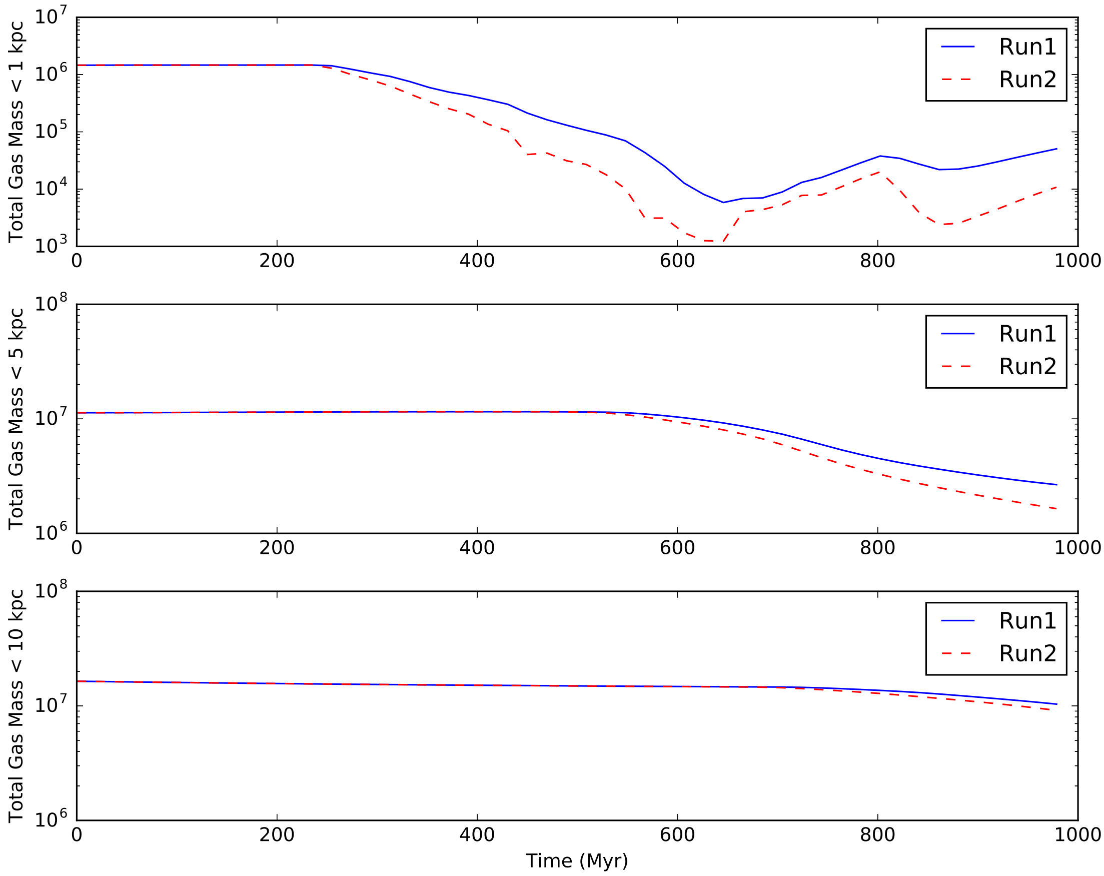

FIGURE 5.8: The total mass contained within a radius of 1 kpc (top plot), 5 kpc (middle) and 10 kpc (bottom) in Runs 1 (blue, solid line) and 2 (red, dashed line), at various times across the simulation.

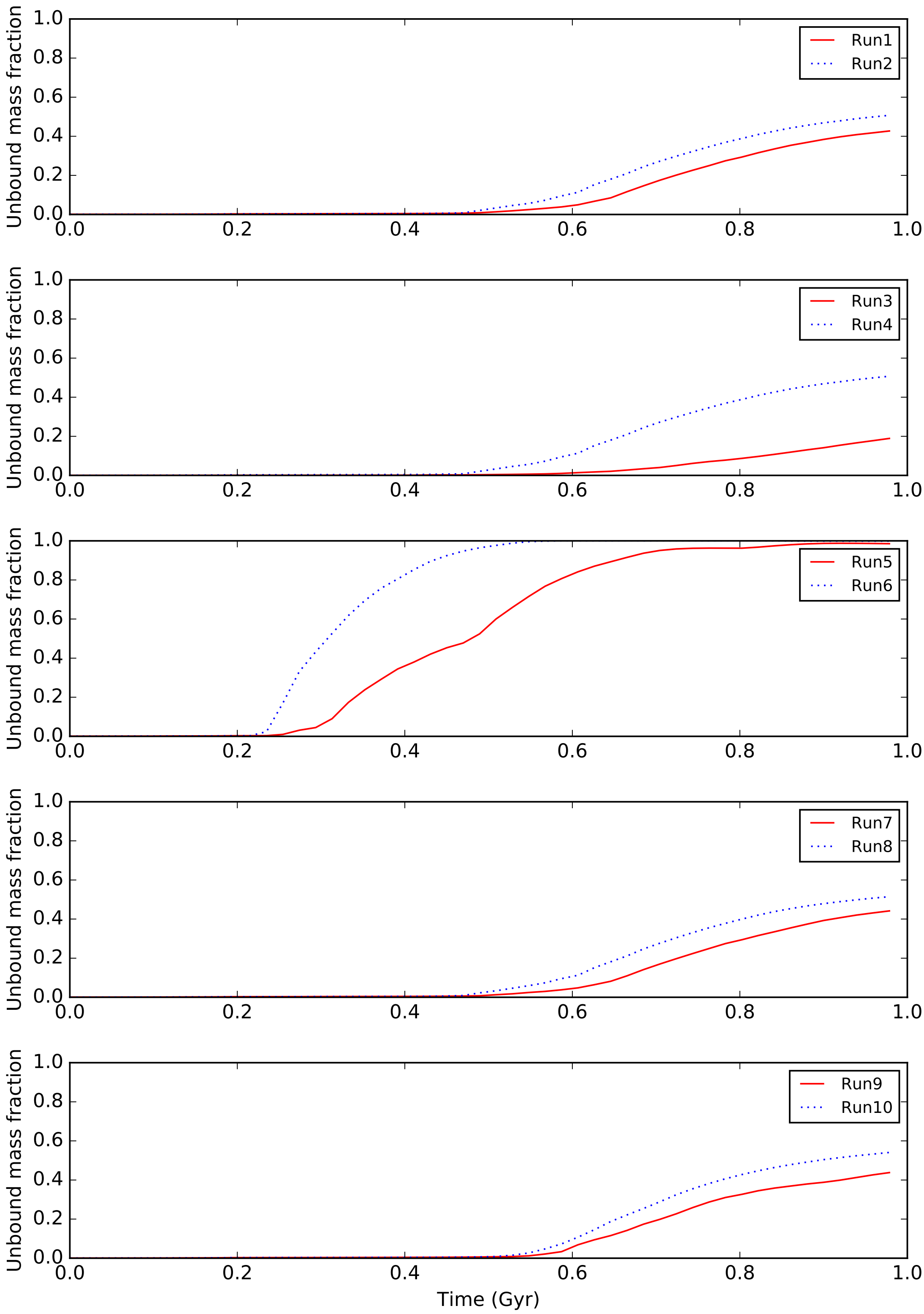

FIGURE 5.9: Plot to show the fraction of the gas which is unbound in runs containing gradual types of feedback alongside SNe feedback (red, solid lines), as well as those containing just SNe feedback (blue, dotted lines). The simulations on each individual plot have identical initial conditions.

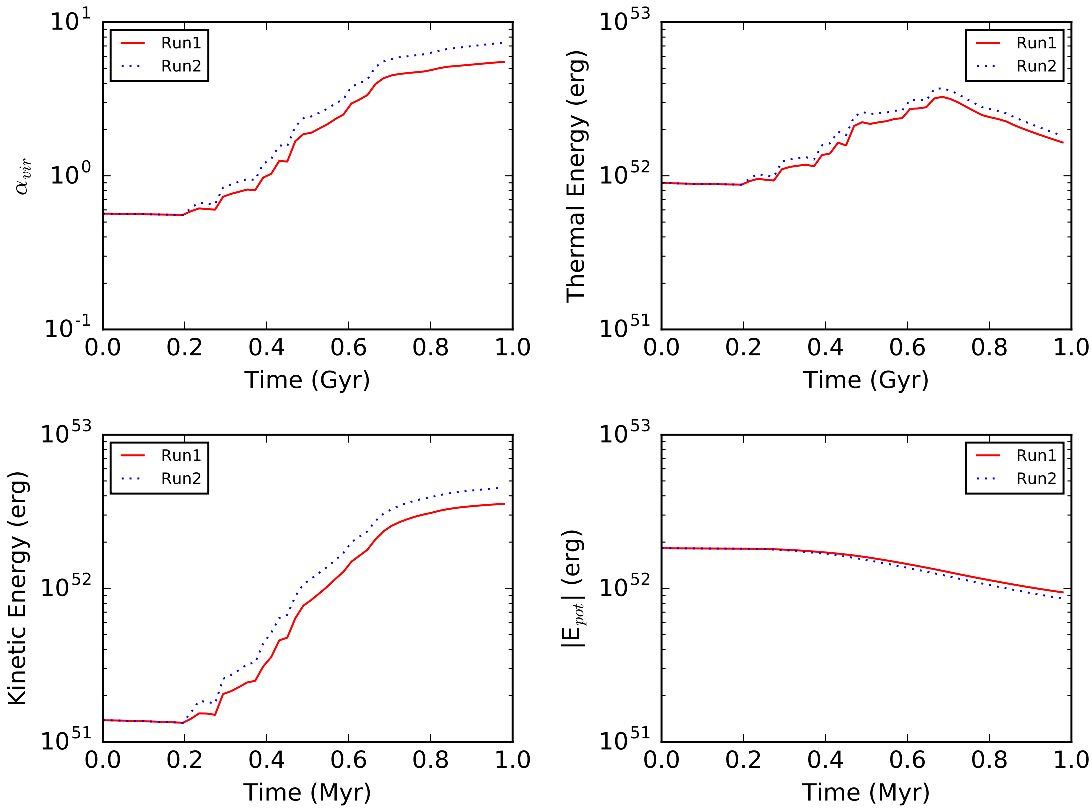

FIGURE 5.10: Plots to compare α_{vir} ($E_{therm} + E_{kin}/|E_{pot}|$ - top left plot), along with the total thermal (top right), kinetic (bottom left) and potential (bottom right) energies of the gas particles in Runs 1 (solid, red line) and 2 (blue, dotted line).

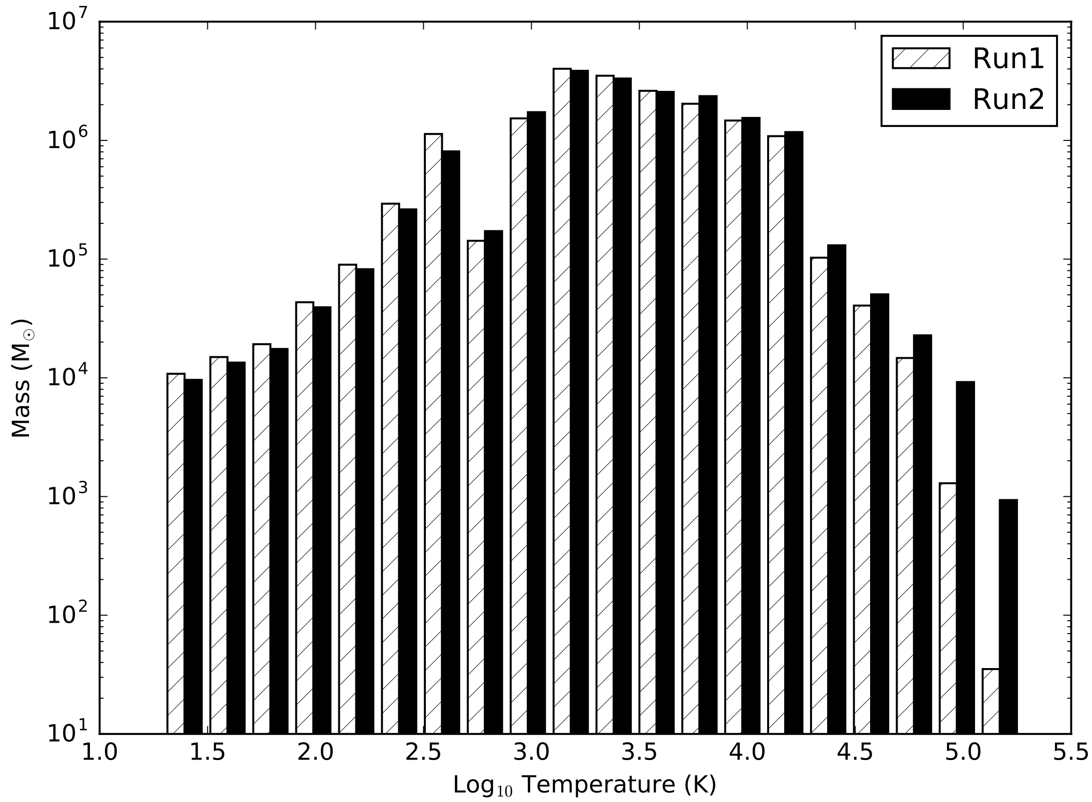

FIGURE 5.11: A plot of the mass contained in 20 temperature bins taken across the total gas particle temperature range of Runs 1 (hatched) and 2 (solid filled).

10^4 K the mass in each temperature bin is larger in Run 2 than Run 1. However, in both runs the majority of the gas mass is at temperatures between 10^{3-4} K, corresponding to the point when collisional excitations become rare. Run 1 also contains an order of magnitude lower gas mass at temperatures above $\sim 10^5$ K compared with Run 2 (however this represents a very small fraction of the overall gas mass; $\sim 0.01\%$). Below $10^{5.5} K$ cooling is dominated by collisional excitations of electrons in atoms, followed by their subsequent de-excitation and emittance of radiation. The lower densities present in Run 2 (figure 5.6) and the resulting decrease in the number of collisions at a specific temperature compared with Run 1, is therefore a likely cause of the inefficient cooling seen in figures 5.10 and 5.11. However, figure 5.12 plots the mean temperature across both runs, alongside the the 90th and 10th percentile temperatures. This figure shows there is marginal difference between the mean temperature of the gas in both runs, only in the mass of gas occupying each temperature bin.

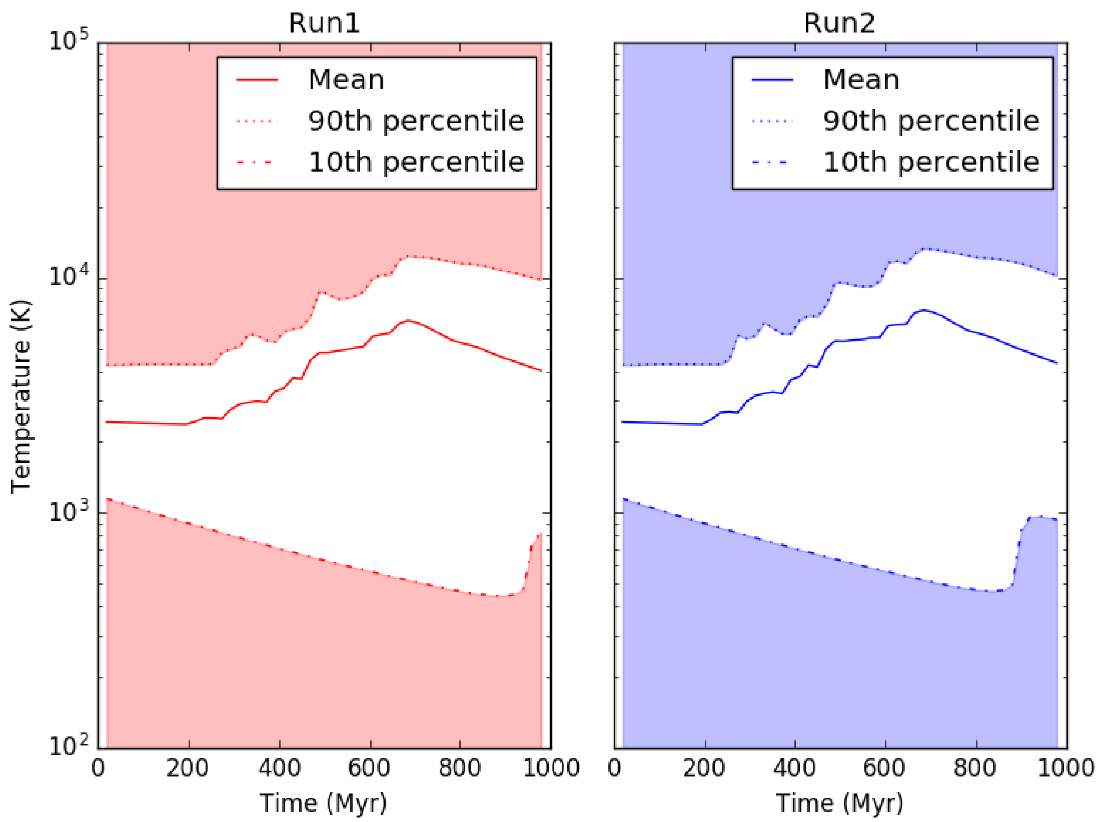

FIGURE 5.12: A plot to show the evolution of the mean (solid lines), 10th percentile (lower shaded areas) and 90th percentile (upper shaded areas) temperatures across the 1 Gyr starburst in Runs 1 (left plot, red) and 2 (right plot, blue).

I also plotted the mean radius of the gas particles across the simulation for both Runs 1 and 2 (see figure 5.13), finding beyond ~ 0.5 Gyr the mean radius is larger in Run 2 than Run 1 and the gap between the two increases with time. By 1 Gyr the mean radius in Run 2 is ~ 1 kpc larger than in Run 1. Since the mean radius is increasing in both simulations, this indicates the presence of gaseous outflows. I investigated this by plotting density/temperature slices of Runs 1 and 2 in all three planes at the end of each simulation, taken with the origin at the centre of each galaxy. The most pronounced difference occurred in the y-z plane (see 5.14). Here it can be seen both the SNe in Run 2 and the combination of SNe/HMXBs/stellar winds in Run 1 have inflated a 20 kpc low density bubble filled with gas between $10^{4-5}K$, bordered by a ring of higher density ($\sim 10^{-28}$ gcm^{-3}) gas. However the ring is broken in Run 2, while in Run 1 it is intact. In Run 2 this has allowed hot gas to escape into regions of lower density and this process can be seen occurring in the bottom right plot of figure 5.14.

This excess of hot/warm, low density gas seen in Run 2 compared with Run 1, is highlighted in Fig. 5.15, which plots the temperature versus density of the gas in Run 1 and 2 at 998 Myr, which has been rendered according to particle number. Comparing the populations of gas particles with densities between 10^{-32} and 10^{-30} gcm^{-3}, we see Run 2 has a higher number of gas particles within this density range, with a wider range of temperatures. In particular, Run 2 has an excess of gas particles with temperatures of between $\sim 15\,000$ K to 17 000 K, which correspond to a peak in the primordial metallicity cooling curve, due to the collisional excitation of H^0 and He^+ (Mo, Bosch, and White, 2010). However, Run 1 contains no gas in this temperature range that has a density less than 10^{-31} gcm^{-3}. This suggests the cooling of the gas is being suppressed in Run 2 compared with Run 1 due to the comparative low density of the gas (which is also shown in Fig. 5.14). This cooling suppression means the hot gas will likely retain enough energy to escape the galaxy entirely and hence constitutes a galactic wind.

In Fig. 5.16 I show the evolution in density of the outflow seen in Fig. 5.14 for Runs 1 (left column) and 2 (right column). By 0.59 Gyr, we can see the interplay of multiple low density bubbles, surrounded by rings of high density gas and driven by the shock-heating from stellar feedback events. The location of SNe events in Runs 1 and 2 largely correspond due to the underlying stellar populations being identical. However, current and previous gradual feedback events in Run 1 have acted to limit the radii of these low density bubbles (for example, comparing

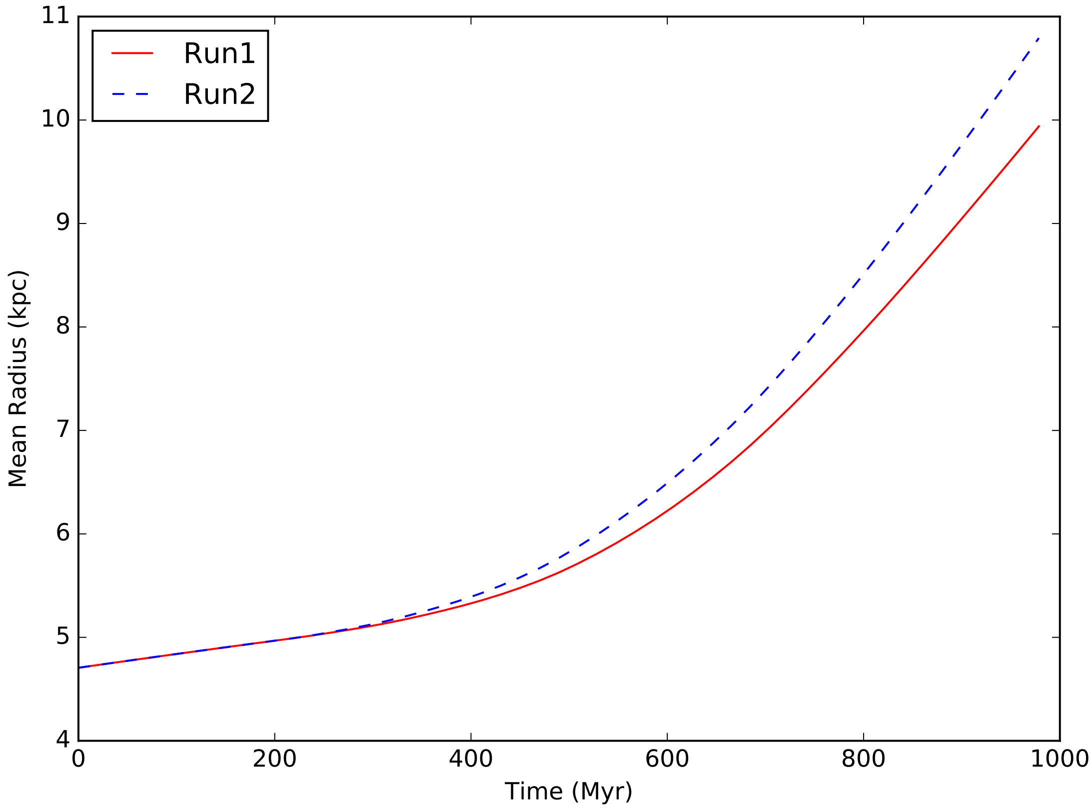

FIGURE 5.13: The mean radius of gas particles across 1 Gyr in Runs 1 (solid, red line) and 2 (dashed, blue line).

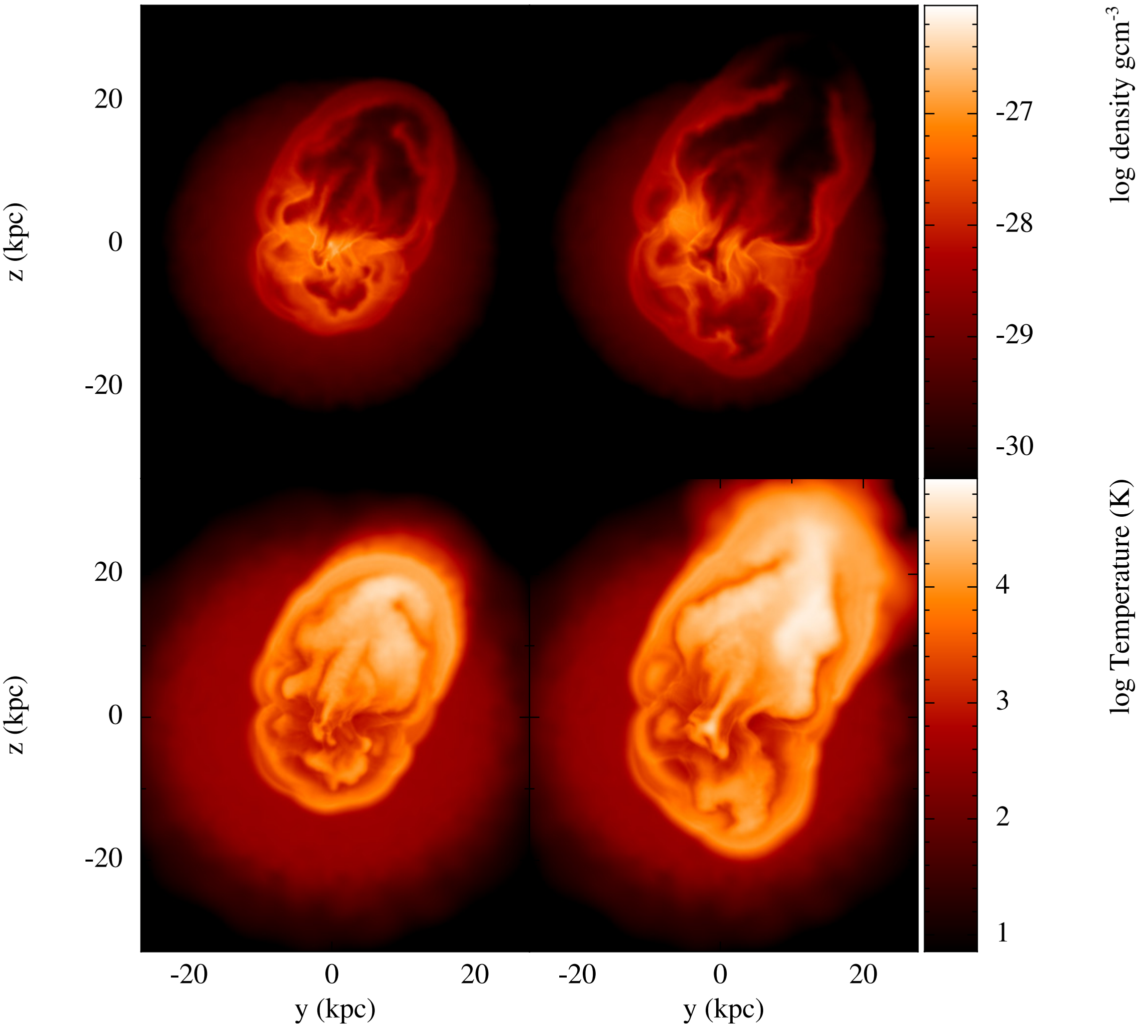

FIGURE 5.14: Top row - density slices taken at x = 0 in the y-z plane 1 Gyr into Runs 1 (left) and 2 (right plot). Bottom row - temperature slices taken at x = 0 in the y-z plane 1 Gyr into Runs 1 (left) and 2 (right).

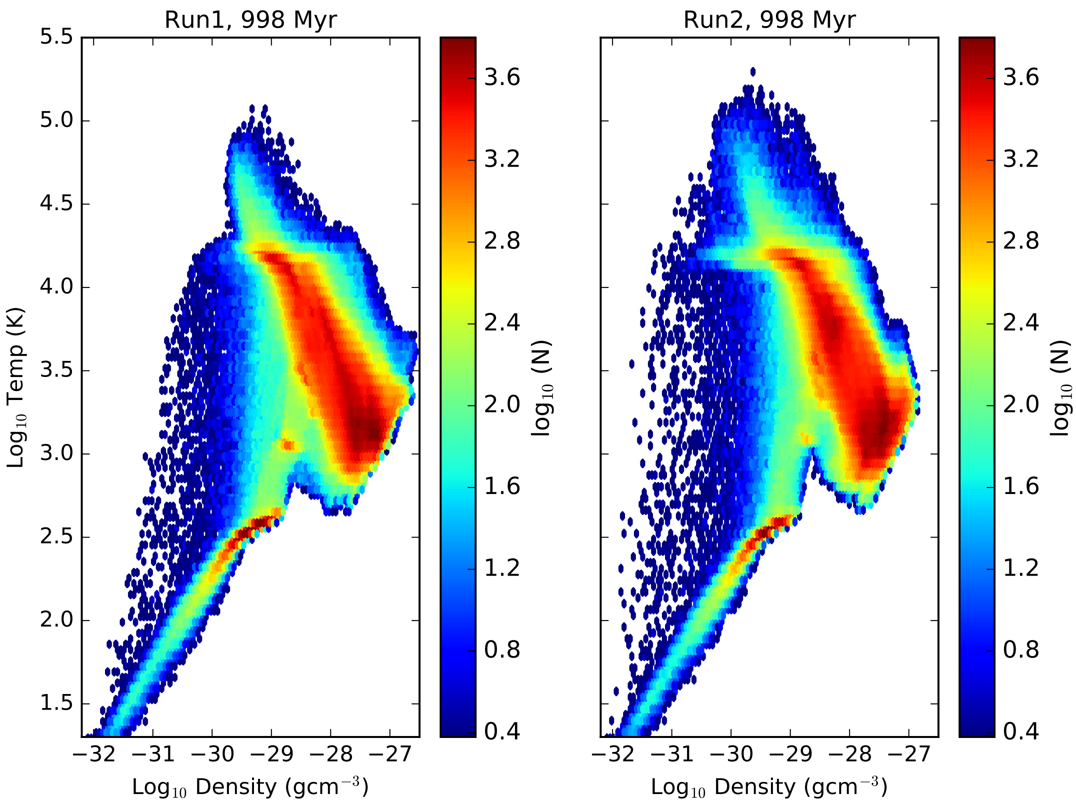

FIGURE 5.15: Plots to show the temperature and density of the gas in Runs 1 (left) and 2 (right) at the end of each simulation, rendered according to particle number.

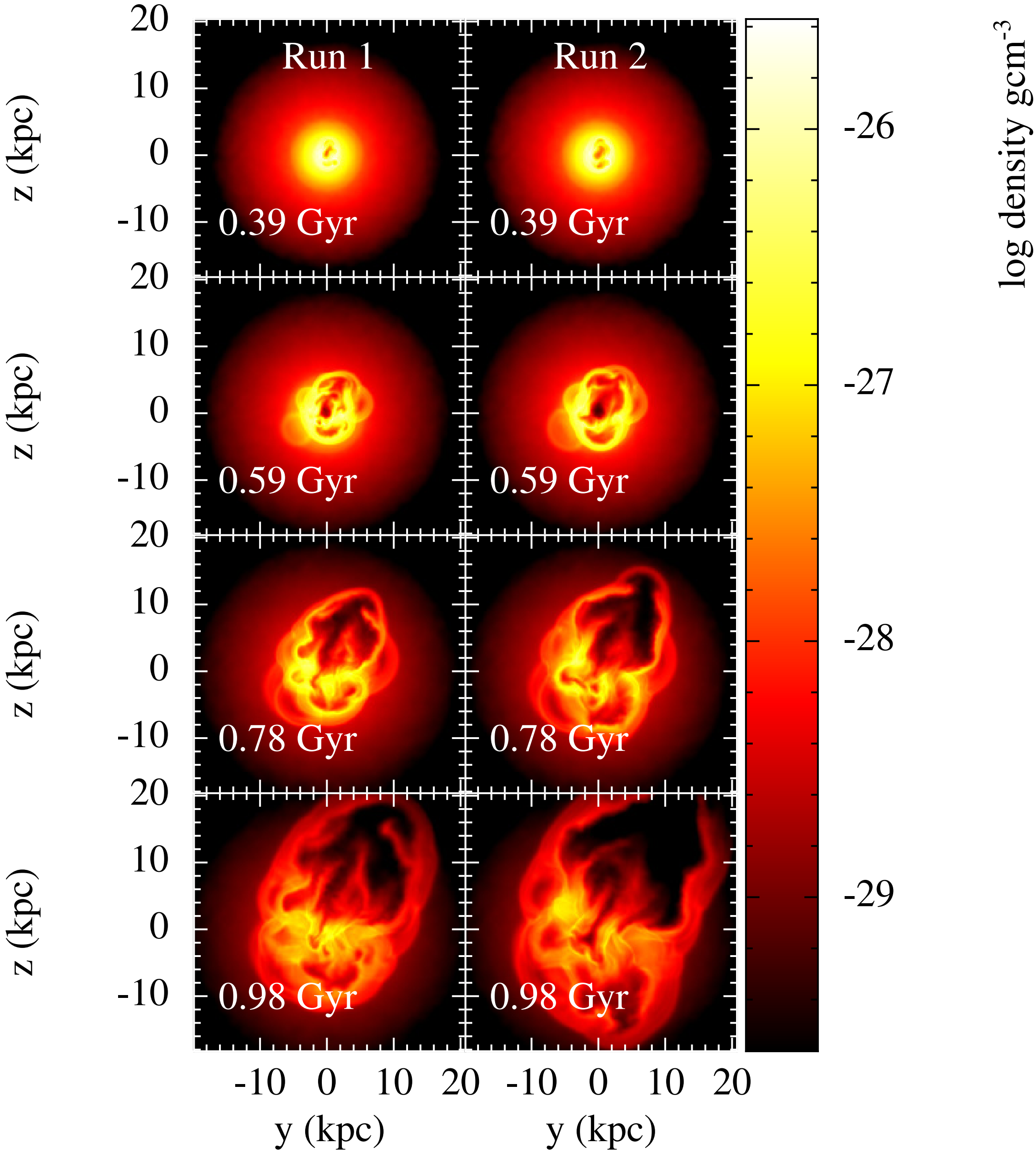

FIGURE 5.16: Plots to show the evolution of the density of the gas contained in a x = 0 slice of the y-z plane in Runs 1 (left column) and 2 (right column), at varying times.

the lower portion of Runs 1 and 2 at 0.59 Gyr). Furthermore, more high density filaments have been retained inside the virial radius (7.78 kpc) of Run 1 than Run 2, suggesting the mixing of the hot feedback-generated bubbles is more efficient in Run 2 than Run 1. Beyond this, by 0.78 Gyr spatially and temporally coincident feedback events have acted to inflate two bubbles in the y-z plane of Run 2; one on the bottom right of Fig. 5.16 and another in the top right. On the other hand, Run 1 also contains low density bubbles at the corresponding locations, however they are less spatially extended and the interior gas is higher in density.

In order to ascertain any effect of the feedback on the underlying dark matter halo, in figure 5.17 I plot the density profile for the dark matter in Runs 1 and 2 at varying times. Run 1 shows a 22 % drop in density at 100 pc, between 0 and 0.67 Gyr, however it also shows a $\sim$ 20 % rise between 0.67 Gyr and 1 Gyr. This means by the end of the simulation the inner dark matter profile has only dropped in density by $\sim$ 7 %. On the other hand, the density of the dark matter above a radius of $\sim$ 200 pc is lower at 1 Gyr than at all other times. Looking instead at Run 2, the main difference arising from neglecting gradual feedback is the inner $\sim$ 200 pc of the density profile, which is lower than Run 1 beyond 0.67 Gyr and also does not show a rise in density to correspond with the density increase seen in Run 1 between 0.67 to 1 Gyr. This increase in the inner density profile of Run 1 could indicate that, post-starburst, recovery of the original dark matter halo profile is possible in the runs which include gradual feedback. However, this increase in density inside the inner 200 pc is comparative to the noise level seen in section 5.5.4, hence it is difficult to ascertain if this result is a result of the gradual feedback or noise in the dark matter profile.

These changes to the underlying dark matter density profile link to work such as Pontzen and Governato (2012) , which shows SNe feedback can lead to galactic winds, which will result in sudden, sharp variations in the galactic potential and an irreversible increase in the total energy of the dark matter. In this case I hypothesise including gradual feedback has acted to make the changes in potential smoother, leading to a smaller increase in the total energy of the dark matter, along with a denser core. I investigate this hypothesis by plotting the time evolution of the total energy (which I evaluate as the sum of the potential and kinetic energy) of dark matter particles taken at various radii within the central 150 pc of the halo in Run 1 and 2 (Fig. 5.18). As a note, I compare the same dark matter

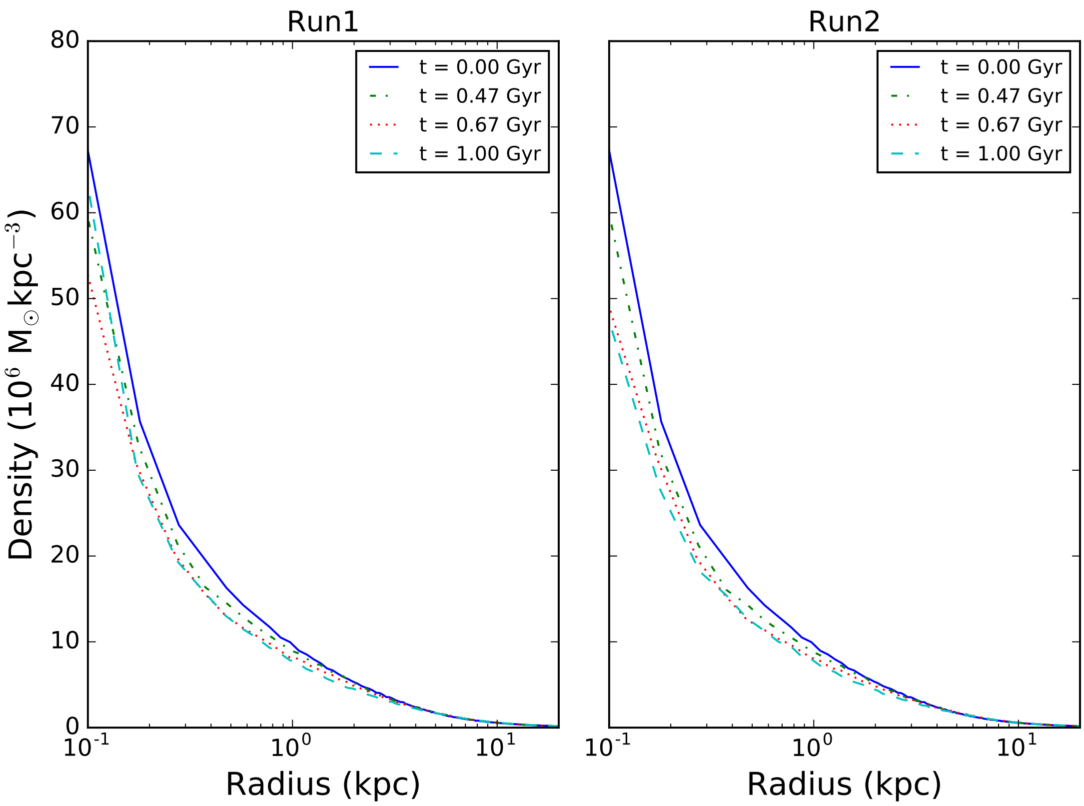

FIGURE 5.17: Dark matter halo density profile taken for Runs 1 (left) and 2 (right) at varying times into each simulation.

particles in each run. In both runs, the feedback has acted to increase the total energy of the particles across time, via rapid changes in the potential of the system caused by galactic winds. Comparing the energy of the innermost dark matter particle (initially situated at a radius of less than 20 pc) between runs, we see prior to the onset of feedback (at $\sim$ 200 Myr) any changes to the total energy of the particle (via gravitational interactions) have been small and reversible. However, once feedback kicks in at 200 Myr, the total energy of the particle increases in both runs. The two runs significantly diverge at $\sim$ 700 Myr, where Run 2 sees 3 peaks in total energy, while Run 1 sees only two. Moreover, the total energy gained is larger by the end of Run 2 than Run 1. The difference in the total energy of the dark matter particle with a radius less than 50 pc is less pronounced. The particle in Run 1 ends the simulation with a total energy of $\sim$ - 4.0 $\times$ 10^{48} erg, while the same particle in Run 2 ends with $\sim$ - 3.9 $\times$ 10^{48} erg. However, the particles at 100 pc and 150 pc both show larger peaks in total energy in Run 2 across the simulation. In particular, Run 2 has a peak in the total energy at 0.9 Myr, which is 0.5 $\times$ 10^{48} erg smaller in Run 1. Despite this, the total energy of the particles at the end of each run is similar.

Overall, the density drop in both runs is marginal when compared with the dark matter density cores seen in work such as Teyssier et al. (2013), along with the density drop seen in the smaller haloes investigated in Cashmore et al. (2017). However, Fig. 5.18 indicates including gradual feedback can reduce the change in the total energy caused by a burst of SNe feedback, which, in the case of the innermost particle, has acted to globally reduce the energy of the particle across the time window of the simulation, compared with the case where only SNe feedback is included.

To conclude, the addition of gradual types of feedback on top of instantaneous feedback in Run 1 has resulted in a lowering of the total internal energy and kinetic energy of the gas in the galaxy, along with a decrease in the mass fraction of gas unbound during the 1 Gyr starburst. Moreover, the lack of any type of gradual feedback has also led to a higher mass of gas at temperatures above 10^5 K, along with a decrease in gas mass below $\sim$ 300 K. Additionally, the mass inflow rate was increased when HMXB and SNe feedback was included. There is also evidence to suggest the addition of gradual feedback results in less energy being transferred to the dark matter by outflowing gas and hence a larger dark matter density in the central 200 pc of the halo.

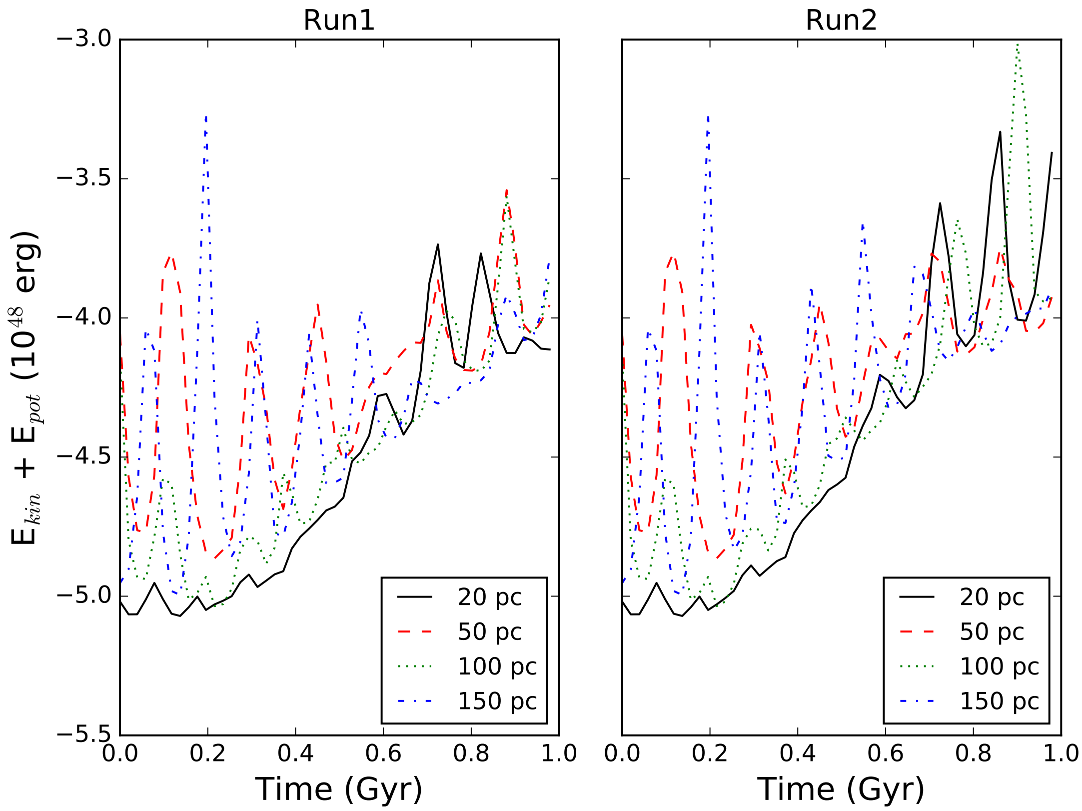

FIGURE 5.18: Figure to show the sum of the kinetic and potential energy of dark matter particles takes within 20 pc, 50 pc, 100 pc and 150 pc of Run 1 (left) and Run 2 (right). The same particles are being evaluated in both runs.

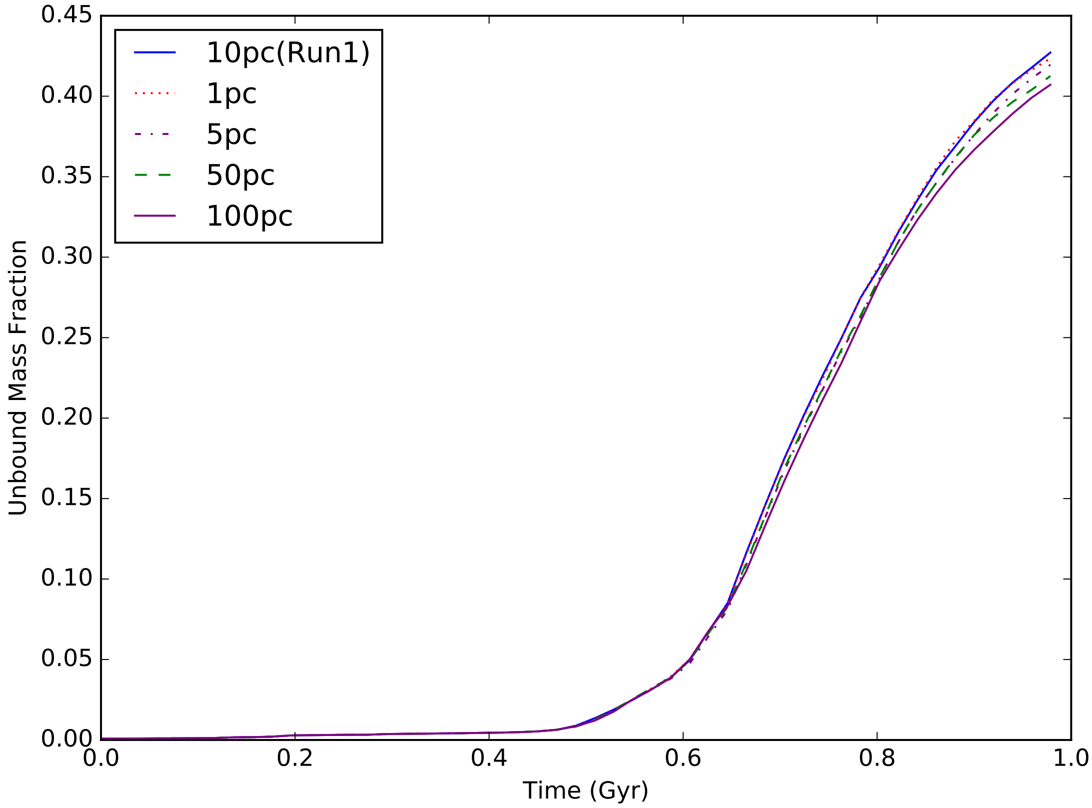

FIGURE 5.19: The time evolution of the fraction of the initial gas mass that has been unbound in simulations that have the same initial conditions (as Run 1), however dark matter softening lengths varying from 1 pc to 100 pc.

5.5.4 Changing the dark matter softening length

In order to ensure my choice in softening length for the dark matter is not determining the results in this chapter, I ran simulations varying the softening length between 1pc to 100 pc.

I plot the time evolution of the unbound mass fractions of each run in Fig. 5.19. Here we see the total unbound mass fraction varies by 0.025, however the run at the highest resolution (with a softening length of 1 pc) is converged with the results run (which uses a softening length of 10 pc). Moreover, when we plot the total kinetic, thermal and potential energies of the gas in each simulation, along with the virial parameter (Fig. 5.20), we see all runs are converged - indicating changing the softening length of the dark matter has had little effect on the final state of the gas in the simulation.

Furthermore, in Fig 5.21 I plot the density profile of the dark matter density

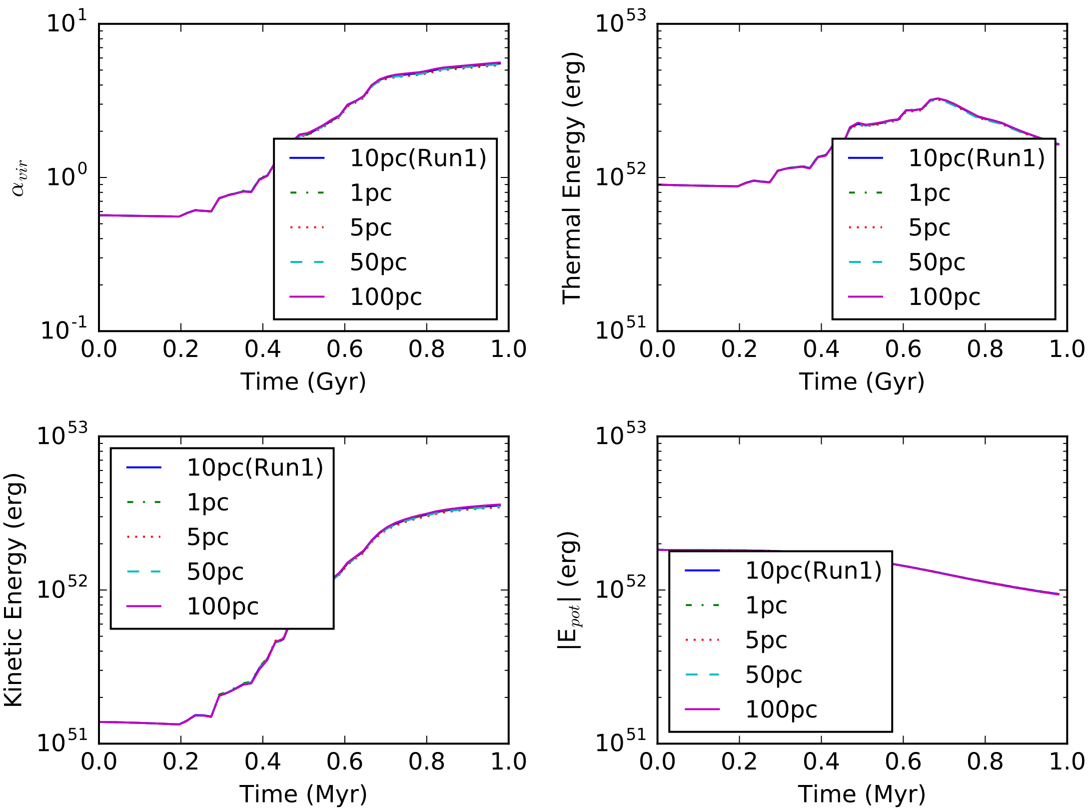

FIGURE 5.20: The time evolution of the virial parameter (evaluated as α_{vir} = E_{kin} + E_{therm} / $|E_{pot}|$), along with the total thermal, kinetic and potential energy of the gas in simulations with the same initial conditions however using different softening lengths for the dark matter.

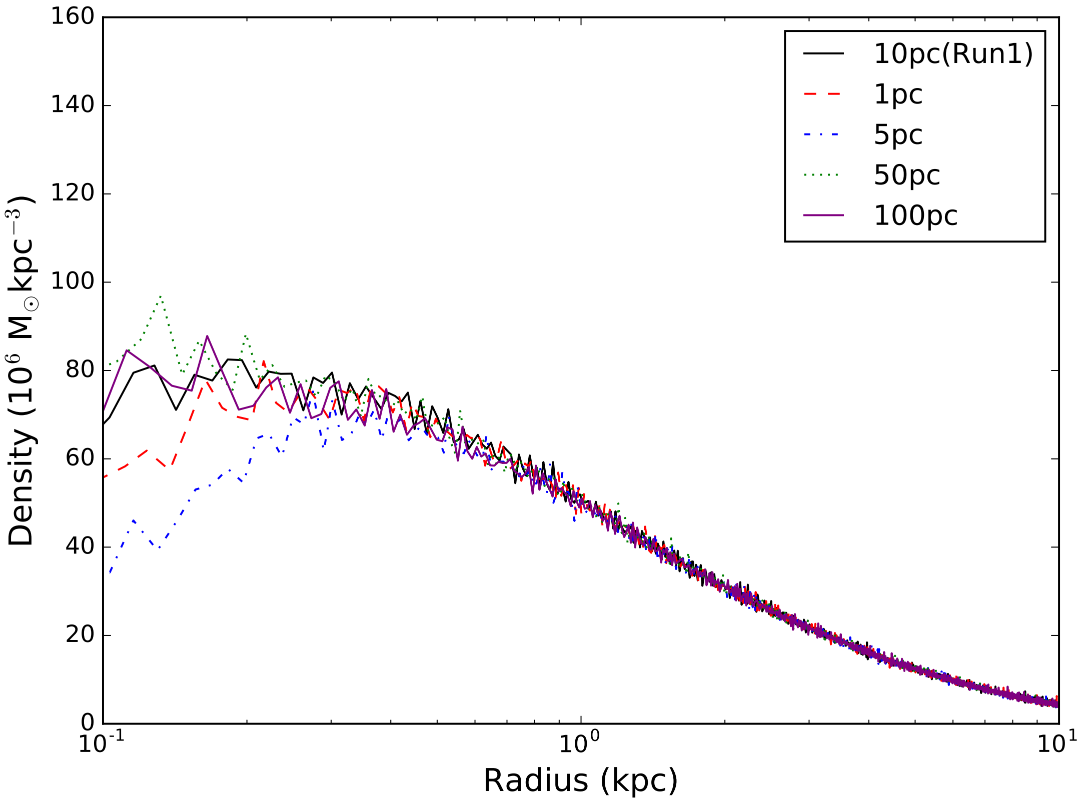

FIGURE 5.21: The dark matter density profiles taken at 1 Gyr for simulations with the same initial conditions, however different softening lengths for the dark matter.

profile in each run. We see the profiles are converged above ~ 0.5 kpc, however at the smallest scales (below 200 pc) the runs diverge, with no clear trend with softening length. This indicates a degree of noise on these scales.

5.5.5 Decreasing σ_{star} (Runs 9 and 10)

In the top two plots of Fig. 5.22 I plot the energy injection by the 3 different mechanisms; stellar winds, HMXBs and SNe, temporally binned in units of 5 Myr for both the σ and 0.5σ primordial metallicity runs where all three feedback types are included (Runs 1 and 9). As expected from Fig. 5.2, by decreasing σ_{star} we have created a more concentrated starburst and by maintaining the same stellar population as the σ_{star} runs, the net result is a more concentrated injection of energy, focused between 350-650 Myr. In both cases the stellar winds create a low-level, near-constant energy injection between SNe events, with HMXB events contributing an order of magnitude more energy, however over shorter timescales towards the second half of the starburst. Given stellar winds are present prior to the first SNe, along with their ubiquity throughout the starburst, this likely means they have a larger overall impact on the simulation than the higher powered, less frequent, HMXB events. We go on to investigate their comparative impact in section 5.5.9. The main difference between the σ_{star} and $0.5\sigma_{star}$ runs is the unsurprisingly larger gaps between feedback events (particularly stellar winds) in the σ_{star} run (Run 1).

Despite the longer times between massive star feedback events in Run 9, Fig. 5.9 indicates there is only marginal difference between the mass fraction of unbound gas between runs with corresponding feedback mechanisms at different σ_{star}. On further analysis, Run 9 had a higher unbound gas mass fraction than Run 1 of 1%, while the fraction in Run 2 was 3% higher than that of Run 10. This indicates the feedback energy injected into Runs 1 and 2 has not been lost to radiative cooling, causing the energetics of the gas in Runs 1 and 2 to converge with Runs 9 and 10 respectively, since the total feedback energy injected is the same in both cases.

Furthermore, in Fig. 5.23 I compare the global energetics of the Runs 1, 2, 9 and 10. As expected the total kinetic and internal energies of the gas in Runs 1 and 2 initially dominate that of the 0.5σ runs (Run 9 and 10), due to the fact feedback kicks in earlier (see figure 5.22). However, at ~ 0.5 Gyr the total internal energies and kinetic energies (along with α_{vir}) of Runs 9 and 10 overtake that of the corresponding larger σ_{star} runs. As was seen at $\sigma_{star} = 0.13$ Gyr, the run at $0.5\sigma_{star}$ (or $\sigma_{star} = 0.06$ Gyr) that lacks any type of gradual feedback (Run 10) has a higher virial parameter, along with global kinetic and thermal energy, than the corresponding run containing stellar winds and HMXBs (Run 9). However, the total kinetic energy of both Runs 1 and 9, along with 2 and 10 converge around 700 Myr. However, the total thermal energy of the gas in both Runs 9 and 10 is lower than in their higher σ_{star} counterparts, indicating the gas in the runs that include a shorter, more violent starburst is able to cool more efficiently. Both Fig. 5.23 and Fig. 5.9 indicate changing the timescale of the starburst has had a marginal impact on the multiphase ISM of the galaxy; the main factor being the presence of stellar winds and HMXB feedback.

In order to investigate the formation of galactic winds in Runs 9 and 10, I

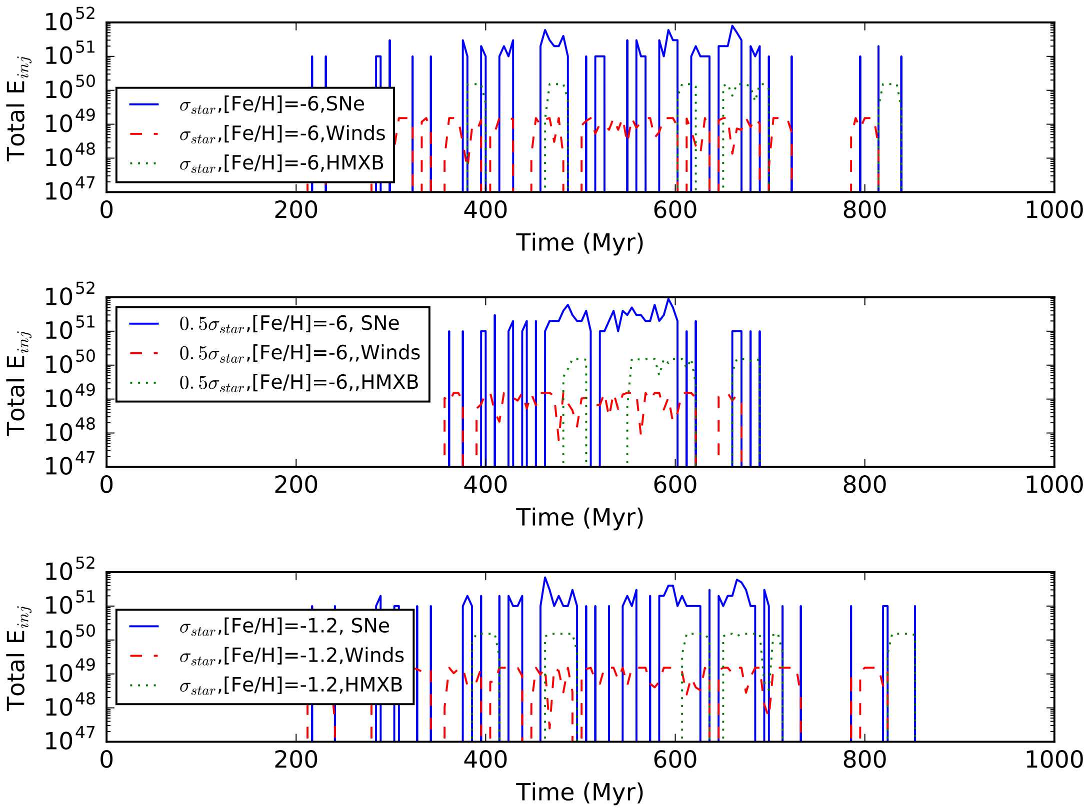

FIGURE 5.22: The total energy injected by SNe (solid, blue lines), stellar winds (red, dashed lines) HMXBs (dotted, green lines) per 5 Myr across Run 1 (top plot), Run 9 (smaller σ_{star}, middle plot) and Run 7 (higher metallicity, bottom plot).

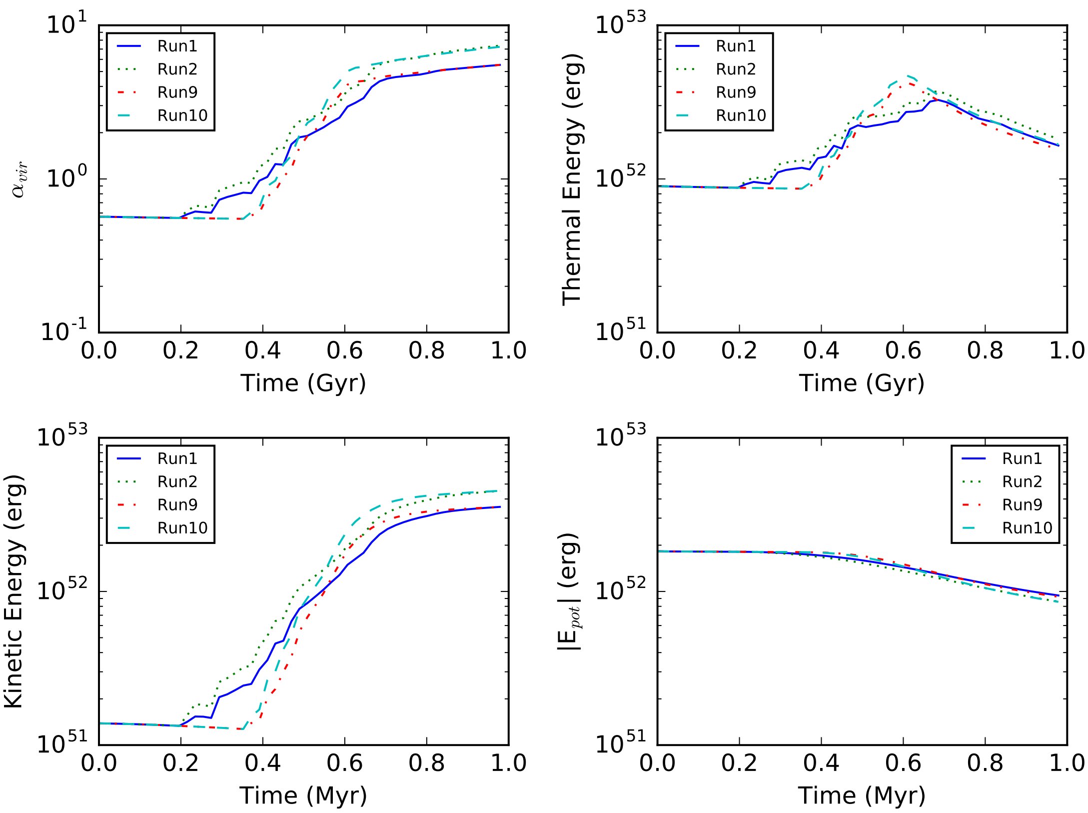

FIGURE 5.23: Plots to compare the global energetics of Runs 1 (navy blue, solid line), 2 (green, dotted line), 9 (red, dot-dash line) and 10 (light blue, dashed line). Top left plot - the time evolution of the virial parameter. Top right plot - the time evolution of the total thermal energy of the gas. Bottom left - the time evolution of the total kinetic energy of the gas. Bottom right - the time evolution of the total potential energy of the gas.

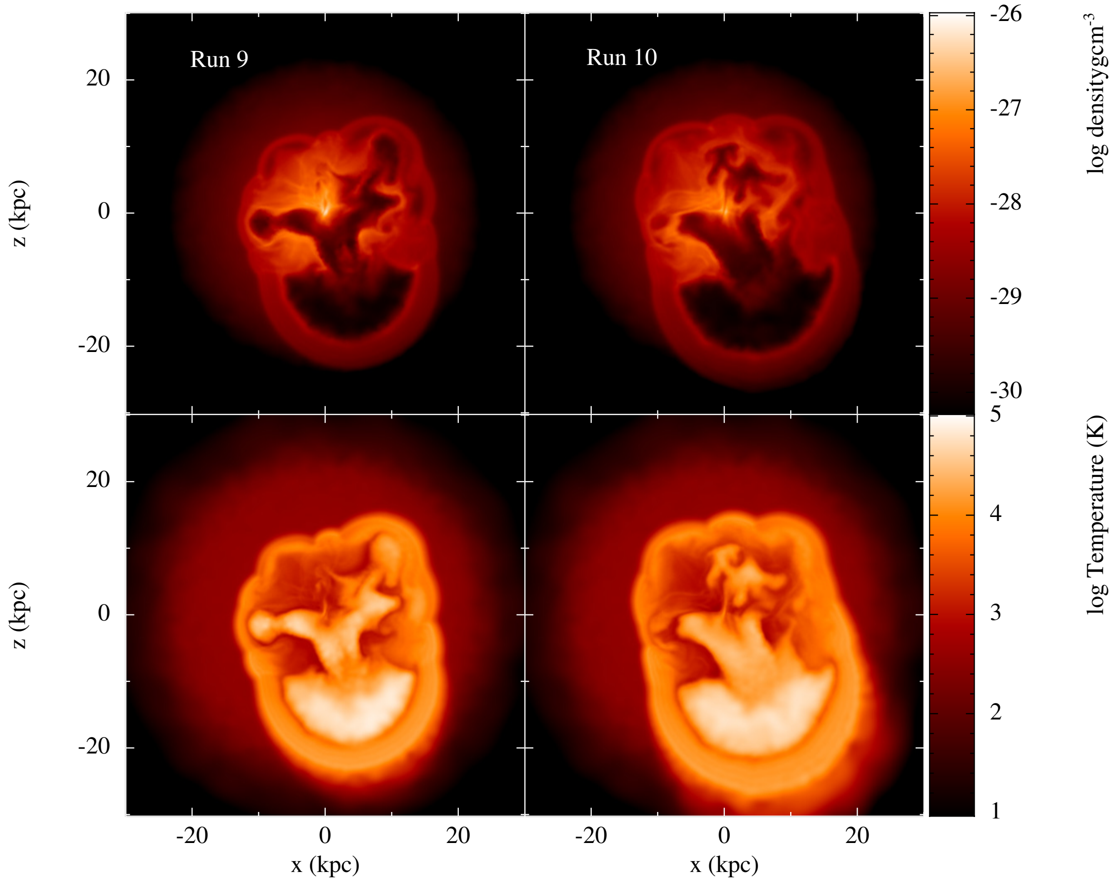

FIGURE 5.24: Density (top row) and temperature (bottom row) slices taken in the x-z plane at y = 0, for Runs 9 (left column) and 10 (right column) at 1 Gyr.

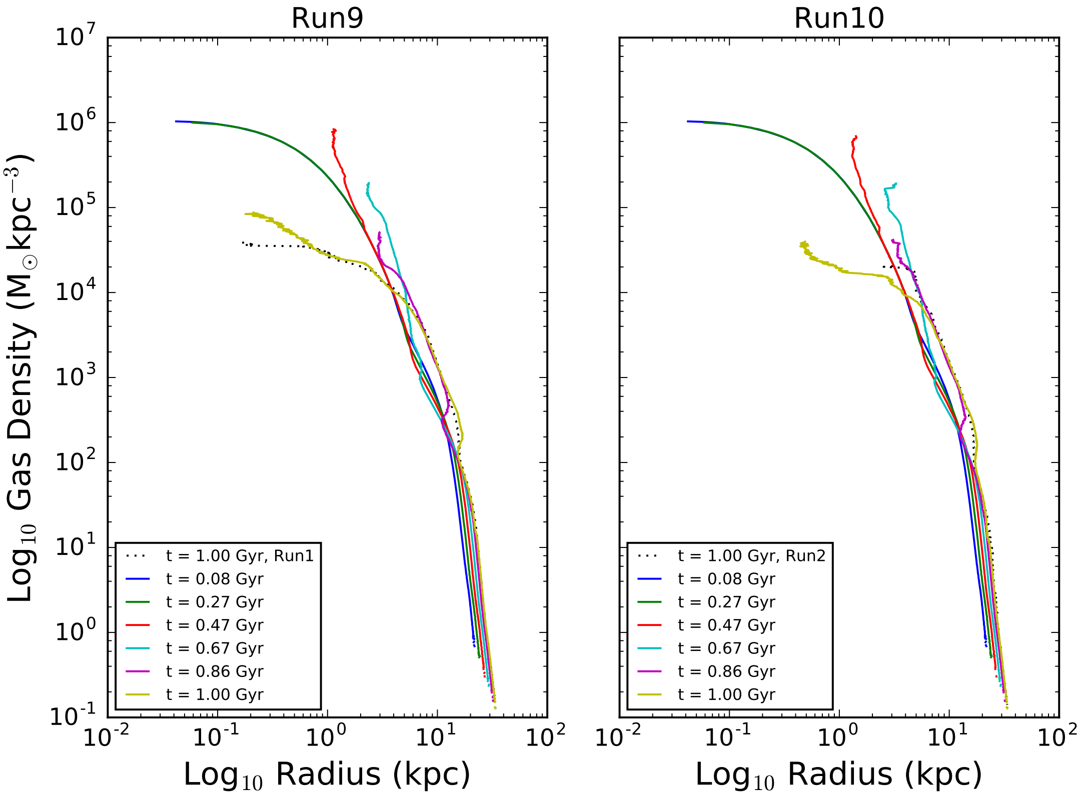

FIGURE 5.25: The gas density profiles taken at various times into Run 9 (left) and 10 (right), with the final density profiles of Runs 1 and 2 overlaid onto Run 9 and 10 respectively (dotted lines).

plotted slices rendered in density and temperature in all three planes, finding the y = 0 slice in the x-z plane (Fig. 5.24) contained low density 'superbubbles' akin to those seen in Fig. 5.14. Comparing Run 9 with Run 10, we see in both cases there appears to be a mushroom-shaped low density bubble filled with gas at $\sim 10^5$ K, towards the bottom half of each plot. In both cases the bubble is surrounded by a shell of higher density ($\sim 10^{-28}$ - 10^{-29} gcm^{-3}), slightly cooler ($\sim 10^4$ K) gas. The bubble in Run 10 is larger than Run 9, indicating excluding gradual feedback aids the development of these large-scale ($\sim$ 20 kpc), wide-angle outflows. On the other hand, Run 9 shows two smaller-angle 'chimneys' of low density, hot gas on the left and right of Fig. 5.24 . These are not present in Run 9, in this case the hot, low density gas associated with these regions has been effectively funneled into the growing larger-scale 'superbubble'. In this way the addition of gradual feedback on top of SNe feedback appears to have facilitated the production of smaller 'chimneys' of hot/warm, low density gas. The energy being funneled through these chimneys would otherwise have been added to the work done on the main 'superbubble' and further driven the large-scale galactic wind.

Fig. 5.25 plots the gas density profiles of Runs 9 and 10 at various times into each simulation, alongside the gas density profiles taken at the end point of Runs 1 and 2 (corresponding to 1 Gyr). We see there is marginal difference between the density profiles of Runs 1 and 9 above 1 kpc, however below this the gas density is higher in Run 9 than Run 1. Therefore, a shorter, more violent starburst has resulted in the retention of a higher gas mass in the centre of the galaxy. As well as this, Run 10 also shows a significantly higher gas mass at radii of 1 kpc than Run 2. By decreasing the starburst duration, this has also minimised the variation between runs which include gradual types of the feedback and runs which just include SNe feedback; Runs 9 and 10 differ less than Runs 1 and 2. Furthermore, Runs 1 and 9 differ less than Runs 2 and 10, indicating gradual feedback acts to reduce the differences in gas radial distributions, which arise by altering the period of a starburst. However, despite the mean radius of the inner density profile being smaller in Run 10, the unbound gas mass fraction is not significantly altered from Run 2. These results indicate the bound gas in Run 10 is located closer to the centre of the galaxy than the same gas in Run 2, likely through efficient cooling or higher resistance to heating via stellar feedback processes.

I next plot the density profile of the dark matter in both Runs 1 and 2, along with Runs 9 and 10 in Fig. 5.26. Here we see the dark matter density inside the inner regions of the galaxy is less in Run 2 than in Run 10, indicating the violent starburst and temporally concentrated SNe feedback has had less of an effect on the underlying dark matter profile than the longer, less violent starburst. On the other hand, comparing the dark matter density profiles of Runs 1 and 9, we see Run 1 reaches a higher peak in density than Run 9 in the inner ~ 150 pc of the halo. However this is within the noise level of the inner dark matter profile (see section 5.5.4). Furthermore, the differences between the density profiles of Runs 9 and 10 are significantly fewer than those between Runs 1 and 2.

I further investigate by plotting the total energy (E_{kin}+ E_{pot}) of 4 dark matter particles at varying radii between 0 and 150 pc (Fig. 5.27). Here we see by shortening the starburst I have reduced the differences between the total energy increase of the dark matter in Runs 9 and 10; the peaks are comparable in magnitude and occur at approximately the same times. It is also apparent the particle located below 20 pc in Run 9 is slightly out of phase with its partner in Run 10. However, the global increase in energy from 0 Gyr to 1 Gyr is comparable in both runs and this is larger than in the longer duration starburst (comparing with Fig. 5.18). It is possible, due to the short duration of the starburst, the SNe are frequent enough to contribute a near-continuous energy source which is comparable to the continuous energy injection from HMXB/ stellar winds on top of SNe in Run 9. Moreover, the shorter starburst has resulted in a more sudden variation in galactic potential which has manifested as a larger change in the global energy of the dark matter particles in Runs 9 and 10.

To conclude, altering the duration of the starburst in the galaxy has had only a marginal impact on the final state of the gas at 1 Gyr. The main factor is still the presence of gradual feedback, which has acted to reduce the unbound gas mass fraction (see Fig. 5.9) and decrease the total kinetic and thermal energy of the gas in the system (Fig. 5.23). Furthermore, the gradual feedback in the shorter starburst has facilitated the production of ~ 10 kpc, comparatively narrow 'chimneys' which have funneled hot, volume-filling gas away from the growing wide-angle superbubble that exists in both Run 9 and 10.

Altering the duration of the starburst does, however, have an effect on the underlying dark matter halo profile. A shorter starburst has increased the total energy transferred to the particles within 150 pc, while also reducing the differences in energy transfer to the dark matter between runs which do and do not

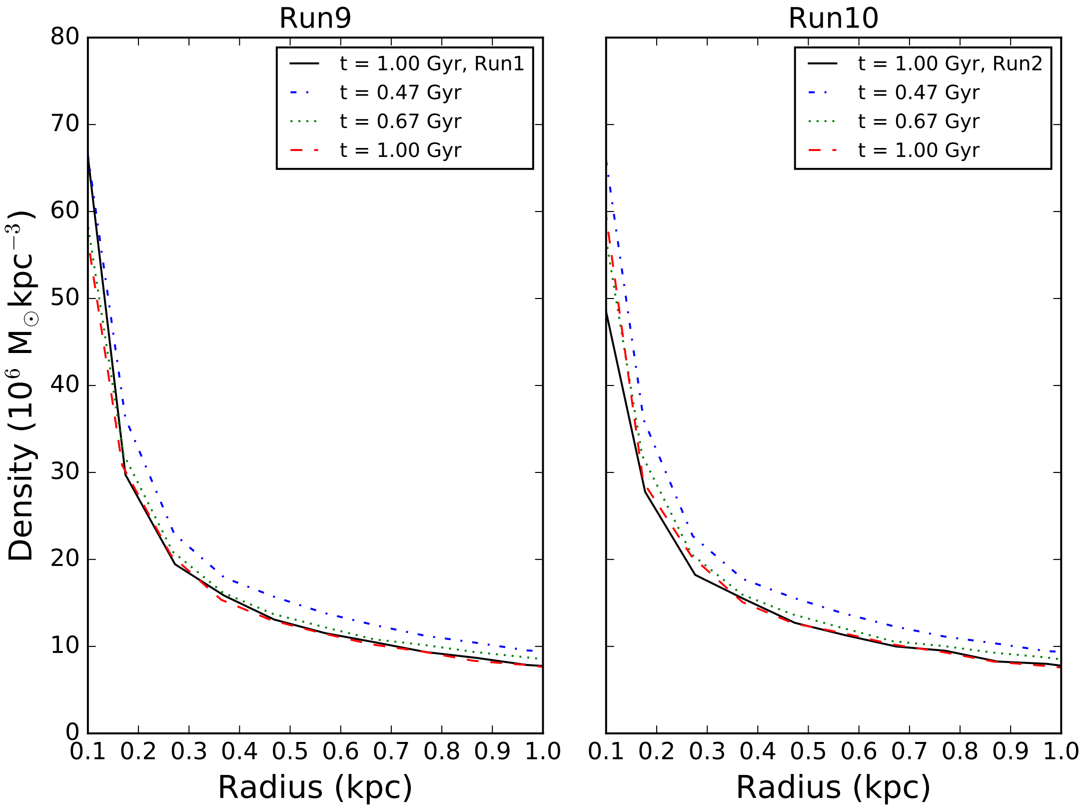

FIGURE 5.26: The dark matter density profiles taken at various times into Run 9 (left) and 10 (right), with the final density profiles of Runs 1 and 2 overlaid onto Run 9 and 10 respectively (dotted lines).

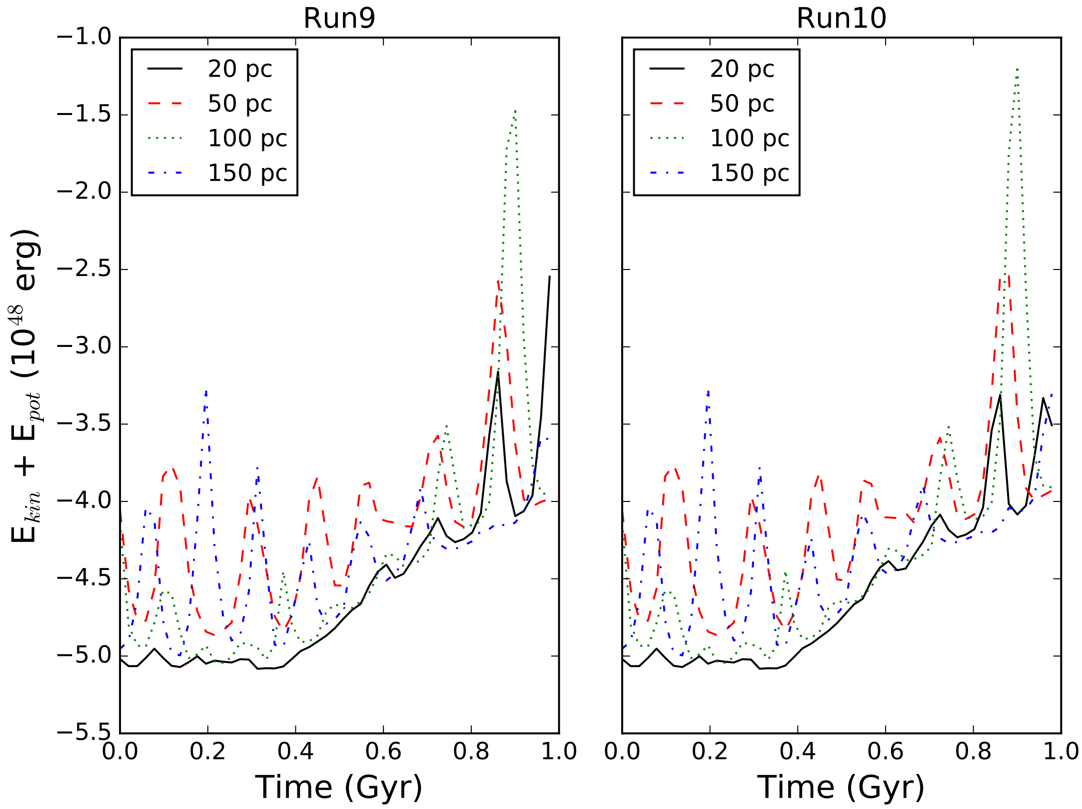

FIGURE 5.27: The time evolution of the total energy of 4 dark matter particles taken from Runs 9 and 10 with radii less than 20 pc, 50 pc, 100 pc and 150 pc. Again, the same particles are being evaluated in each run.

include gradual feedback mechanisms.

5.5.6 Changing metallicity (Runs 7 and 8)

Changing the metallicity of the gas in the galaxy has had very little impact on the unbound mass fraction (see figure 5.9). As was seen at primordial metallicity, the [Fe/H] = -1.2 run containing gradual feedback on top of SNe feedback (Run 7) has a lower unbound mass fraction across the simulation than equivalent Z run containing just SNe feedback (Run 8).

In Fig. 5.28 we can see the net radial momentum, mean temperature and the mean radius of the gas in Run 8 is greater than Run 7, once again showing including gradual feedback can lessen the efficiency of galactic winds. Furthermore, the mean temperature is the same for runs at primordial metallicity as those at [Fe/H] = - 1.2. In both runs the majority of the gas is at $\sim$ 6000 K, which corresponds to the virial temperature of the halo. The fact the mean temperature of the gas is similar between different metallicity runs indicates the bulk of the gas is at a high enough density to have a similar cooling timescale.

Moreover, Fig. 5.29 shows the gas density of Runs 7 and 8 do not vary significantly for their low metallicity counterparts (Runs 1 and 2). The same trends that are present in Runs 1 and 2 are also present at higher metallicity, namely the inclusion of gradual feedback has prevented the efficient clearing of gas below 1 kpc. As well as this, the central dark matter profiles of Runs 7 and 8 follow the same trend as Run 1 and 2 (see Fig. 5.30); the inner 200 pc has a higher density in the run with gradual feedback included.

Overall, altering the metallicity of the dwarf galaxy has had very little impact on both the gas phase and the dark matter/ gaseous halo. This is most likely due to the fact the density of the ISM at the location of the SNe events is high, resulting in similar cooling timescales between different metallicity runs and hence the gas in both runs converging on the same temperature (see Fig. 5.28 and Fig. 5.12). Furthermore, since by altering the metallicity I have effectively altered the lifetimes of the stellar wind and HMXB phase (see Fig. 5.2), these results indicate the additional energy input from winds and HMXB has had little impact on the state of the gas in the galaxy.

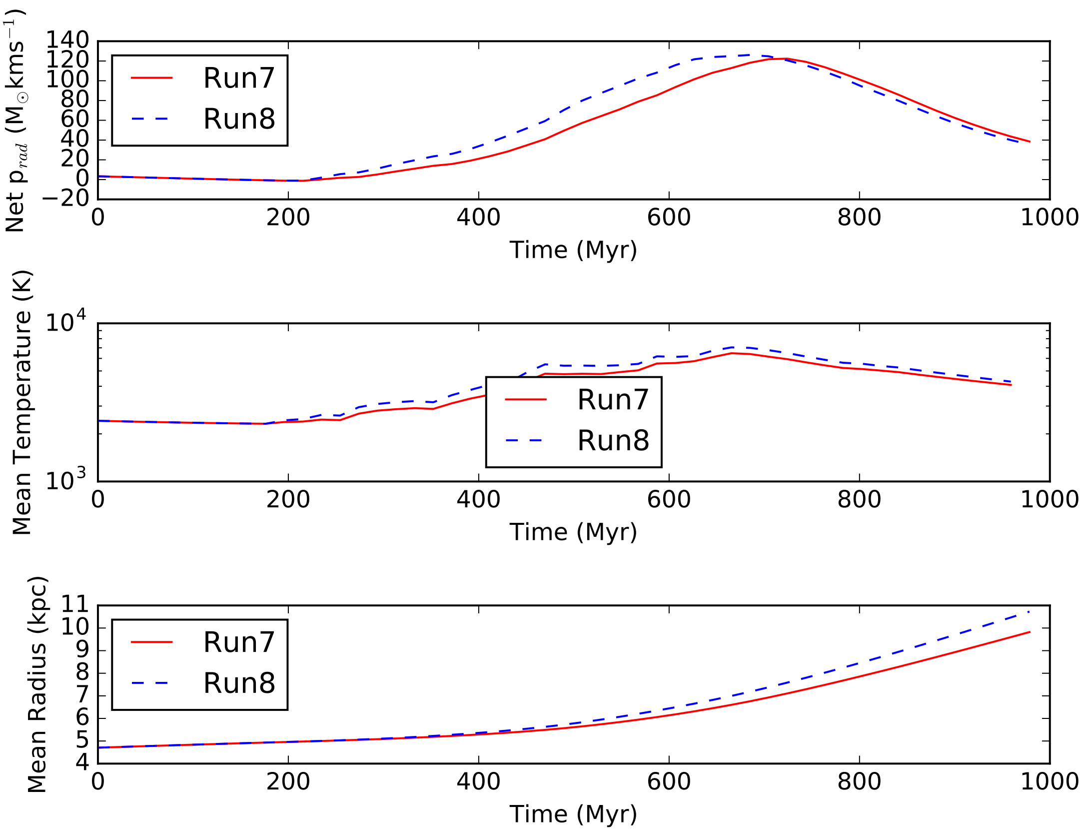

FIGURE 5.28: Top plot - the time evolution of the net radial momentum of the gas in Run 7 (solid, red line) and 8 (blue, dashed line). Middle plot - the time evolution of the mean temperature of the gas in Runs 7 and 8. Bottom plot - the time evolution of the mean radius of the gas in Runs 7 and 8.

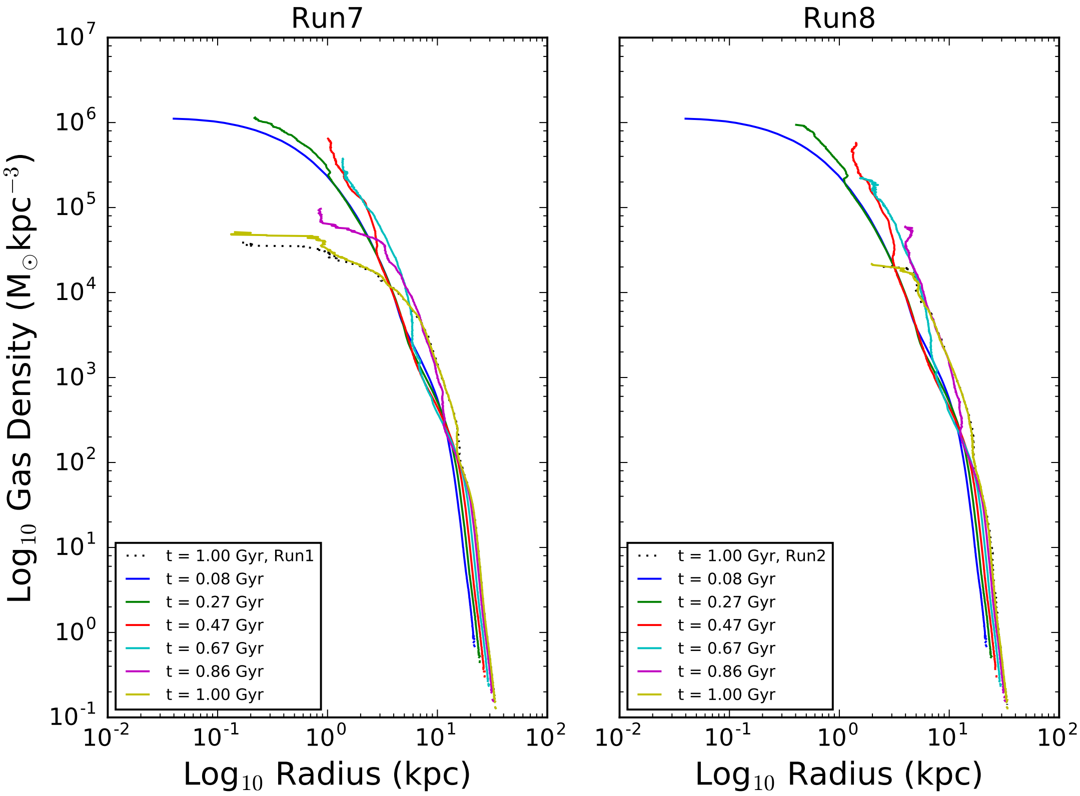

FIGURE 5.29: The gas density profiles of Run 7 (left) and 8 (right) taken at varying intervals into each simulation. The final gas density profiles of Run 1 and 2 (taken at 1 Gyr) were over-plotted on Run 7 and 8 respectively.

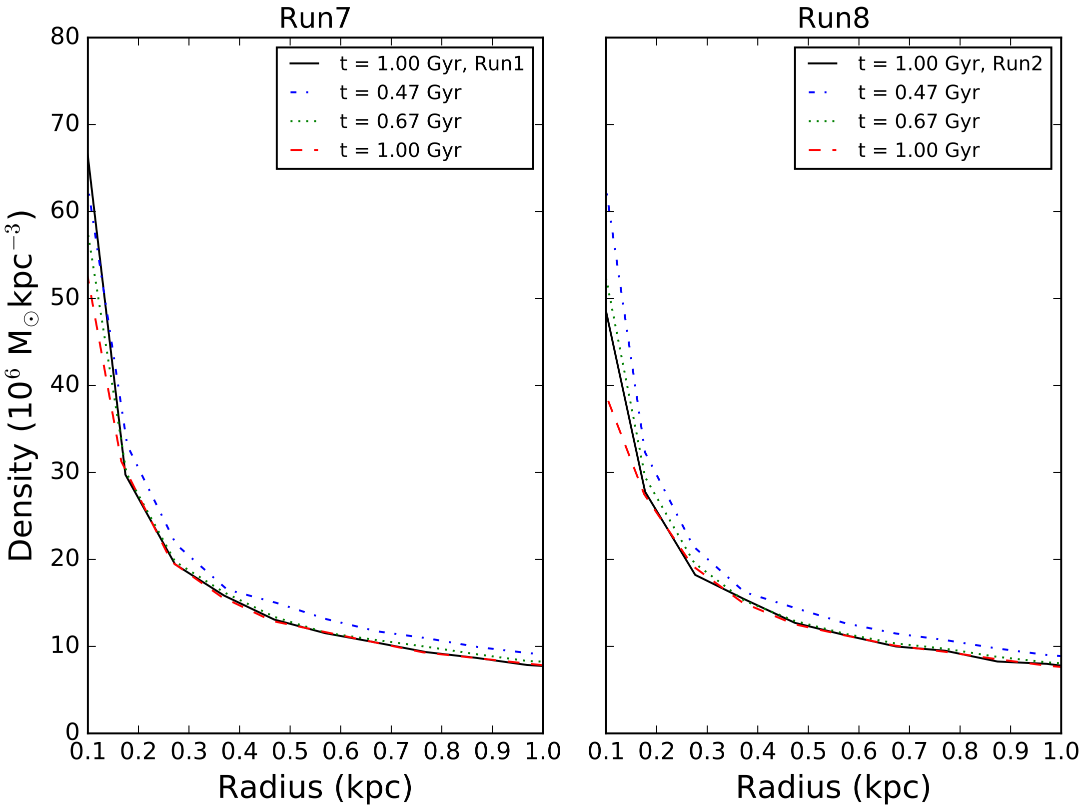

FIGURE 5.30: The inner 1 kpc of the dark matter halo density profiles of Run 7 (left) and 8 (right) taken at varying intervals into each simulation. The final dark matter density profile of Run 1 and 2 (taken at 1 Gyr) were over-plotted on Run 7 and 8 respectively.

5.5.7 Increasing the concentration parameter (Runs 3 and 4)

Firstly, from Fig. 5.9 it is clear by increasing the concentration parameter, the amount of gas that has been unbound in the galaxy has dropped by 20%. This is expected since the potential in the centre of the dark matter halo will be higher for a more concentrated halo, hence feedback will have to do more work on the ISM to unbind the gas. However, Runs 3 and 4 also show the addition of gradual feedback has reduced the amount of gas being unbound, despite more energy being injected into the ISM.

In order to investigate whether or not the 'superbubbles' seen in Fig. 5.24 and Fig. 5.14 also occur in Runs 3 and 4, I plotted density and temperature slices in the x, y and z planes. In Fig. 5.31 I show an example in the y-z plane at x = 0. Here we see both the SNe and HMXB/stellar winds have successfully produced warm/hot (10^4 - 10^5 K) lobes of low density gas in the upper left hand corner of the plot. Unlike in previous instances, these lobes still contain smaller ring-like structures of dense gas less than 10 kpc in scale. Furthermore, two smaller ($\sim$ 5 kpc in diameter) bubbles of warm gas at densities of $\sim 10^{29}$ gcm^{-3} can be seen in the bottom right of both Runs 3 and 4. As seen previously, the run which excludes gradual types of feedback (4), contains a larger 'superbubble'.

From Fig. 5.32 we can see the gas density profile is much less affected by feedback than the runs that have a lower dark matter halo concentration. As seen previously, once feedback has switched off (prior to 850 Myr) the gas has re-accreted onto the inner 1 kpc of the halo, increasing the density of the gas in this region between 0.86 Gyr to 1 Gyr. Furthermore, the gas density inside the inner 1 kpc of Run 3 is higher than Run 4. In this way, once again including gradual feedback has increased the re-accretion of gas onto the centre of the halo once the starburst has ended. The density profiles of Run 2 and Run 4 differ significantly at the end of the simulation; with the gas in Run 4 extending to an order of magnitude smaller radius than Run 2. The difference is less drastic when comparing Runs 1 and 3, however, the density is approximately an order of magnitude greater inside the inner kpc of Run 3.

I next plot the time evolution of the global energetics of the gas in Run 3 and 4 in Fig. 5.33. As expected from Fig. 5.9, the total kinetic and thermal energy of the gas in Run 4 is larger than Run 3, along with the virial parameter, while the potential energy is correspondingly lower. This is due to more efficient cooling

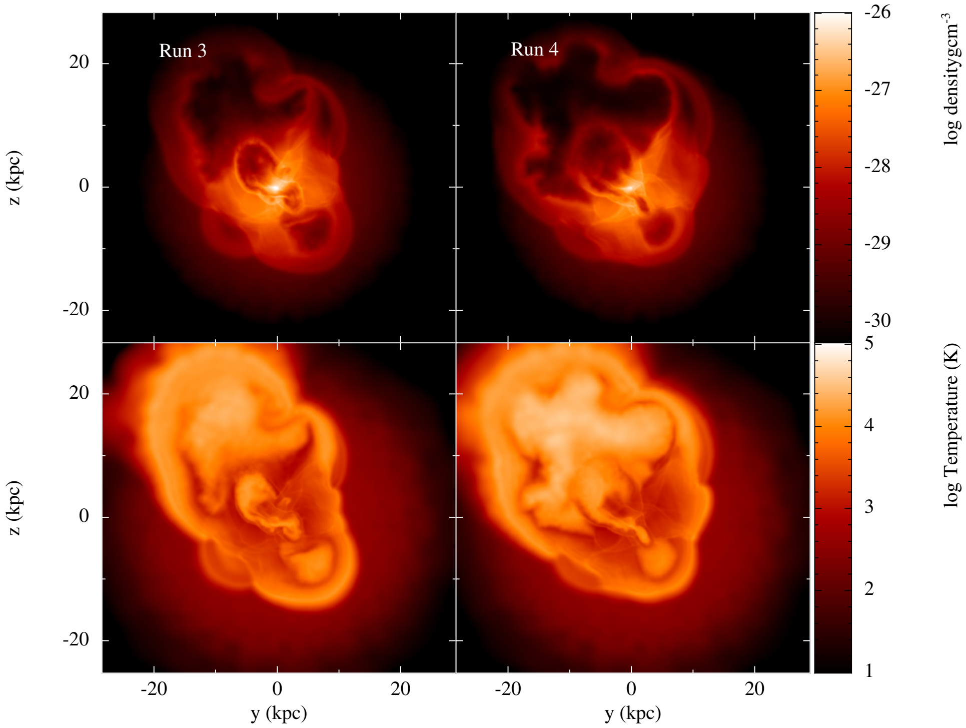

FIGURE 5.31: Density (top row) and temperature (bottom row) slices taken in the y-z plane at x = 0, for Runs 3 (left column) and 4 (right column) at 1 Gyr.

in Run 3, which is most likely caused by the increased density of the majority of the gas (as seen in Fig. 5.32).

Looking instead at the time evolution of the inner 1 kpc of the dark matter density profile in Fig. 5.34, we can see the dark matter density is largely unchanging in both Runs 3 and 4. As in previous runs, I also plot the time evolution of the sum of the kinetic and potential energy of dark matter particles taken from a range of radii (see Fig. 5.35). Comparing with Fig. 5.18 and Fig. 5.27, we see the oscillations in total energy of the dark matter particles in Runs 3 and 4 are 2 orders of magnitude larger, however they fluctuate about a largely unchanging mean potential, which contrasts with the increase in potential seen for the runs with a lower concentration parameter. The only particle that seems to be uniformly increasing in energy is the particle at $\sim$ 150 pc. This is occurring in both Runs 3 and 4. Comparing Run 3 with Run 4, the particles at 20 pc and 50 pc end the simulation with a higher total energy in Run 3, since they appear to be slightly out of phase with the oscillations in Run 4. This helps to explain the smaller density peak seen in Fig. 5.32 at 1 Gyr.

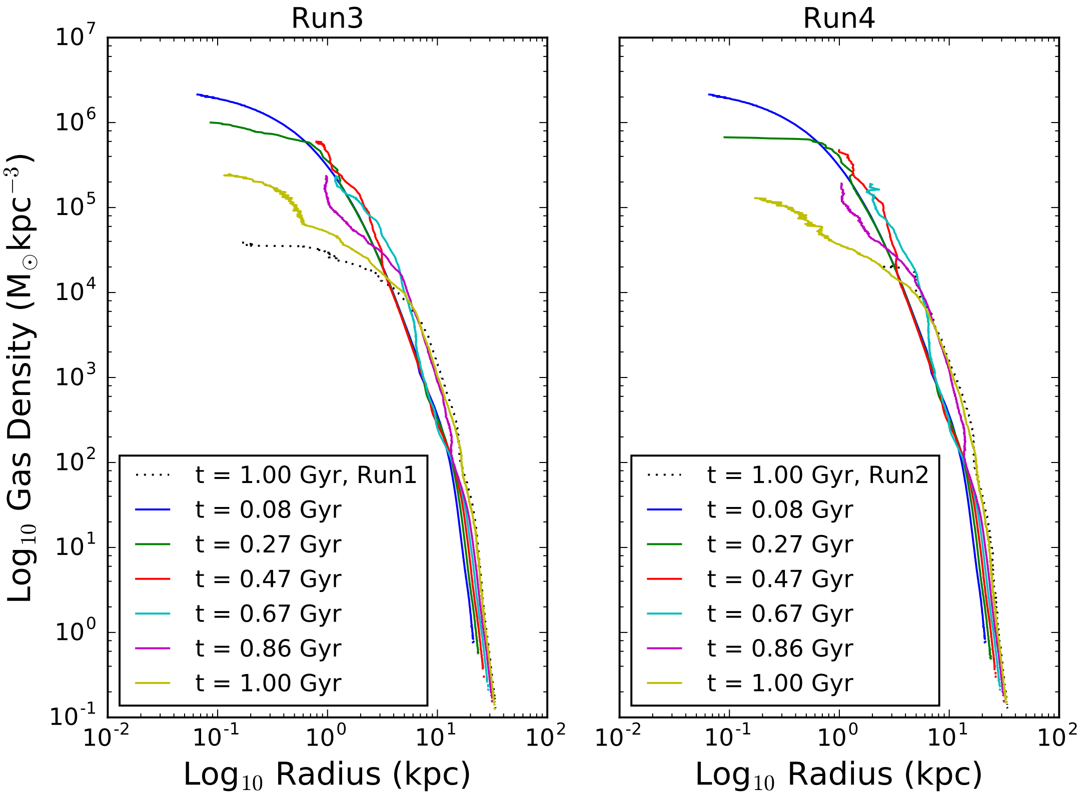

FIGURE 5.32: The density profile of the gas in Runs 3 (left) and 4 (right) taken at various times into each simulation. The final density profiles (taken at 1 Gyr) for Run 1 and 2 (dotted lines) have been over-plotted on Run 3 and 4 respectively.

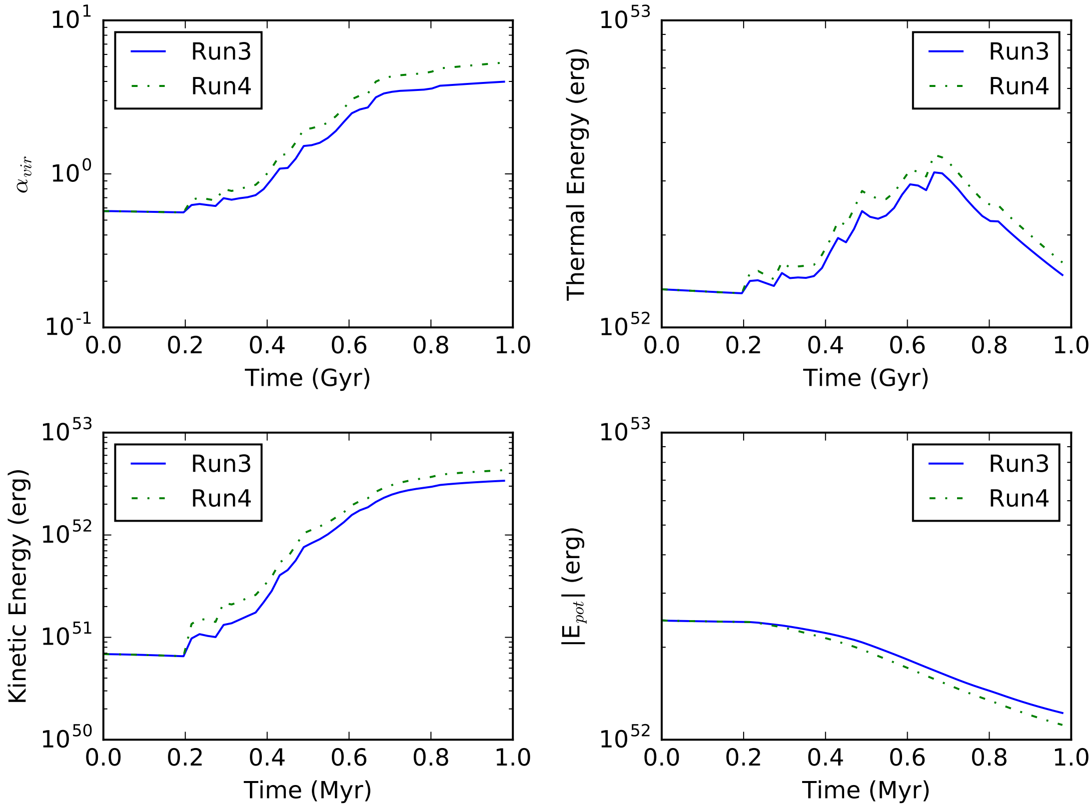

FIGURE 5.33: The time evolution of the virial parameter (top left plot, where α_{vir} = E_{kin} + E_{therm} / $|E_{pot}|$) and the total thermal (top right), kinetic (bottom left) and potential (bottom right) energy of the gas in Run 3 (solid, blue lines) and 4 (dot-dashed, green lines).

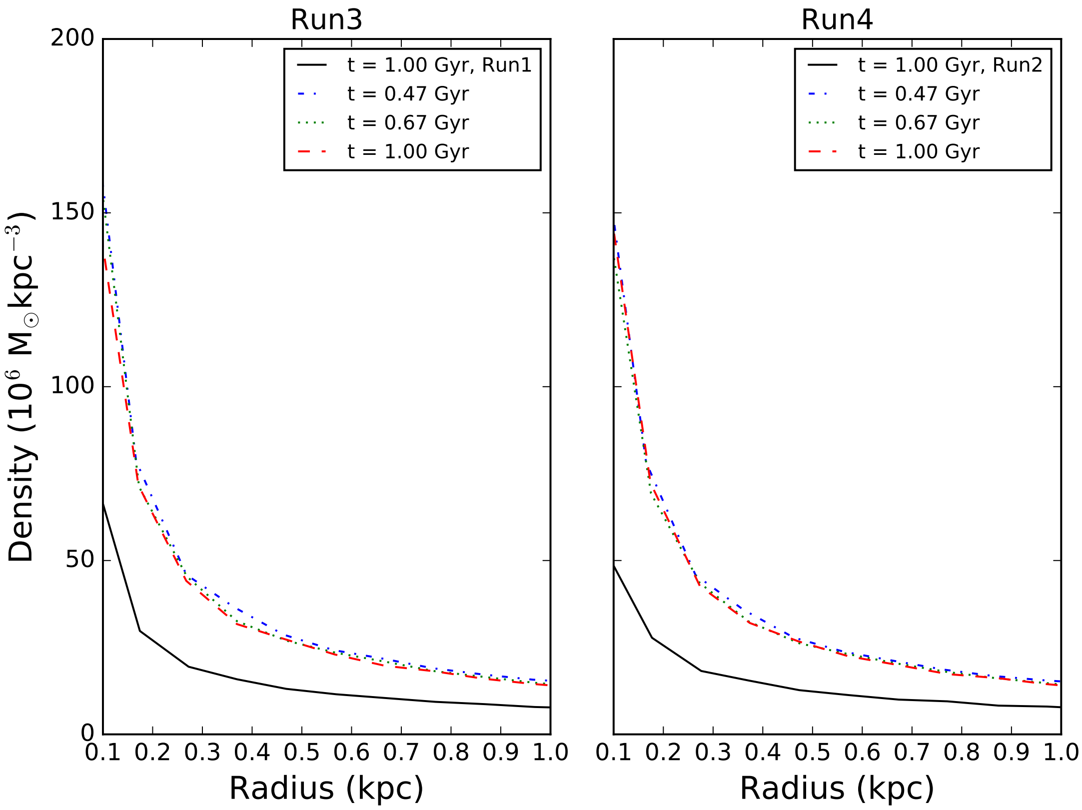

FIGURE 5.34: The inner (1 kpc) dark matter density profiles taken at varying times into Run 3 (left plot) and 4 (right plot). The dark matter density profile taken at the end (corresponding to t = 1 Gyr) of Run 1 and 2 have been over-plotted on Run 3 and 4 respectively.

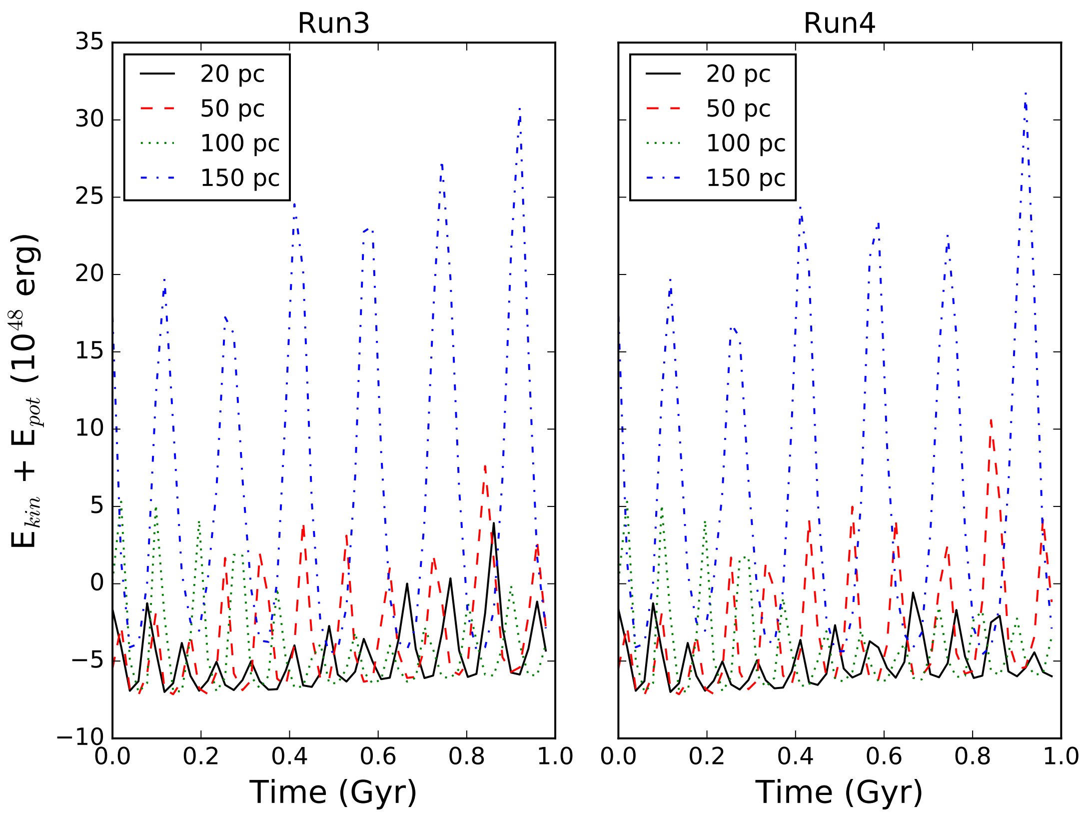

FIGURE 5.35: Figure to show the sum of the kinetic and potential energy of dark matter particles takes within 20 pc, 50 pc, 100 pc and 150 pc of Run 3 (left) and Run 4 (right). The same particles are being evaluated in both runs.

Overall, as is expected, increasing the concentration of the dark matter halo (and thereby increasing the potential at the centre of the halo) has resulted in less gas being unbound by stellar feedback. Furthermore, the underlying dark matter halo is less affected by the galactic winds, largely recovering from changes in the galactic potential caused by the outflow of gas particles. These runs also show the same trend that has been seen throughout this chapter; gradual feedback has acted to decrease the amount of gas unbound by the feedback and also increase the central gas density (below 1 kpc) of the halo at the end of the simulation.

5.5.8 A smaller galaxy (Runs 5 and 6)

From Fig. 5.9 we can see altering the size of the galaxy has had the largest impact on the amount of gas unbound from the halo. In both Run 5 and 6 the fraction of the initial gas mass that has been unbound approaches unity by the end of the simulation. However, including gradual feedback has had a large impact on the timescale over which the majority of the gas has been unbound; by 0.5 Myr $\sim$ 100% of the gas has been unbound in Run 6, however, approximately 50 % has been unbound in Run 5.

Looking at the corresponding temperature and density slices taken in the x-z plane at y=0 (Fig. 5.36), we see Run 5 has gas extending to beyond 200 kpc, while the gas in Run 6 is confined to below 100 kpc. The central 40 kpc of Run 6 has been uniformly heated to 10^6 K, while the same radius in Run 5 contains regions of cooler ($< 10^3$ K) gas. Run 5 appears to be in the process of funneling hot (10^5 - 10^6 K) gas away from the galactic centre, via multiple lower density ($< 10^{-32}$ gcm^{-3}) 'chimneys' or channels, similar to those seen in Chapters 3 and 4. This chimney can also been seen in the corresponding y-z and x-y planes.

To investigate the large difference between the mass fraction of unbound gas seen for Run 5 and 6 in Fig. 5.9 approximately half way through the simulation, I plot the temperature and density of the gas in both runs for a snapshot at 489 Myr (Fig. 5.37). Here we see a large difference in the gas phases between runs. There is a branch of low density ($< 10^{-29}$ gcm^{-3}) gas spanning a temperature range from 20 K to 3×10^4 K in Run 6 that is not present in Run 5. I explore the origins of this gas in Run 6 by coloring a subset of these particles red and plotting both the radial velocity and the density of all particle in the simulations, as a function of radius (Fig. 5.38 and Fig. 5.39) respectively. Here we see multiple SNe in the centre of the

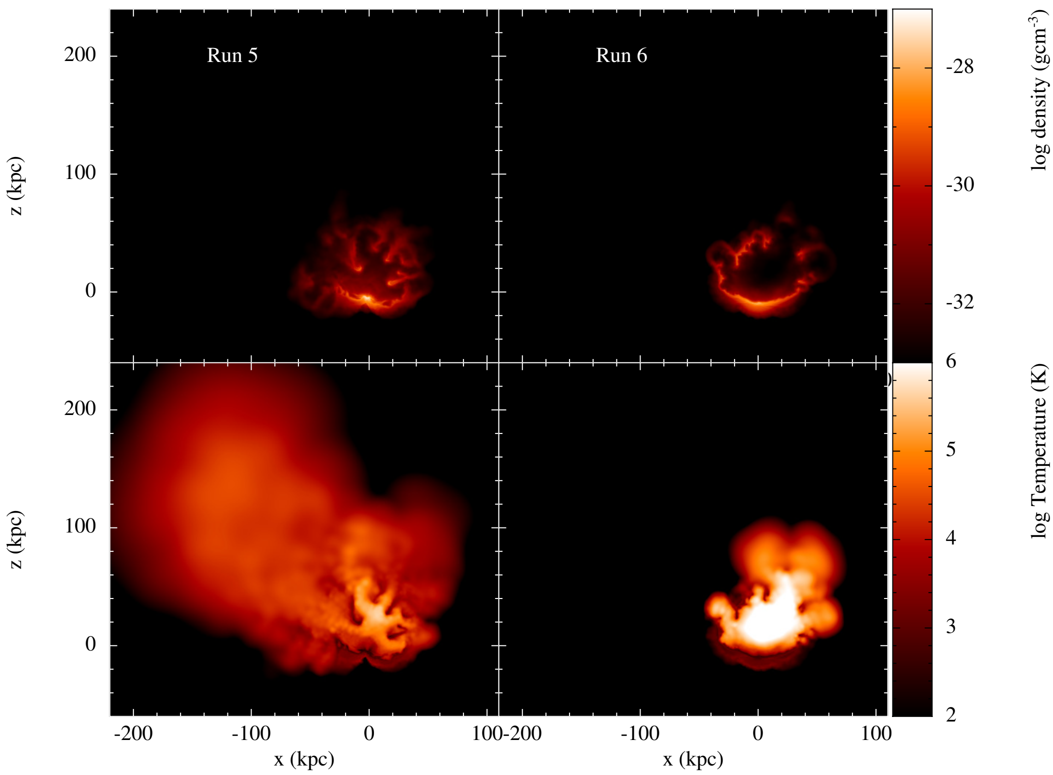

FIGURE 5.36: Density and temperature slices (upper row and bottom row respectively) for Runs 5 (left column) and 6 (right column), taken at 1 Gyr in the x-z plane at y = 0.

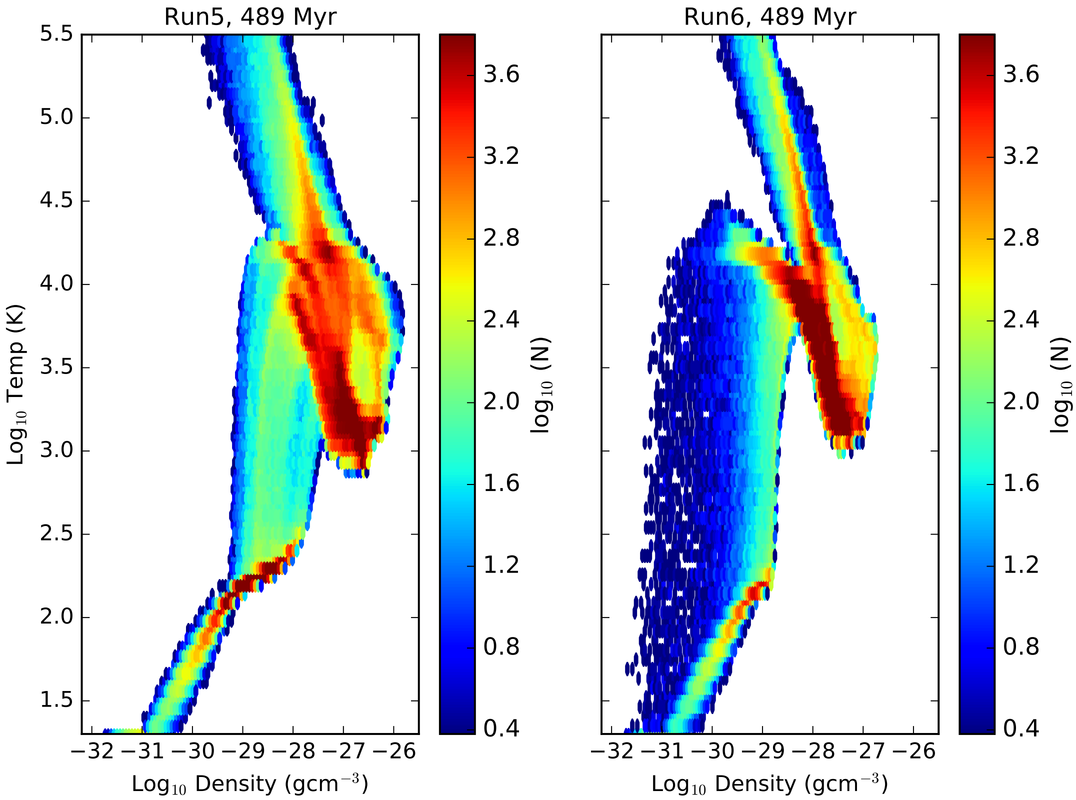

FIGURE 5.37: The density and temperature of gas particles 489 Myr into Runs 5 (left) and 6 (right), rendered according to particle number.

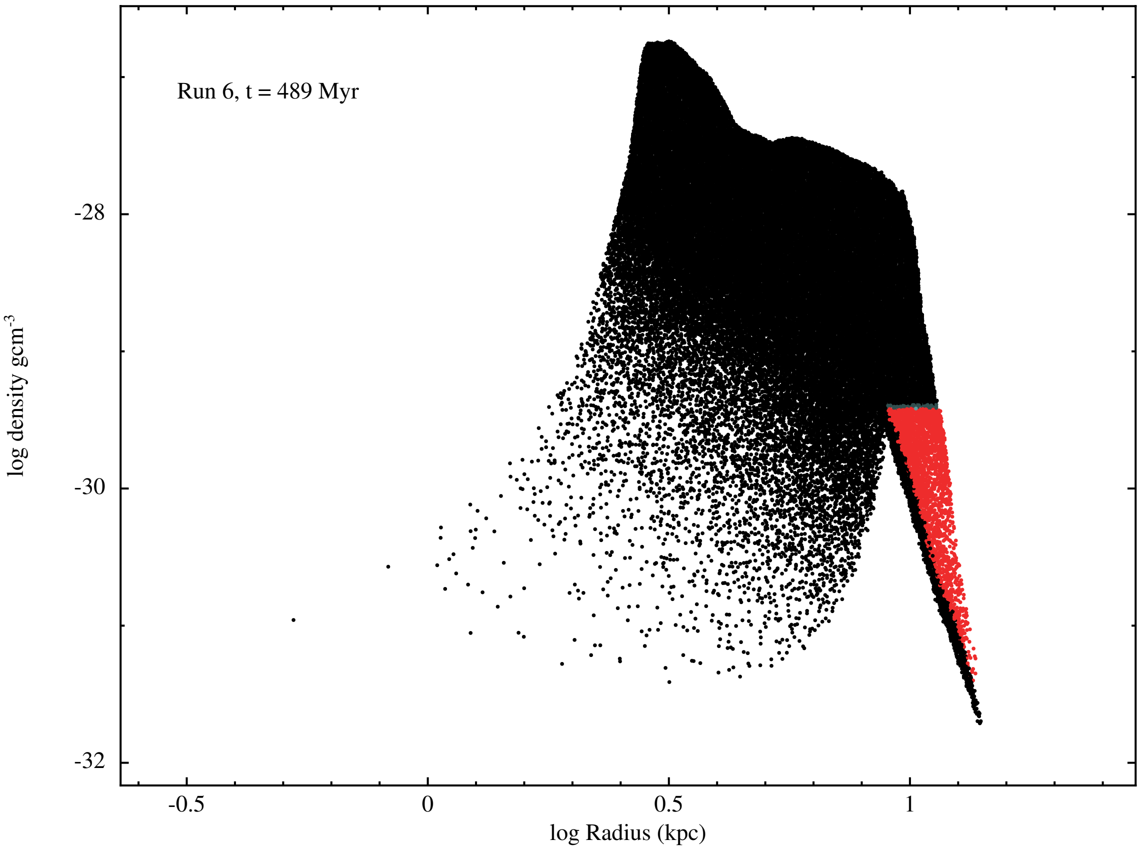

FIGURE 5.38: The density versus radius of all gas particles in Run 6 at 489 Myr, with a subset colored red according to their position in Fig. 5.37. These particles have a density lower than 10^{-29} gcm^{-3} temperatures spanning 20 K to 3×10^4K. Particles with this temperature and density range are missing from Run 5.

galaxy have resulted in a roughly spherical shock front, indicated by the density peak in Fig. 5.38. The low density particles we are interested in constitute the swept-up mass of the shock. Here the gas has been accelerated radially (shown by the positive radial velocity) to the outskirts of the gas halo. If I also plot the density profile for the particles in Run 5 (Fig. 5.40), this swept-up mass is absent, while the global density peak is more fragmented, consisting of multiple shocks that are out of phase with one another (as opposed to the smoother density peak of Run 6).

I also plot the x-z density and temperature y = 0 slices for Run 5 and Run 6 at 489 Myr (Fig. 5.41), to investigate the origin of the swept-up mass that is present in Run 6 (Fig. 5.38) and absent in Run 5 (Fig. 5.40). Here we see, as was indicated by Fig 5.38, multiple SNe have created a more or less isotropic, hot bubble of gas, which is expanding and sweeping up the surrounding ISM to produce a dense,

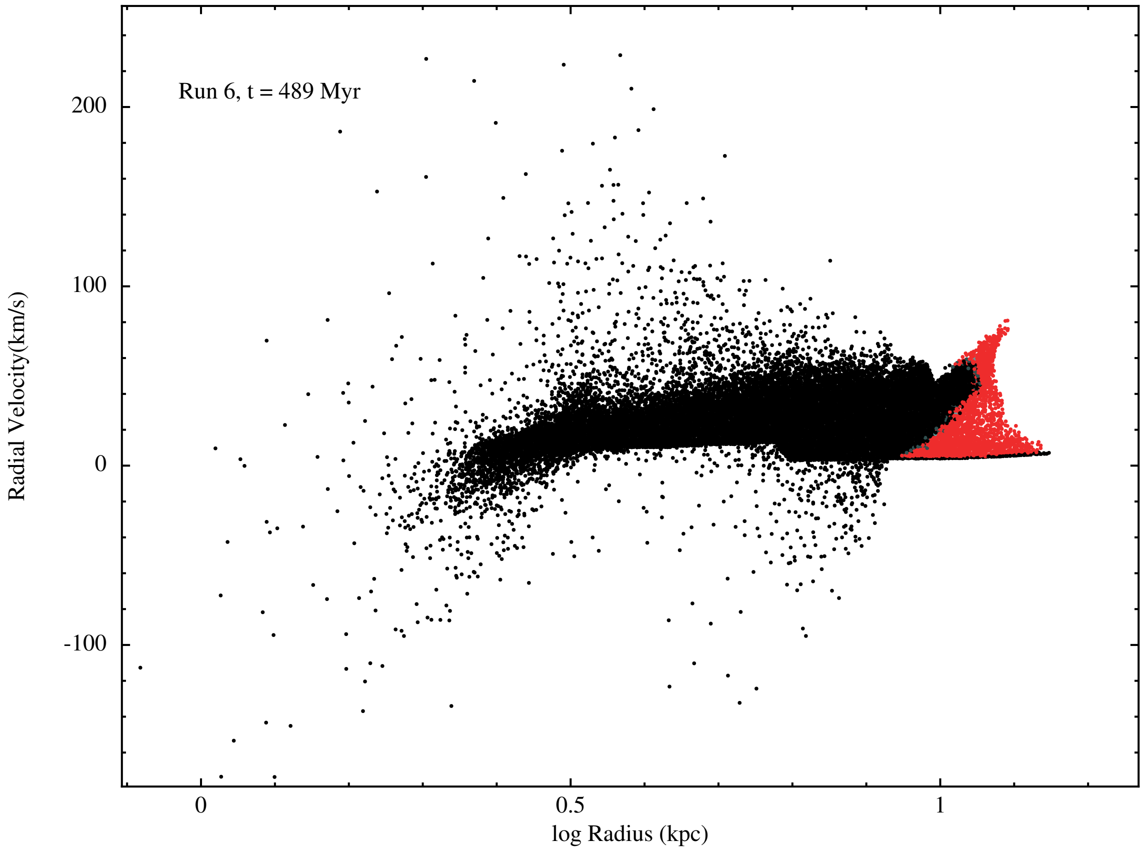

FIGURE 5.39: The radial velocity versus radius of all gas particles in Run 6 at 489 Myr, with a subset colored red according to their position in Fig. 5.37. These particles have a density lower than 10^{-29} gcm^{-3} temperatures spanning 20 K to 3×10^4K.

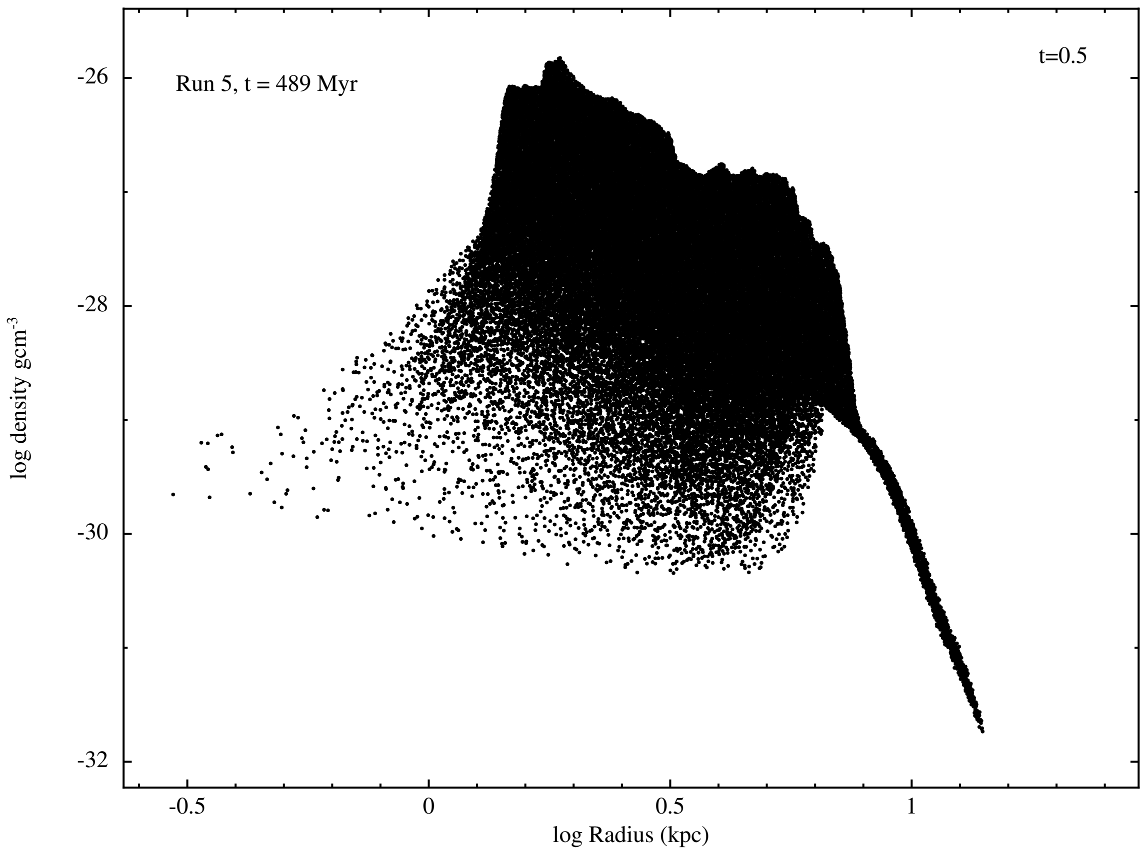

FIGURE 5.40: The density versus radius of all gas particles in Run 5 at 489 Myr.

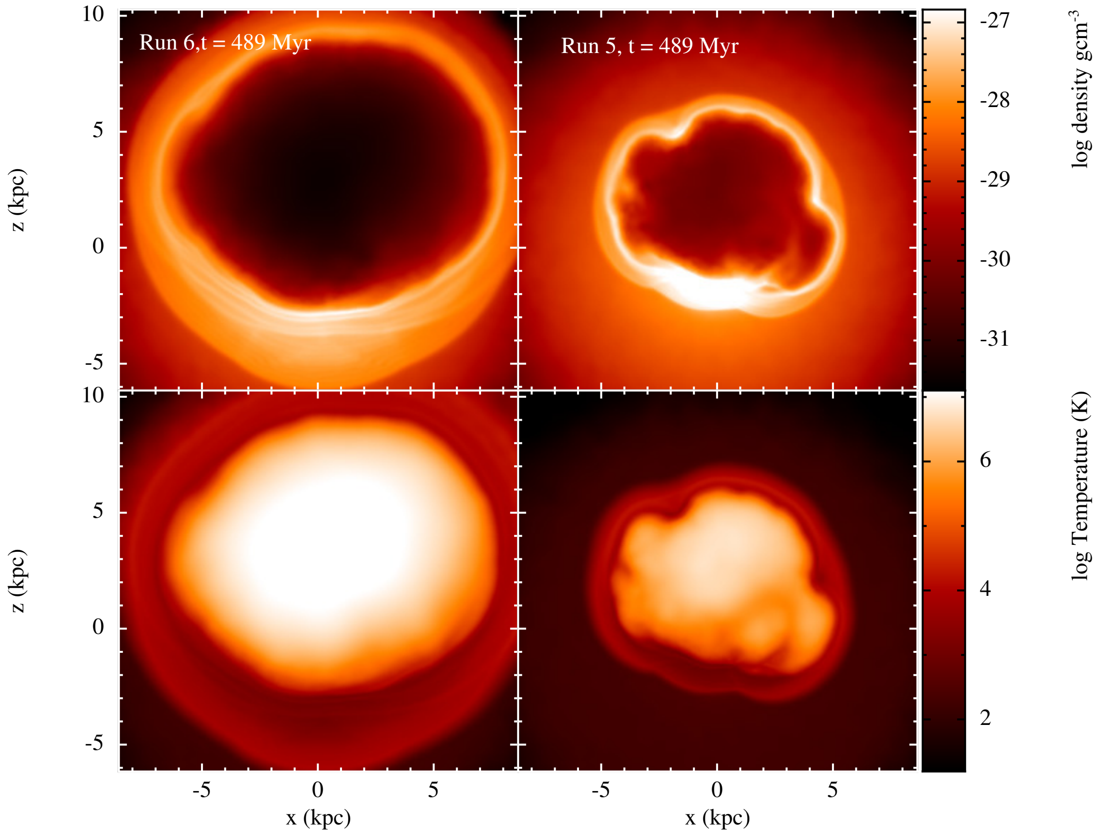

FIGURE 5.41: Density and temperature slices (upper row and bottom row respectively) for Runs 5 (right column) and 6 (left column), taken at 489 Myr in the x-z plane at y = 0.

cool/warm ($\sim 10^4$-10^2 K, as was seen in Fig. 5.37) shell of gas, which is 4 kpc thick in places. On the contrary, adding HMXB and wind feedback to Run 5 has resulted in a bubble that is less spatially extended and 'pinched' in places. These 'pinches' represent regions of high density, cold gas that have survived the expansion of the feedback-heated ISM. In this way, the gradual feedback has acted to reduce the mixing of the feedback-heated gas and the colder, denser gas. In particular, dense regions have formed between feedback-heated bubbles, representing areas where shells of swept-up mass have collided. In the case of Run 6 these have been efficiently heated and hence destroyed by the more powerful SNe explosions. However, since the stellar winds are less powerful, the warm gas inside the bubbles has instead escaped through the low density channels either side, carving low density chimneys as they do so. These then provide a path of least resistance for the SNe energy to escape the galaxy and less efficiently couple to the cold, dense ISM.

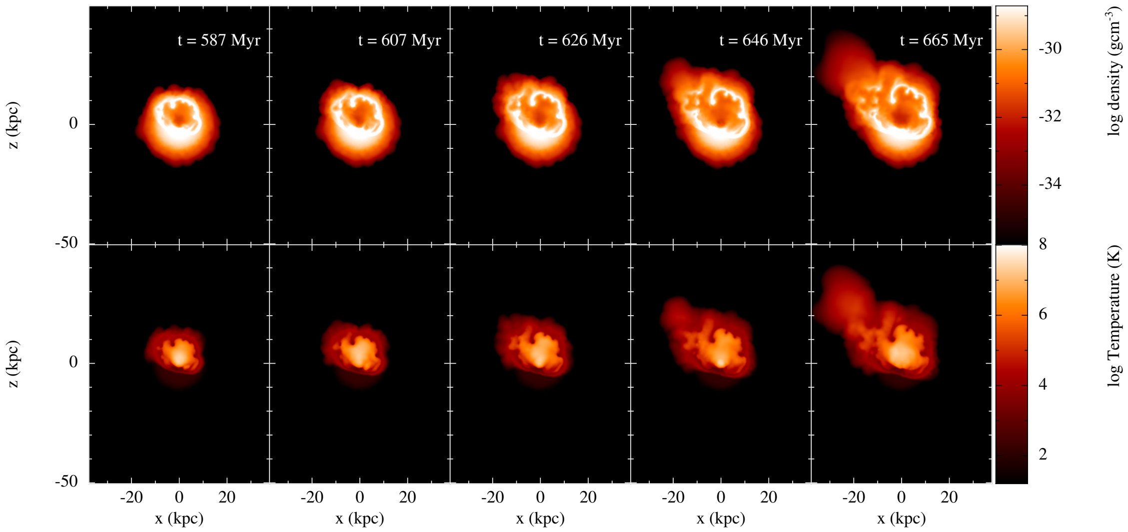

FIGURE 5.42: Density and temperature slices (upper row and bottom row respectively) for Run 5, taken at times ranging from 587 Gyr to 665 Gyr in the x-z plane at y = 0.

In Fig. 5.42 I follow the evolution of Run 5 across 78 Myr from 587 Myr to 665 Myr in order to track the development of the chimney seen in Fig. 5.36. Comparing with Fig. 5.22, we see winds are ubiquitous throughout this period, however there are also two episodes of HMXB feedback between 600 Myr and 700 Myr. It is at this point the hot, pressurised gas inside the bubble punches through the least dense areas of the surrounding shell (to the left of the plots) and beyond this hot gas is in the process of being vented through these gaps. This suggests the more powerful HMXB events facilitate the formation of 'chimneys' in the swept-up high density shell, which act to vent hot gas. Looking at Fig. 5.36, at 1 Gyr it appears these chimneys have acted to reduce the temperature of the gas in the centre of the halo, as well as maintain regions of high density, cold gas in the central 10 kpc of the halo. We can also see this when I plot the maximum, mean and minimum temperature of the gas located in the central 10 kpc of the halo for both Runs 5 and 6 (Fig. 5.43). Here we see the maximum, mean and minimum temperatures are generally higher in Run 6 than Run 5. Furthermore, the steep rise in the minimum temperature of the gas in Run 6 beyond 600 Myr, is not present in Run 5, while the maximum gas temperature converges at this time, indicating the effect of the chimney seen in Fig 5.42 has been to prevent the coldest gas from

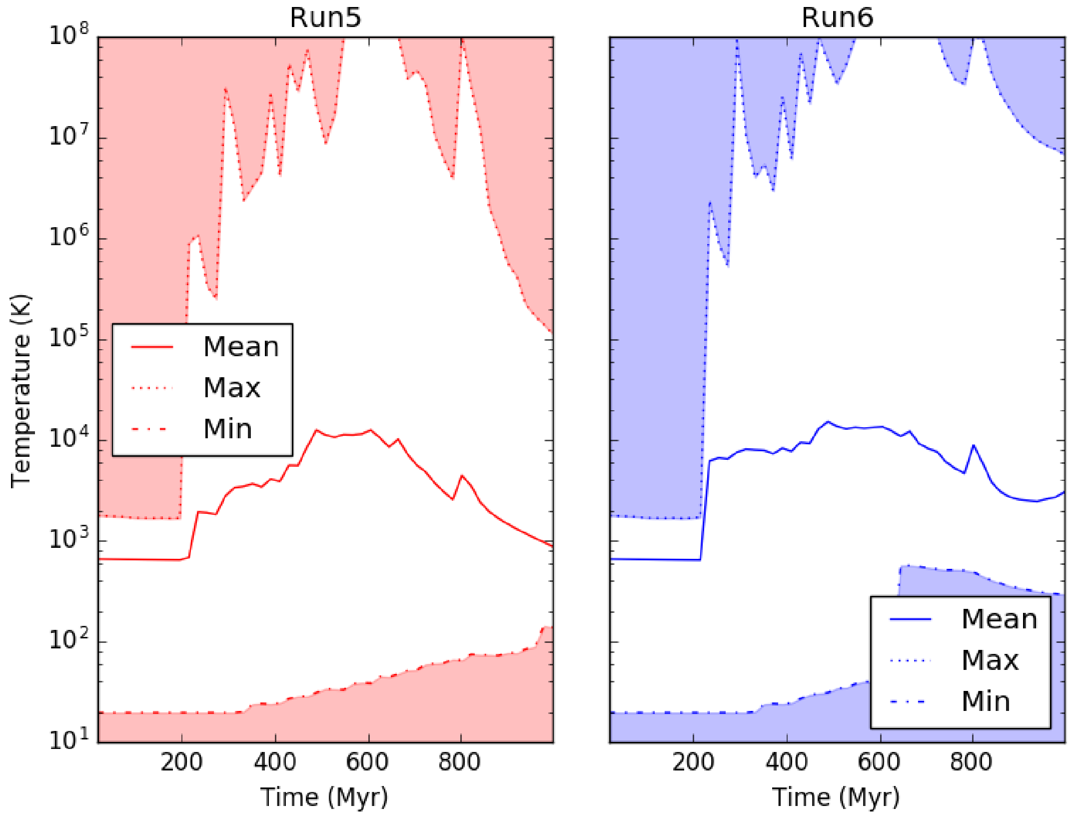

FIGURE 5.43: A plot to show the evolution of the mean (solid lines), minimum (dot-dashed line, bordering the lower shaded areas) and maximum (dotted line, bordering the upper shaded areas) temperature of the gas inside a radius of 10 kpc, across the 1 Gyr starburst in Runs 5 (left plot, red) and 6 (right plot, blue).

being heated by an order of magnitude.

Fig. 5.44 shows the total thermal and kinetic energy of the gas in Run 5 is lower than in Run 6, until beyond 600 Myr, where the total kinetic energies of the two runs converge. Moreover, due to the fact the thermal energy of the gas in Run 6 is higher throughout the simulation, the virial parameter is also consistently higher. Looking instead at the gas density profile (Fig. 5.45), we see the gas density in the inner 10 kpc of the halo is uniformly higher in Run 5 than Run 6, however beyond this radius the gas in Run 5 extends to lower densities than the gas in Run 6 - indicating the low density, warm/hot outflowing gas seen in Fig. 5.36. Moreover, contrary to the simulations with the larger halo mass, there is no evidence for inflowing gas from the density profile of the smaller halo runs.

Interestingly, when I plot the evolution of the inner dark matter halo density

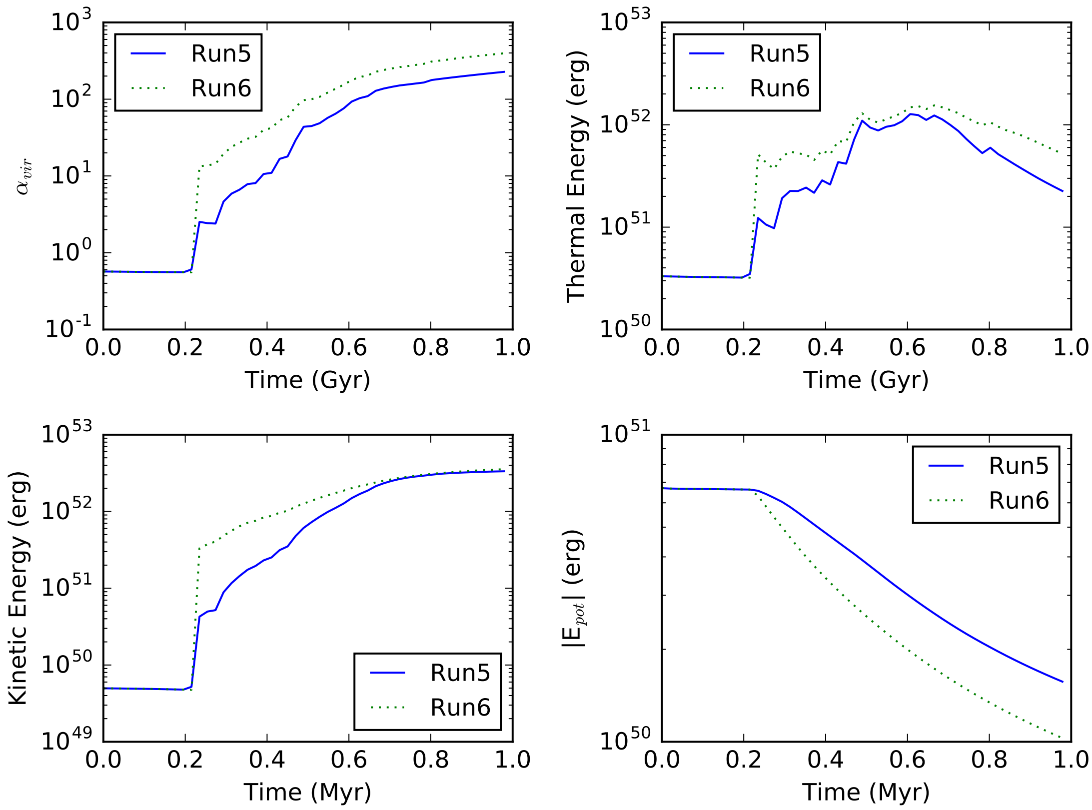

FIGURE 5.44: The time evolution of the virial parameter (top left plot, where α_{vir} = E$_{kin}$ + E$_{therm}$ / |E$_{pot}$|) and the total thermal (top right), kinetic (bottom left) and potential (bottom right) energy of the gas in Run 5 (solid, blue lines) and 6 (dotted, green lines).

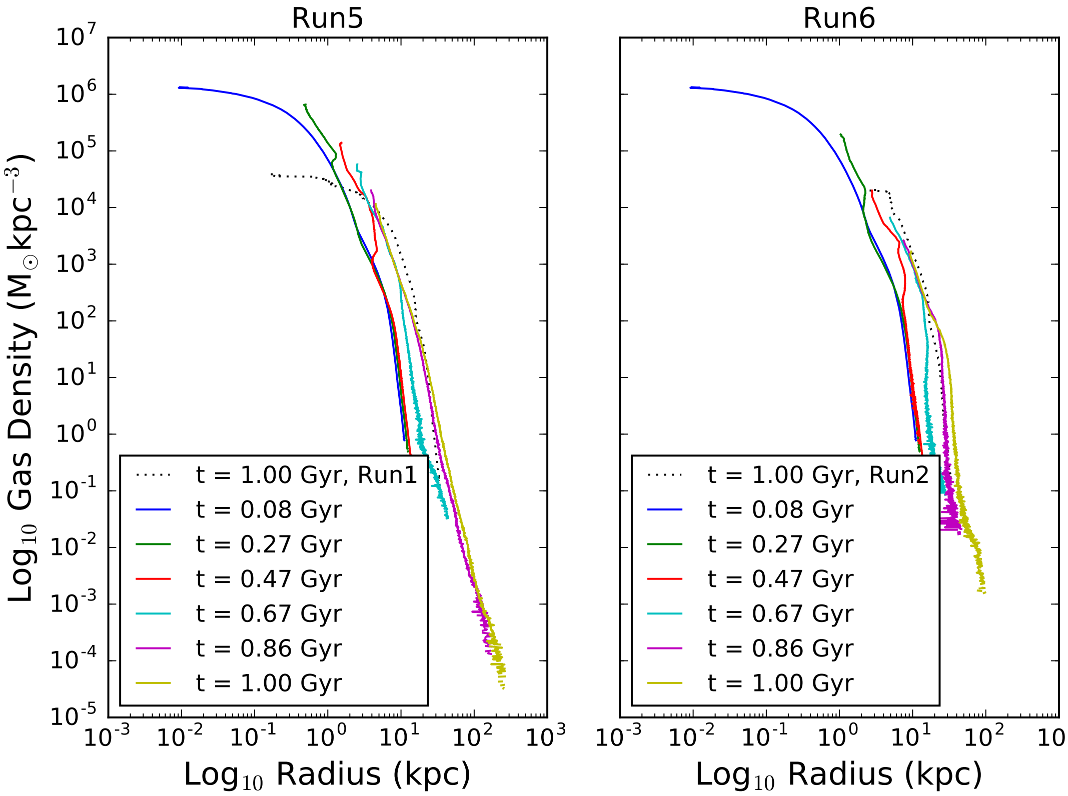

FIGURE 5.45: The density profile of the gas in Runs 5 (left) and 6 (right) taken at various times into each simulation. The final density profiles (taken at 1 Gyr) for Run 1 and 2 (dotted lines) have been over-plotted on Run 5 and 6 respectively.

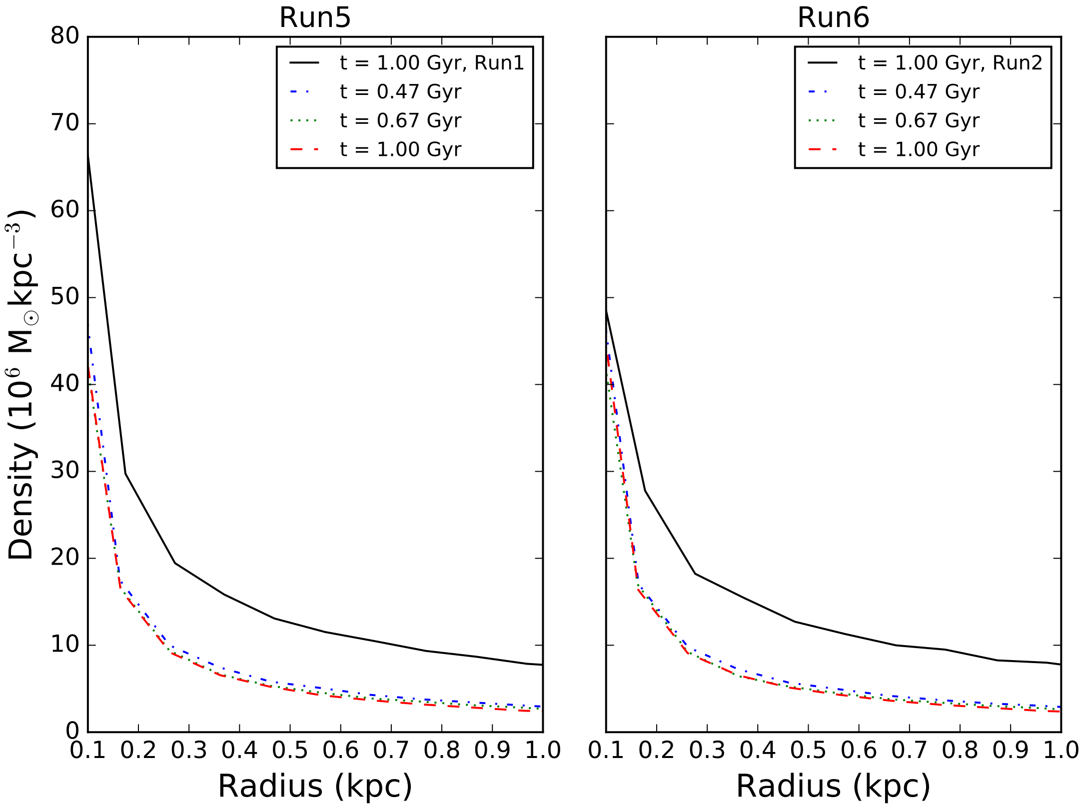

FIGURE 5.46: The inner (1 kpc) dark matter density profiles taken at varying times into Run 5 (left plot) and 6 (right plot). The dark matter density profile taken at the end (corresponding to t = 1 Gyr) of Run 1 and 2 have been over-plotted on Run 5 and 6 respectively.

(Fig. 5.46), we can see very little evolution of the density profile across both simulations, indicating the changes to the total energy of the dark matter caused by the outflowing baryons have been reversible. We see this when I plot the time evolution of the total energy (E_{kin} + E_{therm}) of the dark matter in Runs 5 and 6 (Fig. 5.47). The dark matter particles gain and lose potential/kinetic energy in such a way as to oscillate about approximately the same total energy. The particles at 20 kpc and 50 kpc show a slight increase in total energy, however the particle at 100 pc is losing energy across the simulations. There are also no significant differences between the fate of the same particles in Runs 5 and 6.

In summary, the inclusion of gradual feedback (on top of SNe feedback) in a smaller galaxy of halo mass 1.5×10^7 M$_\odot$ has increased the time it has taken to unbind the majority of the gas. It has also facilitated the production of chimneys,

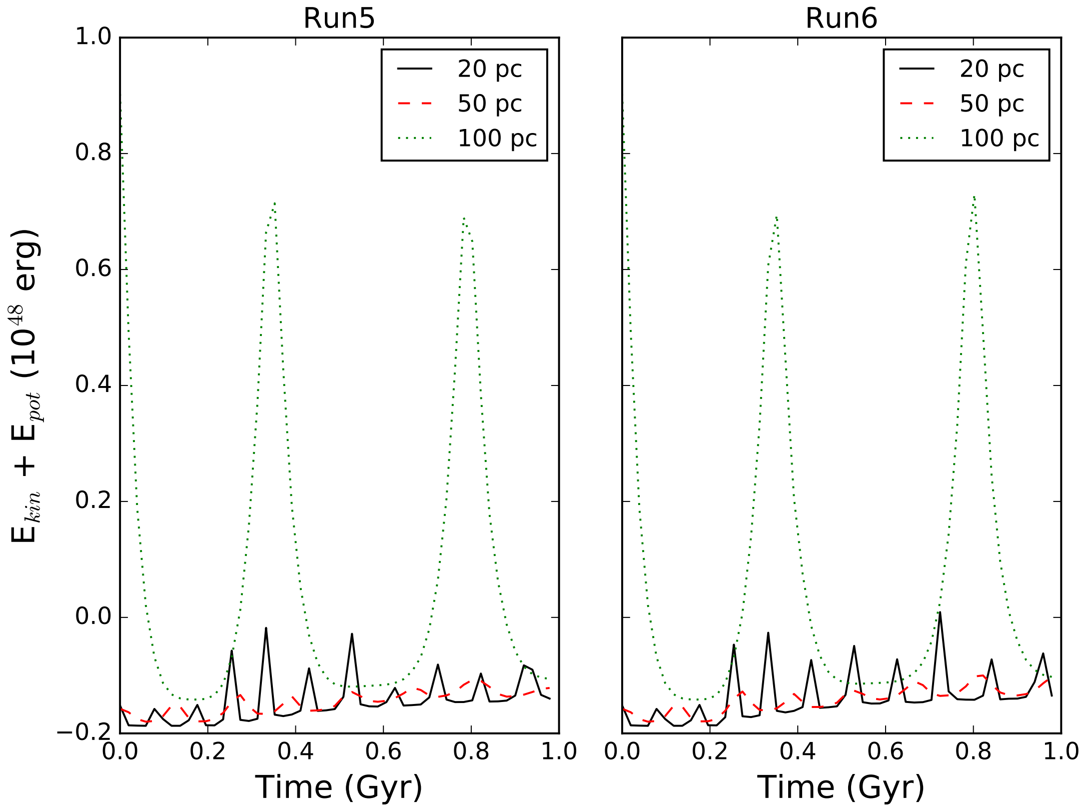

FIGURE 5.47: Figure to show the sum of the kinetic and potential energy of particles takes within 20 pc, 50 pc and 100 pc of Run 5 (left) and Run 6 (right). Again, the same particles are being evaluated in both runs.

which have vented hot gas from the centre of the halo and lowered the temperature of the gas in the central 10 kpc. Furthermore, the centre of the dark matter halo was largely unaffected in both Run 5 and 6, due to the fact the increase in the total energy of the dark matter particles (via gaseous outflows) was reversible.

5.5.9 Evaluating the relative impact of HMXBs and stellar winds (Runs NoHMXB and NoWinds)

Fig. 5.48 plots the unbound gas mass as a fraction of the initial mass in Runs 1, 2, NoWinds and NoHMXB. All runs had the same initial conditions (halo mass - 1.1×10^8 $M_\odot$, [Fe/H] = - 6), however used different combinations of stellar feedback (see Table 3.1). We can see Runs 1 and NoHMXB are in good agreement, indicating the decrease in the amount of gas unbound via the addition of gradual feedback in Run 1 (compared with Run 2) is due to stellar winds, rather than HMXB feedback. Furthermore, by excluding stellar winds the unbound mass fraction has converged with Run 2, which just includes SNe feedback. Again, this points to the fact the ubiquity of stellar winds (seen in Fig. 5.22), despite their relatively low power compared with HMXBs, means they have a far more significant impact on the fate of the gas in the galaxy.

The same trends can be seen in the virial parameter, along with the total thermal, kinetic and potential energies of the gas in Runs 1, 2, NoWinds and NoHMXB (Fig. 5.49). Once again, Runs 2 and NoWinds are converged, indicating HMXBs have had little impact on the energetics of the gas when added on top of SNe feedback. Moreover, Run 1 and NoHMXB also converge, indicating including stellar winds is the defining factor in determining the total kinetic, thermal energy of the galactic ISM.

Focusing on the dark matter profile in Fig. 5.50, we see Run 1 converges with the run without HMXB feedback (NoHMXB), while Run 2 converges with the run without stellar winds (NoWinds), indicating the addition of HMXB feedback has an insignificant affect on the underlying dark matter profile.

Overall, it is the inclusion of stellar winds that has driven the observed trends in the gas and dark matter that are the key results of this chapter.

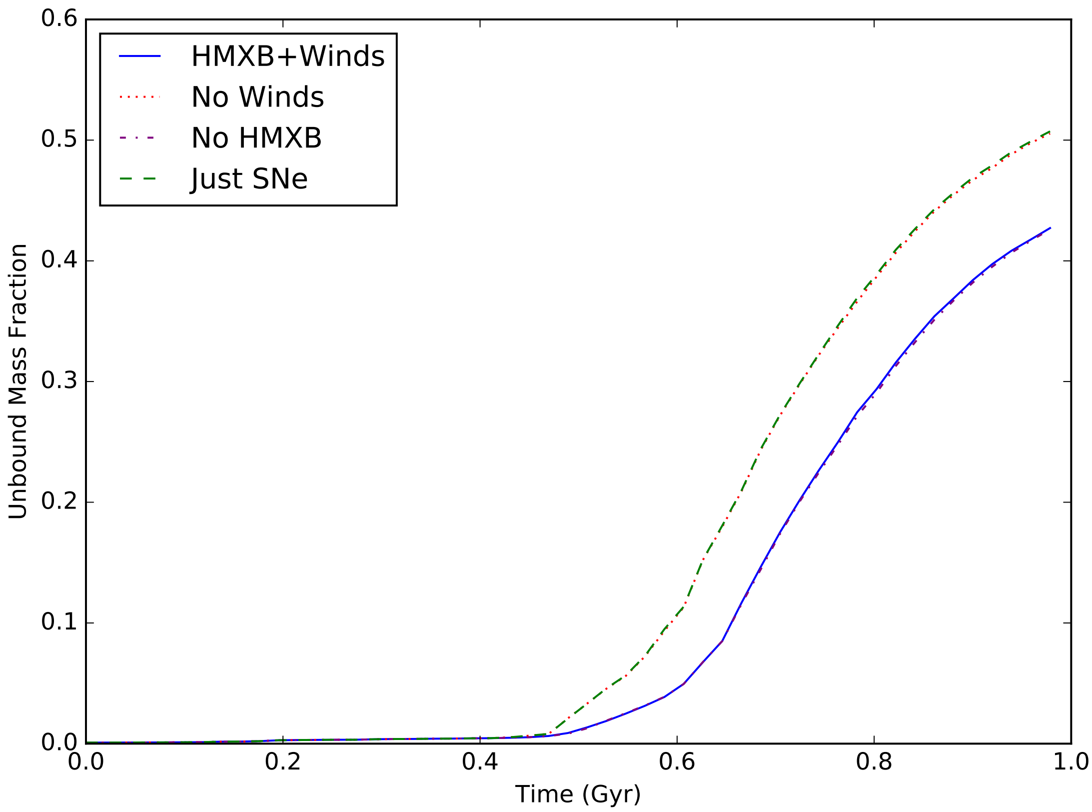

FIGURE 5.48: The time evolution of the fraction of the initial gas mass that has been unbound in Run 1 (which includes SNe, HMXB and stellar wind feedback, solid line), 2 (just SNe, dashed line), NoWinds (HMXBs and SNe, dotted line) and NoHMXB (winds and SNe, dot-dashed line).

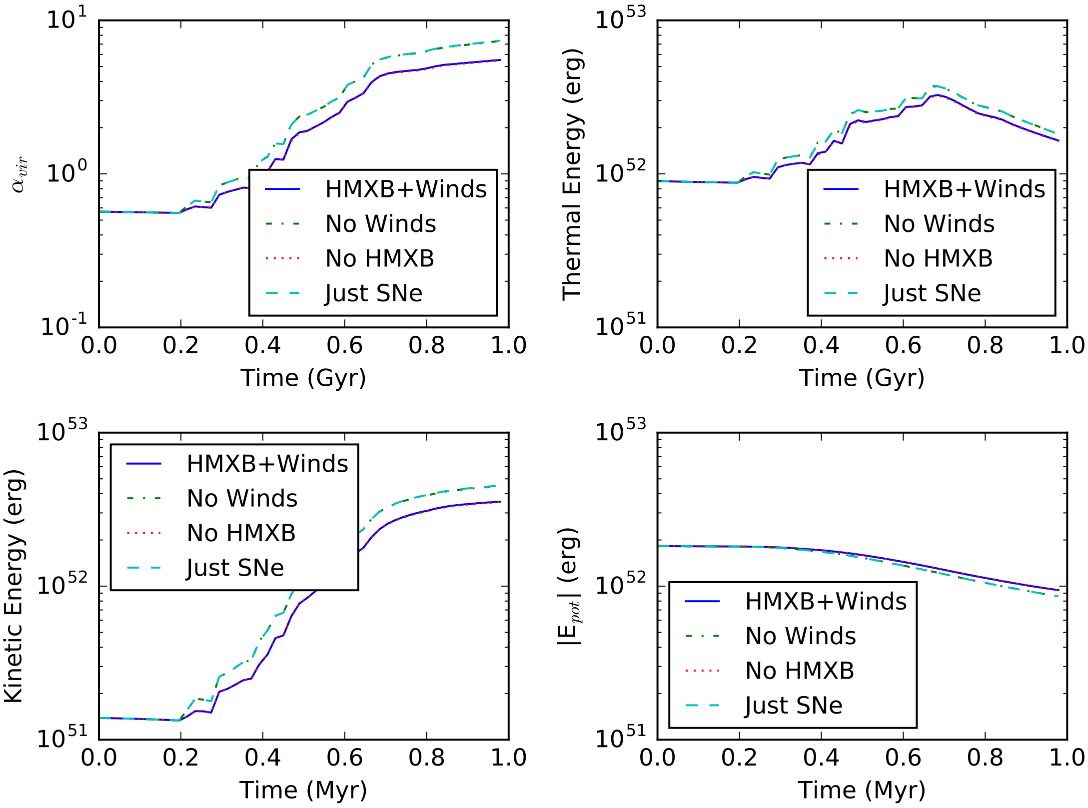

FIGURE 5.49: Plots to compare α_{vir} ($E_{therm} + E_{kin}/|E_{pot}|$ - top left plot), along with the total thermal (top right), kinetic (bottom left) and potential (bottom right) energies of the gas particles in Runs 1 (solid line), NoWinds (dot-dashed line line), NoHMXB (dotted line) and 2 (dashed line).

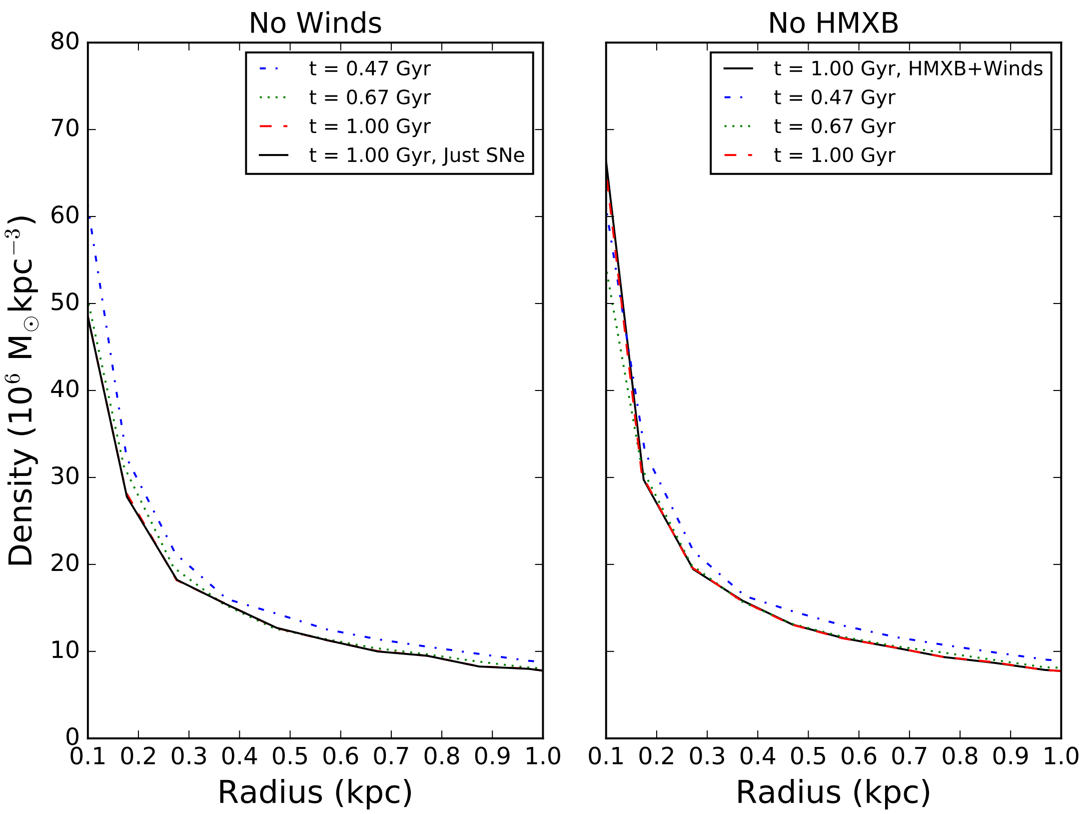

FIGURE 5.50: The dark matter density profiles taken at various times into Run NoWinds (left) and NoHMXB (right), with the final density profiles of Runs 1 and 2 overlaid onto Run NoHMXB and NoWinds respectively (dotted lines).

5.6 Discussion

In this chapter I investigated the inclusion of 'gradual' feedback types on top of SNe feedback in high redshift isolated dwarf galaxies with halo masses between 1.1×10^{8} $M_{\odot}$ and 1.5×10^{7} $M_{\odot}$. The main results of this chapter are as follows:

- The fraction of the initial gas mass that has been unbound after 1 Gyr starburst is uniformly lower in the galaxies that include gradual feedback mechanisms on top of SNe feedback. This result holds across the galaxy masses I tested, along with varying metallicity, halo concentration and the duration of the starburst.

- In all runs the dark matter density in the central 1 kpc of the halo is reduced by less than an order of magnitude. There is also evidence to suggest gradual feedback has acted to reduce the amount of energy transferred to the dark matter via changes in potential resulting from gaseous outflows. However this result is dependent on both the starburst duration and the galaxy mass.

- By varying the standard deviation (σ_{star}) of the 'wake-up' times of the stars (and therefore the duration of the starburst), I found the total kinetic energy of the gas in the simulations with varying σ_{star} converged beyond 800 Myr. Moreover, the total internal energy of the gas was marginally lower in the $\sigma_{0.5}$ runs, indicating the gas was able to cool more efficiently in the shorter, more violent starburst.

- Moreover, decreasing the duration of the starburst (while keeping the total number of feedback events the same) increased the gas density below 10 kpc at the end of the runs which just included SNe feedback, along with inside the inner 1 kpc of runs which also included gradual feedback.

- However, a more concentrated, violent starburst also transfered more energy to the dark matter in the central 150 pc. The differences in this energy transfer between runs which did or did not include gradual feedback was also reduced.

- Altering the metallicity of the gas in the galaxy from [Fe/H] = -6 to [Fe/H] = - 1.2 had very little impact on the state of the gas and the underlying dark matter halo. This was due to the fact the density of the gas in the galaxy resulted in comparable cooling times for high and low metallicity gas.

- As expected, increasing the concentration parameter lowered the amount of gas unbound by the stellar feedback by increasing the potential at the centre of the halo. As well as this, the dark matter halo was largely unaffected by the stellar feedback.
- Altering the size of the galaxy had the largest impact on the results. In these runs the majority of the gas was unbound in both simulations. However, the addition of gradual feedback acted to delay the unbinding of the gas. Furthermore, the addition of stellar winds facilitated the production of chimneys; which are holes in the high density shell surrounding the volume-filling, pressurised gas that vent the hot gas from the centre of the halo. These chimneys globally reduce the temperature of the gas in the central 10 kpc of the galaxy.
- Additionally, the central 1 kpc of the dark matter halo density profile was largely unaffected by the stellar feedback in the smaller galaxy, since any changes to the total energy of the dark matter particles were reversible.
- Finally, I evaluated the relative impact of HMXB feedback and stellar winds on the results, finding the ubiquity of stellar winds means they are more or less solely responsible for changes in the unbound mass and gas/ dark matter energetics seen in the 1.1×10^{8} $M_{\odot}$ galaxy. How this changes with galaxy mass and metallicity would be interesting to follow-up, however is beyond the scope of this thesis. It would also be interesting to investigate how this result varies if the HMXB feedback is no longer implemented isotropically.

5.6.1 The results in context

The results of this chapter point to the importance of considering time-resolved feedback events, including both instantaneous, spatially resolved SNe, along with the continuous low-powered energy injection of winds. For example, the chimney seen in Run 5 was formed via colliding wind-fed bubbles, a process which is only possible if individual massive stars are resolved spatially. This result links to work by Su et al. (2017), who found modelling discrete SNe events was essential to capturing the multiphase ISM along with forming galactic winds with physical mass loading factors. Moreover, since the mean temperature of the gas in the simulations was typically below 10^4 K, the results also highlight the need to include low temperature cooling prescriptions in these low mass galaxies.

There is an existing large volume of work on SNe-generated superbubbles, similar to the 10 kpc-scale bubble of hot pressurised gas seen in Fig. 5.41. This includes both analytical work (e.g. Weaver et al., 1977; Tomisaka, Habe, and Ikeuchi, 1981), along with multiple observations of superbubbles such as Pidopryhora, Lockman, and Shields (2007) and Ochsendorf et al. (2015). Typically the radii of these superbubbles are an order of magnitude lower than the superbubble seen in Run 6, however once I included gradual feedback this radius is reduced.

The superbubbles seen in Run 5 and 6 (see Fig. 5.41) have similar properties to the superbubbles investigated in Kim, Ostriker, and Raileanu (2017). Like the superbubbles presented in Kim, Ostriker, and Raileanu (2017), the gas in the centre of the bubble has been heated to between 10^{6-7} K and accelerated to $\sim 10^2$ km/s. The expansion velocity of between 10-100 km/s is enough to unbind the gas from the shallow potential well of the dwarf galaxy. In this work the bubble in Run 6 is also surrounded by a cooler high density shell, which was also present in Kim, Ostriker, and Raileanu (2017). In Kim, Ostriker, and Raileanu (2017), this shell was formed of warm, swept-up gas that has cooled. The range of (cool) temperatures seen in this shell in the simulations would also fit with this hypothesis. In Run 5, the shell has a more complicated morphology, while the shell is less spatially extended. This makes it easier for the hot, feedback-heated gas to clear low density channels or 'chimneys' in the shell. These chimneys have the capacity to launch hot, high velocity gas to a radius of $\sim 10^2$ kpc (as seen in Fig. 5.36).

The production of 'chimneys' via stellar winds has been found previously, particularly in GMCs. In particular, Rogers and Pittard (2013) found winds acting prior to SNe feedback preferentially escape the inner molecular cloud via paths of least resistance, creating low density channels through which the proceeding SNe energy can escape with weak coupling to the higher density molecular clumps at the centre of the cloud. We can see this process in action in the simulations, in particular Fig. 5.42.

The result that the addition of HMXB feedback does not significantly alter the state of the gas in the galaxies is contrary to work by Artale, Tissera, and Pellizza (2015), who found the addition of HMXB feedback on top of SNe feedback can significantly impact the removal of gas in low mass haloes (less than 10^{10} $M_\odot$).

However, the halo masses of 10^7 $M_\odot$ and 10^8 $M_\odot$ are below their mass range and hence are not directly comparable. Moreover, it is also possible these results are dependent on metallicity, as was seen in Chapter 4.

This work neglects the stellar luminosities of the massive stars, which for a star with a mass of 8 $M_\odot$ is $\sim 10^{37}$ erg/s (following calculations by Bressan et al., 1993, at solar metallicity). However the impact of this radiation and its ability to produce momentum-driven outflows depends on the coupling of this energy to the ISM. For example, Krumholz and Matzner (2009) find if the expansion of massive star wind-fed bubbles are energy driven, the kinetic energy of the momentum-driven shell produced by the stellar radiation is $\sim$ 100 times smaller. Moreover, Rogers and Pittard (2013) argue, based on Krumholz and Matzner (2009), provided the leakage of wind energy is comparable to the leakage of stellar photons, radiation pressure will be of the same order as the wind pressure. However, in future work I would like to investigate the inclusion of stellar radiation and HII region expansion on top of line-driven winds in order to assess their comparative impact on the ISM in dwarf galaxies.

Fundamentally, the fact the dwarf galaxies retain more gas if gradual feedback is included, means they can fuel further star formation. This can help explain the star formation histories seen in dwarf satellite galaxies such as Fornax, Leo I, And VI and Carina, which show multiple starbursts across $\sim$ 12 Gyr (Weisz et al., 2014).

Chapter 6

Conclusions

6.1 Investigating stellar feedback in GMCs

In Chapters 3 and 4 I explored the effect of gradual heating feedback, as well as SNe feedback, in GMCs of varying metallicity, size and virial parameter. This gradual heating can arise from different mechanisms and in this work I focussed on feedback from HMXBs. The primary result was that the two types of feedback combine to produce kpc-scale chimneys of low density, hot gas. These chimneys help funnel energy away from the inner regions of the cloud, allowing star formation to continue there. The chimneys are present in runs that just include SNe feedback, however the addition of the gradual power input from HMXBs into the ISM can help to prevent the gas inside the chimneys from cooling by increasing its temperature to beyond 10^7 K, where the cooling is Bremsstrahlung dominated and relatively inefficient. The chimneys are more prevalent in larger clouds at higher metallicity. Moreover, the combined effects of SNe and HMXBs are largely washed out in smaller clouds due to the lower binding energy of the gas. The most important factor in determining the fate of a cloud was its ability to cool efficiently; clouds that cooled very efficiently had a large number of lower mass sink particles and as such a smaller number of HMXB/ SNe events. On the other hand the runs that showed suppressed cooling, in particular those at low metallicity, had a smaller number of sink particles with higher masses; resulting in a higher number of HMXB and SNe events.

6.2 Investigating stellar feedback in dSphs

In Chapter 5 I investigated the inclusion of stellar winds and HMXBs on top of SNe in high redshift isolated dSphs of varying mass, metallicity and concentration parameter. The main result was that the mass of gas unbound by stellar feedback across a 1 Gyr starburst is uniformly lowered if gradual feedback mechanisms are included, independent of metallicity, galaxy mass, halo concentration and the duration of the starburst. Furthermore, including gradual feedback in the smallest galaxies (of halo mass $\sim 10^7$ M$_\odot$) delays the unbinding of the majority of the gas and facilitates the production of chimneys in the dense shell surrounding a feedback-generated hot, pressurised 'superbubble'. Moreover, the underlying dark matter halo of the smallest galaxy was less effected by the gaseous outflows generated by the stellar feedback than the larger halo, despite more gas being unbound. Additionally, I found that the global energetics of the gas in simulations that included a short, violent starburst converged with those that had a longer, less concentrated starburst by the end of the stellar feedback. Finally, I investigated the relative impact of HMXB feedback and stellar winds on the results, finding HMXB feedback has had a negligible impact on the final state of the gas in the galaxy. On the other hand, the ubiquity of stellar winds throughout each starburst makes them a defining factor in the final state of the ISM, despite their relatively low mechanical power.

6.3 Future work

Beyond the scope of this work, I have become interested in how the galactic environment of the molecular clouds shapes their star formation histories and the formation of the chimneys seen in Chapter 3. I am keen to develop simulations of clouds which take into their location within host galaxies by the inclusion of the galactic potential and shear (building on work by Rey-Raposo et al., 2017), as well as any galactic winds/ outflows driven by AGN. In this way, I would be interested in following the evolution of cool (below 10^4 K)/ molecular gas in the context of wider galaxy simulations that include both stellar feedback and feedback from AGN (both in the form of winds and jets). Moreover, I would also be interested in conducting simulations which include the radiative feedback processes from stars alongside their mechanical feedback. In particular, I would like to model the ISM of a galaxy during re-ionisation and investigate the comparative and combined effect of the X-ray luminosity and mechanical luminosity from ULXs on the ISM, specifically looking for any enhancements in the escape fraction of ionising photons. Furthermore, the initial conditions in this thesis represent the idealised conditions often used when studying isolated molecular clouds (e.g. Dale, Ercolano, and Bonnell, 2012; Federrath et al., 2014). In reality, molecular clouds are dynamic and often unbound (Dobbs, Burkert, and Pringle, 2011). Therefore, I would be interested in developing a scheme to allow the evolution of an unbound cloud to be traced, with self-gravity turned on, that would also prevent the majority of the initial turbulent molecular gas from shock heating, efficiently cooling and becoming bound, while still allowing a small fraction of the gas to collapse and form stars.

Leading on from Chapter 5, I would enjoy expanding the scope of my work to include larger scale galaxies ($> 10^{10}$ M$_\odot$). It would also be very interesting to investigate the timing, location and efficiency of star formation in these galaxies - for example, whether in some cases it is triggered by stellar feedback and the timescales of any quenching by stellar processes/ AGN feedback. Furthermore, I think it would be of interest to continue to investigate HMXBs in terms of dSph galaxies, particularly by taking into account the different evolutionary pathways and how these change with redshift (e.g. Linden et al., 2010), along with the anisotropy associated with these sources on local scales. I would also like to continue modelling dSphs across multiple starbursts, taking into account their galactic environment, in order to investigate the recycling of gas across a longer timescale and how this is affected by the ongoing stellar feedback processes.

Bibliography

Aaronson, M. (1983). "Accurate radial velocities for carbon stars in Draco and Ursa Minor - The first hint of a dwarf spheroidal mass-to-light ratio". In: *ApJ* 266, pp. L11–L15.

Abbott, B. P. et al. (2016). "Observation of Gravitational Waves from a Binary Black Hole Merger". In: *Physical Review Letters* 116.6, p. 061102.

Abel, Tom, Greg L. Bryan, and Michael L. Norman (2002). "The formation of the first star in the universe. (Research Article)". In: *Science* 295.5552, p. 93.

Abolmasov, P. (2011). "Understanding ULX nebulae in the framework of supercritical accretion". In: *New Astron.* 16, pp. 138–146.

Agertz, O., R. Teyssier, and B. Moore (2011). "The formation of disc galaxies in a ΛCDM universe". In: *MNRAS* 410, pp. 1391–1408.

Agertz, O. et al. (2013). "Toward a Complete Accounting of Energy and Momentum from Stellar Feedback in Galaxy Formation Simulations". In: *ApJ* 770, p. 25.

Aird, J., A. L. Coil, and A. Georgakakis (2017). "X-rays across the galaxy population - I. Tracing the main sequence of star formation". In: *MNRAS* 465, pp. 3390–3415.

Andrews, B. H. and P. Martini (2013). "The Mass-Metallicity Relation with the Direct Method on Stacked Spectra of SDSS Galaxies". In: *ApJ* 765, p. 140.

Arribas, S. et al. (2014). "Ionized gas outflows and global kinematics of low-z luminous star-forming galaxies". In: *A&A* 568, A14.

Artale, M. C., P. B. Tissera, and L. J. Pellizza (2015). "Stellar feedback from high-mass X-ray binaries in cosmological hydrodynamical simulations". In: *Monthly Notices of the Royal Astronomical Society* 448.4, p. 3071.

Baade, W. and F. Zwicky (1934a). "Cosmic Rays from Super-novae". In: *Contributions from the Mount Wilson Observatory, vol. 3, pp.79-83* 3, pp. 79–83.

— (1934b). "On Super-novae". In: *Contributions from the Mount Wilson Observatory, vol. 3, pp.73-78* 3, pp. 73–78.

Ballesteros-Paredes, J. and L. Hartmann (2007). "Remarks on Rapid vs. Slow Star Formation". In: *Rev. Mex. Astron. Astrofis.* 43, pp. 123–136.

Bally, J. (2016). "Protostellar Outflows". In: *ARA&A* 54, pp. 491–528.

Balsara, D. S. (1989). PhD thesis. , Univ. Illinois at Urbana-Champaign, (1989).

Barbon, R. et al. (1999). "The Asiago Supernova Catalogue - 10 years after". In: *A&AS* 139, pp. 531–536.

Barnes, J. and P. Hut (1986). "A hierarchical O(N log N) force-calculation algorithm". In: *Nature* 324, pp. 446–449.

Basu-Zych, A. R. et al. (2013a). "Evidence for Elevated X-Ray Emission in Local Lyman Break Galaxy Analogs". In: *ApJ* 774, 152, p. 152.

Basu-Zych, A. R. et al. (2013b). "The X-Ray Star Formation Story as Told by Lyman Break Galaxies in the 4 Ms CDF-S". In: *ApJ* 762, p. 45.

Bate, M. R. (2009). "The importance of radiative feedback for the stellar initial mass function". In: *MNRAS* 392, pp. 1363–1380.

Bate, Matthew R. and Andreas Burkert (1997). In: *MNRAS* 288.4, pp. 1060–1072.

Becker, G. D. and J. S. Bolton (2013). "New measurements of the ionizing ultraviolet background over $2 < z < 5$ and implications for hydrogen reionization". In: *MNRAS* 436, pp. 1023–1039.

Begelman, M. C., Andrew R. King, and J. E. Pringle (2006). "The nature of SS433 and the ultraluminous X-ray sources". In: *MNRAS* 370, pp. 399–404.

Bell, A. R. (1978). "The acceleration of cosmic rays in shock fronts. I". In: *MNRAS* 182, pp. 147–156.

Binney, J. and S. Tremaine (2008). *Galactic Dynamics: Second Edition*. Princeton University Press.

Blandford, R. D. and J. P. Ostriker (1978). "Particle acceleration by astrophysical shocks". In: *ApJ* 221, pp. L29–L32.

Blundell, Katherine M. (2001). "Images of an equatorial outflow in SS 433". In: *Astrophysical Journal* 562.1, pp. L79–L82.

Bonnell, I. A., C. J. Clarke, and M. R. Bate (2006). "The Jeans mass and the origin of the knee in the IMF". In: *MNRAS* 368.3, pp. 1296–1300.

Borgani, S. et al. (2008). "The Chemical Enrichment of the ICM from Hydrodynamical Simulations". In: *Space Sci. Rev.* 134, pp. 379–403.

Bourne, M. A. and D. Sijacki (2017). "AGN jet feedback on a moving mesh: cocoon inflation, gas flows and turbulence". In: *MNRAS* 472, pp. 4707–4735.

Bressan, A. et al. (1993). “Evolutionary sequences of stellar models with new radiative opacities. II - Z = 0.02”. In: *A&AS* 100, pp. 647–664.

Brinkmann, W., T. Kotani, and N. Kawai (2005). “XMM-Newton observations of SS 433 I. EPIC spectral analysis”. In: *A&A* 431, pp. 575–586.

Bromm, V. and R. B. Larson (2004). “The First Stars”. In: *ARA&A* 42, pp. 79–118. DOI: 10.1146/annurev.astro.42.053102.134034. eprint: astro-ph/0311019.

Bromm, Volker, Paolo S. Coppi, and Richard B. Larson (2002). “The formation of the first stars. i. the primordial star- forming cloud”. In: *ApJ* 564.1, pp. 23–51.

Brorby, M., P. Kaaret, and A. Prestwich (2014). “X-ray binary formation in low-metallicity blue compact dwarf galaxies”. In: *MNRAS* 441, pp. 2346–2353.

Brorby, M. et al. (2016). “Enhanced X-ray emission from Lyman break analogues and a possible L_X-SFR-metallicity plane”. In: *MNRAS* 457, pp. 4081–4088.

Bullock, James S. and Michael Boylan-Kolchin (2017). “Small-Scale Challenges to the ΛCDM Paradigm”. In: *Annual Review of Astronomy and Astrophysics* 55, pp. 343–387.

Bykov, A. M. et al. (2018). “Cosmic Ray Production in Supernovae”. In: *Space Sci. Rev.* 214, 41, p. 41.

Carigi, L., X. Hernandez, and G. Gilmore (2002). “Chemical evolution models of local dwarf spheroidal galaxies”. In: *MNRAS* 334, pp. 117–128.

Cashmore, C. R. et al. (2017). “Too small to succeed: the difficulty of sustaining star formation in low-mass haloes”. In: *MNRAS* 468, pp. 451–468.

Castor, J., R. McCray, and R. Weaver (1975). “Interstellar bubbles”. In: *ApJ* 200, pp. L107–L110.

Chini, R. et al. (2012). “A spectroscopic survey on the multiplicity of high-mass stars”. In: *MNRAS* 424.3, pp. 1925–1929.

Chornock, R. et al. (2013). “GRB 130606A as a Probe of the Intergalactic Medium and the Interstellar Medium in a Star-forming Galaxy in the First Gyr after the Big Bang”. In: *ApJ* 774, 26, p. 26.

Cioffi, D. F., C. F. McKee, and E. Bertschinger (1988). “Dynamics of radiative supernova remnants”. In: *ApJ* 334, pp. 252–265.

Clark, P. C. et al. (2011). “The Formation and Fragmentation of Disks Around Primordial Protostars”. In: *Science* 331, p. 1040.

Cohen, R. S. et al. (1980). In: *ApJ* 239, p. L53.

Correa, C. A. et al. (2015). "The accretion history of dark matter haloes - III. A physical model for the concentration-mass relation". In: *MNRAS* 452, pp. 1217–1232.

Courant, R., K. Friedrichs, and H. Lewy (1928). "Über die partiellen Differenzengleichungen der mathematischen Physik". In: *Mathematische Annalen* 100, pp. 32–74.

Creasey, P., T. Theuns, and R. G. Bower (2013). "How supernova explosions power galactic winds". In: *MNRAS* 429, pp. 1922–1948.

Creasey, P. et al. (2011). "Numerical overcooling in shocks". In: *MNRAS* 415.4, pp. 3706–3720.

Cullen, L. and W. Dehnen (2010). "Inviscid smoothed particle hydrodynamics". In: *MNRAS* 408, pp. 669–683.

Dale, J. E. (2015). "The modelling of feedback in star formation simulations". In: *New Astron. Rev.* 68, pp. 1–33.

— (2017). "The effect of the virial state of molecular clouds on the influence of feedback from massive stars". In: *MNRAS* 467, pp. 1067–1082.

Dale, J. E., B. Ercolano, and I. A. Bonnell (2012). "Ionizing feedback from massive stars in massive clusters ˘ II. Disruption of bound clusters by photoionization". In: *MNRAS* 424.1, pp. 377–392.

Dale, J. E. et al. (2014). "Before the first supernova: combined effects of H II regions and winds on molecular clouds". In: *MNRAS* 442, pp. 694–712.

Dale, James E. and Ian Bonnell (2011). "Ionizing feedback from massive stars in massive clusters: fake bubbles and untriggered star formation". In: *MNRAS* 414.1, pp. 321–328.

Dalla Vecchia, C. and J. Schaye (2012). "Simulating galactic outflows with thermal supernova feedback". In: *MNRAS* 426, pp. 140–158.

Davé, R., R. Thompson, and P. F. Hopkins (2016). "MUFASA: galaxy formation simulations with meshless hydrodynamics". In: *MNRAS* 462, pp. 3265–3284.

De Young, David S. and John S. Gallagher III (1990). "Selective loss of metals from low- mass galaxies". In: *ApJ* 356.1, pp. L15–L19.

Dehnen, Walter and Hossam Aly (2012). "Improving convergence in smoothed particle hydrodynamics simulations without pairing instability". In: *MNRAS* 425.2, pp. 1068–1082.

Dobbs, C. L., A. Burkert, and J. E. Pringle (2011). "Why are most molecular clouds not gravitationally bound?" In: *MNRAS* 413.4, pp. 2935–2942.

Dobbs, C. L. and J. E. Pringle (2013). "The exciting lives of giant molecular clouds". In: *MNRAS* 432, pp. 653–667.

Dorfi, E. A. and D. Breitschwerdt (2012). "Time-dependent galactic winds. I. Structure and evolution of galactic outflows accompanied by cosmic ray acceleration". In: *A&A* 540, A77.

Douna, V. M. et al. (2015). "Metallicity dependence of high-mass X-ray binary populations". In: *A&A* 579, A44, A44.

Dray, L. M. (2006). "On the metallicity dependence of high-mass X-ray binaries". In: *MNRAS* 370, pp. 2079–2090.

Dubinski, J., R. Narayan, and T. G. Phillips (1995). "Turbulence in Molecular Clouds". In: *ApJ* 448, p. 226.

Dwarkadas, V. V. and J. Gruszko (2012). "What are published X-ray light curves telling us about young supernova expansion?" In: *MNRAS* 419, pp. 1515–1524.

Ekström, S. et al. (2008). "Effects of rotation on the evolution of primordial stars". In: *A&A* 489, pp. 685–698.

Eldridge, J. J., R. G. Izzard, and C. A. Tout (2008). "The effect of massive binaries on stellar populations and supernova progenitors". In: *MNRAS* 384, pp. 1109–1118.

Eldridge, J. J. and E. R. Stanway (2009). "Spectral population synthesis including massive binaries". In: *MNRAS* 400, pp. 1019–1028.

Eldridge, J. J. and C. A. Tout (2004). "The progenitors of core- collapse supernovae". In: *MNRAS* 353.1, pp. 87–97.

Eldridge, J. J. et al. (2017). "Binary Population and Spectral Synthesis Version 2.1: Construction, Observational Verification, and New Results". In: *Publ. Astron. Soc. Australia* 34, e058.

Elias, J. H. et al. (1985). "Type I supernovae in the infrared and their use as distance indicators". In: *ApJ* 296, pp. 379–389.

Elmegreen, Bg (2000). "Star formation in a crossing time". In: *ApJ* 530.1, pp. 277–281.

Emerick, A. et al. (2016). "Gas Loss by Ram Pressure Stripping and Internal Feedback from Low-mass Milky Way Satellites". In: *ApJ* 826, p. 148.

Evans II, N. J. et al. (2009). "The Spitzer c2d Legacy Results: Star-Formation Rates and Efficiencies; Evolution and Lifetimes". In: *ApJS* 181, pp. 321–350.

Fabbiano, G. (2006). "Populations of X-Ray Sources in Galaxies". In: *ARA&A* 44, pp. 323–366.

Fan, X. et al. (2002). "Evolution of the Ionizing Background and the Epoch of Reionization from the Spectra of z˜6 Quasars". In: *AJ* 123, pp. 1247–1257.

Faucher-Giguère, C.-A. et al. (2008). "Evolution of the Intergalactic Opacity: Implications for the Ionizing Background, Cosmic Star Formation, and Quasar Activity". In: *ApJ* 688, pp. 85–107.

Federrath, C. et al. (2014). "Modeling Jet and Outflow Feedback during Star Cluster Formation". In: *ApJ* 790, p. 128.

Fender, R. P., T. M. Belloni, and E. Gallo (2004). "Towards a unified model for black hole X- ray binary jets". In: *MNRAS* 355.4, pp. 1105–1118.

Fender, R. P. et al. (2006). "A transient relativistic radio jet from Cygnus X- 1". In: *MNRAS* 369.2, pp. 603–607.

Fender, Rob and Teo Muñoz-Darias (2015). "The balance of power: accretion and feedback in stellar mass black holes". In: *Lecture Notes in Physics, Berlin Springer Verlag*. Vol. 905. Lecture Notes in Physics, Berlin Springer Verlag, p. 65.

Fierlinger, Katharina M. et al. (2015). "Stellar feedback efficiencies: supernovae versus stellar winds". In: *Monthly Notices of the Royal Astronomical Society* 456.1, pp. 710–730.

Finkelstein, S. L. et al. (2015). "The Evolution of the Galaxy Rest-frame Ultraviolet Luminosity Function over the First Two Billion Years". In: *ApJ* 810, p. 71.

Flores, R. A. and J. R. Primack (1994). "Observational and theoretical constraints on singular dark matter halos". In: *ApJ* 427, pp. L1–L4. eprint: `astro-ph/9402004`.

Fragos, T. et al. (2013a). "Energy Feedback from X-Ray Binaries in the Early Universe". In: *ApJ* 776, p. L31.

Fragos, T. et al. (2013b). "X-Ray Binary Evolution Across Cosmic Time". In: *ApJ* 764, 41, p. 41.

Freyer, T., G. Hensler, and H. W. Yorke (2003). "Massive Stars and the Energy Balance of the Interstellar Medium. I. The Impact of an Isolated 60 M_{solar} Star". In: *ApJ* 594, pp. 888–910.

Frye, B., T. Broadhurst, and N. Benítez (2002). "Spectral Evidence for Widespread Galaxy Outflows at $z > 4$". In: *ApJ* 568, pp. 558–575.

Gallo, Elena et al. (2005). "A dark jet dominates the power output of the stellar black hole Cygnus X- 1". In: *Nature* 436.7052, p. 819.

Garrison-Kimmel, S. et al. (2014). "ELVIS: Exploring the Local Volume in Simulations". In: *MNRAS* 438, pp. 2578–2596.

Gatto, A. et al. (2013). “Unveiling the corona of the Milky Way via ram-pressure stripping of dwarf satellites”. In: *MNRAS* 433, pp. 2749–2763.

Gatto, A. et al. (2015). “Modelling the supernova-driven ISM in different environments”. In: *MNRAS* 449, pp. 1057–1075.

Geen, S. et al. (2015). “A detailed study of feedback from a massive star”. In: *MNRAS* 448, pp. 3248–3264.

Geisler, D. et al. (2007). “Chemical Abundances and Kinematics in Globular Clusters and Local Group Dwarf Galaxies and Their Implications for Formation Theories of the Galactic Halo”. In: *PASP* 119, pp. 939–961.

Gilmore, G. et al. (2007). “The Observed Properties of Dark Matter on Small Spatial Scales”. In: *ApJ* 663, pp. 948–959.

Gingold, R. A. and J. J. Monaghan (1977). “Smoothed particle hydrodynamics - Theory and application to non-spherical stars”. In: *MNRAS* 181, pp. 375–389.

Girichidis, P. et al. (2016). “Launching Cosmic-Ray-driven Outflows from the Magnetized Interstellar Medium”. In: *ApJ* 816, p. L19.

Glover, S. (2005). “The Formation Of The First Stars In The Universe”. In: *Space Sci. Rev.* 117, pp. 445–508.

Goodall, Paul T., Fathallah Alouani-Bibi, and Katherine M. Blundell (2011). “When microquasar jets and supernova collide: hydrodynamically simulating the SS 433–W 50 interaction”. In: *Monthly Notices of the Royal Astronomical Society* 414.4, pp. 2838–2859.

Governato, F. et al. (2010). “Bulgeless dwarf galaxies and dark matter cores from supernova-driven outflows”. In: *Nature* 463, pp. 203–206.

Grebel, E. K. and J. S. Gallagher III (2004). “The Impact of Reionization on the Stellar Populations of Nearby Dwarf Galaxies”. In: *ApJ* 610, pp. L89–L92.

Griffen, B. F. et al. (2016). “The Caterpillar Project: A Large Suite of Milky Way Sized Halos”. In: *ApJ* 818, p. 10.

Gritschneder, M. et al. (2010). “Detailed Numerical Simulations on the Formation of Pillars Around H II Regions”. In: *ApJ* 723, pp. 971–984.

Gunn, J. E. and B. A. Peterson (1965). “On the Density of Neutral Hydrogen in Intergalactic Space.” In: *ApJ* 142, pp. 1633–1641.

Haid, S. et al. (2016). “Supernova blast waves in wind-blown bubbles, turbulent, and power-law ambient media”. In: *MNRAS* 460, pp. 2962–2978.

Hanasz, M. et al. (2013). “Cosmic Rays Can Drive Strong Outflows from Gas-rich High-redshift Disk Galaxies”. In: *ApJ* 777, p. L38.

Harper-Clark, E. and N. Murray (2009). "One-Dimensional Dynamical Models of the Carina Nebula Bubble". In: *ApJ* 693, pp. 1696–1712.

Hartmann, Lee, Javier Ballesteros-Paredes, and Edwin A. Bergin (2001). "Rapid formation of molecular clouds and stars in the solar neighborhood". In: *ApJ* 562.2, pp. 852–868.

Hernquist, L. (1990). "An analytical model for spherical galaxies and bulges". In: *ApJ* 356, pp. 359–364.

Heyer, M. et al. (2009). "Re-Examining Larson's Scaling Relationships in Galactic Molecular Clouds". In: *ApJ* 699, pp. 1092–1103.

Heyer, Mark and T. M. Dame (2015). "Molecular Clouds in the Milky Way". In: *ARA&A* 53, pp. 583–629.

Hodge, P. W. (1971). "Dwarf Galaxies". In: *ARA&A* 9, p. 35.

Hopkins, P. F., E. Quataert, and N. Murray (2012). "Stellar feedback in galaxies and the origin of galaxy-scale winds". In: *MNRAS* 421, pp. 3522–3537.

Hopkins, P. F. et al. (2014). "Galaxies on FIRE (Feedback In Realistic Environments): stellar feedback explains cosmologically inefficient star formation". In: *MNRAS* 445, pp. 581–603.

Hoyle, F. and W. A. Fowler (1960). "Nucleosynthesis in Supernovae." In: *ApJ* 132, p. 565.

Hurley, J. R., C. A. Tout, and O. R. Pols (2002). "Evolution of binary stars and the effect of tides on binary populations". In: *MNRAS* 329, pp. 897–928.

Ibáñez-Mejía, Juan C. et al. (2016). "Gravitational contraction versus supernova driving and the origin of the velocity dispersion– size relation in molecular clouds". In: *ApJ* 824.1, p. 41.

Iffrig, O. and P. Hennebelle (2015). "Mutual influence of supernovae and molecular clouds". In: *A&A* 576, A95.

Izzard, R. G., E. Ramirez-Ruiz, and C. A. Tout (2004). "Formation rates of core-collapse supernovae and gamma-ray bursts". In: *MNRAS* 348, pp. 1215–1228.

Janka, Hans-Thomas (2012). "Explosion Mechanisms of Core-Collapse Supernovae". In: *Annual Review of Nuclear and Particle Science* 62.1, pp. 407–451.

Jappsen, Ak et al. (2005). "The stellar mass spectrum from non- isothermal gravo-turbulent fragmentation". In: *A&A* 435.2, 611–U66.

Justham, Stephen and Kevin Schawinski (2012). "Another thread in the tapestry of stellar feedback: X- ray binaries". In: *MNRAS* 423.2, pp. 1641–1651.

Kaaret, P., J. Schmitt, and M. Gorski (2011). "X-Rays from Blue Compact Dwarf Galaxies". In: *ApJ* 741, p. 10.

Katz, N., D. H. Weinberg, and L. Hernquist (1996). "Cosmological Simulations with TreeSPH". In: *ApJS* 105, p. 19.

Kawamura, Akiko et al. (2009). "The second survey of the molecular clouds in the large magellanic cloud by nanten. ii. star formation". In: *ApJS* 1, pp. 1–17.

Kennicutt Jr., R. C. (1998). "Star Formation in Galaxies Along the Hubble Sequence". In: *ARA&A* 36, pp. 189–232. eprint: astro-ph/9807187.

Kim, C.-G. and E. C. Ostriker (2015). "Momentum Injection by Supernovae in the Interstellar Medium". In: *ApJ* 802, p. 99.

Kim, C.-G., E. C. Ostriker, and W.-T. Kim (2013). "Three-dimensional Hydrodynamic Simulations of Multiphase Galactic Disks with Star Formation Feedback. I. Regulation of Star Formation Rates". In: *ApJ* 776, 1, p. 1.

Kim, C.-G., E. C. Ostriker, and R. Raileanu (2017). "Superbubbles in the Multiphase ISM and the Loading of Galactic Winds". In: *ApJ* 834, 25, p. 25.

Kim, Jeong-Gyu, Woong-Tae Kim, and Eve C. Ostriker (2016). "Disruption of molecular clouds by expansion of dusty h ii regions". In: *ApJ* 819.2, p. 137.

Kimm, Taysun et al. (2015). "Towards simulating star formation in turbulent high-z galaxies with mechanical supernova feedback". In: *MNRAS* 451.3, pp. 2900–2921.

King, Andrew R., Ronald E. Taam, and Mitchell C. Begelman (2000). "The evolutionary status of SS 433". In: *ApJ* 530.1, pp. L25–L28.

Klessen, R. S. and S. C. O. Glover (2016). "Physical Processes in the Interstellar Medium". In: *Star Formation in Galaxy Evolution: Connecting Numerical Models to Reality, Saas-Fee Advanced Course, Volume 43. ISBN 978-3-662-47889-9. Springer-Verlag Berlin Heidelberg, 2016, p. 85* 43, p. 85.

Klypin, A. et al. (1999). "Where Are the Missing Galactic Satellites?" In: *ApJ* 522, pp. 82–92.

Knevitt, G. et al. (2014). "Heating and ionization of the primordial intergalactic medium by high-mass X-ray binaries". In: *MNRAS* 445, pp. 2034–2048.

Komatsu, E. and U. Seljak (2001). "Universal gas density and temperature profile". In: *MNRAS* 327, pp. 1353–1366.

Koposov, S. et al. (2008). "The Luminosity Function of the Milky Way Satellites". In: *ApJ* 686, pp. 279–291.

Kornei, K. A. et al. (2012). “The Properties and Prevalence of Galactic Outflows at z ˜ 1 in the Extended Groth Strip”. In: *ApJ* 758, p. 135.

Kroupa, P. (2001). “On the variation of the initial mass function”. In: *MNRAS* 322, pp. 231–246.

— (2002). “The Initial Mass Function of Stars: Evidence for Uniformity in Variable Systems”. In: *Science* 295, pp. 82–91.

Krumholz, M. R. and C. D. Matzner (2009). “The Dynamics of Radiation-pressure-dominated H II Regions”. In: *ApJ* 703, pp. 1352–1362.

Krumholz, M. R. and T. A. Thompson (2012). “Direct Numerical Simulation of Radiation Pressure-driven Turbulence and Winds in Star Clusters and Galactic Disks”. In: *ApJ* 760, 155, p. 155.

Krumholz, M.R. (2014). In: *Physics Reports-Review Section Of Physics Letters* 539.2, pp. 49–134.

Krymskii, G. F. (1977). “A regular mechanism for the acceleration of charged particles on the front of a shock wave”. In: *Akademiia Nauk SSSR Doklady* 234, pp. 1306–1308.

Kuzio de Naray, Rachel, Stacy S. McGaugh, and W. J. G. de Blok (2008). “Mass Models for Low Surface Brightness Galaxies with High-Resolution Optical Velocity Fields”. In: *ApJ* 676, p. 920.

Larson, R. B. (1981). “Turbulence and star formation in molecular clouds”. In: *MNRAS* 194.4, pp. 809–826.

Larson, Richard B. (2005). “Thermal physics, cloud geometry and the stellar initial mass function”. In: *MNRAS* 359.1, pp. 211–222.

Lehmer, B. D. et al. (2010). “A Chandra Perspective on Galaxy-wide X-ray Binary Emission and its Correlation with Star Formation Rate and Stellar Mass: New Results from Luminous Infrared Galaxies”. In: *ApJ* 724, pp. 559–571.

Lehmer, B. D. et al. (2014). “The X-Ray Luminosity Functions of Field Low-mass X-Ray Binaries in Early-type Galaxies: Evidence for a Stellar Age Dependence”. In: *ApJ* 789, p. 52.

Leitherer, C., C. Robert, and L. Drissen (1992). “Deposition of mass, momentum, and energy by massive stars into the interstellar medium”. In: *ApJ* 401, pp. 596–617.

Lequeux, J. et al. (1979). “Chemical composition and evolution of irregular and blue compact galaxies”. In: *A&A* 80, pp. 155–166.

Li, M. et al. (2015). “Supernova Feedback and the Hot Gas Filling Fraction of the Interstellar Medium”. In: *ApJ* 814, p. 4.

Lian, J. H. et al. (2015). “The mass-metallicity relation of Lyman-break analogues and its dependence on galaxy properties”. In: *MNRAS* 446, pp. 1449–1457.

Linden, T. et al. (2010). “The Effect of Starburst Metallicity on Bright X-ray Binary Formation Pathways”. In: *ApJ* 725, pp. 1984–1994.

Lockman, F. J., K. M. Blundell, and W. M. Goss (2007). “The distance to SS433/W50 and its interaction with the interstellar medium”. In: *MNRAS* 381, pp. 881–893.

Lopez, L. A. et al. (2011). “What Drives the Expansion of Giant H II Regions?: A Study of Stellar Feedback in 30 Doradus”. In: *ApJ* 731, 91, p. 91.

Lucy, L. B. and P. M. Solomon (1970). “Mass Loss by Hot Stars”. In: *ApJ* 159, p. 879.

Ma, X. et al. (2016). “Binary stars can provide the ‘missing photons’ needed for reionization”. In: *MNRAS* 459, pp. 3614–3619.

Mac Low, Mordecai-Mark and Andrea Ferrara (1999). “Starburst- driven mass loss from dwarf galaxies: efficiency and metal ejection”. In: *ApJ* 513.1, pp. 142–155.

Mackey, J. et al. (2015). “Wind bubbles within H ii regions around slowly moving stars”. In: *A&A* 573, A10.

Madau, P., A. Ferrara, and M. J. Rees (2001). “Early Metal Enrichment of the Intergalactic Medium by Pregalactic Outflows”. In: *ApJ* 555, pp. 92–105.

Madau, P., F. Haardt, and M. J. Rees (1999). “Radiative Transfer in a Clumpy Universe. III. The Nature of Cosmological Ionizing Sources”. In: *ApJ* 514, pp. 648–659.

Maeder, A. (1992). “Stellar yields as a function of initial metallicity and mass limit for black hole formation”. In: *A&A* 264, pp. 105–120.

Maoz, D., F. Mannucci, and G. Nelemans (2014). “Observational Clues to the Progenitors of Type Ia Supernovae”. In: *ARA&A* 52, pp. 107–170.

Martizzi, D., C.-A. Faucher-Giguère, and E. Quataert (2015). “Supernova feedback in an inhomogeneous interstellar medium”. In: *MNRAS* 450, pp. 504–522.

Martizzi, D. et al. (2016). “Supernova feedback in a local vertically stratified medium: interstellar turbulence and galactic winds”. In: *MNRAS* 459, pp. 2311–2326.

Mashchenko, Sergey, James Wadsley, and H. M. P. Couchman (2008). “Stellar Feedback in Dwarf Galaxy Formation”. In: *Science* 319.5860, pp. 174–177.

Mateo, M. (1994). “Dark Matter in Dwarf Spheroidal Galaxies: Observational Constraints”. In: *European Southern Observatory Conference and Workshop Proceedings*. Ed. by G. Meylan and P. Prugniel. Vol. 49. European Southern Observatory Conference and Workshop Proceedings, p. 309.

Mateo, M. L. (1998). “Dwarf Galaxies of the Local Group”. In: *ARA&A* 36, pp. 435–506.

Matzner, C. D. (2007). “Protostellar Outflow-driven Turbulence”. In: *ApJ* 659, pp. 1394–1403.

Matzner, Christopher D. (2002). In: *ApJ* 566, p. 302.

McConnachie, A. W. (2012). “The Observed Properties of Dwarf Galaxies in and around the Local Group”. In: *AJ* 144, p. 4.

McGreer, I. D., A. Mesinger, and V. D’Odorico (2015). “Model-independent evidence in favour of an end to reionization by z $\sim$ 6”. In: *MNRAS* 447, pp. 499–505.

McQuinn, M. (2016). “The Evolution of the Intergalactic Medium”. In: *ARA&A* 54, pp. 313–362.

Mennekens, N. and D. Vanbeveren (2016). “The delay time distribution of massive double compact star mergers”. In: *A&A* 589, A64.

Meynet, G. and A. Maeder (2000). “Stellar evolution with rotation. V. Changes in all the outputs of massive star models”. In: *A&A* 361, pp. 101–120.

Mineo, S., M. Gilfanov, and R. Sunyaev (2012). “X-ray emission from star-forming galaxies - I. High-mass X-ray binaries”. In: *MNRAS* 419, pp. 2095–2115.

Minkowski, R. (1941). “Spectra of Supernovae”. In: *PASP* 53, p. 224.

Mirabel, I. F. et al. (2011). “Stellar black holes at the dawn of the universe”. In: *Astronomy And Astrophysics* 528, A149.

Mo, Houjun, Frank Van Den Bosch, and Simon White (2010). *Galaxy Formation and Evolution*. GB: Cambridge University Press - M.U.A.

Monaghan, J. J. (1985). “Extrapolating B. Splines for Interpolation”. In: *Journal of Computational Physics* 60, pp. 253–262.

Moore, B. (1994). “Evidence against dissipation-less dark matter from observations of galaxy haloes”. In: *Nature* 370, pp. 629–631. DOI: 10.1038/370629a0.

Moore, B. et al. (1999). “Dark Matter Substructure within Galactic Halos”. In: *ApJ* 524, pp. L19–L22.

Moore, B. et al. (2006). “Globular clusters, satellite galaxies and stellar haloes from early dark matter peaks”. In: *MNRAS* 368, pp. 563–570.

Murray, N., E. Quataert, and T. A. Thompson (2010). "The Disruption of Giant Molecular Clouds by Radiation Pressure & the Efficiency of Star Formation in Galaxies". In: *ApJ* 709, pp. 191–209.

Murray, Norman (2011). In: *ApJ* 729, p. 133.

Myers, P. C. et al. (1986). "Molecular clouds and star formation in the inner galaxy - A comparison of CO, H II, and far-infrared surveys". In: *ApJ* 301, pp. 398–422.

Naab, T. et al. (2014). "The ATLAS^{3D} project - XXV. Two-dimensional kinematic analysis of simulated galaxies and the cosmological origin of fast and slow rotators". In: *MNRAS* 444, pp. 3357–3387.

Ngoumou, J. et al. (2015). "First Investigation of the Combined Impact of Ionizing Radiation and Momentum Winds from a Massive Star on a Self-gravitating Core". In: *ApJ* 798, 32, p. 32.

Nickerson, S. et al. (2011). "Mechanisms of baryon loss for dark satellites in cosmological smoothed particle hydrodynamics simulations". In: *MNRAS* 415, pp. 257–270.

Ntormousi, E. et al. (2011). "Formation of Cold Filamentary Structure from Wind-blown Superbubbles". In: *ApJ* 731, 13, p. 13.

Ochsendorf, B. B. et al. (2015). "Nested Shells Reveal the Rejuvenation of the Orion-Eridanus Superbubble". In: *ApJ* 808, 111, p. 111.

Olszewski, E. W. (1998). "Internal Kinematics of Dwarf Spheroidal Galaxies". In: *Galactic Halos*. Ed. by D. Zaritsky. Vol. 136. ASP Conf. Ser. P. 70.

Oppenheimer, B. D. et al. (2010). "Feedback and recycled wind accretion: assembling the z = 0 galaxy mass function". In: *MNRAS* 406, pp. 2325–2338.

Orosz, J. A. et al. (2011). "The Mass of the Black Hole in Cygnus X-1". In: *ApJ* 742, 84, p. 84.

OShea, Brian W. and Michael L. Norman (2007). "Population iii star formation in a cdm universe. i. the effect of formation redshift and environment on protostellar accretion rate". In: *ApJ* 654.1, pp. 66–92.

Ostriker, J. P. and C. F. McKee (1988). "Astrophysical blastwaves". In: *Rev. Mod. Phys.* 60, pp. 1–68.

Ott, J., F. Walter, and E. Brinks (2005). "A Chandra X-ray survey of nearby dwarf starburst galaxies - II. Starburst properties and outflows". In: *MNRAS* 358, pp. 1453–1471.

Pakull, Manfred W., Roberto Soria, and Christian Motch (2010). "A 300- parsec-long jet- inflated bubble around a powerful microquasar in the galaxy NGC 7793". In: *Nature* 466.7303, p. 209.

Pelupessy, F. I. and S. Portegies Zwart (2012). "The evolution of embedded star clusters". In: *MNRAS* 420, pp. 1503–1517.

Peters, T. et al. (2015). "Impact of Supernova and Cosmic-Ray Driving on the Surface Brightness of the Galactic Halo in Soft X-Rays". In: *ApJ* 813, p. L27.

Pidopryhora, Y., F. J. Lockman, and J. C. Shields (2007). "The Ophiuchus Superbubble: A Gigantic Eruption from the Inner Disk of the Milky Way". In: *ApJ* 656, pp. 928–942. eprint: astro-ph/0610894.

Planck Collaboration et al. (2014). "Planck 2013 results. XVI. Cosmological parameters". In: *A&A* 571, A16, A16.

Pontzen, A. and F. Governato (2012). "How supernova feedback turns dark matter cusps into cores". In: *MNRAS* 421, pp. 3464–3471.

— (2014). "Cold dark matter heats up". In: *Nature* 506, pp. 171–178.

Power, C. et al. (2009). "Primordial globular clusters, X-ray binaries and cosmological reionization". In: *MNRAS* 395, pp. 1146–1152.

Power, C. et al. (2014). "Stochastic Star Formation & Feedback: Mapping Low-Mass Galaxies to Dark Matter Haloes". In: *ArXiv e-prints*.

Price, D. J. (2007). "splash: An Interactive Visualisation Tool for Smoothed Particle Hydrodynamics Simulations". In: *Publ. Astron. Soc. Australia* 24, pp. 159–173.

— (2012). "Smoothed particle hydrodynamics and magnetohydrodynamics". In: *Journal of Computational Physics* 231, pp. 759–794.

Puls, J., J. S. Vink, and F. Najarro (2008). "Mass loss from hot massive stars". In: *A&ARv* 16, pp. 209–325.

Quinn, T. et al. (1997). "Time stepping N-body simulations". In: *ArXiv Astrophysics e-prints*.

Rahner, Daniel et al. (2017). "Winds and radiation in unison: a new semi- analytic feedback model for cloud dissolution". In: *MNRAS* 470.4, pp. 4453–4472.

Read, J. I. and T. Hayfield (2012). "SPHS: smoothed particle hydrodynamics with a higher order dissipation switch". In: *MNRAS* 422, pp. 3037–3055.

Renaud, F. et al. (2013). "A sub-parsec resolution simulation of the Milky Way: global structure of the interstellar medium and properties of molecular clouds". In: *MNRAS* 436, pp. 1836–1851.

Repolust, T., J. Puls, and A. Herrero (2004). "Stellar and wind parameters of Galactic O-stars. The influence of line-blocking/blanketing". In: *A&A* 415, pp. 349–376.

Rey-Raposo, R. et al. (2017). "The roles of stellar feedback and galactic environment in star-forming molecular clouds". In: *MNRAS* 464, pp. 3536–3551.

Ricotti, M. and N. Y. Gnedin (2005). "Formation Histories of Dwarf Galaxies in the Local Group". In: *ApJ* 629, pp. 259–267.

Robertson, B. E. et al. (2013). "New Constraints on Cosmic Reionization from the 2012 Hubble Ultra Deep Field Campaign". In: *ApJ* 768, 71, p. 71.

Robertson, B. E. et al. (2015). "Cosmic Reionization and Early Star-forming Galaxies: A Joint Analysis of New Constraints from Planck and the Hubble Space Telescope". In: *ApJ* 802, p. L19.

Rogers, H. and J. M. Pittard (2013). "Feedback from winds and supernovae in massive stellar clusters – I. Hydrodynamics". In: *MNRAS* 431.2, pp. 1337–1351.

Rosen, A. L. et al. (2014). "Gone with the wind: Where is the missing stellar wind energy from massive star clusters?" In: *MNRAS* 442, pp. 2701–2716.

Rosolowsky, E. (2005). "The Mass Spectra of Giant Molecular Clouds in the Local Group". In: *PASP* 117.838, pp. 1403–1410.

Russell, D. M., R. P. Fender, and P. G. Jonker (2007). "Evidence for a jet contribution to the optical/ infrared light of neutron star X- ray binaries". In: *MNRAS* 379.3, pp. 1108–1116.

Russell, D. M. et al. (2011). "New observations of ULX supershells, and their implications". In: *Astronomische Nachrichten* 332, p. 371.

Sana, H., G. James, and E. Gosset (2011). "The massive star binary fraction in young open clusters − III. IC 2944 and the Cen OB2 association". In: *MNRAS* 416.2, pp. 817–831.

Sana, H. et al. (2013). "The VLT-FLAMES Tarantula Survey. VIII. Multiplicity properties of the O-type star population". In: *A&A* 550, A107.

Sandage, A. and B. Binggeli (1984). "Studies of the Virgo cluster. III - A classification system and an illustrated atlas of Virgo cluster dwarf galaxies". In: *AJ* 89, pp. 919–931.

Saslaw, W. C. and D. Zipoy (1967). "Molecular Hydrogen in Pre-galactic Gas Clouds". In: *Nature* 216, pp. 976–978. DOI: 10.1038/216976a0.

Sawala, T. et al. (2010). "Formation of isolated dwarf galaxies with feedback". In: *MNRAS* 402.

Sawala, T. et al. (2015). "Bent by baryons: the low-mass galaxy-halo relation". In: *MNRAS* 448, pp. 2941–2947.

Sawala, T. et al. (2016). "The chosen few: the low-mass haloes that host faint galaxies". In: *MNRAS* 456, pp. 85–97.

Schaller, G. et al. (1992). "New grids of stellar models from 0.8 to 120 solar masses at Z = 0.020 and Z = 0.001". In: *ApJS* 96, pp. 269–331.

Schaye, J. et al. (2003). "Metallicity of the Intergalactic Medium Using Pixel Statistics. II. The Distribution of Metals as Traced by C IV". In: *ApJ* 596, pp. 768–796.

Schaye, J. et al. (2015). "The EAGLE project: simulating the evolution and assembly of galaxies and their environments". In: *MNRAS* 446, pp. 521–554.

Schoenberg, I. J. (1946). "Contributions to the problem of approximation of equidistant data by analytic functions. Part A." In: *Quart. Appl. Math.* 4, pp. 45–99.

Sedov, L. I. (1959). *Similarity and Dimensional Methods in Mechanics*.

Sell, P. H. et al. (2010). "Parsec-scale Bipolar X-ray Shocks Produced by Powerful Jets from the Neutron Star Circinus X-1". In: *ApJ* 719, pp. L194–L198.

Sell, Ph et al. (2015). "Shell- shocked: the interstellar medium near Cygnus X- 1". In: *MNRAS* 446.4, pp. 3579–3592.

Sharma, P. et al. (2014). "In a hot bubble: why does superbubble feedback work, but isolated supernovae do not?" In: *MNRAS* 443, pp. 3463–3476.

Shen, S. et al. (2014). "The Baryon Cycle of Dwarf Galaxies: Dark, Bursty, Gas-rich Polluters". In: *ApJ* 792, p. 99.

Simpson, C. M. et al. (2017). "Quenching and ram pressure stripping of simulated Milky Way satellite galaxies". In:

Skinner, M. A. and Eve C. Ostriker (2015). "Numerical simulations of turbulent molecular clouds regulated by reprocessed radiation feedback from nascent super star clusters". In: *ApJ* 809.2, p. 187.

Smith, M. C., D. Sijacki, and S. Shen (2017). "Supernova feedback in numerical simulations of galaxy formation: separating physics from numerics". In: *ArXiv e-prints*.

Smith, N. (2014). "Mass Loss: Its Effect on the Evolution and Fate of High-Mass Stars". In: *ARA&A* 52, pp. 487–528.

Song, H. F. et al. (2016). "Massive star evolution in close binaries. Conditions for homogeneous chemical evolution". In: *A&A* 585, A120.

Soria, R. et al. (2010). “Radio lobes and X-ray hotspots in the microquasar S26”. In: *MNRAS* 409, pp. 541–551.

Spitzer, L. (1978). *Physical processes in the interstellar medium*.

Springel, V. (2005). “The cosmological simulation code GADGET-2”. In: *MNRAS* 364, pp. 1105–1134.

Springel, V., N. Yoshida, and S. D. M. White (2001). “GADGET: a code for collisionless and gasdynamical cosmological simulations”. In: *New Astron.* 6, pp. 79–117.

Springel, Volker and Lars Hernquist (2003). “Cosmological smoothed particle hydrodynamics simulations: a hybrid multiphase model for star formation”. In: *MNRAS* 339.2, pp. 289–311.

Srbinovsky, J. A. and J. S. B. Wyithe (2007). “Constraining the quasar contribution to the reionization of cosmic hydrogen”. In: *MNRAS* 374, pp. 627–633.

Stanway, E. R., J. J. Eldridge, and G. D. Becker (2016). “Stellar population effects on the inferred photon density at reionization”. In: *MNRAS* 456, pp. 485–499.

Stevens, I. R. and J. M. Hartwell (2003). “The cluster wind from local massive star clusters”. In: *MNRAS* 339, pp. 280–288.

Stinson, G. et al. (2006). “Star formation and feedback in smoothed particle hydrodynamic simulations - I. Isolated galaxies”. In: *MNRAS* 373, pp. 1074–1090.

Stinson, G. S. et al. (2013). “Making Galaxies In a Cosmological Context: the need for early stellar feedback”. In: *MNRAS* 428, pp. 129–140.

Su, K.-Y. et al. (2017). “Discrete Effects in Stellar Feedback: Individual Supernovae, Hypernovae, and IMF Sampling in Dwarf Galaxies”. In: *ArXiv e-prints*.

Sukhbold, Tuguldur et al. (2016). “Core- collapse supernovae from 9 to 120 solar masses based on neutrino- powered explosions”. In: *ApJ* 821.1, p. 38.

Sutherland, Ralph S. and M. A. Dopita (1993). “Cooling functions for low-density astrophysical plasmas”. In: *ApJS* 88.1, pp. 253–327.

Tang, Y. et al. (2014). “Probing Outflows in z = 1 ˜ 2 Galaxies through Fe II/Fe II* Multiplets”. In: *ApJ* 793, p. 92.

Taylor, G. (1950). “The Formation of a Blast Wave by a Very Intense Explosion. I. Theoretical Discussion”. In: *Proceedings of the Royal Society of London Series A* 201, pp. 159–174.

Tenorio-Tagle, G. (1979). “The gas dynamics of H II regions. I - The champagne model”. In: *A&A* 71, pp. 59–65.

Teyssier, R. et al. (2013). "Cusp-core transformations in dwarf galaxies: observational predictions". In: *MNRAS* 429, pp. 3068–3078.

Tilvi, V. et al. (2014). "Rapid Decline of Lyα Emission toward the Reionization Era". In: *ApJ* 794, p. 5.

Tolstoy, E., V. Hill, and M. Tosi (2009). "Star-Formation Histories, Abundances, and Kinematics of Dwarf Galaxies in the Local Group". In: *ARA&A* 47, pp. 371–425.

Tomisaka, K., A. Habe, and S. Ikeuchi (1981). "Sequential explosions of supernovae in an OB association and formation of a superbubble". In: *Ap&SS* 78, pp. 273–285.

Trujillo-Gomez, S. et al. (2015). "Low-mass galaxy assembly in simulations: regulation of early star formation by radiation from massive stars". In: *MNRAS* 446, pp. 1140–1162.

Vink, J. (2012). "Supernova remnants: the X-ray perspective". In: *A&ARv* 20, 49, p. 49.

Vink, J. S., A. de Koter, and H. J. G. L. M. Lamers (2001). "Mass-loss predictions for O and B stars as a function of metallicity". In: *A&A* 369, pp. 574–588.

Vogelsberger, M. et al. (2014). "Introducing the Illustris Project: simulating the coevolution of dark and visible matter in the Universe". In: *MNRAS* 444, pp. 1518–1547.

Walch, S. and T. Naab (2015a). "The energy and momentum input of supernova explosions in structured and ionized molecular clouds". In: *MNRAS* 451, pp. 2757–2771.

— (2015b). "The energy and momentum input of supernova explosions in structured and ionized molecular clouds". In: *MNRAS* 451, pp. 2757–2771.

Walch, S. et al. (2013). "Clumps and triggered star formation in ionized molecular clouds". In: *MNRAS* 435, pp. 917–927.

Walch, S. et al. (2015). "Comparing simulations of ionization triggered star formation and observations in RCW 120". In: *MNRAS* 452, pp. 2794–2803.

Walch, S. K. et al. (2012). "Dispersal of molecular clouds by ionizing radiation". In: *MNRAS* 427, pp. 625–636.

Walker, M. G., M. Mateo, and E. Olszewski (2007). "Distribution Of Dark Matter In The Smallest Galaxies". In: *American Astronomical Society Meeting Abstracts*. Vol. 39. Bulletin of the American Astronomical Society, p. 776.

Walker, M. G. and J. Peñarrubia (2011). "A Method for Measuring (Slopes of) the Mass Profiles of Dwarf Spheroidal Galaxies". In: *ApJ* 742, p. 20.

Weaver, R. et al. (1977). "Interstellar bubbles. II - Structure and evolution". In: *ApJ* 218, pp. 377–395.

Weisz, D. R. et al. (2014). "The Star Formation Histories of Local Group Dwarf Galaxies. I. Hubble Space Telescope/Wide Field Planetary Camera 2 Observations". In: *ApJ* 789, 147, p. 147.

Wendland, Holger (1995). "Piecewise polynomial, positive definite and compactly supported radial functions of minimal degree". In: *Advances in Computational Mathematics* 4.1, pp. 389–396.

Wetzel, A. R. et al. (2016). "Reconciling Dwarf Galaxies with ΛCDM Cosmology: Simulating a Realistic Population of Satellites around a Milky Way-mass Galaxy". In: *ApJ* 827, p. L23.

Wheeler, C. et al. (2015). "Sweating the small stuff: simulating dwarf galaxies, ultra-faint dwarf galaxies, and their own tiny satellites". In: *MNRAS* 453, pp. 1305–1316.

Wilkinson, Mark I. et al. (2004). "Kinematically Cold Populations at Large Radii in the Draco and Ursa Minor Dwarf Spheroidal Galaxies". In: *ApJ* 611, pp. L21–L24.

Williams, Jonathan P. and Christopher F. McKee (1997). "The galactic distribution of ob associations in molecular clouds". In: *ApJ* 476.1, pp. 166–183.

Woltjer, L. (1972). "Supernova Remnants". In: *ARA&A* 10, p. 129.

Xiao, L., E. R. Stanway, and J. J. Eldridge (2018). "Emission-line diagnostics of nearby H II regions including interacting binary populations". In: *MNRAS* 477, pp. 904–934.

Yoon, S.-C., S. E. Woosley, and N. Langer (2010). "Type Ib/c Supernovae in Binary Systems. I. Evolution and Properties of the Progenitor Stars". In: *ApJ* 725, pp. 940–954.

Yoshida, Naoki, Kazuyuki Omukai, and Lars Hernquist (2007). "Formation of massive primordial stars in a reionized gas". In: *ApJ* 667.2, pp. L117–L120.

Zapartas, E. et al. (2017). "Delay-time distribution of core-collapse supernovae with late events resulting from binary interaction". In: *A&A* 601, A29.

Zhang, Weiqun, S. E. Woosley, and A. Heger (2008). "Fallback and black hole production in massive stars". In: *ApJ* 679.1, pp. 639–654.

Zhu, Q. et al. (2016). "Baryonic impact on the dark matter distribution in Milky Way-sized galaxies and their satellites". In: *MNRAS* 458, pp. 1559–1580.

Zubovas, Kastytis, Graham A. Wynn, and Alessia Gualandris (2013). "Supernovae in the central parsec: a mechanism for producing spatially anisotropic hypervelocity stars". In: *ApJ* 771.2, p. 118.